Airborne Observations of the Physical and Optical Properties of Atmospheric Aerosol

Jennifer Kathleen Brooke

Submitted in accordance with the requirements for the degree of
Doctor of Philosophy

The University of Leeds

School of Earth and Environment

March 2014

The candidate confirms that the work submitted is her own, except where work which has formed part of jointly-authored publications has been included. The contribution of the candidate and the other authors to this work has been explicitly indicated overleaf. The candidate confirms that appropriate credit has been given within the thesis where reference has been made to the work of others.

This copy has been supplied on the understanding that it is copyright material and that no quotation from the thesis may be published without proper acknowledgement.

The right of Jennifer Kathleen Brooke to be identified as Author of this work has been asserted by her in accordance with the Copyright, Designs and Patents Act 1988.

Paper status and collaborator contributions

Parts of this thesis contain papers prepared for publication where the scientific content has been contributed to by multiple authors. The role of each author is clarified below.

Chapter 4 contributed to the paper: 'Ryder, C.L., Highwood, E.J., Rosenberg, P.D., Trembath, J., Brooke, J.K., Bart, M., Dean, A., Crosier, J., Dorsey, J., Brindley, H., Banks, J., Marsham, J.H., McQuaid, J.B., Sodemann, H., Washington, R., 2013b. Optical properties of Saharan dust aerosol and contribution from the coarse mode as measured during the Fennec 2011 aircraft campaign. Atmos. Chem. Phys. 13. 303 –325, 2013.

The candidate was one of two instrument operators of the Low Turbulence Inlet during the 2011 Fennec campaign. The second instrument operator, M. Bart is a co-author on the paper. The candidate quality-controlled the Low Turbulence Inlet data and performed corrections for refractive index on the Grimm OPC data set, with guidance from co-authors C.L. Ryder and R.D. Rosenberg. The instrument sub-sampler correction step was performed by J. Trembath, and is acknowledged in chapter 4. Investigation of Low Turbulence Inlet performance and comparisons of size distributions measured forms the majority of chapter 4 within the thesis. A processed dataset incorporating refractive index corrections was supplied to the first author, C.L. Ryder. The text and figures within the publication were written by the first author of the paper C.L. Ryder, University of Reading.

Acknowledgements

First and foremost, I would like to express my sincere thanks and gratitude to my supervisors, Jim McQuaid and Barbara Brooks for all their help, guidance and encouragement throughout my PhD. The research in this thesis was supported the Natural Environmental Research Council, studentship reference NE/H524673/1 and via a CASE award from the U.K. Met Office, and I am grateful to them for making this project possible. I would like to thank my Met Office co-supervisor, Simon Osborne for his support, many helpful discussions and for the opportunity to make a number of visits to the Met Office Cardington site during my PhD. The Fennec project was funded by the Natural Environment Research Council grant NE/G017166/1 and the SAMBBA project was supported by a Natural Environment Research Council grant NE/J010073/1. Thank you to the dedicated effort by FAAM, DirectFlight and Avalon during both of the aircraft campaigns.

I am grateful to the Fennec and SAMBBA participants for sharing their data with me. The aerosol mass spectrometer and single particle soot photometer were operated by the University of Manchester and thank you to Will Morgan for providing the data from it, and for a number of interesting discussions over the past year. Lidar data was provided by Franco Marenco and Grimm Sky-OPC data was provided by Jamie Trembath. Thank you to the efforts of Graeme Nott for organising the SAMBBA instrument mega-calibration. I am grateful to Phil Rosenberg for many helpful aerosol discussions and to Mark Bart for his help and support during the early stages of my PhD. Thanks also go to Justin Langridge, Kate Szpek, Franco Marenco and Jim Haywood for their thoughts and helpful discussions.

Thank you to all the people from the field campaigns that have left me with some fantastic memories. ICAS has been a great department to be a part of and though there are too many to name, Sarah, Cat and Jackie deserve a specific mention. To the lovely ladies, past and present, of 10.127 for their wonderful company in the office and the constant supply of cake and Percy pigs! T hank you to my housemates Ali, Laura and Carly for inviting me in to such a wonderful house, I would not have gotten this far without you all! To David for being my escape and being the most relaxed person I know. I owe an overwhelming thank you to my extended family, my brother and my parents for their continual support, belief and encouragement.

Abstract

Aerosols have a significant influence on both human health and global climate, and are associated with a potentially important role in future climate change. The microphysical and optical properties of aerosols need to be well quantified to understand the radiative impact, important in weather and climate models. This work focuses on two globally significant species from two different aircraft campaigns, mineral dust and biomass burning aerosol.

An analysis is presented of mineral dust properties from the Saharan region during the Fennec campaign in June 2011 and 2012. In making observations it is crucial to understand the associated measurement limitations. The Low Turbulence Inlet (LTI) was designed to improve inlet efficiency and is shown to quantifiably measure coarse mode mineral dust up to 10 μm. This has allowed for Rosemount inlet characterisation with enhancements relative to the LTI determined to be 8 times for particles up to 3.0 μm.

The physical and optical properties and vertical structure of aged Rondônian regional haze from the SAMBBA campaign in Rondônia, Brazil in September 2012 are characterised. Good agreement is shown between *in-situ* extinction coefficients and those retrieved using lidar remote sensing. Characterisation of airborne thermo-optical techniques for measuring black carbon content is achieved through comparisons with SP2 measurements. Total number concentration was reduced by 77 % compared with 96 % for the SP2, suggesting not all volatile material was removed with the thermo-optical technique.

The imaginary part of the aerosol refractive index was 40 % lower using the Maxwell-Garnett mixing rule compared with the volume-mixing rule for Rondônian regional haze. This difference is small compared with the uncertainty derived from the assumed refractive index of the sub-components, particularly for organic carbon; the single-scattering albedo at 550 nm is shown to range from 0.88 to 0.95. Humidification effects on the optical properties of biomass burning aerosol were found to be negligible due to modest ambient relative humidities. Comparisons with retrieved properties from the SCAR-B campaign in 1995 suggest consistency in biomass burning and agricultural practices over time.

Table of Contents

List of figures

List of tables

Abbreviations

AATSR	Advanced Along-Track Scanning Radiometer
AERONET	AErosol RObotic NETwork
AMAZE-08	Amazonian Aerosol Characterization Experiment
AMMA	African Monsoon Multidisciplinary Analysis
AM	Accumulation Mode
AMS	Aerosol Mass Spectrometer
AOD	Aerosol Optical Depth
ARL	Air Resources Laboratory
AR4	Fourth Assessment Report (IPCC)
AR5	Fifth Assessment Report (IPCC)
ASASPX	Active Scattering Aerosol Spectrometer Probe
BC	Black Carbon
BL	Boundary Layer
BoDEx	Bodele Dust Experiment
CCN	Cloud Condensation Nuclei
CDP	Cloud Droplet Probe
CM	Coarse Mode
CMD	Count Median Diameter
CMIP3	Coupled Model Intercomparison Project
CMR	Count Median Radius
CO	Carbon Monoxide
CO_2	Carbon Dioxide
CPC	Condensation Particle Counter
C-ToF	Compact Time-of-Flight
DABEX	Dust and Biomass Burning Experiment
DDA	Discrete Dipole Approximation
DEHS	Di-Ethyl-Hexyl-Sebacate
DMA	Differential Mobility Analyser
DMT	Droplet Measurement Technologies
DODO	Dust Outflow and Deposition
ECMWF	European Centre Medium-Range Weather Forecast
EM	Electromagnetic
FAAM	Facility for Airborne Atmospheric Measurements
FAR	First Assessment Report

FGAM	Facility for Ground based Atmospheric Measurements
FUE	Fuerteventura
GAW	Global Atmosphere Watch
GCM	Global Climate Models
GERBILS	Geostationary Earth Radiation Budget Intercomparison of Longwave and Shortwave radiation
GHG	Green House Gases
GMD	Geometric Mean Diameter
GMR	Geometric Mean Radius
GOES	Geostationary Operational Environmental Satellite
GOME	Global Ozone Monitoring Experiment
HULIS	Humic-Like Species
HYSPLIT	Hybrid Single Particle Lagrangian Integrated Trajectory Model
LBA-SMOCC	Large-Scale Biosphere Atmosphere Experiment in Amazonia – Smoke Aerosols, Clouds, Rainfall, and Climate
IN	Ice Nuclei
INPE	Instituto Nacional de Pesquisas Espaciais
IPCC	Intergovernmental Panel Climate Change
IR	Infra-Red
ITCZ	Intertropical Convergence Zone
ITD	Intertropical Discontinuity
LTI	Low Turbulence Inlet
LAC	Light Absorbing Carbon
LAM	Limited Area Model
LLJ	Low Level Jet
LIDAR	LIght Detection And Ranging
LOSU	Level of Scientific Understanding
MATLAB	Computation and visualisation software
MetUM	Met Office Unified Model
MIEV0	Mie Theory Code (written by Wiscombe)
MISR	Multi-angle Imaging SpectroRadiometer
MODIS	Moderate Resolution Imaging Spectroradiometer
MMD	Mass Median Diameter
MMR	Mass Median Radius
MSA	Minimum Safe Altitude
MSG	Meteosat Second Generation

MSPL	Mean Sea Level Pressure
NCAR	National Centre for Atmospheric Research
NERC	Natural Environment Research Council
NOAA	National Oceanic and Atmospheric Administration
NWP	Numerical Weather Predication
O_3	Ozone
OA	Organic Aerosol
OLR	Outgoing Longwave Radiation
OPC	Optical Particle Counter
P	Profile
PBL	Planetary Boundary Layer
PCASP	Passive Cavity Aerosol Spectrometer Probe
PM	Particulate Matter
$PM_{2.5}$	Particulate Matter with an aerodynamic diameter of up to 2.5 µm
PM_{10}	Particulate Matter with an aerodynamic diameter of up to 10 µm
PMS	Particle Measurement Systems
PMSL	Pressure at Mean Sea Level
POA	Primary Organic Aerosol
PRIDE	Puerto Rico Dust Experiment
PSAP	Particle Soot Absorption Photometer
PSL	Polystyrene Latex Spheres
PVH	Porto Vehlo
Re	Reynolds Number
RF	Radiative Forcing
RH	Relative Humidity
RI	Refractive Index
SAFARI	Southern AFricAn Regional science Initiative
SAFIRE	Service des Avions Francais Instrumentés pour la Recherche en Environnement
SAMBBA	South American Biomass Burning Analysis
SAMUM	Saharan Mineral Dust Experiment
SAVEX	Sun-photometer Airborne Validation Experiment
SCAR-B	Smoke, Clouds, and Radiation-Brazil
SEVIRI	Spinning Enhanced Visible and Infrared Imager
SHADE	Saharan Dust Experiment
SHL	Saharan Heat Low

SID	Small Ice Detector
SLR	Straight and Level Runs
SMPS	Scanning Mobility Particle Sizer
SOA	Secondary Organic Aerosol
SP2	Single Particle Soot Photometer
TAR	Third Assessment Report
UM	Unified Model
UTC	Coordinated Universal Time
UV	Ultra Violet
VACC	Volatile Aerosol Concentration and Composition
VOC	Volatile Organic Carbon
VMD	Volume Median Diameter
VMR	Volume Median Radius

Parameters

α	Size Parameter (no units)
Å	Angstrom Exponent (no units)
A_{PSAP}	Area Spot Size (mm^2)
b_{abs}	Absorption coefficient (m^{-1} / Mm^{-1})
b_{ext}	Extinction coefficient (m^{-1} / Mm^{-1})
b_{scat}	Scattering coefficient (m^{-1} / Mm^{-1})
C_{spot}	Spot Size Correction (no units)
CMD	Count Median Diameter (μm)
dN/dlogD	Number size distribution (cm^{-3})
dS/dlogD	Surface area size distribution (μm^2 cm^{-3})
D_{core}	Median diameter of core (μm)
D_g	Geometric number mean diameter (μm)
D_gV	Geometric volume mean diameter (μm)
D_p	Mean Diameter (μm)
D_{shell}	Median diameter of shell (μm)
D_{shell}/D_{core}	Median shell-to-core diameter ratio (no units)
ε_{eff}	Complex effective dielectric constant of the mixture (no units)
ε_{incl}	Complex dielectric constant of the absorbing compounds (no units)
ε_{part}	Complex dielectric constant of non-absorbing compounds (no units)

f_i	Volume fraction (no units)
g	Asymmetry parameter (no units)
I_{abs}	Energy absorbed (W m^{-2})
I_{scat}	Energy scattered (W m^{-2})
k	Imaginary part of refractive index (no units)
K_{abs}	Mass absorption efficiency (m^2 g^{-1})
K_{ext}	Mass extinction efficiency (m^2 g^{-1})
K_{scat}	Mass scattering efficiency (m^2 g^{-1})
m	Complex refractive index (no units)
n	Real part of the refractive index (no units)
N	Number concentration (cm^{-3})
N_{frac}	Fraction of number concentration in each lognormal mode (no units)
N_{shell}/N_{core}	Median shell-to-core number concentration ration (no units)
N_{tot}	Total number concentration in each lognormal mode (cm^{-3})
$P(\theta)$	Scattering phase function (sr^{-1})
ρ	Density (g m^{-3})
Q_{abs}	Absorption efficiency (no units)
Q_{ext}	Extinction efficiency (no units)
Q_{scat}	Scattering efficiency (no units)
R	Mean particle radius (μm)
σ_{abs}	Absorption cross section (μm^2)
σ_{ext}	Extinction cross section (μm^2)
σ_g	Geometric number standard deviation (no units)
$\sigma_g V$	Geometric volume standard deviation (no units)
σ_{scat}	Scattering cross section (μm^2)
$\sigma_s(RH)/\sigma$	Hygroscopic growth factor (units)
τ	Atmospheric lifetime
V_d	Deposition velocity (cm s^{-1})
V_{incl}	Volume fraction of the scattering particle (no units)
V_{part}	Volume fraction of the absorbing inclusions (no units)
λ	Wavelength (nm)
λ_0	Wavelength of incident ray of light (nm)
λ_S	Wavelength of scattered light (nm)
ω_0	Single-scattering albedo (no units)
$1 - \omega_0$	Single scattering co-albedo (no units)

1 Introduction and Review of Current Literature

Aerosols have a significant influence on both human health and global climate, with a potentially important role in future climate change. The Intergovernmental Panel on Climate Change (IPCC) was established by the World Meteorological Organisation (WMO) and the United Nations Environment Program (UNEP) in 1988. The IPCC are the leading international body providing an assessment of the current scientific basis of climate change, its potential impacts on changing weather and climate extremes, and the mitigation of climate change.

Radiative forcings (RF) are described by Ramaswamy et al. (2001) as the net (downwelling shortwave minus upwelling longwave) irradiance flux at the top of the atmosphere due to an external perturbation that has the potential to change the energy balance, measured in units of Watts per square meter (W m^{-2}) (Houghton et al., 1996). A *positive* forcing (decrease in solar radiation reflected back to space at the top of the atmosphere) tends to warm the atmosphere, while a *negative* forcing (increase in solar radiation reflected back to space at the top of the atmosphere) tends to cool the atmosphere.

The IPCC Fifth Assessment Report (AR5) concluded that it is extremely likely (95 %) that human influence has been the dominant cause of the observed warming since the mid-20th century (Stocker et al., 2013). The AR5 introduces a second concept, the *adjusted forcing (AF)*, which accounts for the rapid adjustment of components in the atmosphere which are assumed to be constant in the RF concept. Such adjustments include the changes to clouds by aerosols and occur on a time scale much faster than the ocean responses to forcing. The total anthropogenic radiative forcing for the year 2011 relative to the preindustrial era (taken to be 1750) is 2.4 $\pm$ 0.6 W m^{-2}, and the adjusted forcing is 2.2 $\pm$ 0.9 Wm^{-2}. The adjusted forcing is smaller than the radiative forcing, with a greater associated uncertainty, due to the inclusion of the impacts of clouds within the best estimate.

The total The IPCC Fourth Assessment Report (AR4) (Forster et al., 2007) presented a total net radiative forcing due to human activities of 1.6 W m^{-2}. This equates to a 43 % increase in the total anthropogenic radiative forcing since the AR4; due to the continued emissions of long-lived greenhouse gases (GHGs) such as carbon dioxide (CO_2) and methane (CH_4), and improved estimates of the aerosol radiative forcing. Concentrations of greenhouse gases have steadily increased with daily mean CO_2 concentrations surpassing 400 parts per million (ppm) in May 2013, for the first time since measurements began in 1958 at the Mauna Loa Observatory. Greenhouse gases have lead to a strong warming as the gases strongly absorb longwave radiation in the atmosphere, and the associated level of scientific understanding have shown significant advances since the First Assessment Report (FAR) in 1990.

The AR5 radiative forcing of the total aerosol effect in the atmosphere, incorporating cloud adjustments due to aerosols is -0.9 W m^{-2}, with an associated uncertainty in the range from -1.9 to -0.1 W m^{-2}. The direct forcing attributed to aerosols is -0.27 W m^{-2} with a range from -0.77 to 0.23 W m^{-2}; AR5 incorporates individual aerosol forcings for mineral dust, sulphate, nitrate, organic carbon and black carbon, with a high level of confidence. The IPCC Fourth Assessment Report (AR4) presented a stronger net cooling effect of all atmospheric aerosols species; a total radiative forcing from the direct aerosol effect is -0.5 W m^{-2}, with an associated uncertainty in the range from -0.1 to -0.9 W m^{-2}. This difference is due to the inclusion of a positive forcing by black carbon absorption of solar radiation (further details are provided in figure 1.15, and referred to in section 1.3.2). The aerosol direct effect relates to the scattering and absorption of shortwave and longwave radiation from the aerosol particle itself.

The aerosol direct radiative forcings requires knowledge of a set of aerosol parameters (defined at a specific wavelength or as a function of wavelength); the aerosol mass extinction efficiency (K_{ext}), the single-scattering albedo (ω_0) and the asymmetry parameter (g) in order to fully define the optical properties of an aerosol. The sign and magnitude of the aerosol radiative forcing can then be determined by additional knowledge of the aerosol mass distribution. The shortwave forcing additionally requires an understanding of the vertical distribution of clouds. The understanding of optical properties is key for validating and improving retrieval algorithms from satellite measurements and in model representation.

Aerosol longwave forcing is also dependent on the aerosol burden throughout the atmospheric column because of changes in temperature with height. Studies have shown that the single-scattering albedo determines the sign of the radiative forcing for a given underlying surface, be it dark ocean or bright cloud, whilst the combination of the asymmetry of the phase function and mass extinction efficiency contribute to the magnitude of the direct radiative forcing (Hansen et al., 1997).

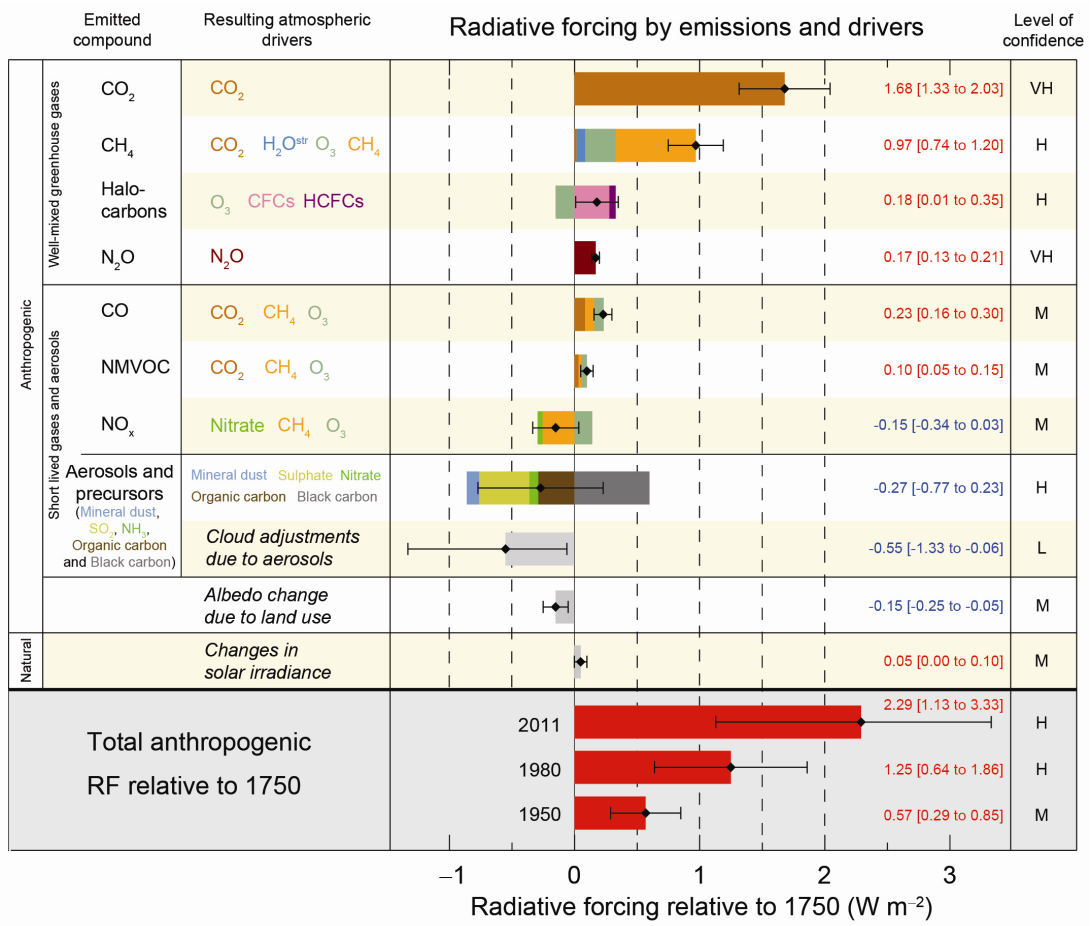

Figure 1.1 Global average radiative forcing (RF) best estimates (W m^{-2}) and uncertainty in the year 2011 relative to those in 1750 for the principal anthropogenic components of the atmosphere. Total anthropogenic radiative forcing is provided for three years (1950, 1980 and 2011) relative to 1750. The bars and whiskers show the best estimates and uncertainties, respectively, for the different climate forcing terms. Indicated is the level of confidence. Reproduced from IPCC Fifth Assessment Report AR5 (Stocker et al., 2013).

The incorporation of cloud adjustments due to aerosol accounts for a radiative forcing in AR5 of -0.55 W m^{-2} (-1.33 to 0.06 W m^{-2}). The largest uncertainty in terms of total aerosol radiative forcing is due to cloud adjustment due to aerosols, that is, the aerosol indirect effect; the influence of aerosols on the lifetime, extent and albedo of clouds. The so-called first indirect effect considers changes in cloud albedo, related to changes in the concentration of cloud condensation nuclei (CCN) and hence cloud droplet number concentration (Twomey, 1977). The second indirect effect accounts for changes in precipitation rates and cloud lifetime due to changes in aerosol concentration (Alberecht, 1989). The high uncertainty associated with the cloud lifetime effect means no best estimate in the radiative forcing was stated in AR4.

Particulate matter (PM) in high concentrations are a concern due to the impact on human health; PM act as irritants to the respiratory system and have been linked with exacerbating conditions such as asthma and bronchitis (Harrison and Yin, 2000). A better understanding of these problems will enable legislation to improve air quality (Oberdorster et al., 2005).

This overview begins with a review of aerosol fundamentals which underline the research presented in this thesis and draws on theories presented in text books such as Seinfeld and Pandis (2006), Hinds (1999) and Kulkarni et al. (2011a). The second half of this review draws on these underlying fundamental concepts and presents the current literature for two globally-important aerosol species; Saharan mineral dust and Amazonian biomass burning aerosol. The largest single source of global mineral dust is the Saharan-Sahel region in Northern Africa. Despite considerable investment in a number of previous campaigns carrying out atmospheric measurements there still remains a sparse dataset of key optical properties and there remains a range in published values of properties such as refractive index, mass extinction efficiency and the asymmetry parameter. Forty percent of global emission of black carbon are from biomass burning, with emissions dominated in regional hotspots such as West Africa and the Amazon Basin region (Streets et al., 2004). Amazonian biomass burning is the largest source of anthropogenic aerosol in the southern hemisphere (Koren et al., 2004). The remote Amazonian region suffers from a critical lack of observational data of their physical and optical aerosol measurements.

The review highlights the current understanding of the physical and optical properties of these two aerosol types and identifies the variability within the present literature of

these key parameters, reflecting the necessity of further observations, for improved parameterisation in models, understanding of key optical properties required in calculating radiative forcing and necessary for validating and improving retrieval algorithms from satellite measurements.

1.1 Aerosol Fundamentals

1.1.1 Aerosol Microphysical Properties: Size Distributions

The accurate characterisation of the aerosol size distribution is a highly important measurable property towards the determination of the effect of atmospheric aerosols on the climate. Size distributions are a microphysical parameter which gives information on concentration and size of an aerosol population. They are typically presented in discrete size intervals (an instrumental artefact, also known as bins) with a corresponding number concentration for this size interval. Along with knowledge of total aerosol concentration, size distributions are important to be able to assess how much an individual particle size contributes to the aerosol budget. Aerosols cover a vast size range and achieving measurements across this range presents a practical challenge.

As a method of representing an aerosol size distribution, for example in models, lognormal modes can be fitted across a size distribution (Whitby, 1978; Willeke and Brockmann, 1977). These represent the nucleation, Aitken, accumulation and coarse mode of an aerosol. The lognormal distribution can be fitted by equation (1.1), (Hinds, 1999) in which the full size distribution is represented by the combination of the geometric mean diameter, geometric standard deviation and total concentration of the individual lognormal modes.

$$\frac{dN}{dlogD} = \sum_{i=1}^{i} \frac{N_i}{\sqrt{2\pi} log\sigma_{gi}} exp\left(-\frac{(logd_p - \log{(CMD_i)^2}}{2(log\sigma_{g_i})^2}\right) \quad (1.1)$$

where d_p mean geometric diameter of the aerosol particle, N_i to the total number concentration in the respective mode, *i*, CMD_i count median diameter of mode *i*. The logarithm is base 10.

The nucleation mode covers the size range of <0.01 μm, and are formed through nucleation processes involving gas to particle conversion. There is no real distinguishing size between molecular clusters and what might be called particles. The lower size limit

is effectively defined by measurement devices. Ultrafine nucleation nuclei have atmospheric lifetimes in the order of minutes to hours, dependent on the rate of coagulation which lead to the growth of particles into the Aitken mode (Kulmala et al., 2013; Kulmala et al., 2004a; Kulmala et al., 2004b).

Aitken mode aerosols are in the size range of 0.01 μm < D_p > 0.1 μm, and have an atmospheric lifetime greater than that of nucleation nuclei in the order of hours to days. Coagulation and condensation processes act to increase particle size from which aerosols fall into the accumulation mode aerosols (Seinfeld and Pandis, 2006). They may maintain chemical integrity to some extent depending on the condensing gases.

Accumulation mode aerosols are in the size range of 0.1 μm < D_p > 2.5 μm and tend to be formed either through the direct emission into the atmosphere (primary particles), through the growth of Aitkin mode particles due to coagulation processes or through gas-to-particle conversion by condensation of sulphates, organics and nitrates. The accumulation mode is often made up of two overlapping sub modes; the condensation mode and droplet mode. The condensation sub-mode is the result of growth of ultrafine particles by coagulation and vapour condensation whilst the droplet sub-mode is formed by cloud processing (that is, contain CCN). Particles in the range of 0.1 to 1 μm diameter are the most effective, per unit of aerosol mass, in reducing visibility, that is, the accumulation mode dominates in terms of light extinction (Kaufman and Fraser, 1983). Accumulation mode particles tend to be chemically complex because of the number of formation processes and their relatively high atmospheric lifetime, that is, particles 'accumulate' with time at these sizes.

Coarse mode aerosols are in the size range of greater than 2.5 μm and are generally primary aerosol particles generated by mechanical action by process of mineral dust uplift, volcanic mineral emissions (Kok, 2012; Song and Carmichael, 1999) and sea salt generated by wave action on coasts and over open ocean.

A size distribution describes the particle number in a size interval $n_N(dD_p)$ against the average diameter of the respective size interval (Jaenicke and Davies, 1976). Integration over $n_N(D_p)$, that is, the area under the curve results in the total number concentration of particles N_t, according to equation (1.2).

$$N_t = \int_0^\infty n_N(D_p) dD_p \ (\mu m^{-1}\ cm^{-3}) \tag{1.2}$$

Aerosol size distributions are generally not presented in regular size intervals, rather the size of the intervals increase with increasing diameter, and as such it is not possible to directly compare the number concentration from one size interval to the next. Size distributions are typically represented by log-log plots, which are needed in order to adequately display the many orders of magnitude; number concentrations range between 10^{-4} to 10^{4} cm^{-3} and particle size range from 0.01 – 100 μm. A size distribution is typically represented as the measured number concentration divided by the diameter interval, that is, the bin size; $dN/dlogD$ (or $dN/dlnD$). The meaning of $\log D_p$ actually refers to $\log(D_p/1)$ where the reference particle is 1.0 μm, but is not typically explicitly stated.

$$N_t = \int_{-\infty}^{\infty} n_N(\log D_p) d \log D_p \ (cm^{-3}) \tag{1.3}$$

The total surface area, S, of an aerosol particle (per cm^3 of air) in the range $\log D_p$ to $(\log D_p + d \log D_p)$, makes an assumption of particles sphericity (πr^2) according to equation (1.4). The representation of an aerosol population in terms of its surface area is highly important from a radiative perspective in terms of understanding how much solar radiation an aerosol particle scatters.

$$S = \pi \int_{-\infty}^{\infty} D_p^2 n_N(\log D_p) d \log D_p = \int_{-\infty}^{\infty} n_s(\log D_p) d \log D_p \ (\mu m^2 cm^{-3}) \tag{1.4}$$

The total volume, V, $(4/3 \pi r^3)$ of an aerosol particle (per cm^3 of air) in the range $\log D_p$ to $(\log D_p + d \log D_p)$ is calculated according to equation (1.5).

$$V = \frac{\pi}{6} \int_{-\infty}^{\infty} D_p^3 n_N(\log D_p) d \log D_p = \int_{-\infty}^{\infty} n_v(\log D_p) d \log D_p \ (\mu m^3 cm^{-3}) \tag{1.5}$$

Mass distributions ($\rho . V$), incorporate aerosol density, ρ ($g\ cm^{-3}$) with respect to particle size, $n_M(\log D_p)$ according to equation (1.6).

$$n_M(\log D_p) = \left(\frac{\rho}{10^6}\right)\left(\frac{\pi}{6}\right) D_p^3 n_N(\log D_p) \ (\mu g\ cm^{-3}) \tag{1.6}$$

Mass distributions are used to quantify the mass of aerosol in the atmosphere; PM_{10} and $PM_{2.5}$ (particulate matter with diameters less than 10 μm and 2.5 μm, respectively) are routinely measured and tightly controlled for air quality purposes. The larger accumulation and coarse modes (0.1 μm < D_p > 50 μm) dominate an aerosol mass distribution, whilst number distributions show a very different representation with ultrafine nucleation and Aitken mode (0.01 μm < D_p > 0.1 μm) aerosol dominating in the number concentration distribution. Number and volume distribution of the nucleation, Aitken, accumulation and coarse mode are demonstrated in figure 1.2.

A log-log representation suggests that the size distribution is symmetric, which is not the case in linear space. Due to the asymmetry of a size distribution, an arithmetic mean diameter does not adequately represent the distribution and as such two parameters; the geometric mean diameter (equation 1.7) and geometric standard deviation (equation 1.8) fully describe the lognormal distribution.

$$\bar{D}_p = \frac{1}{N}\int_0^{\infty} D_p n_N(D_p) dD_p \tag{1.7}$$

$$\sigma_g{}^2 = \frac{1}{N_t}\sum_{k=1}^{M} N_k \left(D_k - \bar{D}_p\right)^2 \tag{1.8}$$

Typically either number count or mass distributions are represented in which the median diameter is described by the count median diameter (CMD) or as the mass median diameter (MMD), respectively. The geometric standard deviation for a lognormal distribution is independent of the power of the diameter, that is, whether the distribution is a number or mass distribution, σ_g will be the same (Kulkarni et al., 2011a). Hatch-Choate equations, presented in table 1 provide a single calculation converting between different diameters of a lognormal distribution.

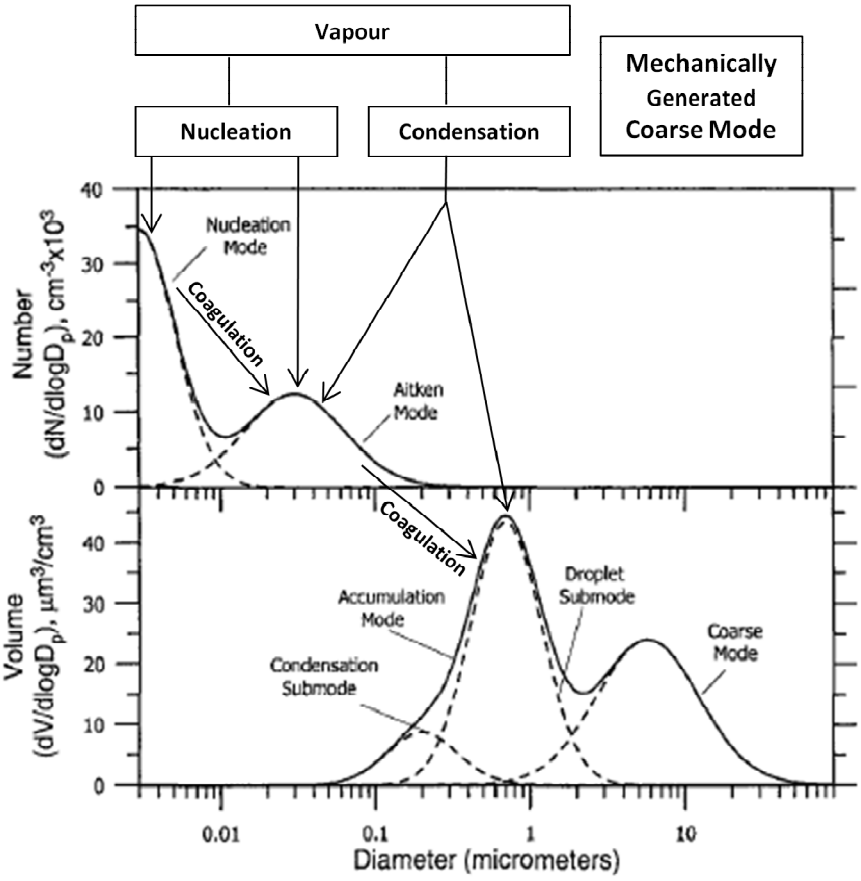

Figure 1.2 (*top*) Number and (*bottom*) volume distributions of nucleation, Aitken, accumulation and coarse mode aerosols. Nucleation and Aitken mode aerosol are best represented by number distributions, where particle number dominates, whilst accumulation and coarse mode are best represented by volume or mass distributions where size dominates over particle concentration. Adapted from Seinfeld and Pandis (2006).

Table 1 Hatch-Choate equations for converting count geometric mean diameters to surface or mass diameters.

Parameter	Equation	Parameter	Hatch-Choate Equation
Mean surface area, $\bar{S}$	$\bar{S} = \frac{1}{N}\int_0^\infty n_S(D_p)dD_p$	Surface median diameter (SMD)	$SMD = CMD\ \exp(2\ln^2\sigma_g)$
Mean mass, $\bar{M}$	$\bar{M} = \frac{1}{N}\int_0^\infty n_M(D_p)dD_p$	Mass median diameter (MMD)	$MMD = CMD\ \exp(3\ln^2\sigma_g)$

Particle diameter is defined by the technique used to measure it, that is, it can be sized differently depending on the instrument making the measurement. An optical equivalent diameter, relates the amount of scattered light into a given solid angle, related to a particle scattering cross section, and is strongly influenced by a particles refractive index and shape (Petzold et al., 2013). A mobility equivalent diameter refers to the measure of electrical mobility or migration velocity of a singularly charged particle in an electric field. A particles aerodynamic diameter has the same terminal velocity in an airflow as a sphere of density 1000 kg m^{-3} (Hinds, 1999). A vacuum aerodynamic diameter, that is, the diameter in a free molecular environment which has the same terminal velocity in an airflow as a sphere of density 1000 kg m^{-3}. Geometric diameter is a measure of size in terms of the two-dimensional projection area. Throughout this thesis the aerosol optical diameter shall largely be referred to.

Aerosol lifetime is controlled by dynamical processes within an aerosol population. *Coagulation* is the process whereby suspended aerosol particles collide and adhere with other individual aerosol particles. The motion of bringing particles together can be brought about by gravitational, hydrodynamic forces and Brownian motion which specifically refers to thermal motion. Coagulation results in the loss of aerosol number concentration whilst conserving aerosol mass. *Condensation* is a phase transition of gases to low volatility vapours by nucleation processes which condense onto a pre-existing particulate surface. Guo et al. (2010) use positive matrix factorization of size distribution data to show that gas-to-particle condensation processes account for 10 % – 60 % of the total mass in the condensation mode (maximum particle size of 0.2 μm), making it an important process in aerosol particle growth.

Aerosol *atmospheric lifetimes* (τ) vary across the four aerosol modes and in the simplest terms depend on the deposition velocity (figure 1.3), v_d, and particle diameter (Slinn et al., 1978). Coarse mode aerosol have the greatest mass fraction with deposition velocities in the order of 1 – 10 cm s^{-1} (Slinn et al., 1978), and are most prone to gravitational settling (Song and Carmichael, 2001). Atmospheric lifetimes are on the length of hours to days, are deposited close to source and are not typically subject to intercontinental transport.

Ultrafine nucleation nuclei rapidly coagulate, which reflect atmospheric lifetimes in the order of minutes to hours. Accumulation mode aerosols have the lowest deposition velocity as particles are large enough that they do not rapidly coagulate and are small

enough that gravitational settling and deposition are not fast removal processes. It is the combinations of these factors that results in the longest lifetime of the whole size distribution and therefore these particles tend to accumulate in the atmosphere and are subject to inter-continental transport (d'Almeida, 1986; Matsui et al., 2011; Prospero and Lamb, 2003; Swap et al., 2011).

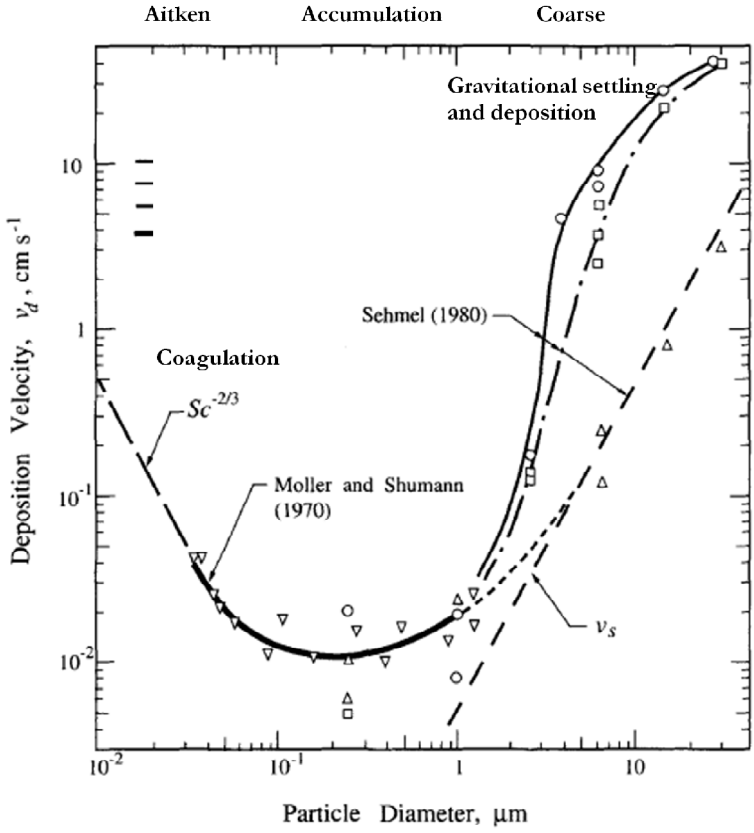

Figure 1.3 Deposition velocity as a function of aerosol particle diameter. Reproduced from Slinn et al. (1978).

1.1.2 Aerosol Microphysical Properties: Mixing State

An aerosol mixing state is a representation of how the sub-constituents within an aerosol particle or population are distributed. Aerosol particles are often thought of as being a single defined species whilst in reality they are a mixture of chemical species; optical properties (for example refractive index) and physical properties (for example hygroscopicity) are highly influenced by mixing state. The chemical composition of aerosol can be size-segregated, that is, the composition can vary across the size distribution (Wang et al., 2010).

In the most simple of terms an aerosol can be treated as *externally mixed*, whereby each particle is composed of a single species, for example, figure 1.4 shows an a) absorbing aerosol, for example black carbon and b) non-absorbing aerosol such as ammonium sulphate.

Figure 1.4. Schematics of externally mixed aerosol.

In the other extreme, within an *internally mixed* aerosol, all particles of a given size contain a uniform composition and as such the particles reflect a combination of properties. Heterogeneous internally mixed aerosol are made up of coatings on pre-existing particulate surfaces formed by the condensation of semi-volatile species (figure 1.5).

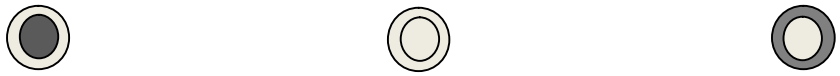

- Absorbing core
- Non-absorbing coating

- Non-absorbing core
- Non-absorbing coating

- Non-absorbing core
- Weakly-absorbing coating, for example, humic-like species (HULIS)

Figure 1.5. Schematics of heterogeneous internally mixed aerosol.

Climate models treat mixing state, particularly internally mixed aerosol, using two methods; either using mixing rules to produce an average refractive index over the multiple components within an aerosol or a coated sphere approach which treat the aerosol as a core with a coating. Both of these approaches to mixing state are used to assess the optical properties of aerosols in radiative models. Climate models constrain mixing state representations through either the bulk representation of composition, that is, size independent representation (Ming et al., 2007), or using a bin or modal representation, that is, it takes into account to some degree the compositional change as a function of size (Gong et al., 2003; Textor et al., 2006). In the same manner some models represent an aerosol to be either an internal mixture (Wang et al., 2010) or externally mixed (Textor et al., 2006).

These microstructures influence aerosol optical properties; for an internally mixed distribution, all particles within the population containing a fraction of absorbing nature

will exhibit some degree of absorption, whilst for an externally mixed aerosol population only a fraction of the population contain absorbing particles.

The absorbing nature of black carbon has been shown to be enhanced through the presence of particle coatings, in cases by a factor of 1.5 – 3 (Bond and Bergstrom, 2006; Lack et al., 2009). Lesins et al. (2002) found a reduction in single-scattering albedo of 22 % for an internally mixed population. Jacobson (2000) varied the particle mixing representation in a global model and showed the radiative forcing for external mixing of +0.27 W m^{-2}, core-shell representation of +0.54 W m^{-2}, and linear volume mixing of +0.78 W m^{-2}; a forcing factor in the range of 1.6 – 2.9 depending on the mixing state representation.

Aerosol mixing state influences microphysical properties such as the hygroscopic growth of an aerosol population. A key challenge is in understanding the spatial and temporal variations in changes to an aerosol's mixing state and the impact on the cloud condensation nucleating ability of the population.

1.1.3 Aerosol Optical Properties: Refractive Index

The aerosol refractive index is perhaps the most fundamental parameter in distinguishing the optical properties of aerosol. Refractive index describes the proportion of scattering and absorption of radiation from aerosol particles. With reference to air, the refractive index can be denoted by;

$$m = n - ik \tag{1.9}$$

where *m* represents the complex refractive index, *n* the real part is the ratio of light velocity in a vacuum to light velocity in the particle and *k* the imaginary part; describes light absorption by the particle. If *k* is zero at a given wavelength, the particle is non-absorbing, and a large value of *k*, indicates strongly absorbing particle. In reality the imaginary part of the refractive index, *k*, is never exactly zero, as all materials absorb to some extent, with *k* values reaching an order of 10^{-8}.

The refractive index of a complex aerosol is strongly influenced by chemical composition (figure 1.6). The real and imaginary parts of the complex refractive index are not independent, and both are wavelength dependent. The common representations of optical properties are presented for a wavelength of 550 nm, which approximates an effective solar energy weighted wavelength. The most scattering atmospheric aerosol is

ammonium nitrate of refractive index, m = 1.611 – 1x10^{-7}i (Weast, 1985), whilst the most strongly light absorbing atmospheric aerosol is black carbon of refractive index, m = 1.95 – 0.79i (Bond and Bergstrom, 2006).

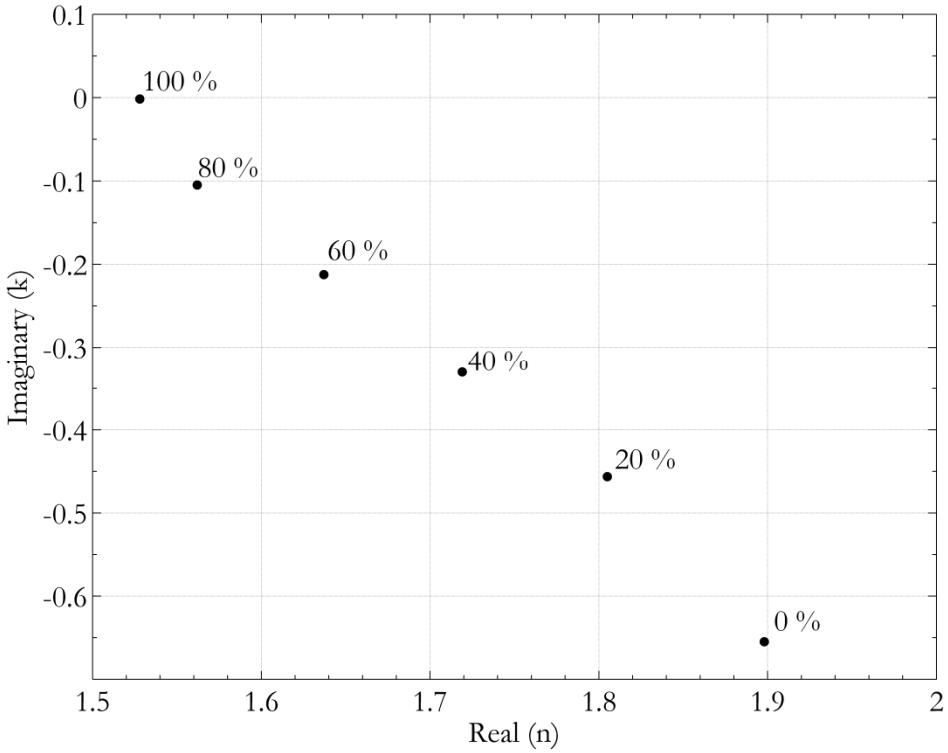

Figure 1.6 Real (n) and imaginary (k) parts of the refractive indices of an internally mixed aerosol with an increasing composition of a scattering aerosol such as ammonium sulphate. Adapted from Seinfeld and Pandis (2006).

Aerosol refractive indicies are most commonly determined through closure studies between empirical measurements and theoretical calculations, that is, light scattering model parameters (including refractive index) are varied until a theoretical parameter matches to the measured parameter. Refractive indicies calculated in this manner are limited by the uncertainty in the initial measurements. The importance of understanding the complex refractive index is two-fold; it is an important representation climate models in order to calculate the radiative properties of aerosol and it is required to extract meaningful information from optical-based instruments.

1.1.4 Aerosol Optical Properties: Scattering and Absorption Cross Sections

Scattering and absorption of light by aerosol particles is an extensive topic, a discussion will be provided here however the author acknowledges the breadth of the topic and refers to texts such as Bohren and Huffman (1983) and Van de Hulst (1957) to provide a thorough approach on the subject. Radiation is classically treated as an electromagnetic wave (Maxwell's theory) or alternatively as quantum theory where the energy lies in individual photons. A dielectric material, such as an atmospheric particle, in the presence of an incident ray of light, becomes polarized, that is, an oscillation is induced within the material known as a dipole moment.

The re-radiation of energy in all directions is known as *scattering* and a process where incident radiation is converted into thermal energy is known as *absorption*. The theories of *Rayleigh scattering, Mie-Lorenz theory* and *Geometric scattering* portray the scattering of light by a homogenous sphere. Elastic scattering refers to the process by which the energy of a photon is conserved during the scattering event, that is, the wavelength of the scattered light is the same as the incident wavelength (λ_0). Electromagnetic processes such as reflection, diffraction and refraction are associated with geometric scattering. These treatments are considered in more detail below, and are presented in figure 1.7. In considering the applicable theory for light scattering, it is important to define the size parameter (α) that relates particle size to the wavelength of incident light;

$$\alpha = \frac{2\pi r m_o}{\lambda_o} \tag{1.10}$$

where r is the radius of the particle, λ_o is the wavelength of incident wave in the ambient medium and m_o is the refractive index of the ambient medium (air). Table 2 presents the light scattering regimes with respect to the size parameter.

Table 2 Light scattering regimes and the particle size parameter.

Light Scattering Regime	Particle Size (μm)	Size Parameter (α)
Rayleigh	< 0.1	$\alpha << 1$ Rayleigh scattering (particle small compared with the incident wavelength)
Mie-Lorenz	Intermediate	$\alpha \approx 1$ Mie scattering (particle of about the same size as the incident wavelength)
Geometric	>10	$\alpha >> 1$ Geometric scattering (particle large compared with the incident wavelength)

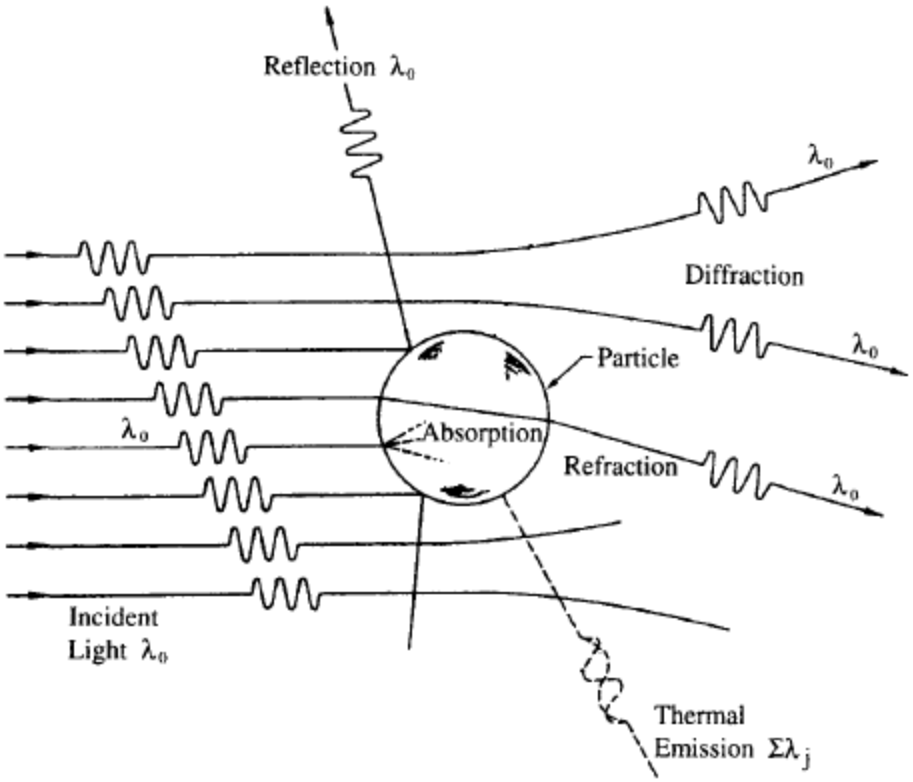

Figure 1.7: Interactions of incident light with aerosol particles. Adapted from Seinfeld and Pandis (2006).

Rayleigh scattering is the theory of scattering from spherical particles of diameter < 0.1 μm ($\alpha << 1$), that is, the particle is small compared with the incident wavelength. In this regime the pattern of scattered light is symmetrical in the forward and backward directions; it is primarily dominated by air molecules (N_2 and O_2). For aerosol, we often turn to *Mie-Lorenz theory* which describes light scattering by homogenous spherical particles (Lorenz, 1890; Mie, 1908). Mie theory has been applied across a broad subject area due to the diversity in the number of application of light scattering from spherical particles. Mie theory can be approximated through a series of expansions of the Maxwell equations for the derivations of the incident, scattered and internal fields (Bohren and Huffman, 1983). Although used to describe scattering in terms of intermediate size parameters, Mie theory has no size limitation and converges to the geometric scattering size regime for large aerosol.

The *scattering cross section*, σ_{scat}, (with units of m^2) describes the amount of light scattered by a particle. The parameter differs from the geometric scattering cross-section due to its dependence on the wavelength of light and the shape and size of the particle. The

extinction cross section, σ_{ext}, is the combined effect of the single-particle scattering cross section and the single-particle *absorption cross section*, σ_{abs}. The extinction cross section accounts for the light lost from the incident light beam by the aerosol particle due to scattering and absorption.

$$\sigma_{ext} = \sigma_{scat} + \sigma_{abs} \tag{1.11}$$

Particle *scattering efficiency*, Q_{scat}, *absorption efficiency*, Q_{abs}, and *extinction efficiency*, Q_{ext}, are related to *particle cross section* using the cross-sectional area of the particle (πr^2), ($\sigma_{scat}/\pi r^2$), ($\sigma_{abs}/\pi r^2$) and ($\sigma_{ext}/\pi r^2$), respectively. The values of Q_{ext}, Q_{scat} and Q_{abs} are dimensionless.

Using the scattering efficiency, Q_{scat}, and the subsequent integration over size distribution yields the scattering coefficient b_{scat}. The same approach is applied for the extinction efficiency, Q_{ext} and the extinction coefficient, b_{ext}. These equations are presented below.

$$b_{scat}(\lambda) = \int_0^{D_p^{max}} \frac{\pi D_p^2}{4} Q_{scat}(m,\alpha) n(D_p) dD_p \tag{1.12}$$

$$b_{ext}(\lambda) = \int_0^{D_p^{max}} \frac{\pi D_p^2}{4} Q_{ext}(m,\alpha) n(D_p) dD_p \tag{1.13}$$

where ($\pi D_p^2/4$) takes into account the particle cross section (σ), number size distribution function of $n(D_p)$ and m is the complex refractive index of the particle of the population.

The extinction efficiency, Q_{ext}, as a function of the size parameter (figure 1.8) highlights that the scattering efficiency (and extinction efficiency) converge on a value of 2 at largest size parameters, that is, in the geometric scattering regime. This suggests that the extinction cross section is twice as large as the geometric scattering cross section a suggested phenomenon so called by Bohren and Huffman (1983) as the extinction paradox. Van de Hulst (1957) suggests that diffraction of the incident light around the particle, is not bound by the true geometric scattering cross section, but instead beyond the physical edges of the particle. The net result is half of the incident energy is removed due to scattering from the true geometric scattering cross section and the second half is removed due to diffraction around the particles edge.

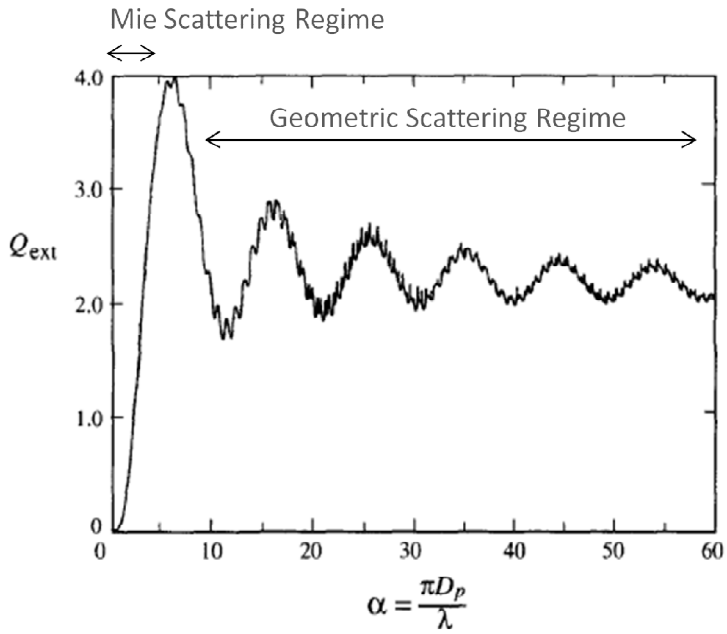

Figure 1.8 Extinction efficiency as a function of the size parameter for a water droplet of refractive index m = 1.33 – 0.00i. Adapted from Seinfeld and Pandis (2006).

The solutions to the Maxwell Equations are typically achieved using computer code; examples include MIEV0 Fortran code (Wiscombe, 1980) or BHMie by Bohren and Huffman (1983). MIEV0 treats the aerosol as a homogeneous aerosol distribution which implies that the particle is characterised by a single refractive index at a given wavelength. If a particle has a complex composition reflecting multiple refractive indicies, an effective refractive index must be calculated. Mie theory, originally the application of single-scattering particle has been extended to coated particles (Bohren and Huffman, 1983). There have been approaches which extend Mie theory to non-spherical particles using a T-matrix approach; a simple approach to non-spherical particles treating them as simple deviations from sphericity such as ellipsoids/spheroids (Osborne et al., 2011). In order to treat aerosol particles as complex irregular particles a fully numerical method must be applied such as Discrete Dipole Approximation (DDA) (Draine and Flatau, 1994). The extension to non-spherical particles will not be a subject of further discussion in this thesis, but it is important to note the uncertainties in assuming sphericity in atmospheric particles.

1.1.5 Aerosol Optical Properties: Single-Scattering Albedo

The aerosol *single-scattering albedo* (ω_0) is an important parameter in calculating the sign of the aerosol direct radiative forcing, and is defined as the ratio of aerosol scattering, Q_{scat} to aerosol extinction, Q_{ext}, according to equation (1.14).

$$\omega_0 = \frac{Q_{scat}}{Q_{ext}} \tag{1.14}$$

Values of the single-scattering albedo range from 0 to 1 and the value can be viewed in quantum theory as the probability of a photon being scattered rather than absorbed. ω_0 of 1 indicates a purely scattering aerosol whilst ω_0 of 0 indicates a purely absorbing aerosol, and ω_0 less than 1 have an absorbing component (Sanford et al., 2008). The single-scattering *co-albedo,* $1 - \omega_0$, is the fraction of radiation that is absorbed.

Studies have shown a wavelength dependence in the aerosol single scattering albedo as a function of aerosol composition and size as highlighted in figure 1.9. The figure contrasts two aerosol species Saharan mineral dust and biomass burning indicating the wavelength dependence in the visible spectrum of the single-scattering albedo (Costa et al., 2004). The single-scattering albedo for mineral dust decreases toward short wavelengths, that is, absorption enhancement occurs at shorter wavelengths (Ångström, 1929) leading Moosmüller et al. (2012) to conclude that single-scattering albedo is dominated by and linearly correlated with the iron volume fraction in mineral dust.

The single-scattering albedo for biomass burning aerosol decreases towards longer wavelengths; for fine mode and/or accumulation mode aerosols the light scattering often decreases faster than absorption so that the single-scattering albedo decreases with wavelength (Bergstrom et al., 2007; Bergstrom et al., 2002; Dubovik et al., 2002; Eck et al., 1999; Reid and Hobbs, 1998; Reid et al., 1998b).

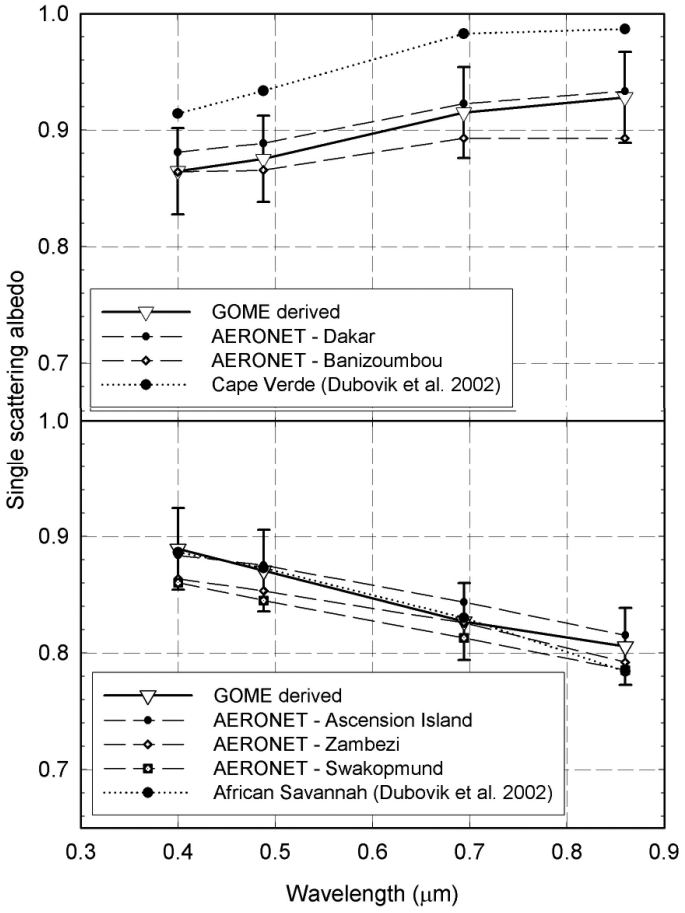

Figure 1.9 Wavelength dependence of aerosol single-scattering albedo; comparison between spectral reflectance measurements from the Global Ozone Monitoring Experiment (GOME) spectrometer and sun-sky photometer measurements from AERONET sites for (*top*) Saharan mineral dust and (*bottom*) biomass burning. Reproduced from Costa et al. (2004).

1.1.6 Aerosol Optical Properties: Scattering Phase Function

The *scattering phase function* represents the probability for scattering of unpolaraised incident light in any given direction (Hansen and Travis, 1974). The scattering phase function in equation (1.15) is the scattered intensity at a particular angle θ relative to the incident beam and normalized by the integral of the scattered intensity at all angles i.e. $\int_0^\infty N(r)dr = 1$.

$$P(\theta) = \frac{\int_{r_1}^{r_2} P(\theta, r)\sigma_{scat}N(r)dr}{\int \sigma_{scat}N(r)dr} \qquad (1.15)$$

The sensitivity of the phase function to the shape of the size distribution and aerosol type is shown in figure 1.10.

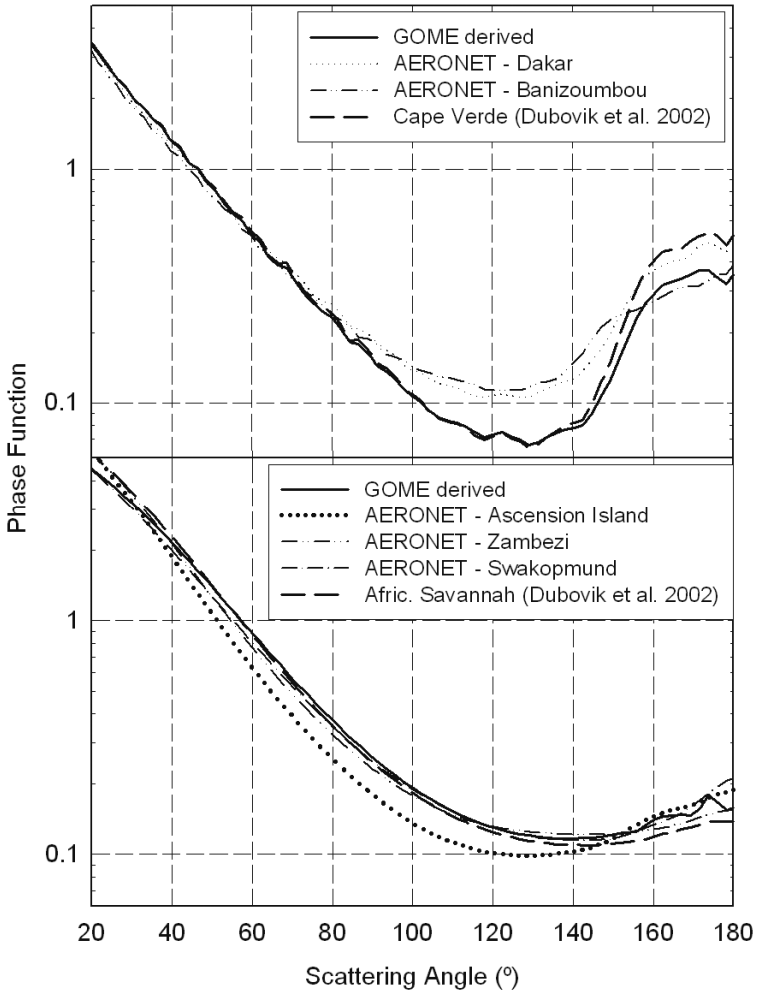

Figure 1.10 Scattering phase function as a function of scattering angle at 550 nm; comparison between spectral reflectance measurements from the Global Ozone Monitoring Experiment (GOME) spectrometer and sun-sky photometer measurements from AERONET sites for (*top*) Saharan mineral dust and (*bottom*) biomass burning. Reproduced from Costa et al. (2004).

For biomass burning aerosols, which tend to dominate in the accumulation mode (Reid et al., 2005b) and are generally thought to be spherical, the light scattering tends to be isotropic. Mineral dust has a large contribution in the coarse mode with a generally accepted non-spherical shape, the directional asymmetry is more pronounced. For thoroughness the scattering phase function is discussed here but is not a topic for future discussion within this thesis; however it is important function relating to the aerosol asymmetry parameter. Knowledge of the aerosol scattering phase function is important for remote sensing applications; the backscatter fraction is used in satellite retrievals, and an accurate scattering phase function should be accounted for.

1.1.7 Aerosol Optical Properties: Asymmetry Parameter

The *asymmetry parameter* (*g*) is defined as the cosine-weighted average of the phase function and is used to represent the shape of the phase function as one single value (Bohren and Huffman, 1983), according to equation (1.16).

$$g = \int_{4\pi} P_{11}(\theta) \cos\theta \frac{d\Omega}{4} \tag{1.16}$$

where θ is the angle between incident light and scattering direction, $P_{11}(\theta)$ is the angular distribution of scattered light (the phase function) and $d\Omega$ is the solid angle. The asymmetry parameter, g, ranges from -1 to +1; and the value of g determines how much radiation is scattered in the forward and backward hemispheres. If g has a value of -1 then all the radiation is scattered in the backward hemisphere ($\theta = 180^o$), if the value is 1 then all the radiation is scattered in the forward hemisphere ($\theta = 0^o$), if $g = 0$ then the radiation is scattered equally in both hemispheres, that is, isotropic scattering. The angular distribution of light and the amount of forward scatter to backscatter strongly influences the radiative forcing.

1.1.8 Aerosol Optical Properties: Mass Extinction Efficiency

Mass extinction efficiency (K_{ext}) is a representation of the total extinction per total of aerosol mass and is the sum of mass scattering (K_{scat}) and absorption (K_{abs}) efficiencies. The extinction efficiency is in principle a particle cross section normalised to volume ($m^2\ cm^3$) or mass ($m^2\ g^{-1}$). It is an important parameter which can be used to convert the aerosol mass into an aerosol optical depth (τ) and in assessing the magnitude of the direct aerosol radiative effects.

1.1.9 Aerosol Optical Properties: Aerosol Optical Depth

Optical depth is a dimensionless measure of the opacity of the atmosphere and the *aerosol optical depth* (AOD) refers to aerosol extinction within the atmospheric column. It is calculated according to equation (1.17) through the vertical integration of the mass extinction efficiency, $K_{ext}(\lambda, z)$, with height between points z_1 and z_{TOA}, that is, Earth's surface and top of the atmosphere.

$$\tau(\lambda, z) = \int_{z_1}^{z_{TOA}} K_{ext}(\lambda, z')\rho dz' \quad (1.17)$$

The Angstrom exponent, $\mathring{A}$, refers to the dependency of the aerosol optical depth with wavelength. The Angstrom exponent depends on the particle size distribution and can be calculated according to equation (1.18).

$$\left(\frac{\tau}{\tau_0}\right) = \left(\frac{\lambda}{\lambda_0}\right)^{-\mathring{A}} \quad (1.18)$$

where τ is the optical depth at wavelength λ, and τ_0 is the optical depth at wavelength λ_0.

1.1.10 Aerosol Robotic Network (AERONET)

Techniques for measuring the AOD include sun photometer measurements of direct-sun radiance or integration of aircraft *in-situ* extinction coefficient measurements. The AErosol RObotic NETwork (AERONET) is a network made up of 500 surface-based Sun photometers (Holben et al., 1998). Almucantar scans of radiance as a function of scattering angle (that is at a fixed solar angle, with varied azimuth angles), combined with an inversion algorithm of Dubovik and King (2000), provide aerosol products including the complex refractive index, size distributions and column-averaged single scattering albedo at 440 nm, 670 nm, 870 nm and 1020 nm wavelengths.

In considering the strength of aerosol retrievals from the ground, sun photometer measurements cover large scattering angles ($0° < \theta_{scat} < 150°$) providing a large information base for a local region with non-intrusive methods. For observations with lower AOD, the retrieval accuracy of $\omega_0(\lambda)$, k (λ), and n (λ) significantly decreases because of a decrease of the aerosol signal. A detailed discussion of AERONET accuracy assessment is provided in Dubovik et al. (2002). Osborne et al. (2008) observed that errors in the AERONET retrieval become relatively large for coarse mode particles attributed to the relatively small contribution they tend to make to the optical depth and also because of the limitation of retrieving information on 5–10 μm sized particles with the longest AERONET wavelength (1250 nm).

AERONET AODs are a fairly robust measurement with relatively high accuracy, compared to the column size distributions which are the product of inversion and for which certain conditions are required for satisfactory inversions (Osborne et al., 2008),

as demonstrated by Dubovik et al. (2002). Integration of aircraft *in-situ* extinction coefficient measurements from vertical profiles; with typical gradients of about 4º, cover a greater distance in the horizontal plane than in the vertical and as such boundary layer variability is an important consideration in making comparisons with the column AOD from AERONET.

Encouraging comparisons of aerosol size distributions have been demonstrated between long-term climatological AERONET data and campaign-averaged Met Office C-130 research aircraft data (Osborne and Haywood, 2005). Osborne et al. (2007) compared aircraft observations with multiple AERONET sites and twice-daily MODIS satellite observations during the Aerosol Direct Radiative Impact Experiment (ADRIEX) campaign. The aerosol optical depths derived from aircraft measurements show a consistent bias to lower values than both the AERONET, differences which can be explained by local variations in the aerosol column loading and by some aircraft instrumental artefacts. The general increase in the fine mode fraction was observed by all methods Mean aircraft fine-mode fractions tended to be slightly smaller than AERONET, with the AERONET daily range of values smaller than both the MODIS and aircraft data suggested.

Comparisons of aircraft measurements during the Dust And Biomass Burning Experiment (DABEX) campaign and AERONET data found errors in the AERONET retrieval become relatively large for coarse mode mineral dust owing to the relatively small contribution they tend to make to the optical depth (Osborne et al., 2008). Good agreement was found between the two data sets in terms of the trends observed; the aircraft AODs were found to be biased to high values compared to AERONET. Osborne et al. (2008) suggested a problem with either the aircraft or AERONET measurements which was more apparent when the dust fraction is high.

1.2 Saharan Mineral Dust

The estimates of global source strength of mineral dust particles vary between 1000 and 5000 Tg yr^{-1} (Weinzierl et al., 2009). The largest single source of global mineral dust is the Saharan-Sahel region in Northern Africa, an area 9 million km^2 (Weinzierl et al., 2009). Mineral dust impacts on many aspects of the Earth system including the radiative balance (Haywood et al., 2003a; Haywood et al., 2005), microphysical properties and clouds (Min et al., 2009; Rosenfeld et al., 2001), dynamical processes

(Marsham et al., 2013a; Marsham et al., 2011; Marsham et al., 2008b), regional air quality and health (Deroubaix et al., 2013; Martiny and Chiapello, 2013) and biogeochemical cycles (Mahowald et al., 2005; Sarthou et al., 2003).

The global net top-of-the atmosphere direct radiative forcing is of the order of -0.3 W m^{-2} with a range of -0.56 W m^{-2} to +0.1 W m^{-2} (Andreae and Rosenfeld, 2008; Andreae et al., 2004; Khain, 2005; Knippertz and Todd, 2012). Direct radiative effects from mineral dust are complex and the ambiguity in estimating the radiative forcing arises from the uncertainties in i) dust emission and atmospheric loadings (Tegen et al., 1996; Todd et al., 2007) ii) dust properties such as size distribution (Weinzierl et al., 2009), mineral dust refractive index (Haywood et al., 2003b; Kandler et al., 2007; Petzold et al., 2009) and vertical variability such as the altitude of dust layers (Liao and Seinfeld, 1998a).

Desert topsoil are laden with bacterial communities and globally averaged, a gram of topsoil contains in the order of 10^9 bacteria (Griffin, 2007). Recent studies have demonstrated the suitability of using aerosol remote sensing in studying meningitis epidemics across the Sahel affected by strong dust events in an area known as the 'meningitis belt' (Deroubaix et al., 2013). However, the exact physical correlation still remains uncertain.

There is a large interest in the magnitude of dust input into the worlds' oceans due to the biogeochemical implications; Saharan dust storms are a major source of iron to the Atlantic Ocean (Sarthou et al., 2003). Iron is an essential micronutrient in enzymes essential to photosynthesis vital to ocean productivity thorough ocean-atmosphere CO_2 exchange, with Shao et al. (2010) identifying that ocean phytoplankton are 40 % iron limited. Current estimates show considerable variability with Shao et al. (2010) suggesting a dust input to the North Atlantic on the order 180 – 260 Tg yr^{-1}.

1.2.1 Mineral Dust Cycle

Mineral dust cycle through the atmosphere is influenced by the processes of emission, transport, transformation, deposition and stabilisation. The uplift potential of dust is primarily a factor of wind speed with dust emissions additionally favoured in arid or semi-arid areas, where precipitation rates < 200 mm yr^{-1} (Engelstaedter and Washington, 2007). Dust emissions in North Africa reflect a 'triplet' pattern of

emissions with two strong dust emission seasons and one season of low dust loadings (Ben-Ami et al., 2011; Knippertz and Todd, 2012). The lowest Saharan mineral dust emissions are between October and December; when dust emissions are driven by dry dynamics. Todd et al. (2007) identified episodic dust emissions from November to March, related to the Bodélé Depression, an area of alluvial deposits in northern Chad laid down during the Pleistocene and Holocene (Washington et al., 2003; Washington et al., 2006). Present day emissions in the Bodélé depression emit in the range of 15 - 20 % of North Africa's emissions (Maher et al., 2010). The localised deposits combined with a dominant south-westward transport ensures a North African mineral dust hot spot (Giles, 2005; Washington et al., 2003). Western Sahara dust emissions have no single major source region; the West African summer monsoon leads to a variety of emission mechanisms and trajectories (Marsham et al., 2008a) and the occurrence of the Saharan Heat Low (SHL); a feature of the summertime Saharan Climate System which develops due to the intense daytime solar heating is correlated with strong dust emissions (Marsham et al., 2013b). Strong solar radiation is converted into sensible heat flux at the land surface, forming a deep convective boundary layer, that is, turbulent motions through which dust can be lofted throughout the Saharan boundary layer.

The presence of mineral dust aerosol is not confined to source areas but can be carried over large distances by prevailing winds (De Reus et al., 2000). Once airborne, dust is transported by turbulence and convection to the upper layers of the Saharan Air Layer (SAL); it is here that it can be influenced by synoptic scale systems and the global circulation (Prospero and Carlson, 1980; Prospero and Carlson, 1972). Estimates of total deposition based on global aerosol models range from about 700 to over 4000 Tg y^{-1} (Knippertz and Todd, 2012).

Dust concentrations strongly correlate to historical climate changes on very long timescales; Maher et al. (2010) found that during glacial periods, dust fluxes were 2 to 5 times greater than in interglacial periods. Global Quaternary records of dust suggest that different historical climatic periods reflect different rates of dust accumulation (Kohfeld and Harrison, 2001); these records include ice cores from Greenland and Antarctica (Petit et al., 1990), the Chinese Loess Plateau record (Ding et al., 1994) and marine sediment records from the Pacific Ocean (Hovan et al., 1991) over the past 400,000 years, spanning several climatic events. Comparing these three historical records, Kohfeld and Harrison (2001) found similar trends in dust accumulation rates

during glacial and inter-glacial periods although the changes in atmospheric dust loadings were not spatially uniform; it was found that the absolute magnitudes of dust accumulation decrease by more than an order of magnitude between terrestrial and marine records, and marine and polar records.

Lambert et al. (2008) investigated dust-climate couplings over the past 800,000 from East Antarctica ice core, observing a 25 times increase in glacial dust flux, during eight glacial periods, which was attributed to strengthened dust sources combined with increase atmospheric lifetime associated with a reduced hydrological cycle during the glacial periods. Mineral dust may potentially play an important role in future climate forcing; changes in dust emissions under a changing climate, coinciding with increasing levels of desertification, still remain one of our most uncertain processes in assessing future climate change (Harrison et al., 2001).

1.2.2 Mineral Dust and Ozone

Photochemical species such as nitric acid (HNO_3), hydroperoxyl radical (HO_2) and ozone (O_3) are known to undergo heterogeneous uptake on mineral dust surfaces (Bauer et al., 2004; Jacob, 2000). Understanding of these reactions have largely stemmed from modelling studies (Bian and Zender, 2003; Dentener et al., 1996) and laboratory studies (Chang et al., 2005; Grassian, 2002; Hanisch and Crowley, 2003) where measurements of uptake coefficients and reaction mechanisms can be investigated. Dentener et al. (1996) presents modelling studies finding ozone depletion on mineral dust surfaces could reduce by 10 % in the dust source areas whilst Bauer et al. (2004) calculated a 5% reduction in global tropospheric ozone. Field observations have shown *in-situ* observations of low ozone concentrations that coincide with times of elevated dust concentration and these observations have been correlated with long-range transport events of mineral dust aerosol. Observations from aircraft altitude profiles during the ACE-2 campaign presented by De Reus et al. (2000) identified an elevated region between 2 and 6 km where the total number of accumulation mode particles increased corresponding with a 30 – 40% reduction of O_3. De Reus et al. (2000) attributed these observations to the direct removal of O_3 by mineral dust.

Further observations by De Reus et al. (2005) at the Global Atmospheric Watch station on Tenerife, found daytime mean O_3 and NO_X mixing ratios decreased by 33% and

35%, respectively, during a Saharan dust event compared with the campaign-average. De Reus et al. (2005) discussed that box modelling of the low ozone mixing ratios observed during observed Saharan dust events was difficult without making assumptions on the concentrations of O_3 in the dust source area. The variability presented here between modelling and field studies is largely due to uncertainty in the uptake coefficients onto mineral dust surfaces (Dentener et al., 1996).

In arid regions, where the atmospheric water vapour column is low, the longwave absorption by ozone is a dominant natural absorbing component in the atmospheric column. With a mean atmospheric lifetime of 22 days (Stevenson et al., 2006), O_3 has a more variable vertical and spatial distribution than other long lived tropospheric gases; the radiative forcing of O_3 is shown to be dependent on vertical distribution (Forster and Shine, 1997; Hansen et al., 1997). The removal pathways for a number of photochemical species by heterogeneous uptake on to mineral dust are presented in the equations below. These are irreversible reactions; the uptake of these photochemical species results in reduced concentrations globally (Bian and Zender, 2003).

$$NO_3(g), HNO_3(g) \rightarrow NO_3^-(aerosol) \quad (1.19)$$

$$N_2O_5(g) \rightarrow 2NO_3^-(aerosol) \quad (1.20)$$

$$O_3(g) \rightarrow O_3(aerosol) \quad (1.21)$$

The final equation can be thought of by the mechanism of ozone depletion in the presence of mineral dust as proposed by Golodets (1983).

$$O_3(g) + ( ) \rightarrow O(a) + O_2 \quad (1.22)$$

$$O_3(g) + O(a) \rightarrow 2O_2(g) + ( )$$

$$2O_3(g) \rightarrow 3O_2(g)$$

$$O(a) + O(a) \rightarrow O_2(g) + 2( )$$

The alkalinity of mineral dust has been shown to enhance the uptake of gases on the surface (Bauer et al., 2004; Grassian, 2002; Hanisch and Crowley, 2003). Bauer et al. (2004) proposed that the coarse mode of mineral dust could be important for heterogeneous uptake; whilst Chang et al. (2005) found that there was no mass accommodation limitation to the rate of ozone uptake coefficients, concluding that

freshly emitted Saharan dust is potentially a significant route of ozone loss. Hanisch and Crowley (2003) discussed that mineral dust surface sites could be deactivated by the extended presence of ozone.

1.2.3 Mineral Dust Measurement Campaigns

Campaigns over the past 13 years have aimed to better understand different aspects of the Saharan climate system. A review of mineral dust size distribution measurements from each of these campaigns is presented in table 3 and mineral dust optical properties are presented in table 4. The current understanding of these physical and optical properties will be discussed in section 1.2.4 and 1.2.5, respectively. The variability within the literature of these parameters will be emphasised.

The Saharan Dust Experiment (SHADE) in September 2000 based at Cape Verde (Formenti et al., 2003; Haywood et al., 2003a) studied the radiative impact of mineral dust from *in-situ* measurements using the UK C-130 aircraft and sun photometer measurements. The Bodélé Dust Experiment (BoDEx) in February 2005 (Todd et al., 2007; Washington et al., 2006) characterised dust emissions from the Bodélé Depression, finding distinctly different optical properties associated with the nature of these alluvial deposits.

The Dust And Biomass Burning Experiment (DABEX) based in Niamey, Niger January 2006, (Haywood et al., 2008) improved understanding of radiative properties of dust and biomass burning aerosol species across the African Sahel region. The Dust Outflow and Deposition to the Ocean experiment (DODO1&2) based in Dakar during both February and August 2006 (McConnell et al., 2008), studied transport processes during the northern hemisphere winter and summer, to improve understandings of dust fluxes to the North Atlantic. The African Monsoon Multidisciplinary Analysis (AMMA) June to August of 2006, (Redelsperger et al., 2006), was carried out to better understand the West African monsoon, climate and hydrological cycle. These processes are underpinned by the vulnerability of West African society and the dependence on the monsoon system.

Saharan Mineral Dust Experiment (SAMUM1&2) first campaign in May/June 2006 Ouarzazate (Heintzenberg, 2009), second campaign based in Cape Verde in May/June 2008 used the DLR Falcon aircraft. SAMUM1 generated a data set of surface and

atmospheric columnar information whilst SAMUM2 aimed to quantify the radiative effects of a mixed plume of Saharan dust and biomass burning aerosols as they were transported out of the source region measured in SAMUM1. The Geostationary Earth Radiation Budget Intercomparison of Longwave and Shortwave radiation (GERBILS) in June 2007, based in Niamey/Nouakchott characterised the microphysical and optical properties of mineral dust, to develop and validate satellite retrievals and model simulations of mineral dust (Haywood et al., 2011).

1.2.4 Mineral Dust Physical Properties

1.2.4.1 Mineral Dust Physical Properties: Size Distributions

A significant mass fraction of Saharan mineral dust is in the coarse mode (Weinzierl et al., 2009). The difficulty in making accurate and reliable measurements of coarse mode aerosol from an aircraft platform is discussed by Wendisch et al. (2004). This is emphasised by the range in the measurements presented in table 3; the lognormal modes of the mean mineral dust size distribution as measured during previous Saharan field campaigns (that were referred to in section 1.2.3).

The size distributions presented for SHADE (Haywood et al., 2003) and GERBILS (Johnson and Osborne, 2011) found count medium radii (CMR) in the range of 1.8 μm – 2.7 μm, with mass concentrations at a radius of 2.25 μm, with a corresponding count median radii of 1.0 μm during DABEX (Osborne et al., 2008). The smallest mineral dust size distributions measured from an aircraft platform over the Sahara were measured during DODO-1 and DODO-2; McConnell et al. (2008) observed count median radii dominated in the accumulation mode between 0.2 – 0.6 μm and 0.7 – 1.5 μm, respectively.

Size distributions measured from the DLR Falcon during SAMUM observed particles larger than 10 μm in all flights, with the geometric mean diameter for the coarse mode between 2 μm and 4.50 μm (Weinzierl et al., 2009). Ground-based measurements at Tinfou, Morocco (Kandler et al., 2009) also observed particles larger than 10 μm diameter, with concentration variations of approximately three orders of magnitude. The authors also identified an 'ultra-giant' particle mode in high dust events at 154 μm diameter. Sizes this large have never been reported from aircraft platforms, possibly

due to the transmission efficiencies of the particles in aircraft sampling systems and also as gravitational settling which will dominate for particles of this size. The Fennec campaign utilised a number of sizing instruments covering the range of 0.1 – 930 μm nominal diameters, with measurement techniques ranging from imaging probes to optical based instruments, with Ryder et al. (2013b) presenting a coarse mode of 5.28 μm.

The importance of making reliable size distribution measurements has been emphasised (Kandler et al., 2009; Weinzierl et al., 2009). The differences in measured size distributions between campaigns discussed here reflect a combination of factors including geographic location and instrumentation availability. DABEX and DODO campaigns sampled dust which had been transported away from the source region, with the aerosol population subject to gravitational settling and transformational processes. SAMUM was based in southern Morocco, close to the Sahara, whilst Fennec flights targeted a number of cases of fresh dust uplift in the central Sahara in Mauritania and Mali. Considerable instrument investment in terms of sizing instruments was used during Fennec and SAMUM campaigns, with SAMUM making measurements from ultrafine particles (0.004 μm) up to 100 μm, and Fennec sizing in a range of 0.1 – 930 μm.

This thesis presents a critical evaluation of the current aerosol sampling aboard the BAe-146 aircraft in order to understand how the sampling of aerosol influences the measured size distributions; the impact of sampling of coarse mode aerosol will be emphasised. The Fennec campaign saw advances in aerosol sampling characterisation and coarse mode aerosol, which coincided with the installation of the Low Turbulence Inlet (LTI). In chapter 5 the contribution of the mineral dust coarse mode to the optical properties is emphasised.

Table 3 Geometric mean radius (GMR) or diameter (GMD) and geometric standard deviations (σ) for each of the lognormal modes of the mean mineral dust size distribution for Saharan field campaigns. CMR is the count median radius, CMD is the count median diameter and MMR is mass median radius.

Mode	Size Distribution		Campaign	Reference
	Geometric Mean Radius / Diameter (μm)	Standard Deviations (σ)		
CMR Mode 1	0.04	1.6	SHADE 2000 Saharan Dust Experiment	(Haywood et al., 2003a)
CMR Mode 2	0.11	1.3		
CMR Mode 3	0.30	1.6		
CMR Mode 4	1.07	1.3		
CMR Mode 5	1.80	1.5		
DODO-1 CMR Mode 1	0.083	1.36	DODO1&2 Dust Outflow and Deposition to the Ocean experiment	(McConnell et al., 2008)
DODO-1 CMR Mode 2	0.160	1.16		
DODO-1 CMR Mode 3	0.310	1.50		
DODO-1 CMR Mode 4	1.00	1.31		
DODO-2 CMR Mode 1	0.061	1.47		
DODO-2 CMR Mode 2	0.165	1.18		
DODO-2 CMR Mode 3	0.230	1.54		
DODO-2 CMR Mode 4	0.960	1.32		
CMR Mode 1	0.075	1.50	DABEX 2006 The Dust And Biomass EXperiment	(Osborne et al., 2008)
CMR Mode 2	1.050	1.63		
MMR Mode 1	0.63	2.20		
MMR Mode 2	2.25	1.73		

Mode	Size Distribution		Campaign	Reference
	Geometric Mean Radius / Diameter (μm)	Standard Deviations (σ)		
High Dust CMD Mode 1	0.07	2.02	SAMUM 2006 Saharan Mineral Dust Experiment Dunes du Tinfou, Ground site	(Kandler et al., 2009)
High Dust CMD Mode 2	0.74	1.79		
High Dust CMD Mode 3	1.72	3.71		
High Dust CMD Mode 4	153.9	1.38		
Low Dust CMD Mode 1	0.085	1.898		
Low Dust CMD Mode 2	0.035	5.2		
Low Dust CMD Mode 3	0.73	1.75		
Low Dust CMD Mode 4	31.08	2.48		
CMD Mode 1	0.070 - 0.075	1.74 – 1.99	SAMUM 2006 Saharan Mineral Dust Experiment South Atlas Mountains and over Casablanca	(Weinzierl et al., 2009)
CMD Mode 2	0.20 – 0.55	1.41 – 1.55		
CMD Mode 3	0.50 – 1.40	1.85 – 1.90		
CMD Mode 4	2.00 – 4.50	1.80 – 1.94		
CMD Aitken	0.053 $\pm$ 0.011	1.54 $\pm$ 0.07	SAMUM 2008 Saharan Mineral Dust Experiment	(Schladitz et al., 2011)
CMD Accumulation	0.177 $\pm$ 0.018	1.52 $\pm$ 0.05		
CMD Coarse 1	0.780 $\pm$ 0.049	1.5 $\pm$ 0.07		
CMD Coarse 2	1.790 $\pm$ 0.328	1.9 $\pm$ 0.11		

Mode	Size Distribution		Campaign	Reference
	Geometric Mean Radius / Diameter (μm)	Standard Deviations (σ)		
CMR Mode 1	0.12	1.30	GERBILS 2007 Geostationary Earth Radiation Budget Intercomparison of Longwave and Shortwave radiation	(Johnson and Osborne, 2011)
CMR Mode 2	0.32	1.68		
CMR Mode 3	1.32	1.40		
CMR Mode 4	2.70	1.85		
CMD Mode 1	0.05	2.5	Fennec 2011	(Ryder et al., 2013b)
CMD Mode 2	0.71	1.33		
CMD Mode 3	2.04	1.45		
CMD Mode 4	5.28	2.00		

1.2.5 Mineral Dust Optical Properties

1.2.5.1 Mineral Dust Optical Properties: Refractive Index

Mineral dust optical properties are strongly influenced by particle mineralogy with the predominant absorbing component of mineral dust being iron oxide, with Tegen et al. (1996) and Schkolnik et al. (2007) relating the mineralogical composition (such as the iron oxide content) to the wavelength-dependent mass absorption efficiencies across the visible spectrum. The refractive indicies presented in the following section (table 4) are most commonly determined through closure studies between empirical measurements and theoretical calculations, that is, light scattering model parameters (including refractive index) are varied until a theoretical parameter matches to the measured parameter. Refractive indicies calculated in this manner are limited by the uncertainty in the initial measurements. The wavelength dependence is particularly evident in retrievals of mineral dust optical properties in studies using Cimel Sun-sky radiometer measurements (Dubovik et al., 2002; Eck et al., 1999; Todd et al., 2007).

Cimel Sun-sky radiometer retrievals of mineral dust emissions from the Bodélé depression during BODEX are used by Todd et al. (2007) to show real part refractive index of n = 1.46 – 1.47 (across the wavelength range of 440 to 670 nm) with an imaginary part of the refractive index of $k = 0.001i - 0.002i$ (across the wavelength range of 440 to 670 nm). The low refractive index reflects the composition of the dust from the Bodélé source region; a diatomite composition from the alluvial deposits when the region was historically part of Mega-Lake Chad. Whilst the BODEX campaign constrained a number of key optical properties for the large dust emissions from the Bodélé source region**,** they may not be representative of dust from other regions of the Sahara that may have higher content of iron oxides and clay minerals (Formenti et al., 2008).

Ryder et al. (2013) calculated a complex refractive index of $m = 1.53 - 0.001i$ for the Fennec campaign, which is in line with the complex refractive index presented for SHADE, DODO and DABEX. McConnell et al. (2008) found the dry season complex refractive index was $m = 1.53 - 0.0005i$, whilst during wet season $m = 1.53 - 0.0014i$. suggesting variations in optical parameters could be seasonally driven due to differences source regions and transport processes. The DODO-1 imaginary part was as low as *k*

= 0.0005i, whilst DABEX found k = 0.0004i; both campaigns identified distributions dominated by accumulation mode with little representation of the mineral dust coarse mode, which offers an explanation for the low imaginary part of the refractive index.

Results from the SAMUM 2006 campaign, for both aircraft (Petzold et al., 2009) and ground based measurements at Tinfou (Kandler et al. 2008), found a real part n of the dust refractive index to be almost constant with values between 1.55 and 1.56, whilst the SAMUM 2008 campaign found a great range from 1.55 – 1.58. The highest reported imaginary parts of the refractive index are from Petzold et al. (2008) found 0.0042 ± 0.0007 at 550 nm during SAMUM 2006, with Muller et al. (2011) showing imaginary parts for a dust case were 0.0047 at a wavelength of 550 nm.

1.2.5.2 Mineral Dust Optical Properties: Single-scattering albedo

The long-term analysis of Saharan mineral dust events from AERONET sites by Dubovik et al. (2002) found a mean ω_0 of 0.95 at 670 nm, indicating it is weakly absorbing at mid-visible wavelengths. Accurate single scattering retrievals (errors of about 0.03) have been shown to be achieved when the aerosol optical depth at 0.44 μm is greater than 0.5 and the solar zenith angle is greater than 50° (Dubovik et al., 2002). The IPCC AR4 (Forster et al., 2007) highlights that at these single scattering values a positive radiative forcing by dust across the shortwave spectrum is unlikely, an earlier debate in publications (Liao and Seinfeld, 1998b; Miller and Tegen, 1998; Sokolik and Toon, 1996).

Derimian et al. (2008b) used Cimel Sun-sky radiometer retrievals to identity case studies of mineral dust events during the AMMA campaign correlating a strong coarse mode fraction of the size distribution, ii) coupled with results from previous study (Derimian et al., 2008a) which identified that the single-scattering albedo for mineral dust usually decreases toward short wavelengths due to the presence of iron oxides. Results from AMMA show lower ω_0 in the range of 0.88 – 0.98 (across the wavelength range of 440 to 1020 nm) indicating proportion of absorbing aerosol (due to proximity to biomass burning conditions) across wavelengths of the Cimel instrument located in M'Bour. Todd et al. (2007) ground based Cimel spectral radiometer retrieval single-scattering albedo of 0.969 – 0.986 across the spectral range of the radiometer (across the wavelength range of 440 to 670 nm).

In-situ measurements from Osborne et al. (2008) and McConnell et al. (2008) characterise the single-scattering albedo for the accumulation mode of ω_0 of 0.99 $\pm$ 0.02 for DABEX and 0.99 ± 0.004 and 0.98 ± 0.012 for DODO-1 and DODO-2 campaigns respectively, reflecting highly scattering particles. Haywood et al. (2011) highlight that mineral dust encountered during the GERBILS campaign, ω_0 of 0.97 at 550 nm, is highly scattering due to the relatively small fraction of iron oxides present (1 – 3%) as identified by chemical analysis (Klaver et al. 2011) and consistent with results from previous analysis of 2.4 % - 4.5 % by Formenti et al. (2008) during DABEX and DODO campaigns. The single-scattering albedo is in good agreement with mineral dust measured during the SHADE campaign (Haywood et al., 2003a).

Johnson and Osborne (2011) discuss the potential for under-estimating absorption measurements during GERBILS and DABEX, owing to losses of the coarse mode mineral dust in the sampling inlet and into the absorption instrument. The authors suggest that absorption measurements could have been an underestimated by a factor of 2, the impact of this could reduce ω_0 from 0.97 to 0.94. Ryder et al. (2013b) addressed the potential for coarse mode undersampling by scattering and absorption instruments, applying corrections in order to account for pipework losses and inlet enhancements (the focus of chapter 4 of this thesis). During Fennec it was observed that freshly uplifted dust has a mean ω_0 of 0.92, whilst regionally aged dust reflected an increase in the scattering potential to ω_0 = 0.94.

1.2.5.3 Mineral Dust Optical Properties: Asymmetry Parameter

The importance of the representation of the coarse mode mineral dust is highlighted in the considerable variability in published asymmetry parameters. McConnell et al. (2008) found asymmetry parameters of 0.68 for the accumulation mode, increasing to 0.73 with the inclusion of the coarse mode. Observations from SAMUM 2006 found large values of 0.79, which reflected a large contribution of coarse mode particles in the dust population, and suggests large forward scattering properties of the mineral dust (Otto et al., 2007). The results of Fennec 2011 find a higher asymmetry parameter which is broadly more consistent with the results from SAMUM (Ryder et al., 2013b).

Although a number of published asymmetry parameters presented here show consistency in the magnitude of the parameter, in most of the investigations the authors

assume mineral dust sphericity. Johnson and Osborne (2011) show that the asymmetry parameter decreases with an increasing irregular representation of the dust. Using a spherical presentation g was found to be 0.73, which is similar to a number of published values which all assumed particle sphericity, whilst with an irregular particle representation found g of 0.62, which suggests that the representation of particle shape reduces the particles forward scatter, whilst increasing side scatter.

The contribution of the coarse mode of mineral dust to the asymmetry parameter during the Fennec shall be emphasised in chapter 5 of this thesis, and the impact of not measuring the coarse mode of mineral dust will be demonstrated.

1.2.5.4 Mineral Dust Optical Properties: Mass Extinction Efficiency

The absence of coarse mode in DODO-1 and DODO-2 is reflected in mass extinction efficiencies of 0.85 $m^2\ g^{-1}$ and 1.14 $m^2\ g^{-1}$, respectively. Mass extinction efficiencies calculated during Fennec 2011 were as low as K_{ext} of 0.15 $m^2 g^{-1}$ reflecting the large coarse mode which was observed (Ryder et al., 2013b). The range from Fennec 2011 was between 0.15 – 0.39 $m^2\ g^{-1}$ consistent with the lower bounds of the mass extinction efficiencies found during the GERBILS campaign using an irregular representation of the shape of the dust; a spherical representation found a larger mass extinction efficiency of 0.48 $\pm$ 0.10 $m^2\ g^{-1}$.

Osborne et al. (2008) showed that the inclusion of the coarse mode halved the mass extinction efficiency from 0.76 $m^2\ g^{-1}$ to 0.33 $m^2\ g^{-1}$, showing the parameter is heavily reliant on the representation of coarse mode. This highlights the effect of natural variability in the size of the coarse mode but also issues with the measurement capability and efficiency. Mass extinction efficiencies from SHADE (Haywood et al., 2003a) fall within the range presented for DODO, DABEX and GERBILS campaigns.

The literature shows that representing the coarse mode of the mineral dust size distribution changes the mass extinction efficiency considerably, due to the large increase in mass associated with the coarse mode. It has also been shown that measurements of mineral dust with a bias to the accumulation mode find a higher mass extinction efficiency as the aerosol mass is represented in a region of the size distribution where the dust is most efficient at scattering radiation (Osborne et al. 2008; McConnell et al. 2008).

Table 4 Summary of mineral dust optical properties collated from Saharan field campaigns at wavelengths of 550 nm (alternative wavelengths are stated in brackets). AM is the accumulation mode and CM is the coarse mode

Field Campaign	Location	Refractive Index		ω_0	g	K_{ext} $(m^2 g^{-1})$	Reference
		n	k				
SHADE 2000 Saharan Dust Experiment	Cape Verde	1.53	0.0015*i*	0.97 $\pm$ 0.02 (AM) -	0.72 (AM) 0.74 (AM+CM)	0.70 (AM) 0.42 (AM+CM)	(Haywood et al., 2003a)
BODEX 2005 Bodélé Dust Experiment	Bodélé, Chad Cimel Sun-sky radiometer	1.46 1.47	0.002*i* (440 nm) 0.001*i* (670 nm)	0.969 (440 nm) 0.986 (670 nm)	-	-	(Todd et al., 2007; Washington et al., 2006)
DABEX 2006 The Dust And Biomass EXperiment	Niamey, Niger	1.53	0.0004*i*	0.99 $\pm$ 0.02 (AM) -	0.71 (AM) 0.75 (AM+CM)	0.76 (AM) 0.33 (AM+CM)	(Osborne et al., 2008)
DODO1&2 Dust Outflow and Deposition to the Ocean experiment	Dakar	1.53 (dry) - 1.53 (wet)	0.0005*i* (dry) - 0.0014*i* (wet)	0.99 $\pm$ 0.004 (AM) - 0.98 $\pm$ 0.012 (AM)	0.68 (AM) 0.73 (AM+CM) 0.68 (AM)	0.85 (AM) 0.41 (AM+CM) 1.14 (AM)	(McConnell et al., 2008)

Field Campaign	Location	Refractive Index		ω_0	g	K_{ext} $(m^2 g^{-1})$	Reference
		n	k				
AMMA 2006 African Monsoon Multidisciplinary Analysis	M'Bour, Senegal Cimel Sun-sky radiometer	-	-	0.91 (440 nm) 0.98 (1020 nm) 0.88 (440 nm) 0.93 (1020 nm)	-	-	(Derimian et al., 2008b)
SAMUM 2006 Saharan Mineral Dust Experiment 1	DLR Falcon	1.55 – 1.56	0.0031*i* – 0.0040*i*	0.96 $\pm$ 0.02 (537 nm)	0.79 (532 nm)	-	(Kandler et al., 2009; Müller et al., 2009; Otto et al., 2009; Petzold et al., 2009; Schladitz et al., 2009)
GERBILS 2007 Geostationary Earth Radiation Budget Intercomparison of Longwave and Shortwave radiation	Niamey/ Nouakchott	1.53	0.0015*i*	Measured 0.97 $\pm$ 0.02 Spheres 0.95 Spheroids 0.96 Irregular 0.97	- 0.73 0.73 0.62	- 0.48 0.44 0.30	(Haywood et al., 2011; Johnson and Osborne, 2011; Osborne et al., 2011)
SAMUM 2008 Saharan Mineral Dust Experiment 2	Cape Verde	1.55 – 1.58	0.0047*i* (550 nm)	0.96 (550 nm)	-	-	(Kandler et al., 2011; Müller et al., 2011)
Fennec 2011	Mauritania / Mali	1.53	0.001*i* (550 nm)	0.95 – 0.98	0.74 – 0.76	0.15 – 0.39	(Ryder et al., 2013a; Ryder et al., 2013b)

1.3 Amazonian Biomass Burning

The Amazon basin forms an area greater than 5 x 10^6 km^2 which spans 9 South American countries. Figure 1.11 shows the geographic boundaries and vegetation type in the Amazon Basin. The equatorial Amazon region consists of primary tropical rainforest, with the southern and western edges, an area called the Brazilian Central Plateau; cerrado (savannah type) vegetation covers approximately 25 % of Brazilian ground. Deforestation of the Amazon prior to the 1950s was less than 1 % of area but by 2003, 15 % had been deforested accounting for 0.02 x 10^6 km^2 deforested annually (Martin et al., 2009).

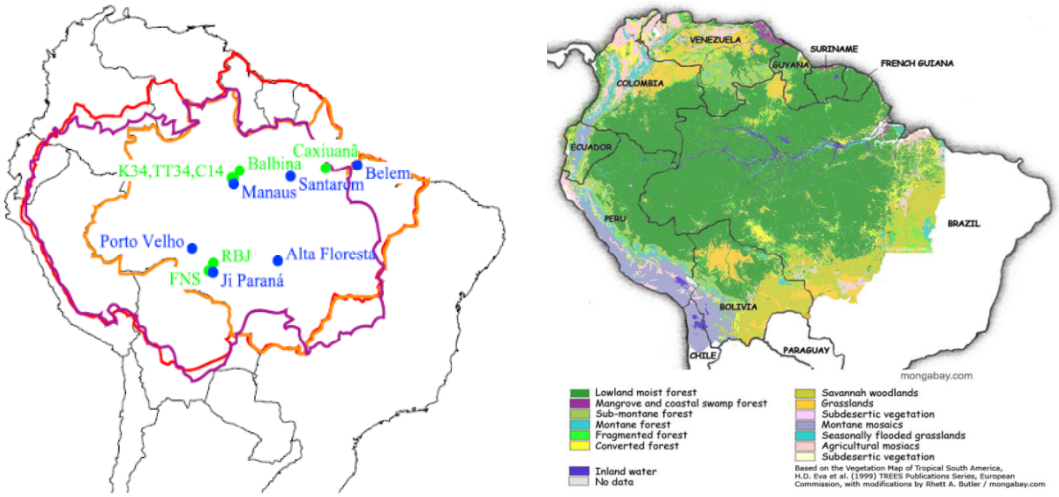

Figure 1.11. (*left*) Map of geographic boundaries of the Amazon forest (*red line)*, Amazon-Tocantins river basins (*purple line)* and Brazilian legal Amazon (*orange line*). Reproduced from Martin et al. (2010). (*Right)* vegetation map of tropical South America. Reproduced from Eva et al. (1999) with modifications by (Butler R. A) / mongabay.com.

Biomass burning aerosols are formed from vegetation fires which originate either naturally from lightning strikes or from anthropogenic sources through the intentional burning of vegetation for deforestation, agricultural land-clearing, and in domestic use for cooking and heating. Forty percent of global emission of black carbon are from biomass burning, with emissions dominated in regional hotspots such as West Africa and the Amazon Basin region (Streets et al., 2004). Amazonian biomass burning is the largest source of anthropogenic aerosol in the southern hemisphere (Koren et al., 2004). At the peak of the biomass burning season a regional haze has been seen to

extend over an area of 5 – 8 million km^2 (Artaxo et al. 1998). In the Brazilian state of Rondônia, in the north-western part of the country, vast areas of rainforest have been cleared; as demonstrated in figure 1.12. In the 1978 (top left panel) the land cleared was equivalent to 4200 km^2; a decade later in 1988 the land cleared was 30 000 km^2, reaching 67 764 km^2 in 2003 (Pedlowski et al., 1997).

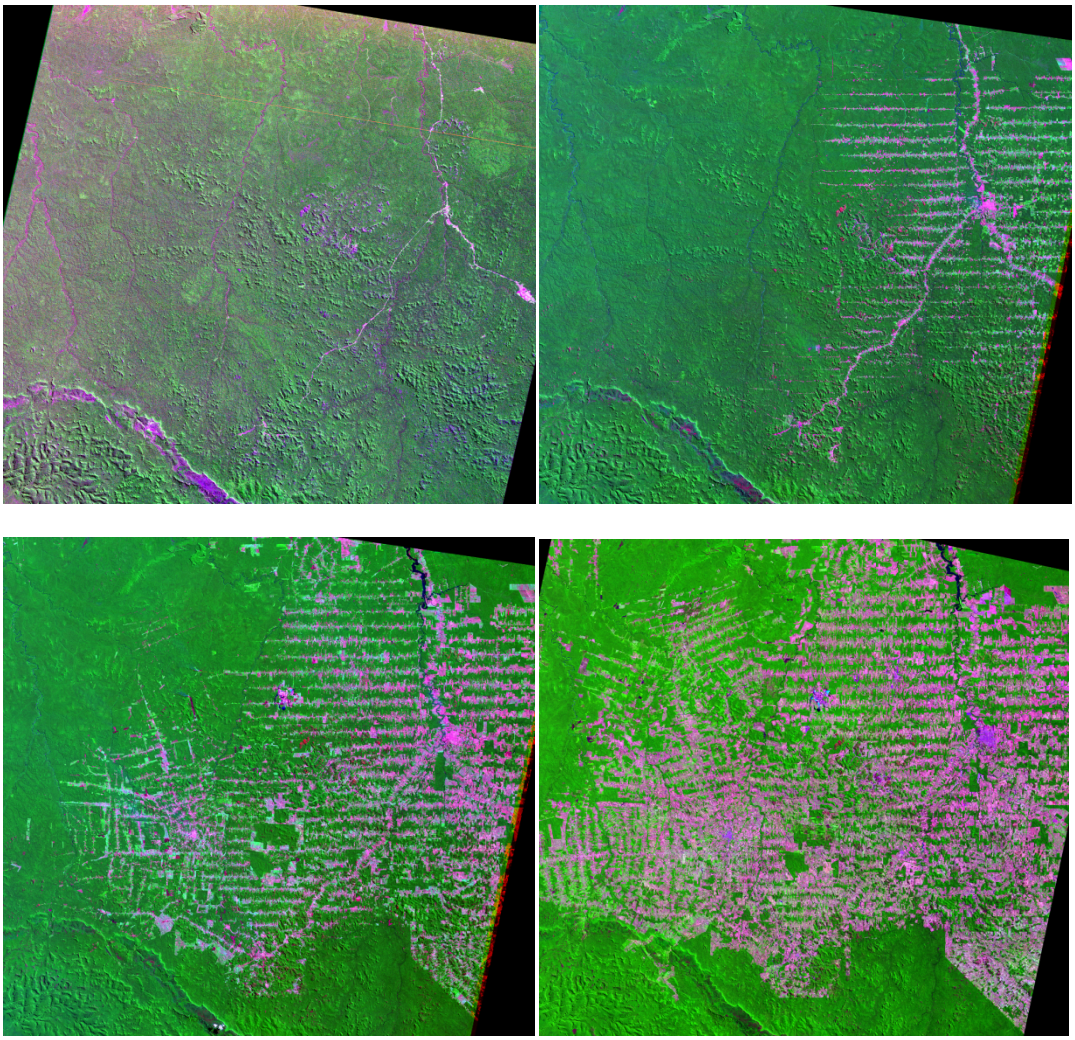

Figure 1.12 Extent of Rondônian deforestation between 1975 and 2013 (*top left*) 19 June 1975, Landsat 2 (*top right*) 22 June 1992, Landsat 4 (*bottom left*) 10 August 2001, Landsat 5 (*bottom right*) 27 August 2013, Landsat 8 (*pink*) deforested land and urban areas (*green*) vegetated land. Reproduced from the U.S. Department of the Interior U.S. Geological Survey.

Deforestation is predominately carried out by small scale farmers in slash and burn processes; clearing 1-2 ha of forest each year (Laurance et al., 2005). The Amazon has been subject to increasing and decreasing trends in deforestation practices over the last 30 year period; Nepstad (1999) and Cochrane et al. (1999) relate El Niño events, which are associated with rainfall levels barely 25 % of normal, to years of high levels of deforestation. Fearnside (2005) discusses deforestation trends in terms of economic recession and recover. A recent report found deforestation levels in 2009 had fallen to the lowest level in 20 years of measurements (Regalado, 2010); although in 2013 reports suggested a 28 % rise interrupted a period of declining deforestation; this has been blamed on a controversial reform to Brazil's forest protection law.

1.3.1 Amazonian Seasonal Cycle

The seasonal cycle in the Amazon Basin is driven by movements in the location of the Inter-tropical Convergence Zone (ITCZ); the confluence of circulation around subtropical highs between north-eastern trade winds from West Africa and south-eastern trade winds (Martin et al., 2009). The ITCZ reaches the northern coast of South America, lying to the south of the equator during the wet season (figure 1.13a) whereas during the dry season (figure 1.13b) the ITCZ lies to the north of the equator. The easterly inflow transports biomass burning aerosol across the Amazon basin, whilst southerly outflow from the basin is along the eastern edge of the Andes cordillera. These conditions are consistent to form a build up of biomass burning emissions in western Amazonia (figure 1.14).

During the wet season, a minimum in the Outgoing Longwave Radiation (OLR) of 190 W m^{-2} is observed over the Amazon Basin, which is representative of large convective systems with high rates of precipitation and cold cloud tops. This minimum weakens with the transition from wet-to-dry season and shifts to the north-west of the Amazon Basin (Martin et al., 2010). The Basin's eastern and southern edges having the strongest dry season, whilst the north-western Amazon is the wettest annually and the central Amazon receives an intermediate degree in seasonality.

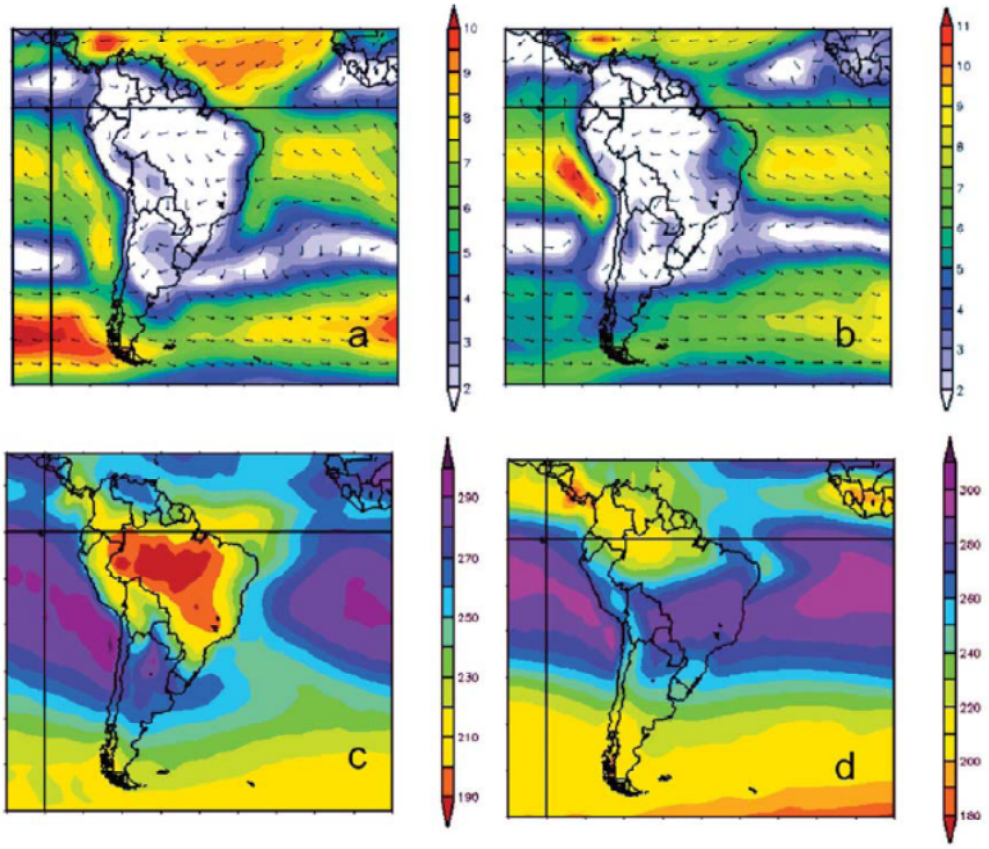

Figure 1.13. Amazonian seasonal cycle (*top left*) wet season; December, January and February (DJF) wind vector and wind speed (m s^{-1}) at 1000 hPa for South America (*top right*) dry season; June, July and August (W m^{-2}) (*bottom left*) OLR for DJF (W m^{-2}) (*bottom right*) OLR for JJA (W m^{-2}). The black horizontal line represents the Equator. Data from the National Centres for Environmental Predication. Reproduced from Martin et al. (2010).

The Amazon Basin, during the wet season, in known as the "green ocean" due to the similarities of very low particle concentrations, and hence low cloud droplet concentration with that of the remote oceanic regions (Williams et al., 2002). During the dry season (June to September), biomass burning becomes the most dominant source of atmospheric particles. During the maximum biomass burning period, Bevan and North (2009) found the mean AOD is in the order of 0.8 to 1.5 reaching a maximum of 2.0; in contrast prior to the onset of the biomass burning period the mean AOD was in the order of 0.3 to 0.4 (figure 1.14).

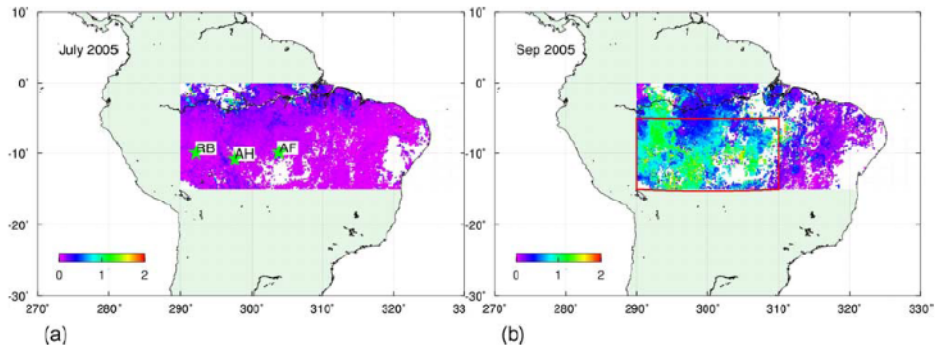

Figure 1.14. AATSR retrieved aerosol optical depth (AOD) for the Amazon Basin for two months; (*left*) July 2005 and (*right*) September 2005. Reproduced from Bevan and North (2009).

1.3.2 Biomass Burning Chemical Composition: Black Carbon

Black carbon (BC), more commonly known as soot is used to describe the strongly light absorbing component of an aerosol at all visible wavelengths (Bond and Bergstrom, 2006; Hansen et al., 1983). BC is the most abundant light absorbing particle in the sub-micrometer size range (Fuller et al., 1999; Hansen 1979). BC has a positive total climate forcing at the top of the atmosphere of +1.1 W m^{-2} with uncertainty bounds of +0.17 to +2.1 W m^{-2}, which reflects contributions summarised in figure 1.15. The direct radiative forcing best estimate is +0.71 W m^{-2} with uncertainty bounds of +0.08 to +1.27 W m^{-2} (Bond et al. 2013), with deposition of BC on highly reflective surfaces (snow and ice) decreases surface albedo, causing a forcing of +0.13 W m^{-2} (uncertainty bounds of +0.04 to +0.33 W m^{-2}); consistent with the IPCC 2007 best estimate. Absorption of radiation by BC causes heating of the air mass, increasing static stability relative to the surface and causes evaporation of cloud droplets, a process known as the *semi-direct effect* (Hansen et al. 19997), whilst the *indirect effect* of BC on clouds properties changes albedo, precipitation rates and lifetime. The sign and magnitude of BC interactions in this manner are very uncertain with current best estimates of the combined cloud and semi-direct effects contribute a best estimate forcing of +0.23 W m^{-2} (-0.47 to +1.0 W m^{-2}).

The BC direct radiative forcing shows the contribution from three main sources; fossil fuels, bio fuels and open burning sources, which contributes just under one third of the total direct forcing (+0.20 W m^{-2}). The final bar in figure 1.15 represents the best estimate of total climate forcing for BC and its co-emitted species (for example organic

matter and sulphate) for BC-rich sources, and demonstrates the importance of including these species. Inclusion of these species produces a negative total climate forcing that is close to zero, -0.06 W m^{-2}, due to the influence of liquid-cloud interactions that inclusion of these species gives rise to. It is only the indirect, cloud effects that bring about this negative change in the radiative forcing, the direct effect remains positive even with the inclusion of co-emitted species. The uncertainty of this term is very large, -1.45 to +1.29 W m^{-2}.

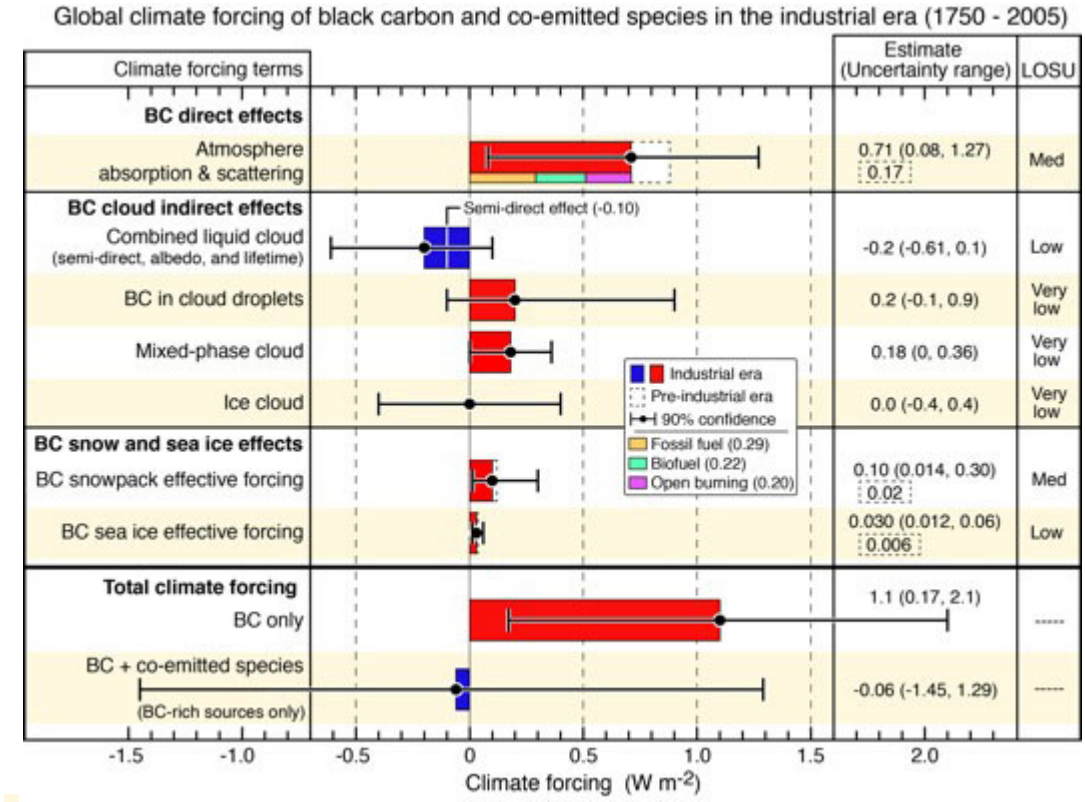

Figure 1.15 Radiative forcing best estimates (in units of W m^{-2}) and uncertainty in the year 2005 relative to those in 1750 for black carbon (BC) emissions. The final bar represents the best estimate of total climate forcing for BC and its co-emitted species for BC-rich sources. The bars and whiskers show the best estimates and uncertainties, respectively, for the different climate forcing terms. Indicated is the level of scientific understanding (LOSU). Reproduced from Bond et al. (2013).

The absorbing nature of BC is derived from its molecular structure; it has a high degree of sp^2 hybridisation, that is, that graphitic and covalent nature of the BC (Bond and Bergstrom, 2006; Hopkins et al., 2007b). Bond (2001) proposed that the light absorbing properties of carbon are associated with the molecular optical gap; defined as the energy required for an electron to reach the first excited state, that is, the difference between the highest-energy occupied molecular orbital and the lowest-energy unoccupied molecular orbital (Bond et al. 2007). Increasing the extent of sp^2 hybridisation, that is, increases the covalent nature of the BC decreases the size of the optical gap, and hence increases the absorbing properties of the BC.

$$\sqrt{\alpha E} = B(E - E_g) \tag{1.23}$$

where α is the absorption coefficient, E is the energy of the incident radiation, B is a constant and E_g is the optical gap.

Hopkins et al. (2007a) illustrate the relationship between the optical and chemical properties of biomass burning; cases of sp^2 hybridisation greater than 80 % were associated with ω_0 less than 0.5, whilst lower sp^2 hybridisation (20 – 60 %) correlated with ω_0 more than 0.8. Pure BC has been seen to have mass absorption cross sections of at least 5 $m^2 g^{-1}$ at 550 nm (Bond et al., 2013).

BC has a mean atmospheric lifetime of 5 to 10 days (Schwarz et al., 2006a), dependent on the aging processes and deposition rates. Freshly emitted BC is externally mixed from other aerosol species; consisting of distinct individual spherules (Pósfai et al., 2004), which form chain-like agglomerates, and are typically hydrophobic in character (Hopkins et al., 2007b). These chain-like aggregates have been observed to collapse into densely packed soot clusters (Fuller et al., 1999; Li et al., 2003; Liousse et al., 1993; Martins et al., 1998a).

It is well recognised that BC contributes to the indirect climate effect; as BC evolves in the atmosphere it becomes internally mixed, becoming coated with other chemical components (Schwarz et al., 2006a). A process which occurs on a short timescales (Moffet and Prather, 2009; Riemer et al., 2004). Chemical oxidation of the organic compounds (section 1.3.3) by atmospheric radicals such as O_3, OH and NO_x, forms polar surface groups on BC surfaces, transforming hydrophobic surface sites to hydrophilic surface sites which by definition interact and absorb water. The physical

aging of a aerosol surface is the mixing processes of condensation and coagulation which add soluble material (Kanakidou et al., 2005). It is the extent of these processes which drive the cloud condensation nucleating (CCN) ability of the particles, lending the potential for activation into cloud droplets.

Reducing BC in the atmosphere is a proposed method of climate mitigation. Climate mitigation involves a reduction of the top-of-the-atmosphere (TOA) direct radiative forcing leading to a reduction of surface heating. The atmospheric lifetime of BC is short, and a reduction of BC emissions may be an effective temporary method of mitigating climate change; such a reduction in BC emissions would equally benefit health and air quality (Bond and Sun, 2005).

1.3.3 Biomass Burning Chemical Composition: Organic Carbon

Biomass burning processes emit primary organic aerosol (POA) directly into the atmosphere with secondary organic aerosols (SOA) formed *in-situ* in the atmosphere from low volatility gas-phase pre-cursors (VOC's). Partitioning of the low volatility vapours to the aerosol phase is dependent on the vapour pressure. A high equilibrium vapour pressure results in a tendency to remain in the gas phase, whereas a low equilibrium vapour pressure favours a partition to the aerosol phase. The chemical composition of organic aerosols is complex and can contain hundreds of different chemical compounds (Graedel, 1979). Biomass burning processes are the largest emission source of these POA into the atmosphere (Liousse et al., 1996). Organic carbon refers solely to the carbon content, excluding the hydrogen and oxygen associated with organic aerosol (Bond et al., 2013).

Levoglucosan, a cellulose combustion product, has been identified as the most abundant individual organic compound (Graham et al., 2002). These water-soluble organic carbon (WSOC) compounds have a complex chemical structures made up of anhydrosugars, aromatics, sugars / sugar alcohols and dicarbonyls (Decesari et al. 2006; Graham et al 2002; Guyon et al 2002; Kundu et al. 2010), and have been shown to dominate in the submicron aerosol fraction (Fuzzi et al., 2007). These hygroscopic compounds influence cloud microphysical properties through the indirect effect, which can be both regionally and globally important.

Light absorbing carbon (known as brown carbon) is a subset of organic carbon with weakly light absorbing properties (Andreae and Gelencsér, 2006). It shows a strong wavelength dependence across the visible spectrum, which can be used to separate the absorption contribution of BC and light absorbing organic carbon (Bond et al., 2013). In contrast to BC, the mass absorption cross section is less than 1 $m^2 g^{-1}$ at 550 nm (Bond et al., 2013). The direct radiative forcing for organic matter for open biomass burning reported in AR4 was -0.10 W m^{-2} (-0.04 to -0.20 W m^{-2}); a more recent report from Bond et al. (2011) showed a similar forcing of -0.14 W m^{-2} (-0.05 to -0.27 W m^{-2}).

1.3.4 Biomass Burning Measurement Campaigns

Logistical difficulties of operating in Amazonia have meant there have been relatively few measurements of Amazonia biomass burning aerosols. The primary aircraft campaign in the region was the Smoke, Clouds, and Radiation-Brazil (SCAR-B) aircraft campaign, with a number of ground based measurement campaigns as part of the Large-Scale Biosphere-Atmosphere Experiment in Amazonia providing studies of aerosols, cloud processes and the Amazonian hydrological system on a more local scale.

The SCAR-B campaign used the NASA ER-2 aircraft during August and September 1995 (Kaufman et al., 1998). The campaign obtained measurements of the rates of emissions of trace gases and particulates from biomass burning, and observed the influence of atmospheric processes on these emission products.

Large-Scale Biosphere-Atmosphere Experiment in Amazonia (Artaxo et al., 2002) is a research program which ran between 1995 – 2005 to understand biogeochemical, hydrological and climatological processes within Amazonia. The LBA-EUSTACH1&2 campaigns carried measurements from a 54 m measurement tower during April – May 1999 and September-October 1999 (dominated by biomass burning processes) in the Jaru Biological Reserve, an area of primary tropical forest situated in the Brazilian state of Rondônia. The LBA – Smoke Aerosols, Clouds, Rainfall, and Climate: Aerosols From Biomass Burning Perturb Global and Regional Climate (LBA-SMOCC) campaign was a ground based site, operational for 66 days from September to November 2002 located in Rondônia, Brazil. The study period covered the transition period between the dry season into the wet season (Andreae et al., 2004; Decesari et al., 2006; Falkovich et al., 2005; Fuzzi et al., 2007).

The range of biomass-burning aerosol physical and optical properties published within the literature reflects the considerable variability associated with biomass-burning. For example the influence of i) vegetation type ii) fuel load iii) fuel dryness and the combustion process i) fire extent ii) frequency and iii) intensity. Table 5 relates the influence of fire intensity on aerosol chemical, physical and optical properties. The understanding of key optical properties is key for validating and improving retrieval algorithms from satellite measurements and in model representation.

Table 5 Influence of fire intensity on aerosol chemical, physical and optical properties.

Smouldering	Flaming
Increased organic carbon content	Increased BC content
Lower imaginary part of the refractive index	Higher imaginary part of the refractive index
Larger mean particle size	Smaller mean particle size
Higher single-scattering albedo	Lower single-scattering albedo
Lower attenuation and absorption Ångström exponent	Higher attenuation and absorption Ångström exponent

A summary of the accumulation lognormal mode of the mean Amazonian biomass burning size distribution from Amazonian field campaigns is presented in table 6, and the corresponding optical properties are presented in table 7. The current understanding of these physical and optical properties shall be discussed in section 1.3.5 and 1.3.6, respectively.

1.3.5 Biomass Burning Physical Properties

1.3.5.1 Biomass Burning Physical Properties: Size Distribution

Emissions of aerosol from biomass burning fall into the accumulation mode in terms of number and mass size distributions (Reid et al., 2005b). This is emphasised by the consistency in the measurements presented in table 6; the lognormal modes of the mean mineral dust size distribution as measured during previous Amazonian biomass burning field campaigns (that were referred to in section 1.3.4). Count median diameter

have been in the range of 0.12 – 0.23 μm and volume median diameters of 0.25 – 0.3 μm are presented by Reid et al. (2005b) with recent published values from Janhall et al. (2010), Rissler et al. (2006) and Schafer et al. (2008) falling within this range.

Particle size distribution evolves in the atmosphere with particle growth occurring in the plume due to condensation and coagulation processes and particle aging with time in the atmosphere. Capes et al. (2008) show that near the source of emission, number concentration peaked at radii of 0.055 μm, whereas aerosol sampled at a distance far from source number concentration peaked at 0.150 μm.

The properties of biomass burning aerosol emitted vary depending on flaming and smouldering phases of combustion, related to combustion temperature, fuel moisture, vegetation type and oxygen supply (Langmann et al., 2009). It is well documented in literature that fire intensity represents the energy released during different phases of a fire (Flannigan et al., 2009), with flaming phase of fires occurring at temperatures between 800 K and 1200 K, whilst smouldering phase occurs with at lower temperatures between 450 K and 850 K (Langmann et al., 2009).

Reid et al. (2005a) highlighted relatively few measurements in the literature investigating the relationship of combustion efficiency of wildfires to aerosol size, and as such this has been the subject of laboratory studies (McMeeking et al., 2009). Particles from smouldering combustion have larger size distributions compared to particles generated by the flaming phase of combustion (Reid et al., 2005b). This is evident from the study by Martins et al. (1998a), which present flaming distributions with CMD of 0.0087 μm and smouldering distribution with CMD of 0.12 μm. Flaming phase combustion produces aerosol with increased BC whilst smouldering phase combustion generates increased organic carbon content (Hopkins et al., 2007a; Reid et al., 2005b).

Biomass burning aerosol number size distributions based on multi-instrument *in-situ* measurements for two case studies of Rondônian regional haze and remote Amazonian aerosol from the SAMBBA 2012 campaign will be presented in chapter 6.

Table 6 Summary of geometric mean diameter (GMD) and geometric standard deviations (σ) for each of the accumulation lognormal mode of the mean Amazonian biomass burning size distribution. CMD is count median diameter, VMR and VMD are the volume median radius and diameter, respectively.

Parameter	Method	Size Distribution		Campaign	Reference
		Geometric Mean Diameter (μm)	Standard Deviations (σ)		
Geometric Mean Diameter (GMD)	DMPS and PCASP Maraba, smouldering Maraba, flaming Porto Vehlo, regional haze	0.12 (D_g), 0.27 (D_gV) 0.087(D_g), 0.25 (D_gV) 0.19(D_g), 0.52 (D_gV)	1.89(σ_g), 1.63 (σ_gV) 1.87(σ_g), 1.62 (σ_gV) 1.78(σ_g), 1.78 (σ_gV)	SCAR-B 1995 Smoke, Clouds, and Radiation-Brazil	(Martins et al., 1998a)
Geometric Mean Diameter (GMD)	DMPS (1 day old) OPC (1 day old) DMPS (2 – 3 days old) OPC (2 – 3 days old)	0.12 $\pm$ 0.03(D_g), 0.29 $\pm$ 0.05 (D_gV) 0.14 $\pm$ 0.03(D_g), 0.26 $\pm$ 0.02 (D_gV) 0.18 $\pm$ 0.03(D_g), 0.35 $\pm$ 0.05 (D_gV) 0.21 $\pm$ 0.02(D_g), 0.30 $\pm$ 0.02 (D_gV)	1.80 $\pm$ 0.15(σ_g), 1.61 $\pm$ 0.2 0(σ_gV) 1.71 $\pm$ 0.16(σ_g), 1.35 $\pm$ 0.06 (σ_gV) 1.65 $\pm$ 0.16(σ_g), 1.49 $\pm$ 0.09 (σ_gV) 1.89 $\pm$ 0.07(σ_g), 1.49 $\pm$ 0.09 (σ_gV)	SCAR-B 1995 Smoke, Clouds, and Radiation-Brazil	(Reid and Hobbs, 1998; Reid et al., 1998b; Reid et al., 2005b)
Volume Median Radius (VMR)	AERONET Cimel Sun-sky radiometer Cerrado and Forest Sites	0.13 $\pm$ 0.2 (AM) 11.5 (CM)	0.60 $\pm$ 0.04 (AM) 1.26 $\pm$ 0.23 (CM)	SCAR-B 1995 Smoke, Clouds, and Radiation-Brazil	(Remer et al., 1998)
Volume Median Diameter (VMD)	AERONET (400 nm) Amazonia Forest South American Cerrado	0.28 $\pm$0.02 (AM) 6.5 $\pm$ 0.09 (CM) 0.28 $\pm$0.02 (AM) 6.5 $\pm$ 0.08 (CM)	1.49 $\pm$ 0.06 (AM), 2.2 $\pm$ 0.1(CM) 1.49 $\pm$ 0.04 (AM), 2.1 $\pm$ 0.1(CM)	AERONET Cimel Sun-sky radiometer	(Dubovik et al., 2002) updates from (Reid et al., 2005b)

Parameter	Method	Size Distribution		Campaign	Reference
		Geometric Mean Diameter (μm)	Standard Deviations (σ)		
Geometric Mean Diameter (GMD)	Scanning mobility particle sizer (SMPS)	0.110 ± 0.015 (within BL) 0.139 ± 0.017 (above BL)	-	LBA-EUSTACH 2 Large-Scale Biosphere Atmosphere Experiment	(Guyon et al., 2003)
Count Median Diameter (CMD) Volume Median Diameter (VMD)	-	0.12 – 0.23 (D_g) 0.26 – 0.35 (D_gV)	-	Review: Biomass burning emissions	(Reid et al., 2005b)
Geometric Mean Diameter (GMD)	Differential Mobility Particle Sizer (DMPS) (diurnal average)	0.012 (Nucleation) 0.092 (Aitken) 0.190 (Accumulation)	1.82 1.63 1.53	LBA-SMOCC Large-Scale Biosphere Atmosphere – Smoke Aerosols, Clouds, Rainfall, and Climate	(Rissler et al., 2006)
Volume Median Radius (VMR)	AERONET Cimel Sun-sky radiometer Northern Forest, Southern Forest. Cerrado	0.13 - 0.17 μm	-	AERONET Cimel Sun-sky radiometer	(Schafer et al., 2008)

1.3.6 Biomass Burning Aerosol Optical Properties

1.3.6.1 Biomass Burning: Refractive Index

Refractive index is not a trivial parameter to measure directly but is achieved indirectly through closure calculations between measurements of optical properties and theoretical calculations. Limitations lie in the uncertainties and variability in input parameters. The literature values presented in table 7 show the spread in published refractive indicies across the Rondônia and Amazonia region, which reflects the complexity in biomass burning composition and uncertainties in measurements of key optical properties, particularly absorption measurements of black carbon and organic.

Guyon et al. (2003) present a refractive index of $m = 1.42 – 0.006i$ measured during the wet season in Rondônian; with a higher imaginary part of the refractive index, $i = 0.013 – 0.016$, during the transition period into the biomass burning season. This change in the imaginary part reflects the increasing levels of atmospheric absorbing carbonaceous material. During the SCAR-B campaign, six methods for measuring aerosol shortwave absorption and/or BC content were employed including an optical extinction cell (a 6.4 m long transmissometer) to provide direct measurements of extinction. Using such techniques, Reid and Hobbs (1998) publish a complex refractive index for Rondônian regional haze of $m = 1.50 – 0.02i$.

AERONET Cimel radiometer measurements have suggested that biomass burning in regions of cerrado vegetation (associated with flaming phases of combustion) produce a mean refractive index $m = 1.52 – 0.0015i$. Biomass burning of Amazon forest commonly shows a smouldering phase of combustion with a refractive index of $m = 1.47 – 0.0015i$ identified by Dubovik et al. (2002). Imaginary refractive index presented by Eck et al. (2003) are in agreement (approximately $0.010i$) with the values from Dubovik et al. (2002).

Schkolnik et al. (2007) and Schmid et al. (2009) present complex refractive index for elemental carbon and organic carbon using ground based filter measurements from the LBA-SMOCC campaign constrained with theoretical Mie calculations. The imaginary part of the refractive index suggested by the authors are lower than recommended by Bond and Bergstrom (2006) and Bond and Sun (2005) for elemental carbon.

Two approaches for representing the complex refractive index of Rondônian regional haze shall be presented in chapter 6 of this thesis; the refractive indicies are constrained by aerosol composition *in-situ* measurements. It will be shown that the continuing complexity of key optical properties, particularly absorption measurements of black carbon and organic carbon remain a significant uncertainty.

1.3.6.2 Biomass Burning Aerosol: Single-scattering albedo

The AR4 report summarised that globally biomass burning aerosol single-scattering albedo are in the order of 0.85 – 0.89 close to source, increasing to 0.91 correlated with atmospheric aging. The range of published single-scattering albedo associated with biomass burning aerosol is driven by the fraction of absorbing BC within the aerosol particle. McMeeking et al. (2009) show the relationship of single-scattering albedo as a function of black carbon/total carbon associated with the strong light-absorbing efficiency of BC. In the case of flaming combustion the single-scattering albedo was as low as 0.4, whilst for smouldering combustion a higher single-scattering albedo of 0.8 – 0.9 is associated.

The results from the SCAR-B campaign found flaming combustion resulted in ω_0 of 0.74 – 0.77, whilst smouldering phases of combustion had higher ω_0 of 0.83 – 0.84. Measurements of regional haze aerosol found ω_0 of 0.87, reflecting the increased content of organic carbon within the aerosol composition (Martins et al., 1998a; Reid and Hobbs, 1998).

1.3.6.3 Biomass Burning Aerosol: Asymmetry Parameter

Reid et al. (2005a) suggested that the asymmetry parameter shows little sensitivity to changes in parameters other than the size distribution; identifying that smaller volume median diameter, and narrower geometric standard deviations, result in a lower asymmetry parameter. This is supported by Dubovik et al. (2002) who showed a decrease of the asymmetry parameter from 0.69 to 0.58 for an increasing wavelength (across the wavelength range of 400 to 670 nm); indicative of biomass burning aerosols dominating in the accumulation mode of the size distribution.

Martins et al. (1998a) show the combustion phase influences the asymmetry parameter; for flaming combustion events Martins et al. (1998a) found g of 0.485 and smouldering

phases of 0.553, in which an increase in the size distribution was associated with smouldering combustion. In regional haze cases the asymmetry parameter was 0.617, reflecting the growth of particles which results in increased forward scatter. Reid et al. (2005a) recommend an asymmetry value of tropical forest fresh 0.59 $\pm$ 0.06 and 0.63 $\pm$ 0.06 for aged smoke, for cerrado vegetation 0.55 $\pm$ 0.06 for fresh emissions and aging smoke from cerrado vegetation 0.58 $\pm$ 0.06 for the use in radiative transfer calculations.

1.3.6.4 Biomass Burning Aerosol: Mass Scattering and Absorption Efficiency

Methods used to determine the mass absorption efficiency include extinction optical cells, cavity ring down techniques or filter measurements such as a PSAP. Mass absorption efficiencies from Reid and Hobbs (1998) suggested flaming combustion produced a higher mass absorption efficiency of 1.0 $m^2\ g^{-1}$ whilst smouldering combustion resulted in 0.7 $m^2\ g^{-1}$. This is consistent with Reid et al. (2005a) who reviewed literature biomass burning across the globe concluding with measurements in the range of 0.6 – 1.0 $m^2\ g^{-1}$ for mixed phase combustion, whilst smouldering combustion resulted in efficiencies less than 0.3 $m^2 g^{-1}$.

Reid and Hobbs (1998) suggest mass scattering efficiency of 2.8 – 3.6 $m^2 g^{-1}$ for fresh young smoke, whilst regional haze reflected higher mass scattering efficiency of 4.1 $m^2 g^{-1}$ indicative of a thicker particle coating associated with particle aging. Chand et al. (2006) found mass scattering efficiencies of 5.0 $m^2\ g^{-1}$ consistent with Guyon et al. (2003), whilst mass absorption efficiencies of 0.33 $m^2\ g^{-1}$ are the lowest values within in the literature. Bond and Bergstrom (2006) suggest a mass-normalised absorption cross section of 7.5 $m^2\ g^{-1}$ at 550 nm for an uncoated BC particle (m = 1.95 – 0.79i) as an upper limit of the light absorption.

Optical parameters comprising the aerosol single-scattering albedo, aerosol mass extinction efficiency and the aerosol asymmetry factor for Rondônian regional haze measured during the SAMBBA 2012 campaign will be presented in chapter 6.

Table 7 Summary of biomass burning aerosol optical properties collated from previous Amazonian field campaigns at wavelengths of 550 nm (alternative wavelengths are stated in brackets).

Campaign	Vegetation Type	Refractive Index		ω_0	g	K_{scat} $(m^2 g^{-1})$	K_{abs} $(m^2 g^{-1})$	Reference
		n	k					
SCAR-B 1995 Smoke, Clouds, and Radiation-Brazil	Fresh Forest Flaming Fresh Forest Smouldering Fresh Cerrado	-	-	0.74 ± 0.06 0.84 ± 0.02 0.77 ± 0.03	-	2.8 ± 0.5 3.6 ± 0.4 3.4 ± 0.6	1.0 ± 0.2 0.7 ± 0.1 1.0 ± 0.1	(Reid and Hobbs, 1998)
SCAR-B 1995 Smoke, Clouds, and Radiation-Brazil	Regional Haze	1.50	- 0.02i	0.86 ± 0.05	-	4.1 + 0.9	0.7 + 0.2	(Reid and Hobbs, 1998)
SCAR-B 1995 Smoke, Clouds, and Radiation-Brazil	AERONET	1.43	- 0.0035i	0.90 (assumed)	0.65 ± 0.04 0.57 ± 0.06 0.50 ± 0.06	-	-	(Remer et al., 1998)
SCAR-B 1995 Smoke, Clouds, and Radiation-Brazil	Maraba, smouldering Maraba, flaming Porto Vehlo, regional haze	2.0	-1.0i	0.83 0.74 0.87	0.533 0.485 0.617	-	-	(Martins et al., 1998b)

Campaign	Vegetation Type	Refractive Index		ω_0	g	$K_{scat}\ (m^2 g^{-1})$	$K_{abs}\ (m^2 g^{-1})$	Reference
		n	k					
AERONET retrieval (1993 – 1995)				(440/670)	(440/670)	(550)	(550)	(Dubovik et al., 2002) updates in (Reid et al., 2005a)
	Amazonian forest	1.47 (± 0.003)	0.0093*i* (± 0.003)	0.94/0.93	0.69/0.58	3.5 – 4.1	0.21 – 0.25	
	S. American cerrado	1.52 (± 0.001)	0.0150*i* (± 0.004)	0.91/0.89	0.67/0.59	4.1 – 4.7	0.36 – 0.42	
	Regional Haze			0.935				
LBA-EUSTACH 1999 Large-Scale Biosphere Atmosphere Experiment	Background Rondônian aerosol	1.42	-0.006*i*	0.93 ± 0.003	0.62 ± 0.02	5.0	-	(Guyon et al., 2003)
	Biomass burning aerosol	1.41	-0.013*i*	0.90 ± 0.030	0.70 ± 0.03			
AERONET retrieval	Jaru biological reserve, Rondônia site Brazil	-	-0.0138*i* (440 nm) -0.0123*i* (675 nm)	0.94 ± 0.03	-	-	-	(Eck et al., 2003)
Review: Biomass burning emissions	-Mean flaming	-	-	~ 0.75	-	3.4	0.5	(Reid et al., 2005a)
	Mean smouldering			~ 0.90		3.7	0.4	

Campaign	Vegetation Type	Refractive Index		ω_0	g	$K_{scat}\ (m^2 g^{-1})$	$K_{abs}\ (m^2 g^{-1})$	Reference
		n	k					
LBA – SMOCC Large-Scale Biosphere Atmosphere – Smoke Aerosols, Clouds, Rainfall, and Climate	Pasture Site	-	-	0.92 + 0.02	-	5.0	0.33	(Chand et al., 2006)
LBA – SMOCC Large-Scale Biosphere Atmosphere – Smoke Aerosols, Clouds, Rainfall, and Climate	Elemental carbon component	1.87	-0.22*i*	-	-	-	-	(Schkolnik et al., 2007)
	Unidentified organic matter fraction	1.4	0*i*					
	Total organic carbon	1.3	0*i*					
LBA – SMOCC Large-Scale Biosphere Atmosphere – Smoke Aerosols, Clouds, Rainfall, and Climate	Elemental carbon component	1.90 (± 0.1)	-0.20*i*	-	-	-	-	(Schmid et al., 2009)
	Organic carbon component	1.46 (± 0.2)	0*i*					
AERONET retrieval	Northern Forest	-	-	0.926 ± 0.026	-	-	-	(Schafer et al., 2008)
	Southern Forest			0.914 ± 0.043				
	Cerrado			0.887 ± 0.039				

1.4 Research Aims

This literature review describes the research background and explains the motivation for pursuing the work carried out within this thesis. The review discusses a number of advances in recent observations of aerosol properties and highlights some of the parameters which remain uncertain. The literature review highlights two globally-important aerosol species with emissions from two key regions of the globe. The largest single source of global mineral dust is the Saharan-Sahel region in Northern Africa. Despite considerable investment in a number of previous campaigns carrying out atmospheric measurements there still remains a sparse dataset of key optical properties and there remains a range in published values of properties such as refractive index, mass extinction efficiency and the asymmetry parameter. Forty percent of global emission of black carbon are from biomass burning, with emissions dominated in regional hotspots such as West Africa and the Amazon Basin region (Streets et al., 2004). Amazonian biomass burning is the largest source of anthropogenic aerosol in the southern hemisphere (Koren et al., 2004). These remote regions suffer from a critical lack of observational data of their physical and optical measurements.

This thesis describes the analysis and interpretation of aircraft observation during two field campaigns, the Fennec campaign measuring mineral dust in the Sahara and the second the South AMerican Biomass Burning Analysis (SAMBBA) observing biomass burning aerosol emissions across Amazonia, Brazil. The microphysical and optical properties of aerosols need to be well quantified to understand the radiative impact, important in climate models and increasingly so in Numerical Weather Predication (NWP). The aerosol direct radiative forcings requires the knowledge of a set of aerosol parameters (as a function of wavelength); the aerosol mass extinction efficiency, the single-scattering albedo and the asymmetry parameter in order to fully define the optical properties of an aerosol. The variability in the literature of a number of the key optical properties reflects the necessity for further observations, for improved parameterisation in models and understanding of key optical properties required in calculating radiative forcing.

The key theme within this thesis is to improve the understanding the microphysical and optical properties of aerosols of mineral dust and biomass burning aerosol, with a focus of the technical aspects of aerosol sampling though aircraft inlets and multi-instrumental assessment. This aim will be broken down into five key questions posed within this thesis:

1. How well is the coarse mode of mineral dust presently measured from an aircraft platform on the FAAM BAe-146 and what influence do the current Rosemount inlets have on the sampling of coarse mode aerosol and aerosol microphysical properties?

The inconsistency in mineral dust size distributions observed across previous North African field campaigns reflects the difficulty in making such measurements. This thesis describes recent improvements to and a critical evaluation of the current aerosol sampling for measuring coarse mode aerosol, a current limitation aboard the FAAM BAe-146 aircraft. The review of mineral dust optical properties shows how each parameter is strongly tied to the representation of coarse mode aerosol and the aim for Fennec was in making improved measurements of coarse mode mineral dust.

This thesis will investigate the technical aspects to coarse mode aerosol measurement comparing size distributions at two inlets on the FAAM BAe-146 aircraft; the standard Rosemount inlet and the LTI. This comparison will achieve a better understanding of the Rosemount inlet efficiencies, through which it will be possible for aircraft users to apply corrections to measurements made at an instrument to account for the aerosol sampling system.

2. What are the impacts of the current measurement limitations on aerosol microphysical and optical properties?

It is necessary to understand the contribution of the aerosol coarse mode to parameters used to constrain and assess the radiative properties of mineral dust, in terms of the single scattering albedo and asymmetry parameter. Mineral dust size distributions measured at the LTI were compared to size distributions measured by the externally-mounted probes; an experiment which draws on the ability to measure the ambient size distribution with an instrument which itself does not sample from

an inlet. The quantification will reduce some of the uncertainty in the impact of inlets on the sampling of coarse mode, and help explain the considerable variability in the microphysical and optical properties of mineral dust which has been observed in previous field campaigns. The variability in the optical properties between the pilot, Fennec 2011 and Fennec 2012 campaigns compared with previous campaigns is additionally investigated.

3. Increased mineral dust surface area associated with fresh dust uplift has been proposed to be correlated with reduced ozone concentrations – are these correlations observed within the Fennec measurements close to the source of fresh dust emissions?

The coarse mode of mineral dust has been proposed as an important for heterogeneous uptake, with freshly emitted Saharan dust suggested as potentially a significant route of ozone loss. The *in-situ* aerosol and chemistry measurements during the Fennec campaigns will be investigated to identify case studies of increased mineral dust surface area associated with fresh dust uplift correlated with reduced ozone concentrations. HYSPLIT back trajectories will be used to identify the source of air masses to understand ozone source regions.

4. How do the different instrumental techniques used in the thermal denuder instrument compare with the SP2 in resolving black carbon size and coating thickness of biomass burning aerosol?

This evaluation draws on two airborne instruments on the research aircraft with the capability to measure coating thickness using different techniques. The thermal denuder which uses thermal volatility technique has not previously been used to investigate coating thickness of biomass burning aerosol from an aircraft platform, whilst comparing to the SP2 instrument which uses laser incandescence which is a well characterised technique for measuring properties of black carbon. Median shell-to-core diameter ratios for each instrument will be derived and compared, which provides a representation of particle coating thickness and mean size distributions of black carbon.

5. How does the advancement in aerosol instrumentation used during SAMBBA improve the understanding of regional haze in two regions Rondônia and Amazonia in terms of size distribution, refractive index and optical properties, compared with the previous SCAR-B campaign in the Rondônian region in 1995?

There has been a significant advance in aerosol instrumentation since the SCAR-B campaign in 1995 including the aerosol mass spectrometer and single particle soot photometer. Observations from SAMBBA campaign will be used to improve understanding of the complexity of biomass burning aerosol which has been demonstrated within this literature review. This thesis will present relationships between biomass burning aerosol properties bringing together size distributions, aerosol mixing state and optical properties from a suite of instruments onboard the FAAM BAe-146. It will be demonstrated that an accurate measurement of size distributions and scattering and absorbing properties of both black carbon and organic carbon are important components in representing the refractive index of biomass burning, and in turn assessing the optical properties of the aerosol.

1.5 Thesis Overview

A description of the Fennec and SAMBBA campaigns, the associated campaign meteorology and flight sorties are detailed in chapter 2. The airborne instrumentation and a methodology providing an overview of the approach taken in the analysis of the campaign data is presented in chapter 3. Chapter 4 will address the first question posed above, and discusses the current limitations in aircraft aerosol sampling and recent advances in aerosol sampling with the installation of the Low Turbulence Inlet and presents a comparison between the Rosemount Inlet and the Low Turbulence Inlet, and mineral dust microphysical properties.

Chapter 5 describes the mineral dust optical properties from the Fennec pilot, 2011 and 2012 field campaigns, and the contribution of the mineral dust coarse mode to the optical properties is demonstrated, answering the second research aim of this thesis. Observations of elevated mineral dust concentrations and ozone depletion events are extended to include a correlation with increased mineral dust surface area

associated with elevated dust concentrations; two case studies are presented providing evidence for the third aim within this thesis.

Chapter 6 will answer the final two aims of this thesis presenting two case studies of Rondônian regional haze and Amazonian aerosol from the South AMerican Biomass Burning Analysis (SAMBBA) campaign highlighting atmospheric profiles and back trajectories, biomass burning microphysical and optical properties, biomass burning mixing state and coating thickness and investigates measurement consistency through optical closure studies. Chapter 7 presents the conclusions drawn within this thesis, along with a discussion of remaining limitations and recommendations for future research.

2 Observational Campaigns

The temporal and spatial scales of atmospheric processes that affect aerosols and clouds call for a multidisciplinary, multi-platform approach to making measurements whilst highlighting the challenge involved in making atmospheric measurements. Atmospheric processes extend from gaseous-phase chemical reactions, to the microphysical scale of aerosol properties and cloud processes, through the regional influence of air quality on human health and visibility up to meso- and synoptic-scale dynamical features of weather systems. The representation of such processes in models is required in understanding perturbations in the Earth System and the impacts and feedbacks upon a changing climate.

Ground based measurements tend to be made up of a multi-instrumented site at a fixed location carrying out long term measurements, examples include the AERONET made up of 500 surface-based Sun photometers (Holben et al., 1998), the UKs Facility for Ground based Atmospheric Measurements (FGAM) (Carpenter et al., 2010) and Global Atmosphere Watch (GAW) program. Long-term ground sites provide the advantage that they build up a climatology of a particular region.

Satellite instruments use remote sensing techniques for atmospheric phenomenon, providing a worldwide coverage within the swath of observation of the satellite. Polar-orbiting satellites are used for longer term sensing and weather forecasting, providing global coverage over the course of a successive orbits, an important requirement for NWP models (Rabier, 2005). Geostationary-orbiting satellites have a high temporal sensing and are suitable for short-range forecasting. The combination of the two types of satellites provides complete global monitoring.

Remote sensing measurements of aerosols are often obscured by cloud cover and require cloud screening. Using remote sensing retrieval algorithms, a number of aerosol parameters must be inferred such as emission rates, concentrations, optical

properties and particle shape, and as such there is a requirement for validating properties retrieved from satellites against *in-situ* measurements.

The atmosphere is a three dimensional space and long-term ground-based and satellite measurements can be complemented with airborne measurements. Airborne remote sensing instruments can be used in the testing and validation of both ground and space borne remote sensing instruments. Airborne measurements can provide high resolution datasets of atmospheric phenomenon, with the added versatility in making such measurements. A multidisciplinary approach incorporating satellite, ground sites and intensive airborne measurements coupled with modelling studies provide a highly effective approach in better understanding atmospheric measurements.

This chapter will discuss the use of the BAe-146 aircraft during two field campaigns; the Fennec campaign in June 2011/12 and the South American Biomass Burning Analysis (SAMBBA) campaign in September 2012. This chapter describes the multidisciplinary approach used during both campaigns; it describes idealised flight patterns used to make aerosol measurements from the BAe-146 research aircraft (section 2.1) and details the aims and objectives of the Fennec (section 2.2) and SAMBBA (section 2.3) campaigns. The chapter describes the representivity of the meteorology encountered during each campaign in order to place the meteorology within the context of the climatology of each campaign region (section 2.2.1 and 2.3.1). Satellite images presented from each campaign were used to identify sources and transport of both mineral dust (section 2.2.3) and biomass burning aerosol (section 2.3.3), crucial tools in planning flight sorties.

The meteorology encountered is crucial in order to understand the mineral dust uplift and transport, which in turn drives the nature of the microphysical and optical properties of mineral dust. The meteorology and corresponding flights during Fennec 2011 and 2012 campaigns is discussed in sections 2.2.4 and 2.2.5, respectively. The meteorology and corresponding flights during SAMBBA is presented in section 2.3.4; it is essential in order to understand the transport of biomass burning aerosol away from the source of combustion.

2.1 Facility for Airborne Atmospheric Measurements

The Facility of Airborne Atmospheric Measurements (FAAM) is a collaborative facility between the Met Office and the Natural Environment Research Council (NERC) providing an aircraft platform for atmospheric airborne measurements for the UK research community. The airborne platform is a modified BAe-146, operated by Directflight and maintained by Avalon Aero. The aircraft is modified to carry a suite of state of the art instruments designed for atmospheric measurements; research flights are up to 5 hours based on the aircraft payload. The aircraft carries a suite of instruments for multi-component weather and climate research including i) cloud physics and dynamical studies, ii) radiative transfer studies iii) tropospheric chemistry measurements iv) boundary layer and turbulence studies and v) remote sensing capabilities for comparison against ground based sites and satellite measurements.

Flight sorties are designed with common aircraft manoeuvres applicable across multiple aircraft campaigns. Aircraft manoeuvres are carried out at a nominal air speed of 110 m s^{-1} with profile descents and ascents from transit cruise altitude through the atmosphere are carried out at climb/descent rate of 5 m s^{-1} (Osborne et al., 2007). It is important to note that profiles, with typical gradients during profiles of about 4º, cover a greater distance in the horizontal plane than in the vertical; as such boundary layer variability is an important consideration. The aircraft pitch angle on science runs is approximately +4.5º.

Flight sorties consist of horizontal transects through the atmosphere which are termed as straight and level runs (SLRs). Flights can consist of stacks of horizontal legs, the exact height of which are often decided in flight with aerosol layers identified through remote sensing techniques such as by Light Detection And Ranging (lidar), and using on-board real time monitoring during profiles. Once the heights of these layers have been identified the aircraft carries out dedicated *in-situ* measurements. Proportions of flights are spent performing SLRs at high altitude (7 – 8 km), which facilitates an increase in the range of the aircraft, and is necessary for dropping radiosondes to provide thermodynamic profiles of the atmosphere.

2.2 Campaign Overview: Fennec

The motivation driving the Fennec campaign was to improve the understanding of the Saharan Climate System (Washington et al., 2012). This stems from a critical lack of observational data throughout the central Sahara and a need to validate and improve model forecasts across this region (Marsham et al., 2013). A feature of the summertime Saharan Climate System is a large low pressure system, the Saharan Heat Low (Lavaysse et al., 2009), which develops due to the intense daytime solar heating. This is the deepest boundary layer on the planet and the summertime aerosol maxima coincides with the heat low (Engelstaedter et al., 2006). Much of what is known about the SHL is from numerical models which often treat the Saharan system differently, for example, in terms of incoming and outgoing solar radiation, surface temperature, mean surface layer pressure (MSLP). Models disagree on the pressure at the centre of the heat low with differences of >2 hPa, whilst the Coupled Model Intercomparison Project (CMIP3) modelled the June climatology of land surface temperature found differences of >6 K. For such a large pressure system, further measurements are needed to understand this system; this was a key objective for the Fennec campaign.

The breakdown and downward mixing of nocturnal Low-Level Jets (LLJ) have been proposed as a mechanism in the deflation and contributing process to mineral dust emission (Fiedler et al., 2013; Schepanski et al., 2009). There are limited observations regarding the representation and modelling of the Saharan nocturnal boundary layer and how the LLJ breaks down in the morning hours. One of the aims of Fennec was to sample the characteristics and associated dust emissions from LLJ breakdown.

Despite considerable investment in a number of campaigns carrying out atmospheric measurements there still remains a sparsity of measurements. Key source regions have shortages of data on dust particle-size distributions, particle shape, and elemental composition and in particular mineralogy, all of which affect dust optical properties. The Fennec campaign saw advances in aerosol sampling characterisation and coarse mode aerosol, which coincided with the installation of the Low Turbulence Inlet (LTI), with the aim to better understand the large range in published values in properties such as refractive index, mass extinction efficiency and the asymmetry parameter.

The observational side of Fennec was supported with multi-platform observations including supersites at Zouerate and Bordj-Mokhtar (Marsham et al., 2013b; Todd et al., 2013), and 8 Automatic Weather Stations (AWS) across the remote Sahara (Hobby et al., 2012). Fennec was also supported by an aircraft campaign including the FAAM BAe-146 and the SAFIRE Falcon-20 based in Fuerteventura. During the Fennec 2011 and 2012 aircraft campaigns, the BAe-146 operated from the El Matorral Airport in Fuerteventura. The aircraft flew a total of 16 flights between the 17 June and 28 June 2011 and 12 flights between 6 June and 18 June 2012. A summary of the flights for Fennec 2011 and Fennec 2012 are presented in table 8 and table 9, respectively. A Fennec pilot campaign was carried out between 5 – 8 April 2011 based at Ouarzazate, Morocco. Idealised flight patterns during Fennec are presented in figure 2.1.

The strength in the measurements of aerosol size distribution during Fennec is derived from the number of instruments deployed. The Passive Cavity Aerosol Spectrometer Probe (PCASP) measured across the accumulation mode, Grimm Sky-OPC (Optical Particle Counter) measured the accumulation and lower coarse mode whilst the upper coarse mode was measured using the Cloud Droplet Probe (CDP), Cloud and Aerosol Spectrometer (CAS), Cloud Imaging Probe (CIP) and Small Ice Detector (SID-2). These instruments are primarily used as cloud physics instrumentation, but have been used in aerosol measurements.

Meteorological instruments on the aircraft measured temperature, pressure, relative humidity, liquid water content, turbulence and winds. Chemistry instrumentation provided measurements of O_3 and carbon monoxide (CO), upwelling and downwelling radiation measurements across the visible and infrared spectrum was achieved with a full suite of radiation instruments, and remote sensing of mineral dust vertical distribution using lidar. A full description of these instruments is provided in chapter 3.

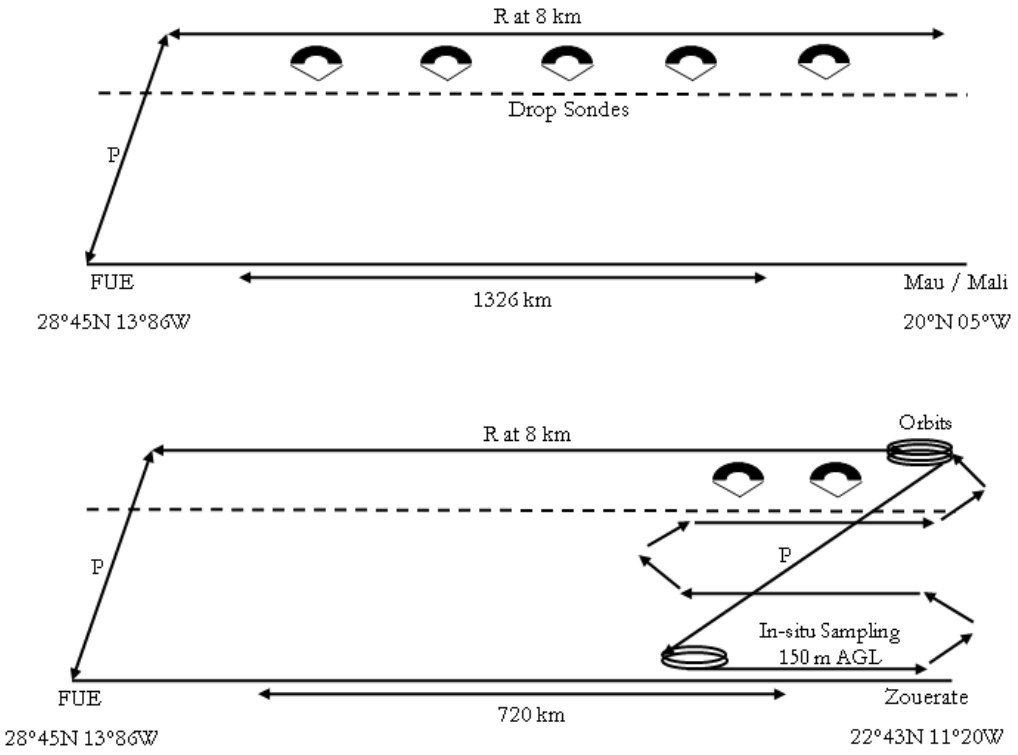

Figure 2.1 Idealised flight patterns during Fennec campaigns between the operating base in Fuerteventura (left-hand side of the figures) and the region of interest, typically Mauritania / Mali (right hand side of the figures). 'R' indicates a SLR, 'P' indicates profiles. (*Top*) Idealised flight pattern from flight B607 a remote sensing flight with a series of dropsondes (*bottom*) Idealised flight pattern from flight B611, a radiation fight with orbits above and within the aerosol layer, with *in-situ* sampling.

Lidar observations in figure 2.2 qualitatively identified a deep Saharan boundary layer, with dust aerosol well mixed throughout. The atmospheric boundary layer is defined the lowest portion of the atmosphere, directly impacted by the Earth's surface (Garratt, 1994)**.** Boundary layer depth ranges from only a few metres to many kilometres deep, influenced by the local meteorology, diurnal component (convection processes during the day, and stratification at night) and complex terrain (Garratt, 1994). Figure 2.2 presents relative depolarisation which is the ratio of depolarisation (instrument channel 1) to non-depolarisation (instrument channel 0), and is a proxy for atmospheric dust content encountered during flight B709 (17 June 2012).

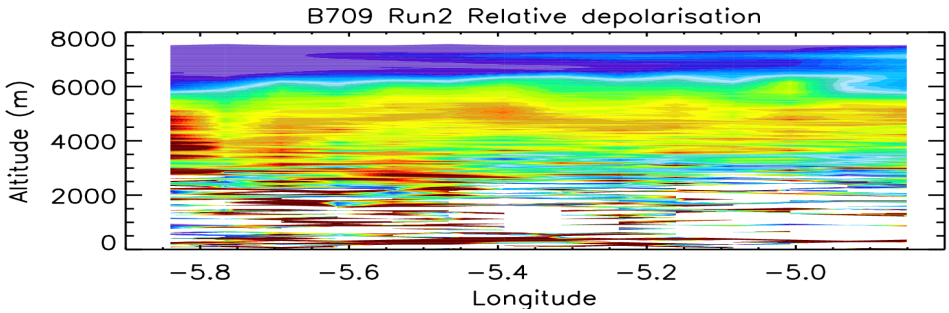

Figure 2.2 Qualitative lidar observations of relative depolarisation for 17 June 2012 (B709) as a function of longitude and altitude. Colour blue to red reflects increasing depolarisation and is a proxy for atmospheric dust content. Figure courtesy of F. Marenco (Met Office).

2.2.1 Fennec Climatology

The National Centres for Environmental Predication (NCEP/NCAR) reanalysis of wind vectors at 925 hPa and mean sea level pressure (MSPL), on a 2.5° latitude/longitudinal grid, are presented in figure 2.3. It shows a composite mean between the start and end of the June 2011 and June 2012 Fennec field campaigns compared with the 1981 – 2010 climatological mean for June for both fields, for the Fennec campaign region of West Africa. The Fennec 2011 mean sea level pressure in figure 2.3 shows the SHL extends further west across Mauritania by comparison to the climatology. This is associated with anomalously intense north-easterly Harmattan flow at 925 hPa winds (anomaly up to 7 – 9 m s^{-1}), extending across northern Mauritania and Mali, and throughout central Algeria, correlated with strong flow to the north of the low. A harmattan flow is a hot, dry north-easterly or easterly wind that occurs in West Africa associated with the outflow of air from subtropical high pressure systems (Knippertz and Todd, 2012). The large scale systems for June 2012 are consistent with the June climatology; during the Fennec 2012 campaign period an anomalous subtropical high, with MSPL 2.5 hPa higher than the climatology. The Fennec 2012 campaign showed a more intense Atlantic inflow with mean winds extending inland across western Sahara into central Mauritania (anomalous 4 m s^{-1}), compared with the June climatology.

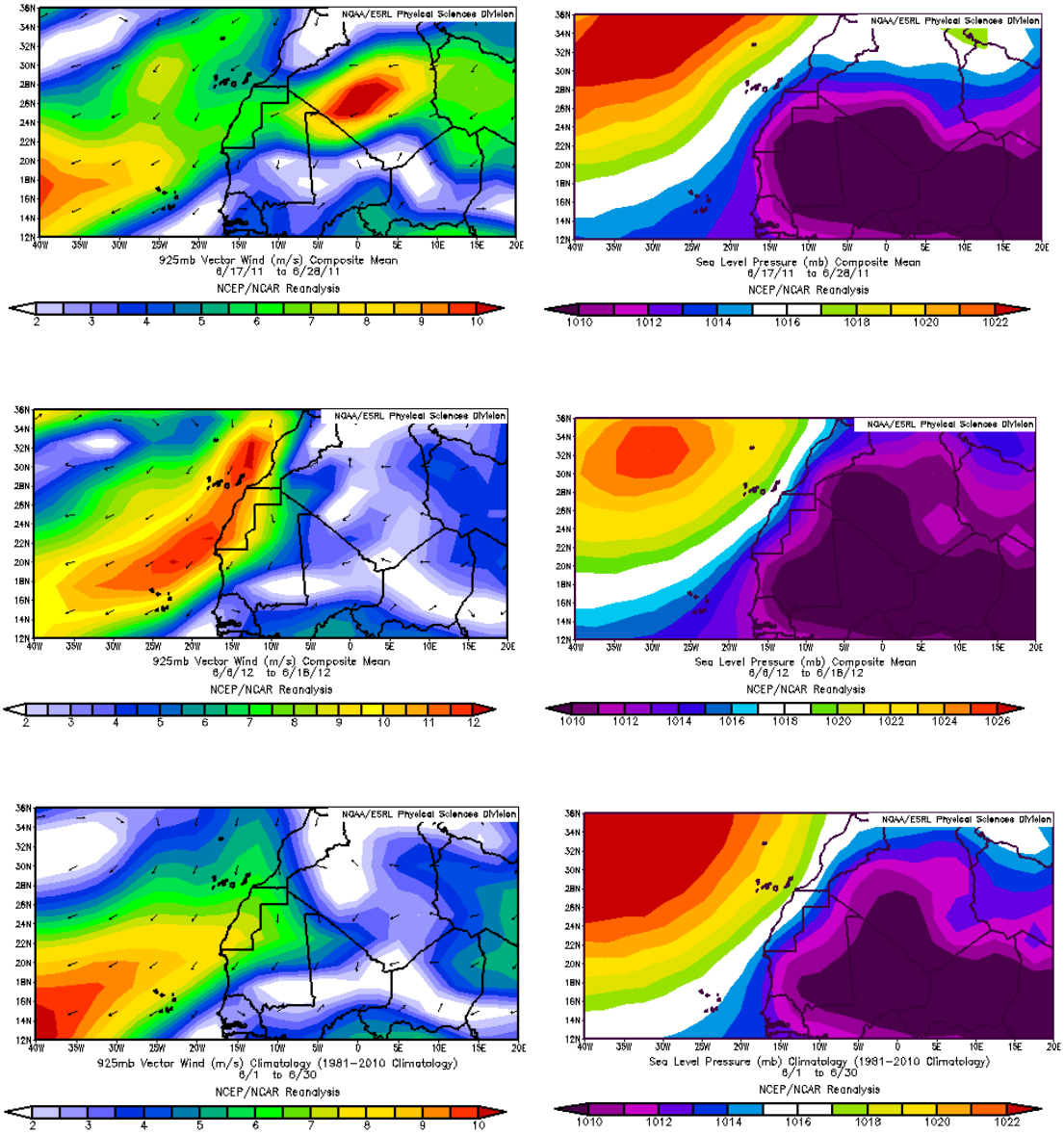

Figure 2.3 Fennec campaign meteorology from NCEP/NCAR re-analysis. The 925 hPa wind vectors (m s^{-1}) and MSPL (mb) for (*top*) Fennec 2011 (17 June – 28 June), (*middle*) Fennec 2012 (6 June – 17 June) and (*bottom*) June climatology. Image provided by the NOAA-ESRL Physical Sciences Division.

Table 8 Summary of BAe-146 aircraft flights during Fennec 2011

Flight Number	Date (2011)	Time (UTC)	Route	Flight Motivation
B600	17 June	07:48 - 12:41	FUE - Mali	Synoptic survey of gradient south-eastwards across Mauritania into North Mali with a low-level leg at the southeast end of the flight track. Characterise strong winds and associated dust uplift.
B601	17 June	14:42 - 19:36	FUE - Mali	Repeat of flight B600, a synoptic survey flight coordinated with the French Falcon that reached the southeast end at the same time as the BAe146 with daytime progression observed. Characterise strong winds and associated dust uplift.
B602	18 June	08:09 - 12:40	FUE - Mali	Synoptic survey to sample the transition from moister air over northern Mauritania and warmer air further east. Characterise strong winds and associated dust uplift.
B603	18 June	14:15 - 15:54	FUE	Calibration of radiation instrumentation
B604	20 June	12:47 - 17:51	FUE - Mau	Characterise dust over Mauritania across dust front for dust model validation purposes (EUFAR-LADUNEX)
B605	21 June	08:10 - 11:58	FUE - Mau	Sample dust-laden cold gust front which propagated overnight from deep convection over Atlas Mountains
B606	21 June	14:04 - 19:20	FUE - Mau	Sample boundary layer profile with SLRs in mixed, entrained and residual dust layers
B607	22 June	08:03 - 12:36	FUE - Mali	Characterise SHL using remote sensing and dropsondes
B608	22 June	15:10 - 20:15	FUE - Mali	Characterise SHL using remote sensing and dropsondes
B609	24 June	11:28 - 16:44	FUE - Mau	Dynamics and radiative measurements of cloud and dust
B610	25 June	07:31 - 12:16	FUE - Mau	LLJ characterisation
B611	25 June	14:14 - 19:16	FUE - Mau	Radiation measurements with an over flight of Zouerate supersite
B612	26 June	07:28 - 12:21	FUE - Mau	Radiation and *in-situ* measurements of Saharan dust - non-cloudy skies
B613	26 June	13:55 - 18:59	FUE - Mau	Heat flux flight
B614	27 June	06:34 - 11:38	FUE - Mau	LLJ characterisation

Table 9 Summary of BAe-146 aircraft flights during Fennec 2012

Flight Number	Date (2012)	Time (UTC)	Route	Flight Motivation
B699	6 June	12:00 – 16:54	FUE - NW Mau / N Mali	Synoptic survey to sample transition from cooler, moister air from Atlantic inflow into northern Mauritania to warmer, dry air to the east
B700	8 June	07:56 – 12:57	FUE - N Mali	Synoptic survey to sample the transition features of Atlantic inflow into northern Mauritania and northern Mali
B701	9 June	07:55 – 13:07	FUE – Mau	*In-situ* observations of dust
B702	10 June	08:04 – 12:41	FUE - S Mau	Sampling advected dust with a refuel at Dakar
B703	10 June	14:12 – 17:19	Dakar - FUE	Transit flight from Dakar to Fuerteventura
B704	11 June	11:27 – 17:07	FUE - S Mau	Low level jet associated with well-developed harmattan inflow in southern Mauritania; Measurement of winds and uplifted dust. Strongest low levels winds north of 10^{o}N
B705	12 June	13:07 – 18:13	FUE - NW Mali	Heat-flux profile of Saharan boundary layer
B706	14 June	09:13 – 14:33	FUE - N Mali	Characterise SHL
B707	15 June	07:56 – 13:08	FUE - N Mali	Strong active low level jet breakdown, crossing into increasingly moist air
B708	16 June	09:16 – 14:30	FUE - E Mau/N Mali	Strong low level jet across central-eastern Mauritania to central-western Mali formed by Atlantic inflow converging with Harmattan flow from Algeria
B709	17 June	12:14 – 17:23	FUE - N Mali	Sample dust which had been transported into the SHL
B710 (SAVEX)	18 June	07:50 – 13:11	FUE - Zouerat	Remote sensing of dust measurements from the aircraft lidar with AERONET retrievals from the Zouerate supersite

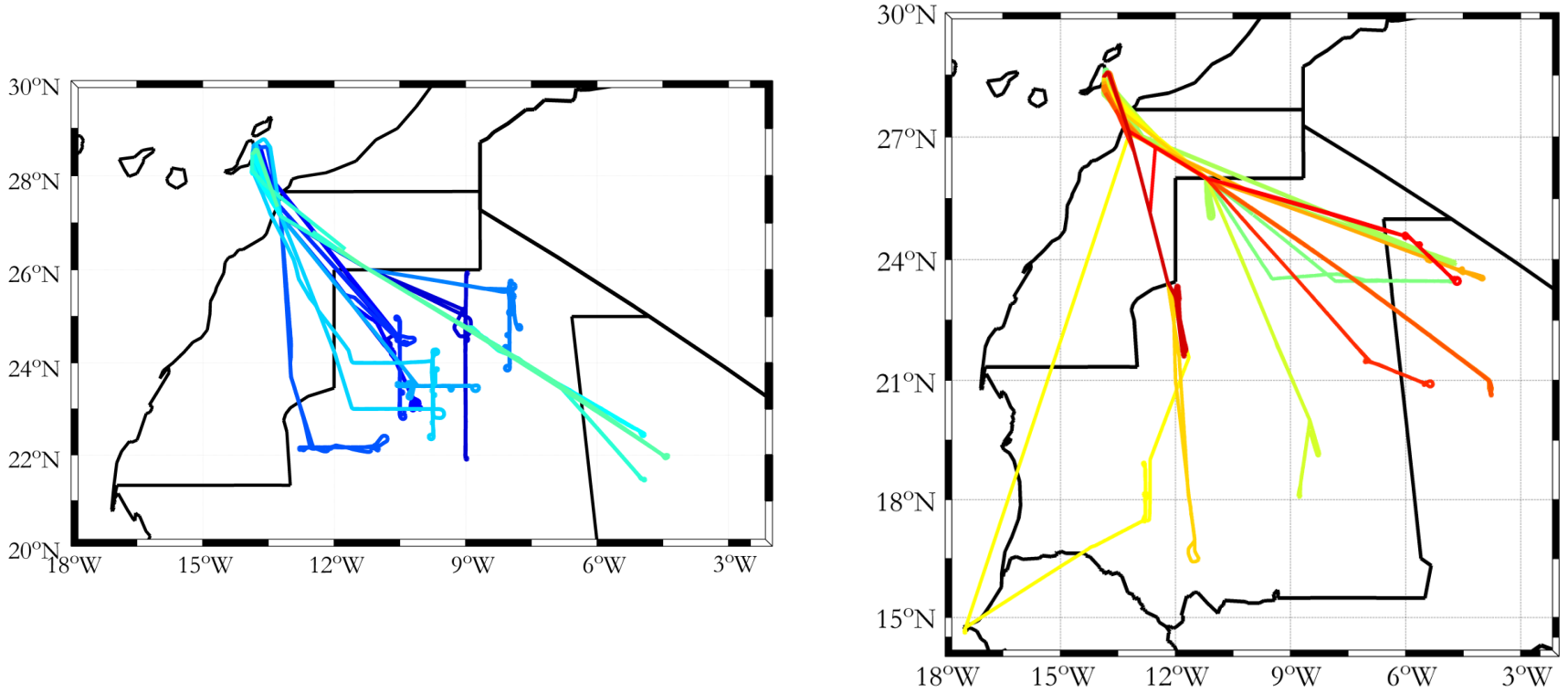

Figure 2.4 (*left*) Flight tracks for the Fennec 2011 campaign and (*right*) the Fennec 2012 campaign. The colour scheme from blue to red corresponds to the flights details in table 8 and table 9, respectively.

2.2.2 Fennec Forecasting: Met Office Africa Model

In chapter 5 the Saharan mineral dust optical properties during the Fennec pilot, Fennec 2011 and 2012 are presented; the meteorology encountered during each campaign is crucial in order to understand the mineral dust uplift and transport, which in turn drives the nature of the microphysical and optical properties of mineral dust. In this section the meteorology is presented using forecasts from the UK Met Office African Limited Area Model (LAM). The African LAM is a configuration of the Met Office Unified Model (MetUM), with a resolution of 20 km by 12 km with 70 vertical layers. The LAM is a nested model, initialised by the unified model boundary conditions. The African LAM provided a 48 hour daily forecast at 0600 UTC and 1800 UTC for 10 m (field dependent), 925 hPa, 850 hPa, 700 hPa, 500 hPa and 350 hPa. Output parameters included temperature, horizontal wind, pressure at mean sea level (PMSL), relative humidity, specific humidity, cloud cover (low, medium, high and total), boundary layer depth, aerosol optical depth at 550 nm and dust concentrations. Figure 2.5 presents selected LAM forecasts of PMSL and 925 hPa horizontal winds used in forecasting the flights during Fennec 2011 and Fennec 2012. A discussion of meteorological conditions for individual flights is presented in section 2.2.4 and 2.2.5.

2.2.3 Fennec Satellite Imagery

The primary payload aboard the Meteosat Second Generation (MSG) Meteosat-9 geostationary satellite is the Spinning Enhanced Visible and Infrared Imager (SEVIRI), an optical imaging radiometer (Schmetz et al., 2002). Geostationary satellites have an orbital period matching the rotation of the Earth with a fixed location above the equatorial plane which allows for repeated observations over its field of view, that is, high temporal resolution. Maximum field of views are set to 70°, due to the curvature of the Earth's surface, which equates to sensing of one third of the Earth's surface. SEVIRI, located at 0°N 0°E with a field of view of 70°N – 70°S and 70°E-70°W, is a scanning radiometer using 12 spectral channels, eight in the infrared (3.9 to 13.4 μm) and four in the visible and near-infrared (0.4 – 1.6 μm). The instrument resolution from a 35 800 km orbit provides 1 km in a high-resolution visible channel with 3 km resolution across the other channels.

Using the red-green-blue dust product it is possible to monitor desert dust events in the thermal infrared channels (Lensky and Rosenfeld, 2008). The technique applies brightness temperature differences between the 8.7, 10.8 and 12.0 μm and colours the 10.8 μm spectral channel blue, the difference between the 12.0 and 10.8 μm a red colour and the difference between 10.8 and 8.7 μm green (Banks et al., 2013; Haywood et al., 2011). Combined with a temporal resolution of 15 minutes SEVIRI is a technique heavily relied upon in the forecasts dust outbreak events. The absorption across the IR range due to water vapour, carbon dioxide and ozone above dust events interfere with dust signals. Brindley et al. (2012) found that in occurrences with high water vapour content in the atmospheric column, mineral dust AODs were masked due to saturation of the blue channel (10.8 μm); this provides perturbations in the characteristic pink colouring indicative of airborne dust.

Despite such limitations, SEVIRI continues provides a crucial technique in studying both global and Saharan dust events. Figure 2.6 and figure 2.7 present SEVIRI images for Fennec 2011 and Fennec 2012, respectively, and will be referred to in the subsequent discussion for identifying dust uplift events for individual Fennec flights.

2.2.4 Fennec 2011

The meteorological situation that dominated the first half of June 2011 was a heat low centred over Algeria. The system deepened over the first week with lowest pressure forecast on the 6 June of 996 hPa, at the same time an Atlantic inflow was present over Western Sahara and Mauritania. The meteorological situation changed into the third week of June, coinciding with the start of the Fennec field campaign. The following section provides a discussion of Met Office forecast products and satellite imagery which motivated the choice of flight sorties across the field campaign.

The situation on the 17 June (figure 2.5i) forecast for slack westerly winds at 10 m field at 0600 UTC (4 – 6 m s^{-1}) with a strong north-easterly winds at 925 hPa (16 m s^{-1}). Intensification of the low level westerly winds at 10 m in the 0900 UTC (T+003) forecast (8 – 10 m s^{-1}) coincided with a weakening of the jet system in 925 hPa horizontal winds (12 m s^{-1}). Flight B600 sortie was a synoptic survey to characterise strong winds and associated dust uplift (figure 2.6i) of a gradient south-eastwards across Mauritania into North Mali with a low-level leg at the southeast end. The flight has a

high level transit to northern Mali, with a descent to minimum safe altitude (MSA) and a SLR return north-westwards for approximately 100 km. A short profile down through the dust layer to 500 ft was carried out at the end of the SLR before transiting to Fuerteventura. Flight B601, in the afternoon of the 17 June was a repeat of flight B600 with the motivation to gain an understanding of the diurnal mixing processes occurring.

The forecast for flight B602 of the 18 June (figure 2.5ii) showed conditions similar to the previous day with strong low level north-easterly winds persisting. B602 was a third synoptic survey flight to these winds and associated dust uplift (figure 2.6iii). On the afternoon of the 18 June flight B603, a radiation calibration flight over a sea surface and above a relatively clean troposphere near the Canary Islands. The aim of the flight was to calibrate the BAe-146 radiation instrumentation.

Flight B604 on the afternoon of 20 June, a EUFAR-LADUNEX flight had the aim of characterising the features of dust front for dust model validation purposes. A convective system was triggered over the Hoggar Mountains in Algeria and around the triple point with Niger and the eastern border with Mali, two days previously on the 18 June 2011. The convection was seen to intensify moving westwards into eastern and central Mali; at 2300 UTC a density current was visible which propagates outwards, north and westwards from the convection. At 1030 UTC on the 19 June, the dust ladened density current and convection reach the south eastern border of Mauritania. Overnight the uplifted dust is picked up by an easterly LLJ which was forecast in the 925 hPa horizontal winds (T+000) field (figure 2.5iii) at 0600 UTC which transports the dust into northern Mauritania. Flight B604 consisted of *in-situ* measurements across the dust front at low level, with remote sensing using lidar and sondes were dropped at high level.

Flight B605 on the morning of 21 June was to sample dust-laden cold gust front that had propagated overnight from deep convection over the Atlas Mountains. This heavy convection was triggered on the 20 June with intensification over the afternoon, identified from SEVIRI (figure 2.6v). The LAM forecast 12 – 14 m s^{-1} 925 hPa easterly winds at the northerly end of the B605 proposed with horizontal winds forecast to decrease to 4 m s^{-1} on exiting the cold pool outflow (figure 2.5iv). The BAe-146 carried out remote sensing of the dust front from above and *in-situ* measurements across the dust front with high concentrations to the north of the flight track, exiting the dust

front at the southern end of the track, with the opportunity to sample the pre-frontal and post-frontal air

The SHL which had been strongly present in central Algeria in early June re-establishes from the 20 June and the mean position of the heat low core deepens and becomes coherent during the 20 June to the 21 June. The low shifts westwards from the 21 June to 23 June, and the LAM forecasts (figure 2.5x) a mean sea level pressure of 1004 hPa present on the Mauritania / Mali border at 0600 UTC, accessible from Fuerteventura on the 22 June. The mean climatological position of the SHL is eastwards in Algeria and Mali (figure 2.3). Flights B607 in the morning, and B608 in the afternoon were both high level sensing flights with sondes dropped to gain an understanding of the spatial and diurnal evolution of the SHL.

On the 24 June the heat low was less pronounced from that of previous three days. An afternoon flight, B609 was planned within the well mixed boundary layer in northern Mauritania, with low horizontal wind speeds forecast in the LAM (figure 2.5xi) for the flight area. The flight consisted of multiple stacked legs through dust and cloud layers (figure 2.6ix) for *in-situ* dynamical and radiative measurements of dust-cloud interactions.

The 0900 UTC winds at 925 hPa were forecast to decrease to 10 – 12 m s^{-1} across the region. Flight B610, in north-eastern Mauritania, with the northern point of the flight track at N25º W7º and the southern point at N23º W7º with a return to northern point, and beyond to 26ºN, W7º. The flight aimed to carry out *in-situ* measurements across the low level jet with the aim of capturing features of the jet breakdown and any associated dust emission. The LAM forecast (figure 2.5vii) for the 25 June in the 0600 UTC run of horizontal winds at 925 hPa of 20 m s^{-1} at the northern end of the flight track decreasing at the southern end of the flight track to 10 – 12 m s^{-1}. Flight B611 on the afternoon of 25 June was a radiation flight in north-western Mauritania including an over flight of the Zouerate supersite.

Flights B612 and B613 on the morning and afternoon, respectively of the 26 June consisted of flights in north-eastern Mauritania with the aim of carrying out heat and dust-flux measurements over the desert with a sortie of multiple horizontal SLR stacked legs throughout the boundary layer. The LAM forecast (figure 2.5viii) clear skies to remain throughout the day, coinciding with the picture from SEVIRI (figure

2.6xii). The LAM forecast a strong eastwards outflow from Algeria into northern Mauritania although the flight track was south of this jet system in a area of lower horizontal winds, by the afternoon flight the LAM forecast winds as low as 4 m s^{-1}.

The LAM for the 27 June forecast a low of 1004 hPa centred on the Algeria / N Mali border, an intensification of the Harmattan flow to the north of this low extending out of central Algeria showed a maximum in the horizontal winds at 925 hPa at 0600 UTC reaching 24 m s^{-1} (figure 2.5ix). The 0900 UTC forecast showed the weakening of the jet with winds decreasing to 12 m s^{-1}, the horizontal winds at 10 m showed little difference between 0600 UTC and 0900 UTC forecast reaching 6 m s^{-1}. Flight B614, the final flight of the 2011 Fennec campaign, consisted of a long low level run southwards into northern Mauritania with a return track travelling north on the same flight path, making *in-situ* observations of the low level jet breakdown in the morning hours.

2.2.5 Fennec 2012

A strong Atlantic inflow dominated the meteorological situation during the early part of Fennec 2012 field campaign. The inflow in part was driven by a low pressure which deepens in Eastern Algeria between 2 June and 6 June with pressures decreasing from 1008 hPa to 1004 hPa. The position of the low brought a north-westerly Atlantic flow, associated with more traditional maritime conditions; lower temperatures across Western Sahara and Mauritania, a shallower boundary layer and higher relative humidity. The Atlantic inflow weakens from the 10 June, and a well-defined heat low establishes on the Algerian/ Mai border. The heat low weakens and extends northwards into central Algeria and southwards to the Mauritania / Mali border from the 13 June / 14 June, with strong jet system with north-easterly flow on the western edge of the heat low. By the 16 June re-established Atlantic inflow converges with Harmattan flow from Algeria and Mediterranean flow from Libya at the Mauritania-Mali to form an intense northerly jet system. The following discussion provides a more detailed overview of the forecast products and satellite imagery which motivated the choice of flight sorties across the 2012 field campaign.

On the 6 June the LAM forecast showed a temperature gradient across Mauritania in the 1.5 m temperature field at 1200 UTC from 28 ^{o}C central Mauritania with

temperatures increasing up to 42 ^{o}C in eastern Mauritania / Mali border region. Boundary layer depth increases from 1500 m in the region dominated by the Atlantic inflow with a sharp transition to the typically deep Saharan boundary layer up to 5000 m towards the east. The conditions motivated flight B699, a synoptic survey to sample this transition from cooler, moister air due to Atlantic inflow to the west of the Sahara. The flight consisted of SLR at high and low levels.

The Atlantic inflow meteorological situation from the 6 June persists (figure 2.5xi) and a very similar situation was forecast for the 8 June which motivated flight B700 a second synoptic survey of the Atlantic inflow focusing on the extent, depth and dust emission within the inflow during morning hours, whilst B699 had sampled the inflow in the afternoon. Flow along a strong thermal gradient with heat to the east and cooler air to the west forecast a thermally driven wind, with higher dust loadings (figure 2.7ii) forecast along this intertropical discontinuity (ITD).

A convective cell in southern Mali intensifies overnight of the 8 June with associated dust emissions (figure 2.7ii) to the north, likely due to density currents. The convection weakens over night of the 9 June and dust emissions are transported in the morning north-easterly jet, formed along the southern edge of the Atlantic inflow with LAM forecasts of horizontal winds of 12 – 14 m s^{-1} (figure 2.5xii). Flight B701, in central Mauritania carried out *in-situ* measurements in the region.

Similar conditions persist on the 10 June for B702 with strong horizontal winds in central / southern Mauritania at the convergence between Atlantic inflow and inflow from central Mali with horizontal winds of 14 – 18 m s^{-1} forecast (figure 2.5xiii). The aircraft refuelled at Dakar, Senegal with a transit return, flight B703 northwards along the Mauritanian and Western Saharan coast.

The 11 June forecast indicated horizontal winds at 0600 UTC at 925 hPa reaching a maximum of 22 m s^{-1} indicating a strong LLJ. The strength of the 925 hPa horizontal wind was forecast to remain of equal intensity in the 0900 UTC forecast. Corresponding surface dust concentrations of up to 2.0 mg m^{-3} were forecast at 1200 UTC, decreasing somewhat by 15 UTC (figure 2.5xiv). The situation motivated flight B704 to 16.5^{o}N, 11.5^{o}W in southern Mauritania with an afternoon flight to sample the dust emissions (figure 2.7vi) from the LLJ rather than investigating the LLJ structure.

The LAM forecast for the 12 June showed a gradient from the coast stretching into Mauritania in multiple fields. The boundary layer depth forecast at 1800 UTC (T+006) was up to 6000 m (figure 2.5xv). These conditions motivated a heat-flux flight, B705 in NW Mali with multiple stacked legs.

The well-defined heat low present on the Algerian / Mali border on the 13 June weakens and extended northwards into central Algeria and southwards to the Mauritania / Mali border with a pressure forecast of 1004 hPa on the 14 June. Flow along the northern edge of the heat low at 0900 UTC horizontal winds forecast 12 – 14 m s^{-1}, with low winds forecast from the 1200 UTC forecast onwards (figure 2.5xvi).

LAM forecast for the 15 June shows a strong jet system with north-easterly flow on the western edge of the heat low, extending out of central Algeria, across northern Mali into central / southern Mauritania with associated horizontal winds of 16 – 18 m s^{-1}. Flights B706 on the 14 June and B707 on the 15 June have the same flight track with a low-level leg NW to SE before reciprocal high-level back, with multiple dropsondes dropped in the same location on both flights.

LAM forecast for the 16 June showed a well-defined heat low with a central pressure of 1002 hPa in central Mali; south of its climatological position (figure 2.5xviii). The 925 hPa horizontal winds at 0600 UTC shows the re-established Atlantic inflow converges with Harmattan flow from Algeria and Mediterranean flow from Libya at the Mauritania-Mali border to form a strong northerly jet system with horizontal winds forecast between 22 – 24 m s^{-1}. The 0900 UTC forecast highlights the weakening of the 925 hPa winds during the morning hours associated with a general turbulent mixing down of air to the surface. Flight B708 had a similar flight track to B706 and B707.

Flight B709 on the 17 June into northern Mali was motivated to sample dust which had been transported into the SHL. Multiple runs making *in-situ* measurements of the vertical distribution of dust throughout the SHL was carried out. The heat low forecast at 1500 UTC on the 17 June had a central pressure of 1002 hPa (figure 2.5xix). The final flight of the 2012 campaign, B710 on the 18 June was part of the Sun-photometer Airborne Validation Experiment (SAVEX) with the aim of comparing remote sensing of dust measurements from the aircraft lidar with AERONET retrievals from the Zouerate supersite.

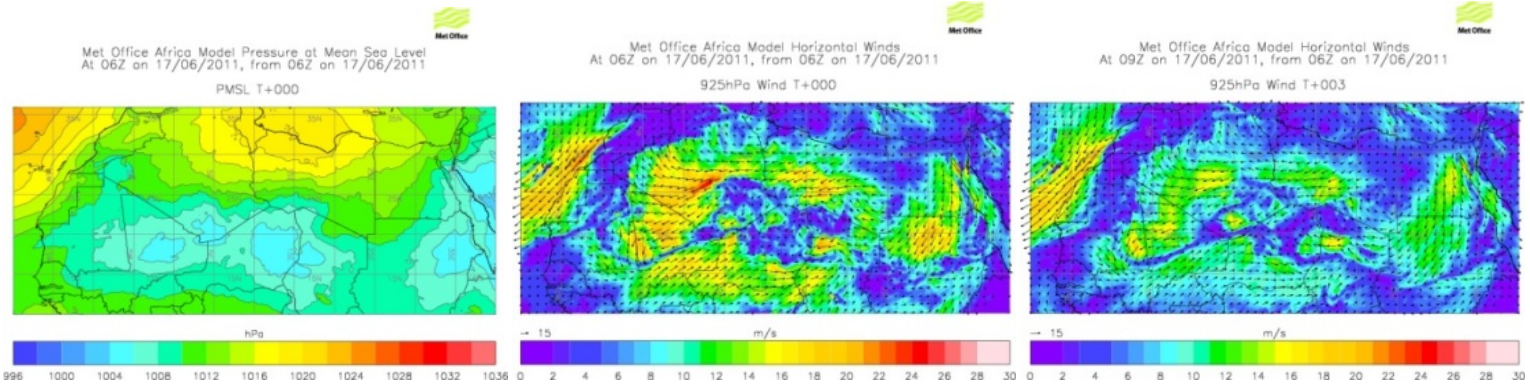

i. 0600 UTC and 0900 UTC on 17 June 2011 from Met Office Africa Model for B600 and B601

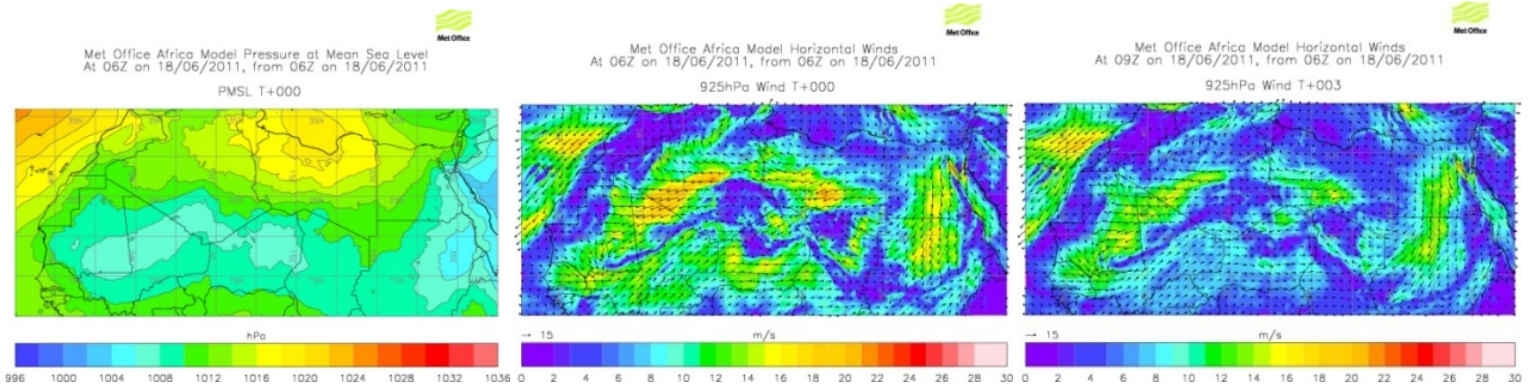

ii. 0600 UTC and 0900 UTC on 18 June 2011 from Met Office Africa Model for B602 and B603

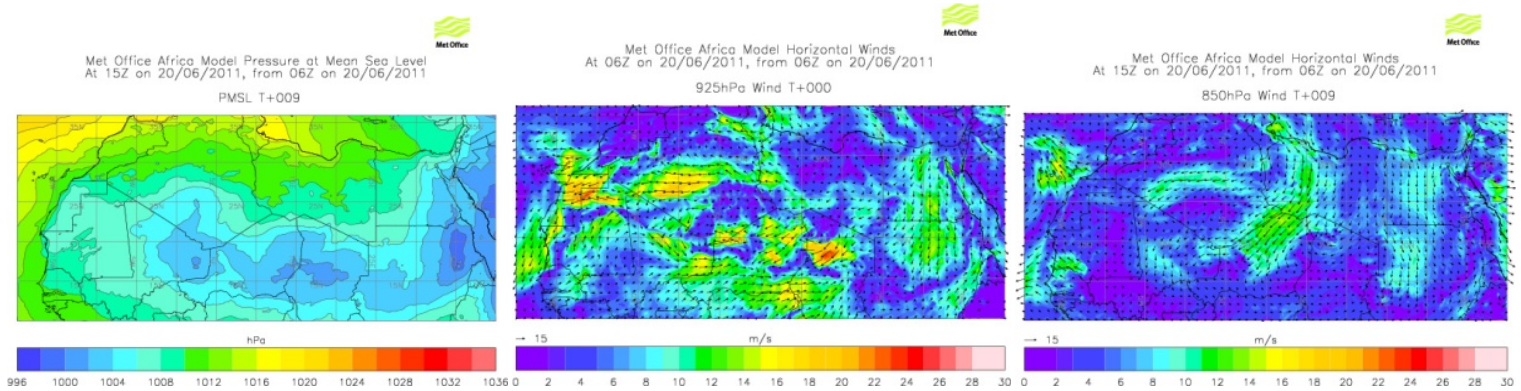

iii. Dust concentration at 0600 UTC, 0900 UTC and 1500 UTC on 20 June 2011 Met Office Africa Model for B604

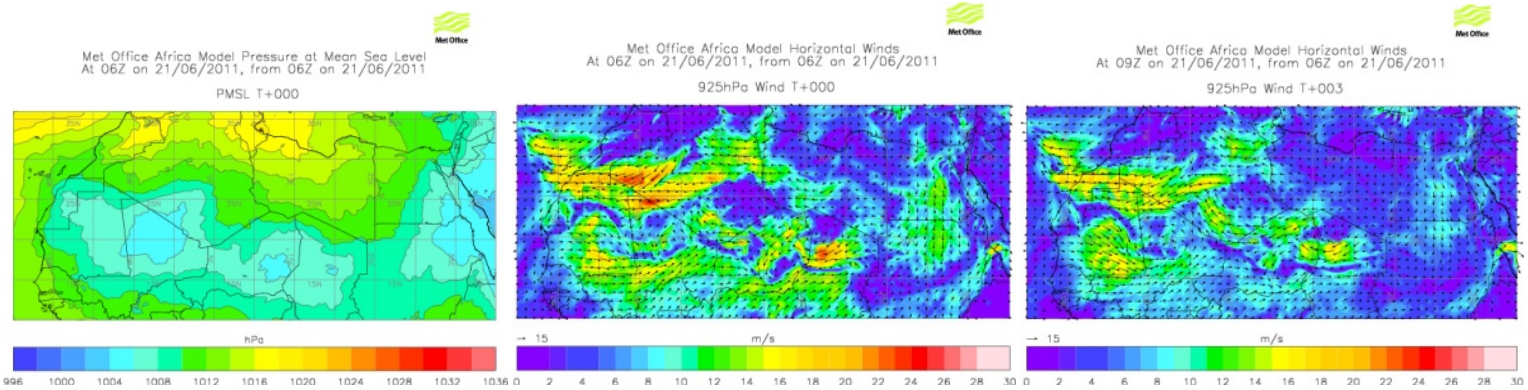

iv. 0600 UTC and 0900 UTC on 21 June 2011 from Met Office Africa Model for B605 and B606

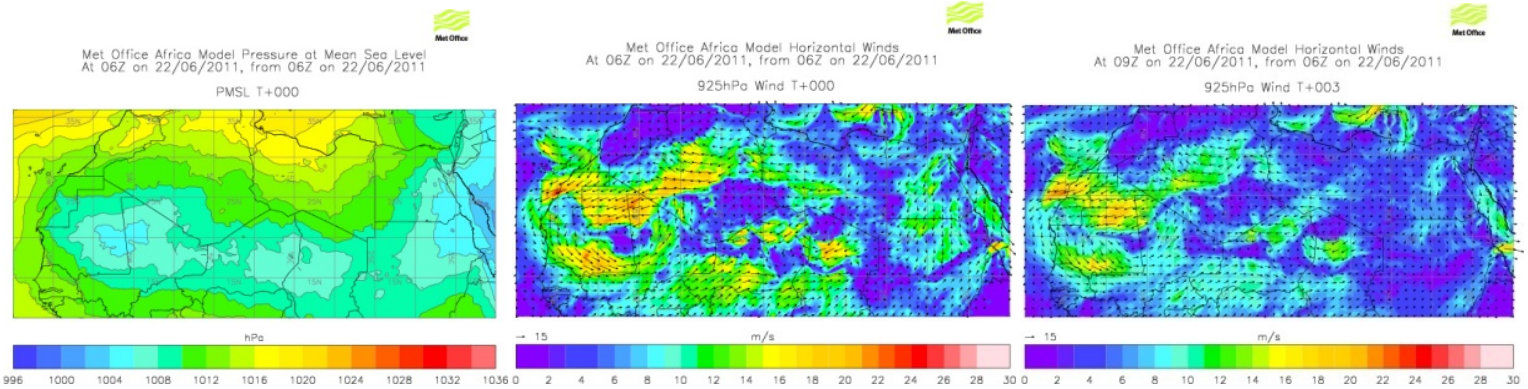

v. 0600 UTC and 0900 UTC on 22 June 2011 from Met Office Africa Model for B607 and B608

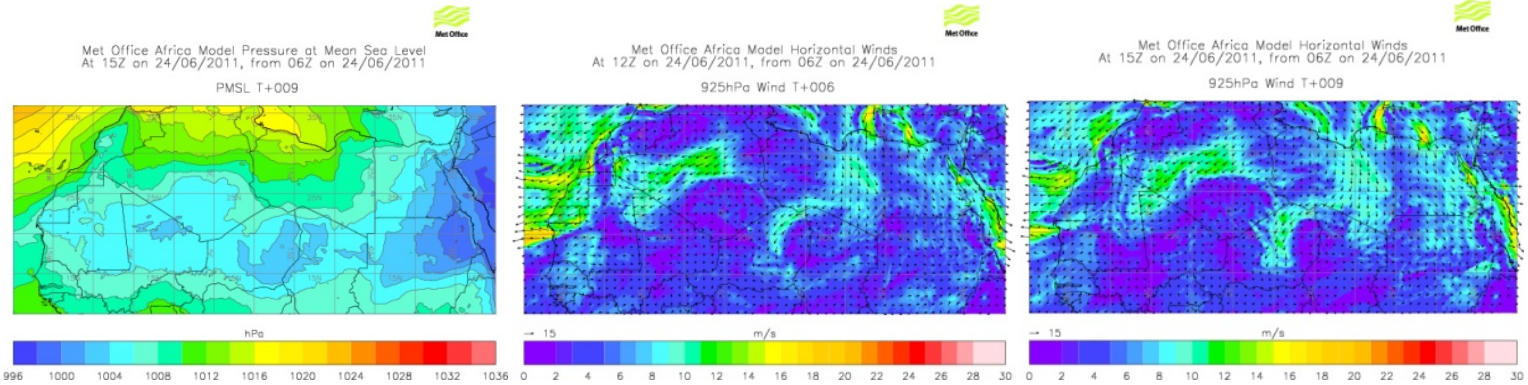

vi. 1200 UTC and 1500 UTC on 24 June 2011 from Met Office Africa Model for B609

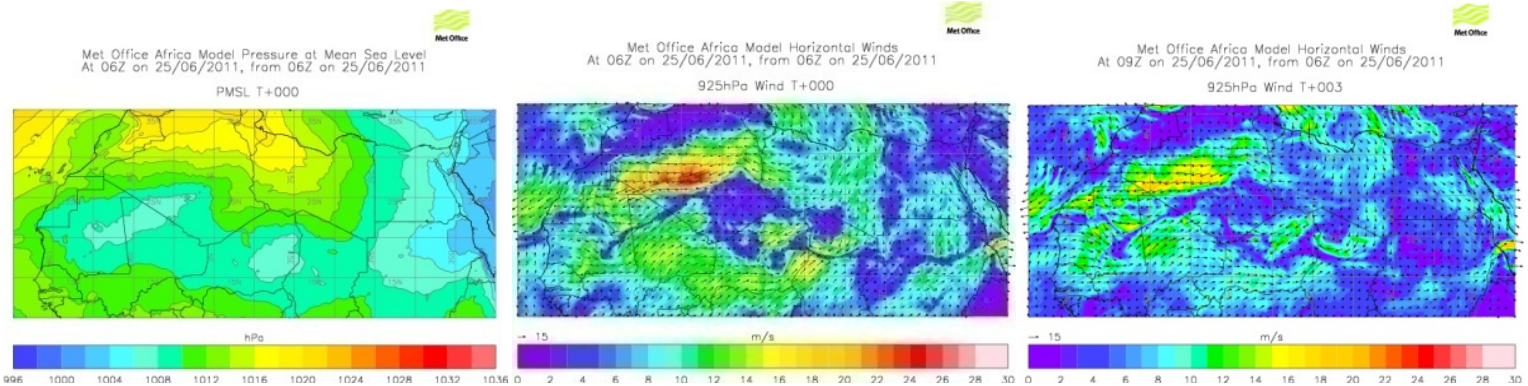

vii. 0600 UTC and 0900 UTC on 25 June 2011 from Met Office Africa Model for B611

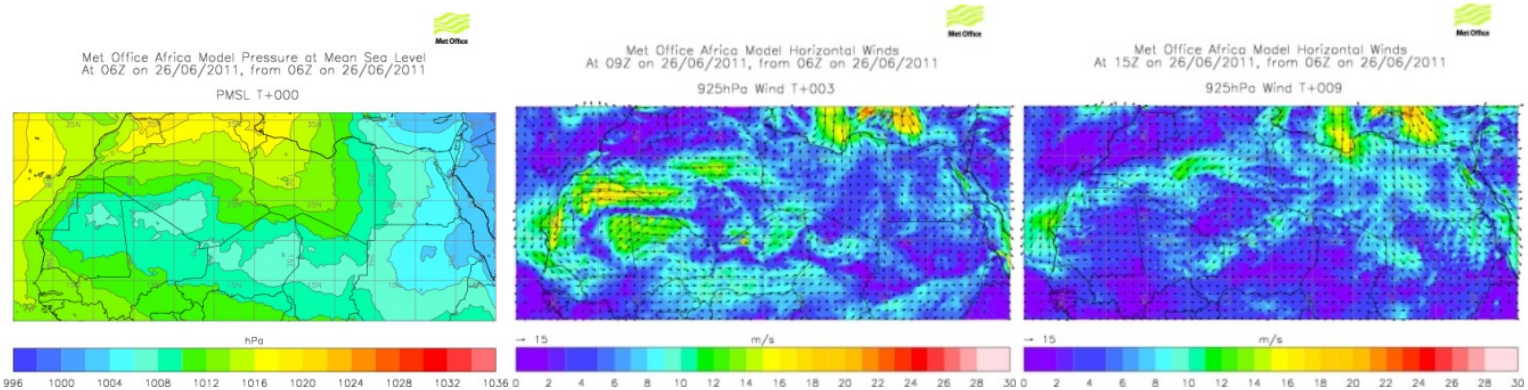

viii. 0600 UTC and 0900 UTC on 26 June 2011 from Met Office Africa Model for B612 and B613

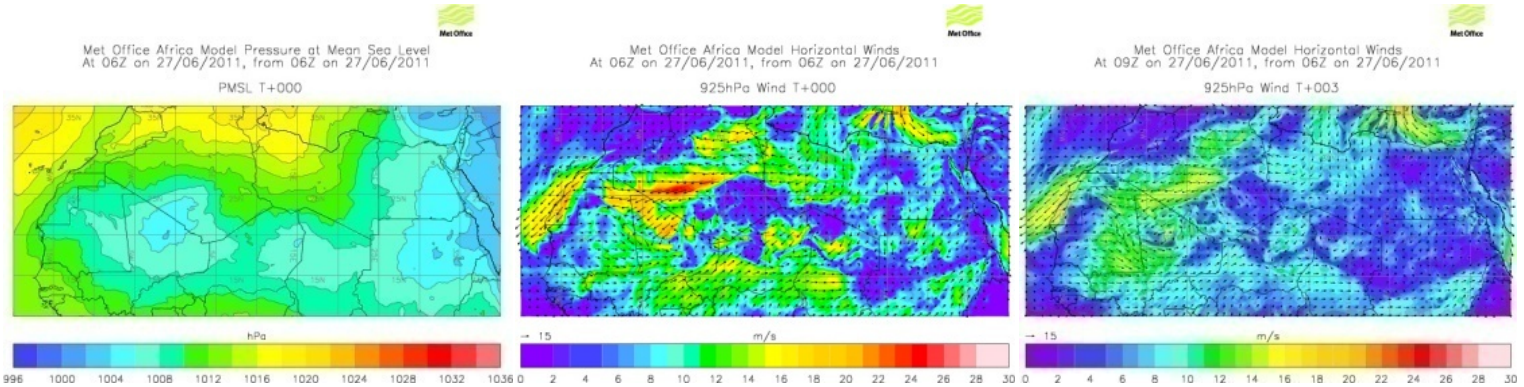

ix. 0600 UTC and 0900 UTC on 27 June 2011 from Met Office Africa Model for B614

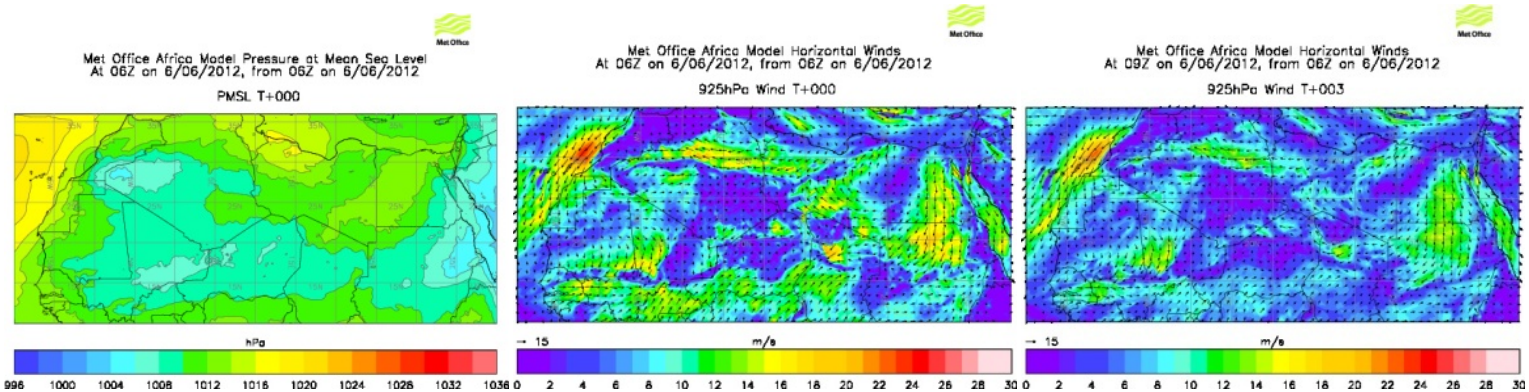

x. 0600 UTC and 0900 UTC on 6 June 2012 from Met Office Africa Model for B699

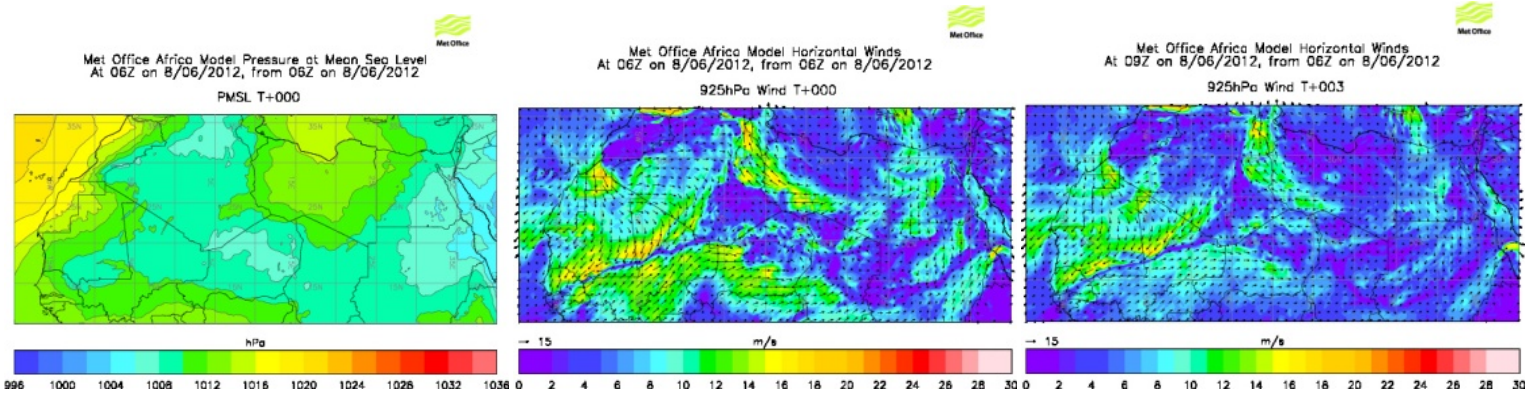

xi. 0600 UTC and 0900 UTC on 8 June 2012 from Met Office Africa Model for B700

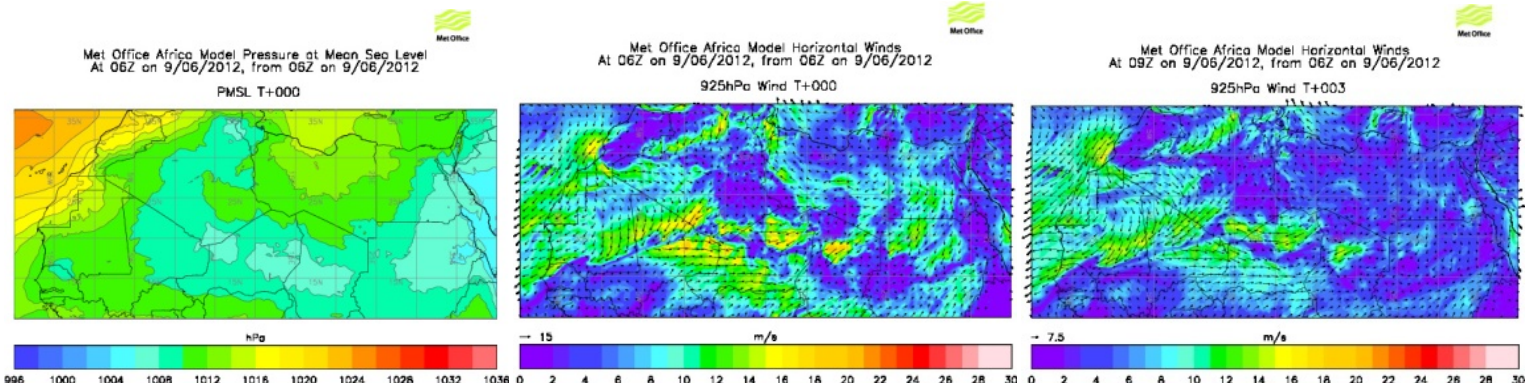

xii. 0600 UTC and 0900 UTC on 9 June 2012 from Met Office Africa Model for B701

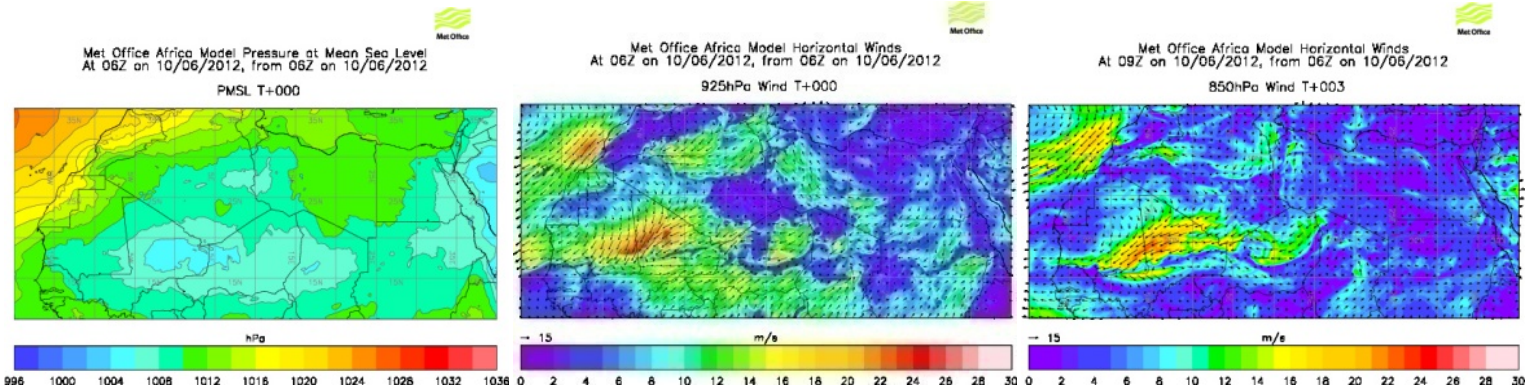

xiii. 0600 UTC and 0900 UTC on 10 June 2012 from Met Office Africa Model for B702 and B703

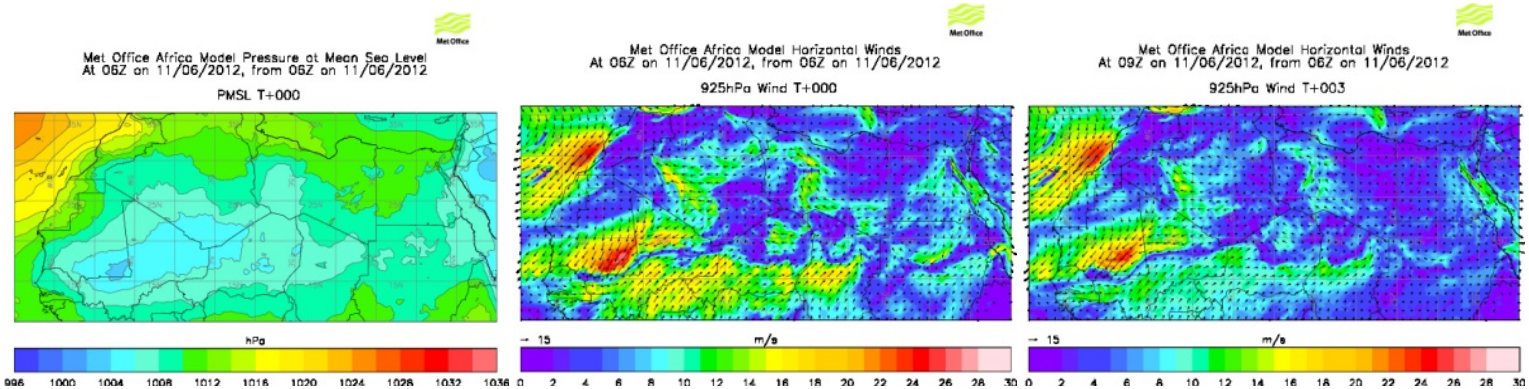

xiv. 0600 UTC and 0900 UTC on 11 June 2012 from Met Office Africa Model for B704

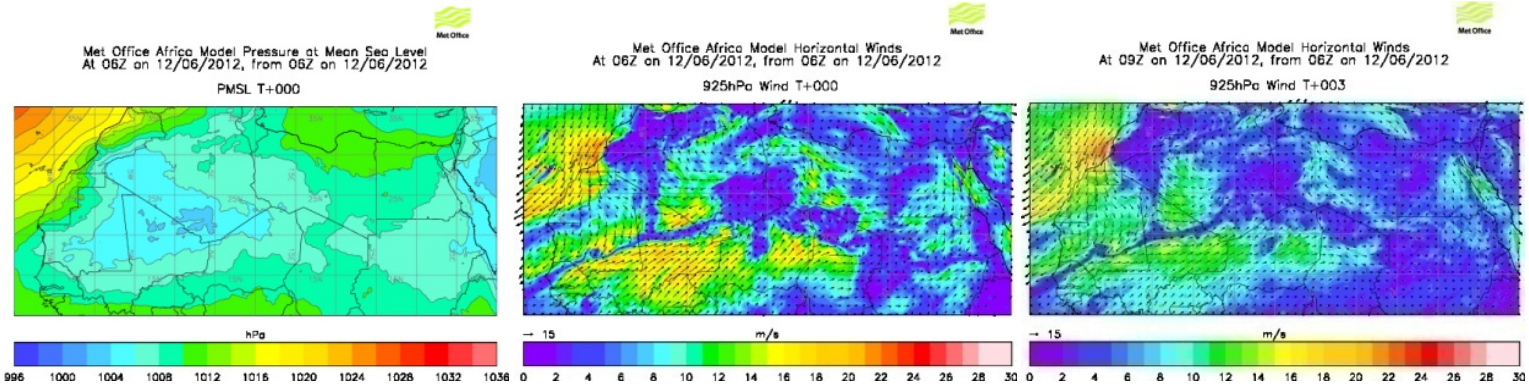

xv. 0600 UTC and 0900 UTC on 12 June 2012 from Met Office Africa Model for B705

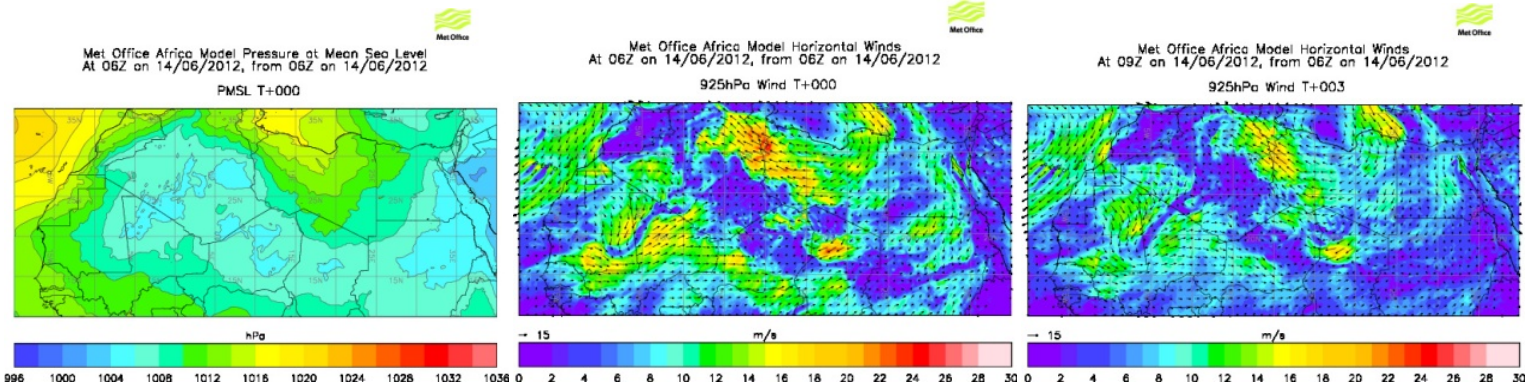

xvi. 0600 UTC and 0900 UTC on 14 June 2012 from Met Office Africa Model for B706

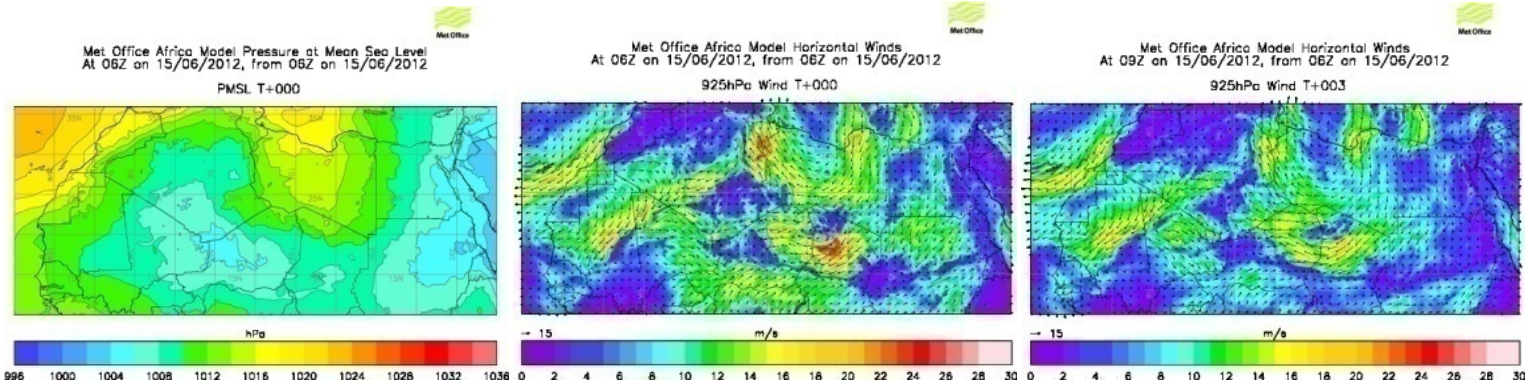

xvii. 0600 UTC and 0900 UTC on 14 June 2012 from Met Office Africa Model for B707

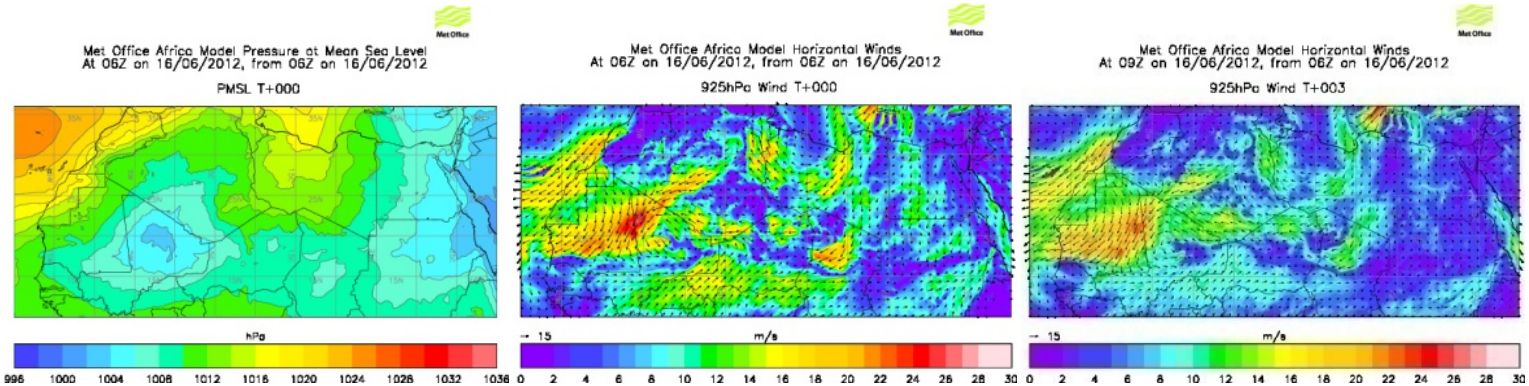

xviii. 0600 UTC and 0900 UTC on 16 June 2012 from Met Office Africa Model for B708

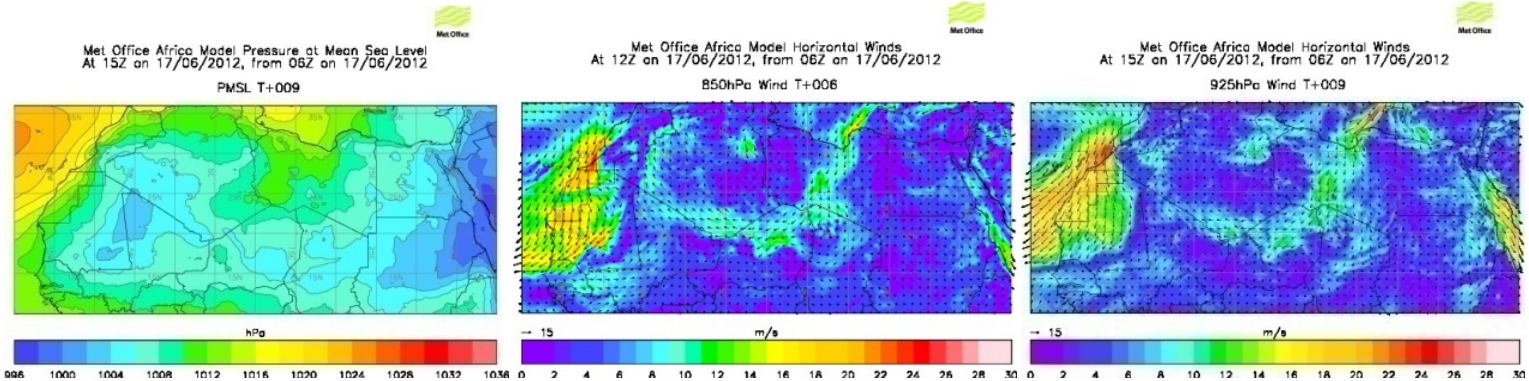

xix. 1200 UTC and 1500 UTC on 17 June 2012 from Met Office Africa Model for B709

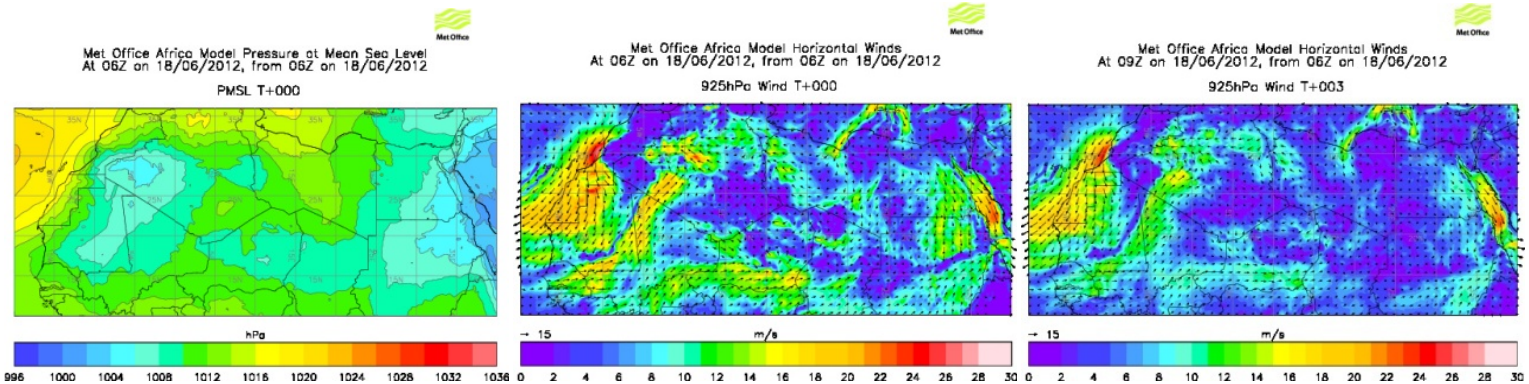

xx. 0600 UTC and 0900 UTC on 18 June 2012 from Met Office Africa Model for B710

Figure 2.5 Met Office LAM forecasts of i) PMSL and ii) 925 hPa horizontal winds for flights B600 – B614 during Fennec 2011 and B699 – B710 during Fennec 2012.

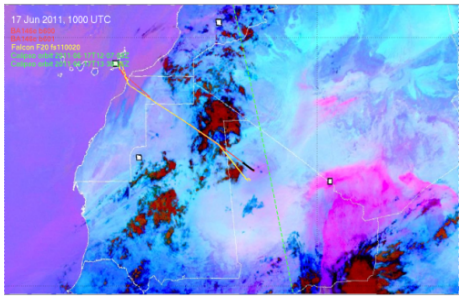

i. 1000 UTC 17 June 2011 B600

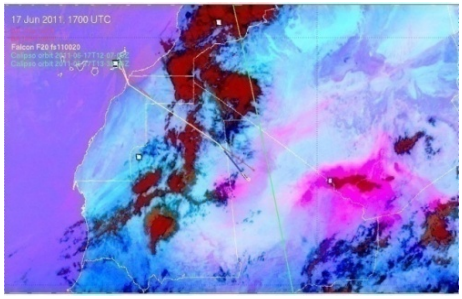

ii. 1700 UTC 17 June 2011 B601

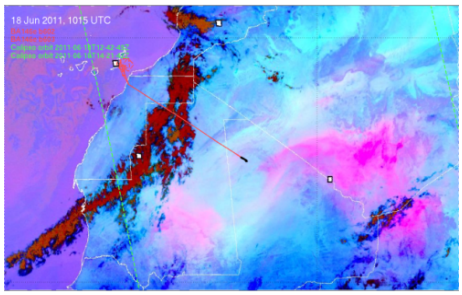

iii. 1015 UTC 18 June 2011 B602

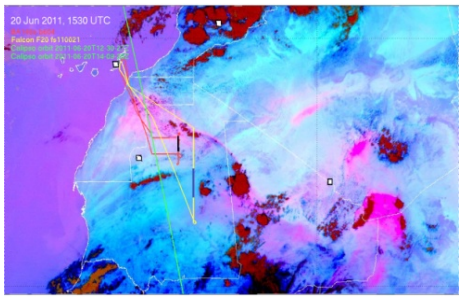

iv. 1530 UTC 20 June 2011 B604

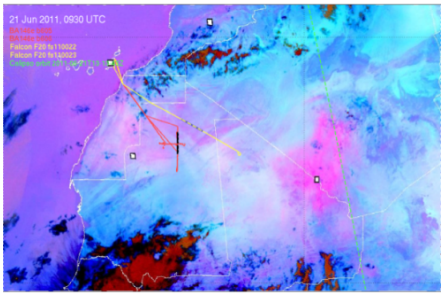

v. 0930 UTC 21 June 2011 B605

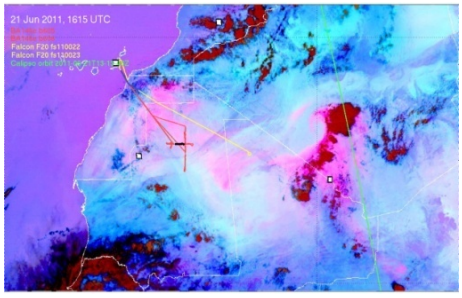

vi. 1615 UTC 21 June 2011 B606

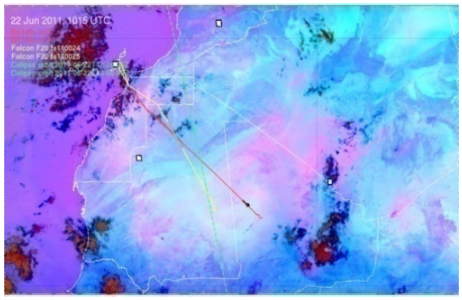

vii. 1015 UTC 22 June 2011 B607

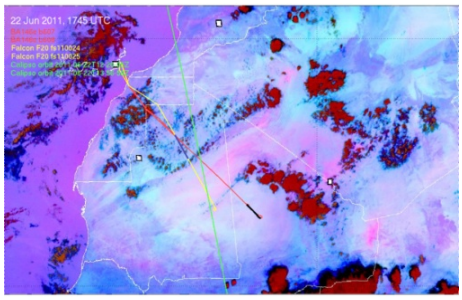

viii. 1745 UTC 22 June 2011 B608

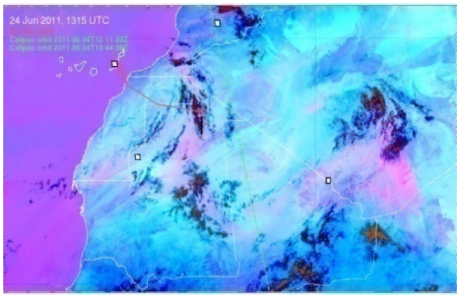

ix. 1315 UTC 24 June 2011 B609

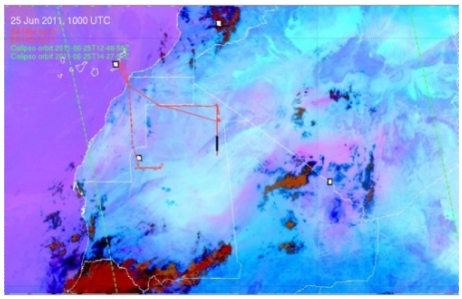

x. 1000 UTC 25 June 2011 B610

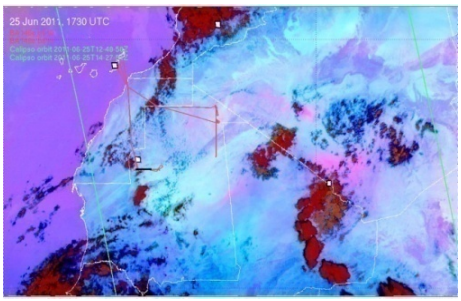

xi. 1730 UTC 25 June 2011 B611

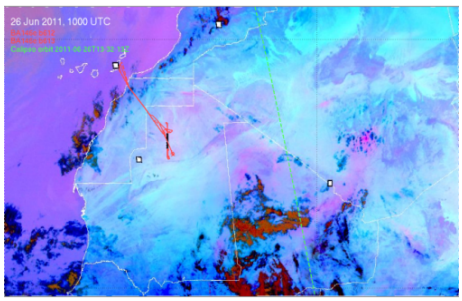

xii. 1000 UTC 26 June 2011 B612

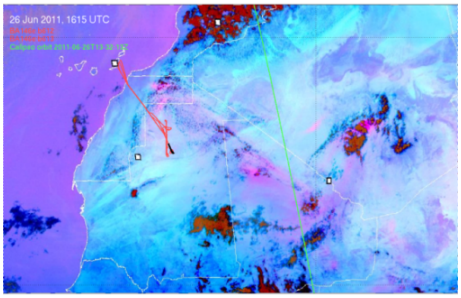

xiii. 1615 UTC 26 June 2011 B613

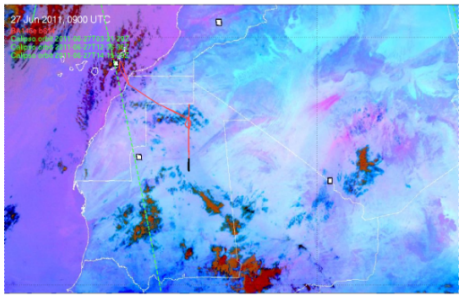

xiv. 0900 UTC 27 June 2011 B614

Figure 2.6 SEVIRI Images for during Fennec 2011

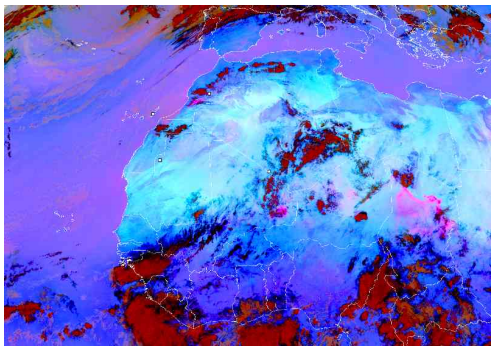

i. 1430 UTC 6 June 2012 B699

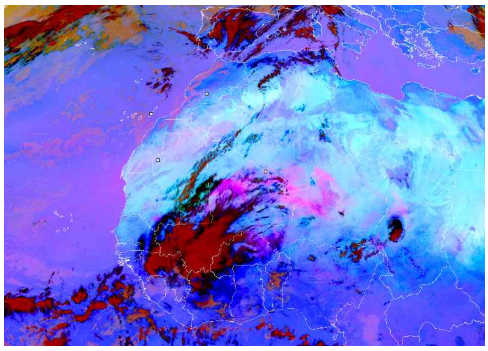

ii. 1000 UTC 8 June 2012 B700

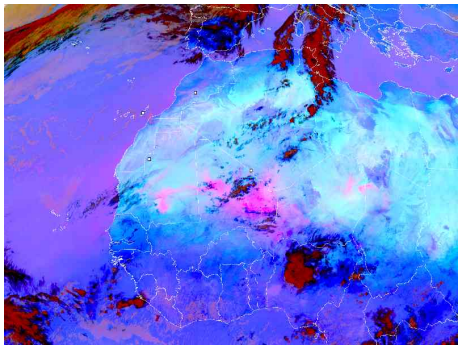

iii. 1100 UTC 9 June 2012 B701

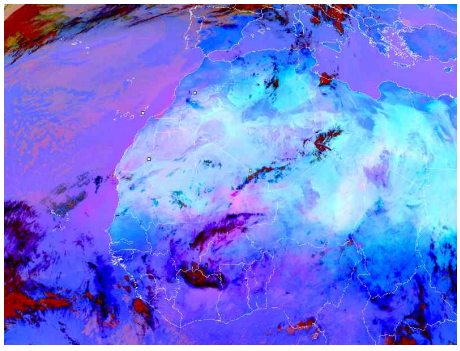

iv. 1000 UTC 10 June 2012 B702

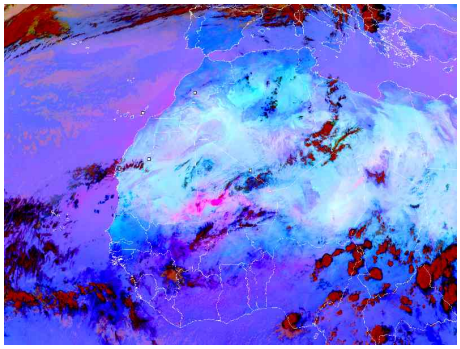

v. 1530 UTC 10 June 2012 B703

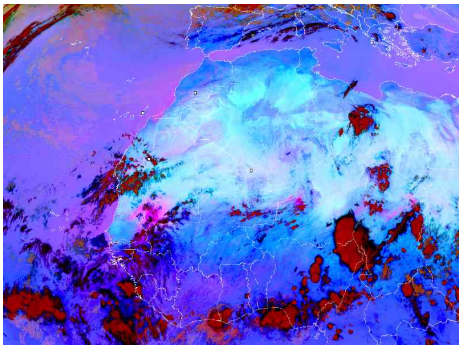

vi. 1500 UTC 11 June 2012 B704

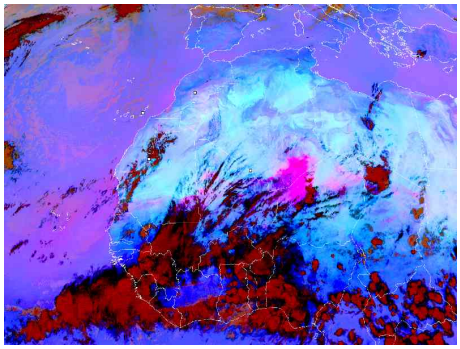

vii. 1600 UTC 12 June 2012 B705

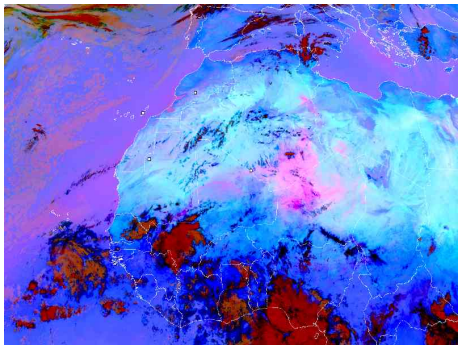

viii. 1100 UTC 14 June 2012 B706

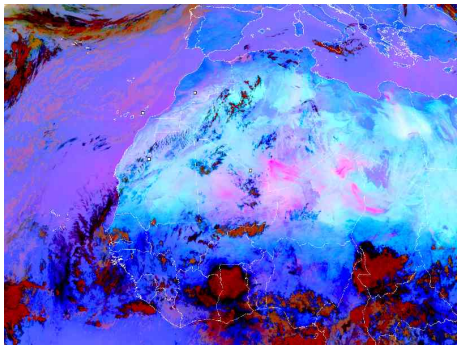

ix. 1030 UTC 15 June 2012 B707

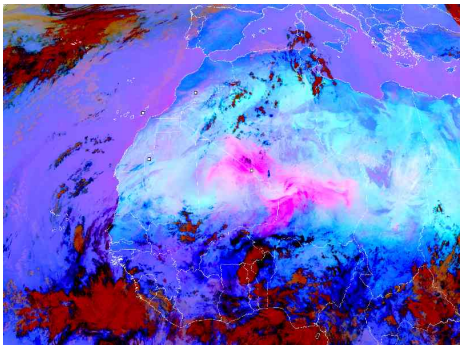

x. 1100 UTC 16 June 2012 B708

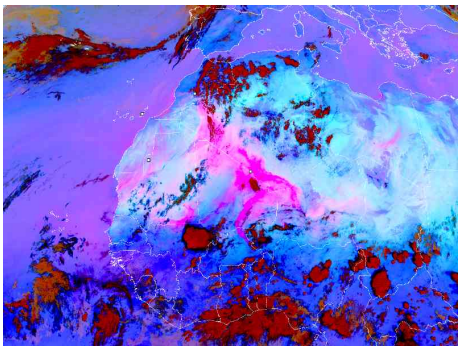

xi. 1500 UTC 17 June 2012 B709

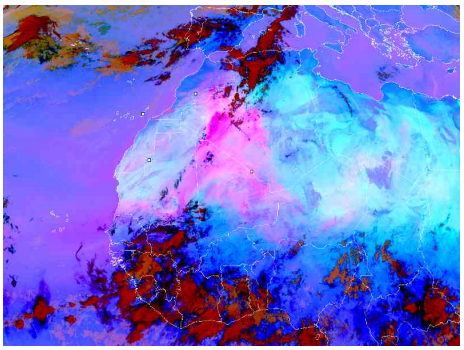

xii. 1030 UTC 18 June 2012 B710

Figure 2.7 SEVIRI Images for during Fennec 2012

2.3 Campaign Overview: SAMBBA

The difference in the sign and magnitude of the global direct forcing between the TAR, AR4 and AR5 signifies to the necessity in assessing the impact of the radiation budget via the direct effect, particularly in key regions such as the Amazon. SAMBBA aimed to produce a dataset of trace gases, aerosols and cloud variability across the Amazonia region to provide an opportunity to characterise the chemical, optical and radiative properties of South American biomass burning aerosol, to understand the impact of Amazon biomass burning on regional aerosol and trace gas budget. *In-situ* measurements in SAMBBA aimed to characterise the primary particulates and organic precursor species in biomass combustion, and improve the understanding of the aging processes and rates of biomass burning aerosol in a range of fire conditions.

Understanding the vertical profiles of absorbing aerosols with respect to cloud height is important for calculating the radiative forcing for both the direct and indirect effects; SAMBBA aimed to characterise the vertical distribution of biomass burning across the region using airborne in-situ and remote sensing measurements, and to validate satellite retrievals using these methods. The influence of biomass burning processes on clouds, both through the semi-direct effects and aerosol-cloud interactions remain highly uncertain; a primary objective of SAMBBA was to examine the influence of biomass burning aerosol on these processes.

The largest emission uncertainty of atmospheric BC is from biomass burning, with global emissions currently underestimated; Bond et al. (2013) suggest a factor of 2 low bias in the current global emissions based on uncertainties in area burned and the fuel load. SAMBBA aimed to validate satellite retrievals of these quantities using remote sensing measurements. Further to this, assessment of model predications of biomass burning aerosol was a key objective of SAMBBA.

During the SAMBBA 2012 aircraft campaign, the BAe-146 operated from the Porto Velho-Governador Jorge Teixeira de Oliveira International Airport with 20 flights between the 14 September and 3 October 2012. A compilation of all flight tracks are summarised in figure 2.12, with the details of the flights in table 10. The campaign studied biomass burning source regions identifying fires located in Rondônia, north-western Mato Grosso and Palmas, as well as observing regional gradients primarily through remote sensing for example the i) north – south regional gradient from the

biomass burning region of Rondônia to Manaus in the state of Amazonas, ii) the east – west regional gradient from Porto Vehlo to Palmas, Tocantins and iii) the east – west gradient from Rio Branco, Acre to Porto Vehlo. Examples of idealised flight patterns during SAMBBA are presented in figure 2.8.

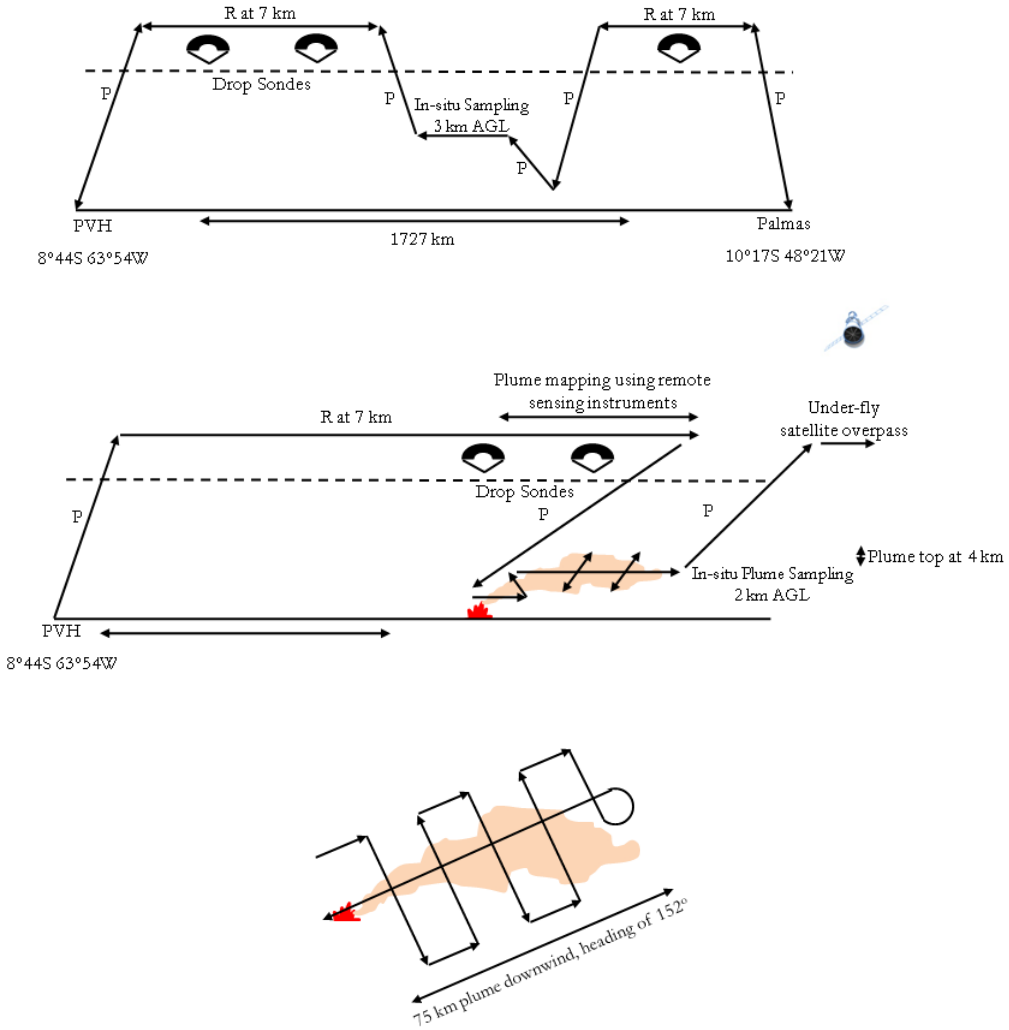

Figure 2.8 Example of idealised flight patterns flow during SAMBBA between the operating base in Porto Vehlo (left-hand side of the figures) and the region of interest (right hand side of the figures). 'R' indicates a SLR and 'P' indicates profiles (*top*) Idealised flight pattern from flight B741/B743; a remote sensing flight with a series of dropsondes (*middle*) Idealised flight pattern from flight B737, a single plume study flight with remote sensing and dropsondes at FL210, *in-situ* instrument observations of biomass burning plume and under-fly a satellite overpass (*bottom*) Aerial view of raster pattern through smoke plume

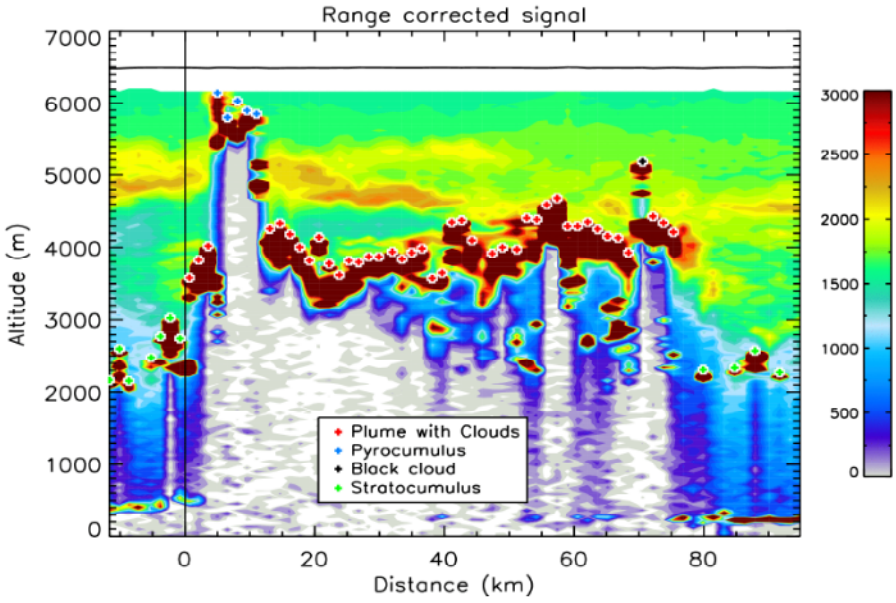

Figure 2.9 Qualitative lidar observations of range corrected signal (arbitrary units) for B737 (20 September 2012) as a function of distance from fire (marked at 0 km) and altitude. Figure courtesy of F. Marenco (Met Office).

The nadir-viewing lidar observations in figure 2.9 are used to map the biomass burning plume during a high-level SLR. They identify the top of the plume at 3500 m altitude close to the source, lifting to 4000 m with increasing distance downwind, whilst the plume extends roughly 75 km downwind. A pyrocumulus cloud can be identified at approximately 5 – 10 km downwind of the fire which reaches a height of 5500 m extending out of the atmospheric boundary layer. Complete attenuation of the lidar signal is observed below the plume top.

2.3.1 SAMBBA Climatology

The NCEP/NCAR reanalysis of 850 hPa wind vectors and surface OLR are presented in figure 2.10 and figure 2.11, respectively. A composite mean between the start and end of the SAMBBA field campaign compared with the 1981 – 2010 climatological mean for the months of August, September and October are shown.

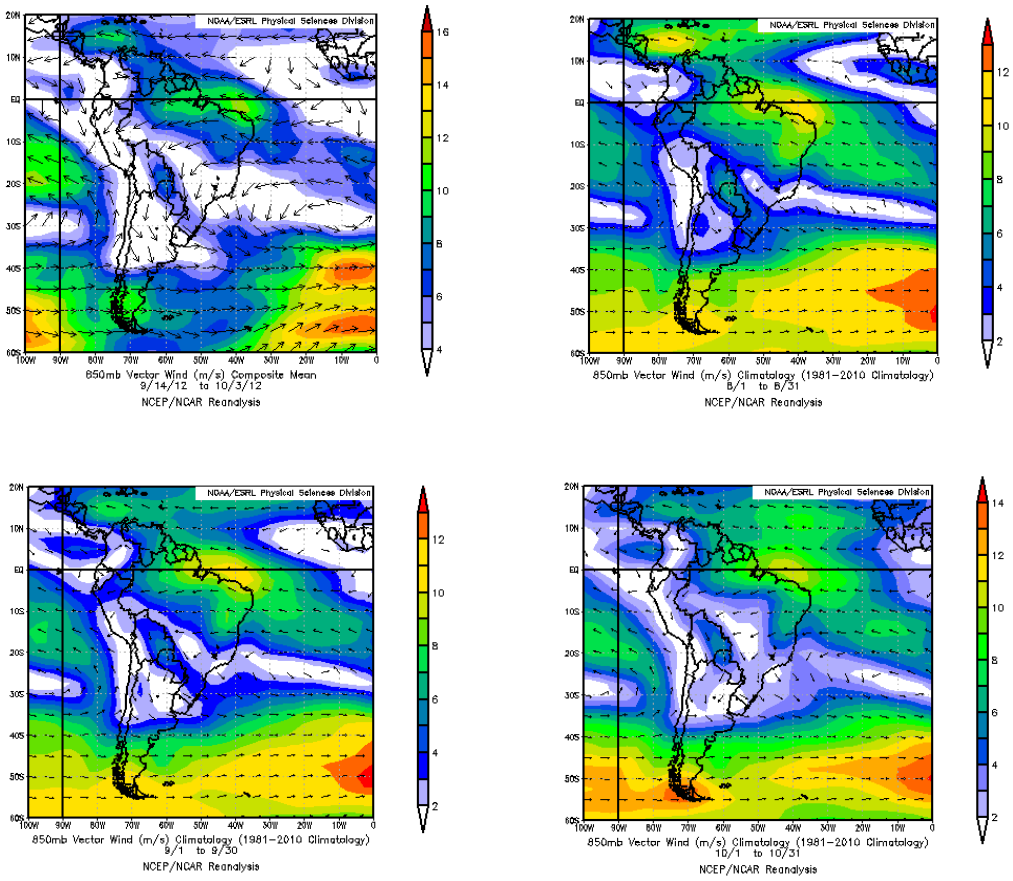

Figure 2.10 SAMBBA campaign meteorology from NCEP/NCAR re-analysis. The 850 hPa wind vectors (m s^{-1}) for (*top left*) SAMBBA 2012 (14 September – 3 October), (*top right*) August climatology, (*bottom left*) September climatology and (*bottom right*) October climatology. Image provided by the NOAA-ESRL Physical Sciences Division.

The SAMBBA mean wind composite in figure 2.10 suggests the position of the south easterly trade winds is consistent with August – October climatology, with peak intensification in the winds along the northern coast, at equatorial latitudes though with a lower intensity of winds compared to the climatology. Anticyclonic flow around the subtropical high penetrates into the continent in an easterly direction with intensification of flow along the eastern edge of the Andes cordillera, due to convergence. The 1981 – 2010 climatology suggests this convergence weakens throughout the dry season into October. The position, structure and intensity of the north-easterly African trade winds appear most consistent with the October mean climatology.

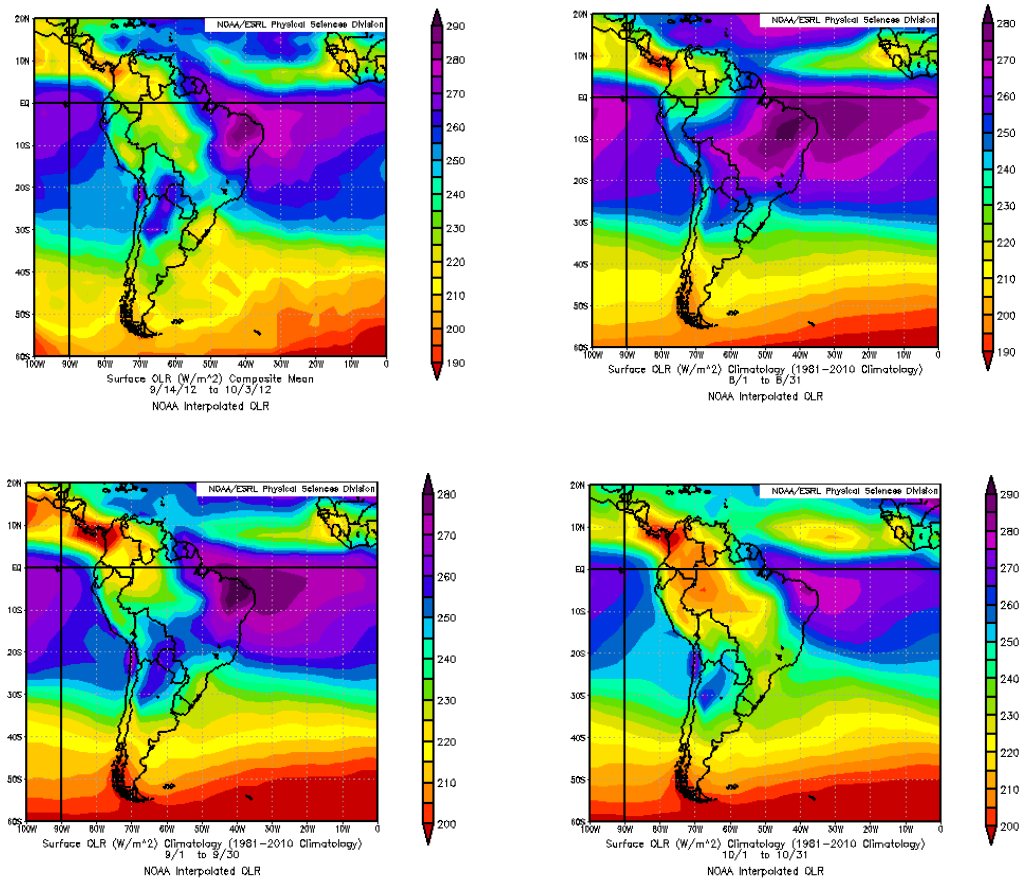

Figure 2.11 SAMBBA campaign meteorology from NCEP/NCAR re-analysis. Surface OLR (W m^{-2}) for (*top left*) SAMBBA 2012 (14 September – 3 October), (*top right*) August climatology, (*bottom left*) September climatology and (*bottom right*) October climatology. Scale to the right of the plot indicates the magnitude of the OLR. Image provided by the NOAA-ESRL Physical Sciences Division.

The extent of the South American dry season is visible during August with the central part of the continent experiencing surface OLR greater than 240 W m^{-2}, by September this shows an eastwards shift consistent with a movement of convection from the northern extreme of the continent into the central Amazon basin. The climatology for October reflects the beginning of the wet season onset with OLR reduced to less than 210 W m^{-2}, consistent with increasing deep convective systems. The SAMBBA mean composite generally compares well with the September climatology, although suggests a greater southern progression of convection, associated with lower OLR, extending into states such as Rondônia.

Table 10 Summary of BAe-146 aircraft flights during SAMBBA 2012

Flight Number	Date (2012)	Time (UTC)	Route	Details
B731	14 September	14:08 – 17:55	East of PVH	Initial shakedown flight; Initial characterisation of aerosol around Porto Vehlo region
B732	15 September	12:29 – 17:32	East of PVH	Multi-fire Sampling; Remote sensing and *in-situ* sampling
B733	16 September	13:51 – 14:45	Rio Branco - PVH	Science transit survey from Rio Branco, Acre to Porto Vehlo
B734	18 September	12:05 – 16:01	South of PVH (central Rondônia)	Regional haze characterisation SW of Porto Vehlo at 3 levels below 2000 metres
B735	19 September	12:07 – 15:47	PVH – Manaus	Manaus; Biogenic aerosol and gases across Amazonas
B736	19 September	18:39 – 20:05	Manaus - PVH	Manaus; Biogenic aerosol and gases across Amazonas
B737	20 September	14:45 – 18:33	South / South East of PVH	Large fire plume study whilst measuring the aging of biomass burning aerosol. CALIPSO validation with lidar.
B738	22 September	15:53 – 17:52	East of PVH	Aborted flight
B739	23 September	11.55 – 15:51	South East of PVH	Multiple-plume study. *In-situ* sampling of smouldering fires in Rondônia.
B740	25 September	11:55 – 15:00	South of PVH	*In-situ* sampling of aerosol layers and smoke plumes south of Porto Vehlo
B741	26 September	12:52 – 16:08	PVH- Palmas	Remote sensing survey from Porto Vehlo – Palmas (Tocantins) using lidar and IR cameras
B742	27 September	12:52 – 16:17	Palmas	*In-situ* measurement of flaming fires near Palmas
B743	27 September	18:08 – 21:34	Palmas – PVH	Remote sensing survey from survey Palmas - Porto Vehlo; Smoke plume transect – East to West
B744	28 September	12:56 – 16:42	South of PVH	Aerosol differences over forest and cleared land. Diurnal cycle
B745	28 September	18:05 – 21:33	South of PVH	Aerosol differences over forest and cleared land. Diurnal cycle
B746	29 September	12:54 – 16:38	West of Alta Floresta	Early morning fires, regional gradient
B747	1 October	15:08 – 18:18	Survey PVH - Palmas	Survey Porto Vehlo – Palmas (Tocantins)
B748	2 October	12:21 – 15:46	Survey Palmas - PVH	*In-situ* sampling smouldering fires in NW Mato Grosso
B749	3 October	13:41 – 17:28	Northwest of PVH	Biogenics; Gradient from pristine to very pristine
B750	3 October	19:15 – 22:24	Northwest of PVH	Biogenics; Gradient from pristine to very pristine; Diurnal cycle

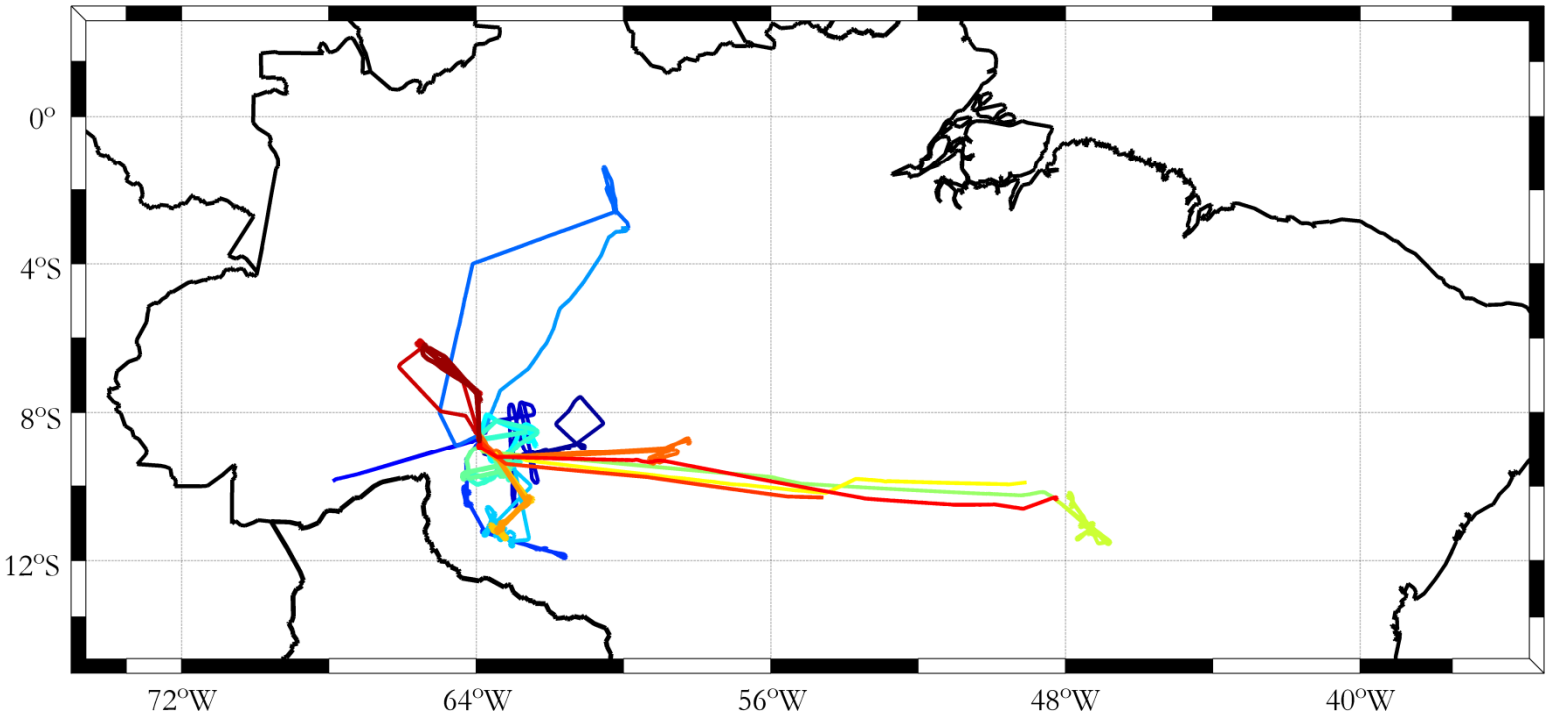

Figure 2.12 Flight tracks for the SAMBBA 2012 campaign. The colour scheme from blue to red corresponds to the flights details in table 10.

2.3.2 SAMBBA Forecasting: Met Office Limited Area Model

In chapter 6 two case studies B734 and B735 from SAMBBA campaign are presented; the meteorology encountered for the two cases are overviewed in section 2.3.4, using the Met Office Limited Area Model (LAM) forecasts. The Met Office LAM was configured with a resolution over the Amazon region of 20 km by 12 km with 70 vertical layers, and is initialised by the unified model boundary conditions. The LAM provided a 48 hour daily forecast at 0000 UTC and a 96 hour forecast at 1800 UTC for 10 m (field dependent), 925 hPa, 850 hPa, 700 hPa, 500 hPa and 350 hPa covering the fields of temperature, horizontal wind, PMSL, relative humidity, specific humidity, cloud cover (low, medium, high and total), boundary layer depth, aerosol optical depth at 550 nm and biomass concentrations. Figure 2.13 shows LAM plots of biomass AOD, 925 hPa horizontal winds and the total model cloud outputs for 12 UTC for flight B734 and B735 and the following discussion provides an overview of the conditions which motivated the BAe-146 sorties.

2.3.3 SAMBBA Satellite Imagery

The number of operational fire products covering Amazonia has increased in past 10 years (Schroeder et al., 2008). Imagery from both the Geostationary Operational Environmental Satellite (GOES-East) and polar orbiting (Aqua and Terra) satellites cover the SAMBBA region of interest. Polar-orbiting satellites are in a sun-synchronous near-polar orbit, that is, the plane of the orbit lies north-south (90^{o} to the equatorial plane), having the same local solar over pass time, an outcome of the satellite maintaining a fixed angle between the orbital path and the Sun which results in consistent solar lighting (important concern for visible sensing instruments). GOES-East is maintained by the National Oceanic and Atmospheric Administration (NOAA) and at an orbit of 35, 500 km and positioned at 0^{o}N 75^{o}W, the GOES East imager produced a 4 x 4 km resolution thermal infrared image which was acquired every 30 minutes.

The use of the Moderate Resolution Imaging Spectroradiometer (MODIS) imagery was a valuable technique for identifying biomass plumes during SAMBBA. MODIS is a multispectral cross-track scanning radiometer that operates in the visible through the thermal infrared spectrum using 36 spectral bands. The MODIS radiometer on NASA's scientific research satellites, Terra (EOS-AM) and Aqua (EOS-PM) provide different

viewing and cloud-cover conditions at the region under-investigation allowing fire activity and biomass burning plume development prior to a flight plan to be monitored. The Terra satellite is in a descending node with a sun-synchronous, near-polar, circular orbit and with a local equatorial crossing time of approximately 10:30 a.m whilst the Aqua satellite is in ascending node with a sun-synchronous, near-polar, circular orbit local equatorial crossing time of approximately 1:30 p.m.

The application of the MODIS fire radiative power algorithm has allowed differences in the rate of energy radiated by fires to be quantified through the use of spectral channels in the near-infrared (3.9 μm) and thermal infrared (11 μm) (Kaufman et al. 1998; Wooster et al. 2003; Butler et al 2004; Smith and Wooster 2005; Ichoku and Kaufman 2005). MODIS active fire product detects fires in 1 km pixels burning at the time of the MODIS overpass under cloud-free. The algorithm uses the middle-infrared and thermal infra-red brightness temperature relative to neighbouring pixels brightness temperature in identifying active fires.

MODIS Terra and Aqua images for flights B734 – B735 are presented in figure 2.14. Terra and Aqua images side-by-side show the development of cloud over the progression of the day. There was a general increase in cloud cover over the period of the field campaign, with convective clouds visible in the satellite images. The images also reflect the difficulty on detecting fires from satellite images due to the presence of cloud cover and convection. Flights were biased to the morning when cloud cover was reduced

2.3.4 SAMBBA 2012

The LAM forecast for the 18 September (figure 2.13i) showed north-westerly horizontal winds (8 – 10 m s^{-1}) in central Rondônia with AODs forecast between 0.3 – 0.5 across the flight region, and the total cloud cover at 1200 UTC showed relatively clear skies. The conditions motivated flight B734, a regional haze style flight south of the operating base in Porto Vehlo in central Rondônia. The flight consisted of one high level SLR for remote sensing using lidar, and three SLRs through the boundary layer.

The LAM for the 19 September (figure 2.13ii) forecast AODs of 0.2 in Rondônia decreasing across the northern region of Amazonia up to Manaus. Total cloud cover was low but forecast to increase across the whole region in the 1800 UTC forecast. The motivation of B735 was to fly a series of deep profiles in a cross section between Porto Vehlo and Manaus, intersected with low level horizontal runs to investigate biogenic

emissions and measure the vertical structure above the central Amazon. The BAe-146 refuelled at Manaus and flight B736 was a return science transit flight with remote sensing of the cross section.

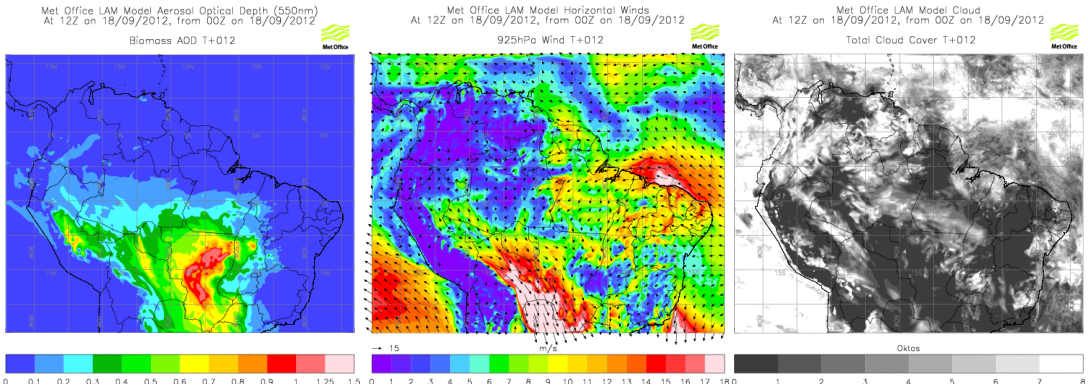

i. 12 UTC on 18 September 2012 from 00 UTC LAM on 18 September 2012 B734

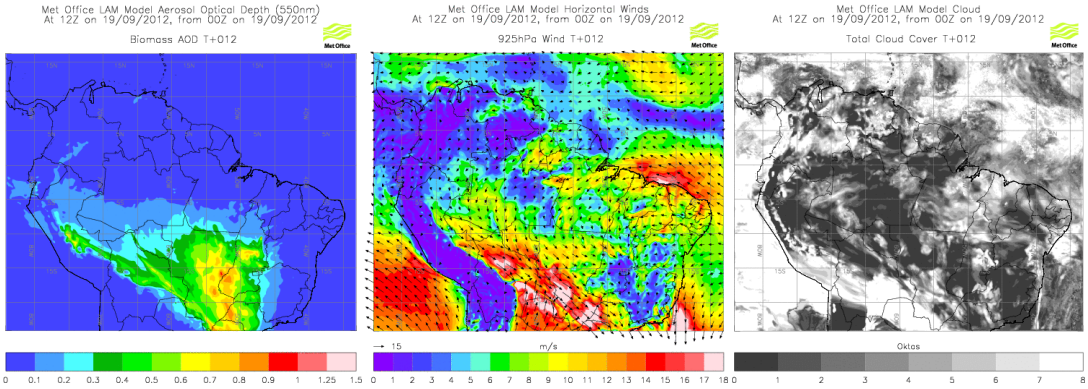

ii. 12 UTC on 18 September 2012 from 00 UTC LAM on 18 September 2012 B735

Figure 2.13 Met Office LAM forecast plots of i) AOD (550 nm), ii) 925hPa horizontal winds and iii) total model cloud cover for SAMBBA flights.

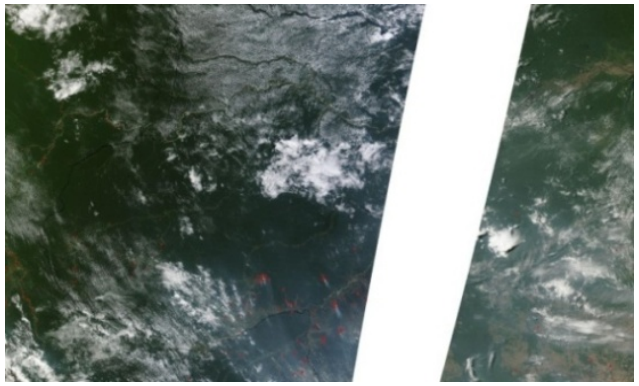

10:30Z 18 September 2012 B734

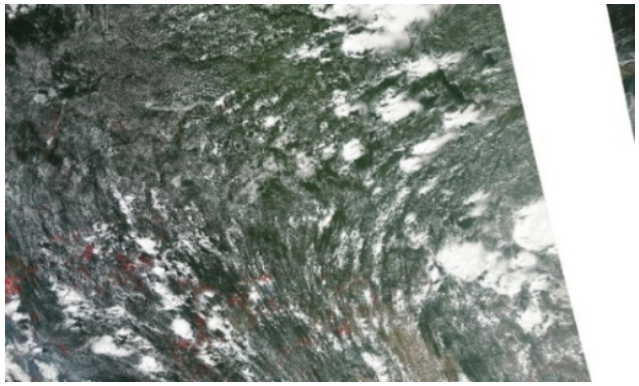

13:30Z September 2012 B734

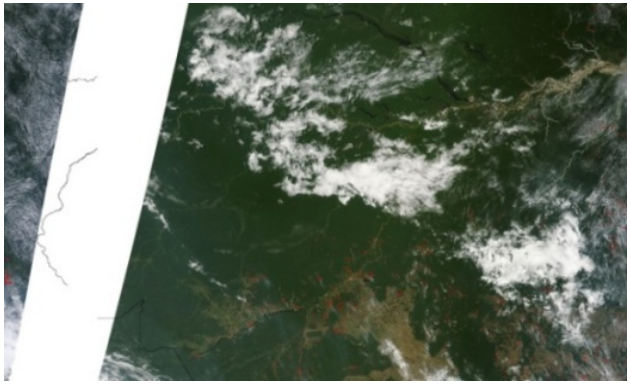

10:30Z 19 September 2012 B735 and B736

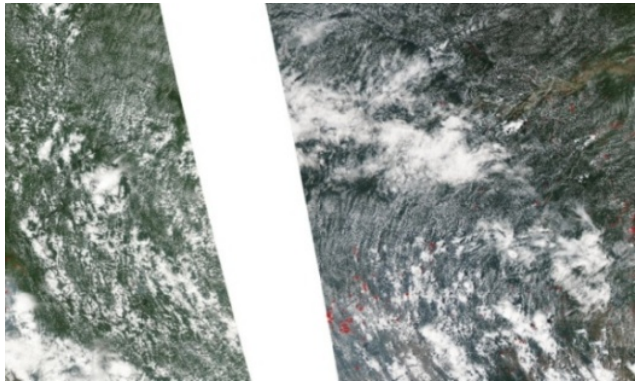

13:30Z 19 September 2012 B735 and B736

Figure 2.14 (*left*) MODIS Terra and (*right*) Aqua 1 km fires and borders for SAMBBA flights B734 – B736 and (*red dots*) MODIS active fire hot spots. Figures from NASA MODIS Active Fire & Burned Area Products and NASA Fire Information for Resource Management System (FIRMS).

3 Instrumentation and Methods

The focus of this section is to present an overview of the instrumentation and techniques applied in making atmospheric observations. An overview of core measurements aboard the research aircraft are presented in table 11. The aircraft altitude, position and velocity are provided through a GPS Inertial Navigation system. Thermodynamic instrumentation include i) total air temperature measured with the use of a deiced and non-deiced Rosemount/Goodrich 102 Total Air Temperature sensors with the use a platinum resistance sensing element ii) General Eastern GE 1011B and Buck CR2 use a Chilled Mirror Hygrometer measuring dew-point temperature and iii) 5-hole turbulence probe mounted on the aircraft nose providing 3-D wind components. Fast Fluorescence AL5002 CO Analyser measured carbon monoxide (CO) and a TECO 49C UV ozone photometer. Johnson-Williams Liquid Water Content (LWC) measures the concentration of liquid water in clouds using a heated wire resistance bridge. The aerosol instrumentation detailed in table 12 uses a variety of different techniques to obtain aerosol microphysical properties.

Optical-based instruments including the PCASP, Grimm Sky-OPC and CDP use a light scattering measurement technique to measure an aerosols optical equivalent diameter assuming a spherical particle of a given refractive index. The Scanning Mobility Particle Sizer (SMPS) uses particle mobility in an electric field to measure an equivalent diameter. This technique is independent of a particles refractive index. The Particle Soot Absorption Photometer (PSAP) designed by Radiance Research is an instrument designed to measure light absorption by aerosol and the nephelometer is an instrument designed to measure total light scattered by aerosol particles. Aerosol compositional data is derived using a compact time-of-flight (C-ToF) Aerosol Mass Spectrometer (AMS) allows for analysis of mass concentrations of sub-micrometer sulphate, nitrate, ammonium and organic material and the Single Particle Soot Photometer (SP2) provides BC mass concentrations and number and/or mass size distribution. The

Leeds airborne VACC (Volatile Aerosol Concentration and Composition) instrument is designed to investigate the volatility properties of different aerosol species in order to determine aerosol composition.

Remote sensing of aerosol was carried out using a nadir-viewing (downward-looking) Leosphere ALS450 elastic backscatter lidar. The lidar operates at 355 nm, and provides a 1.5 m vertical resolution and 2 s integration time, with subsequent data processing provides a vertical resolution of 45 m and integration of 1 minute; this reduces the signal-to-noise (Marenco et al., 2011). It is possible to distinguish between aerosol and thin cloud observations using features of the instrument's depolarisation capability.

Table 11 Overview of core measurements and chemistry measurements aboard the BAe-146.

Instrument	Measurement Technique	Measurement Range	Parameter measured	Time resolution	Calibration Technique	Aircraft Position	Primary Reference
GPS-aided Inertial Navigation System	GPS	-	Altitude, Position and Velocity	32 Hz		Externally Mounted	(Allen et al., 2011)
Rosemount Total Air Temperature Sensors (Deiced and non-deiced)	Platinum Resistance	-50 ^{o}C to + 50 ^{o}C	Total Air Temperature	32 Hz		Externally mounted on aircraft fuselage	(Allen et al., 2011)
Turbulence probe (5-hole)	Incident airflow and 3-d wind components	-	Turbulence	32 Hz		Externally mounted on aircraft fuselage	(Allen et al., 2011)
Buck CR2	Chilled Mirror Hygrometer	-80 °C to +20 °C	Dew Point Temperature	1 Hz		Externally mounted on aircraft fuselage	
General Eastern	Chilled Mirror Hygrometer	-75 °C to +50 °C	Dew Point Temperature	4 Hz		Externally mounted on aircraft fuselage	
Johnson-Williams Liquid Water Content (LWC)	Heated wire resistance bridge	0 – 3 g m^{-3}	Liquid water content	4 Hz		Externally mounted on aircraft fuselage	
Ozone Photometer	UV Absorption ($\lambda = 254$ nm)	1 – 500 ppbv	Ozone Concentration	4 s	Manufacture calibration	Internally Mounted	(Nedelec et al., 2003)
Fast Fluorescence CO Analyser	UV Fluorescence ($\lambda = 150$ nm)	3 – 2000 ppbv	Carbon Monoxide Concentration	1 Hz	Calibrated at 500 ppbv	Internally Mounted	(Gerbig et al., 1999)

Table 12 Overview of airborne microphysical, optical and composition instruments for aerosol measurements.

Instrument	Measurement Technique	Measurement Range	Parameter measured	Resolution	Calibration Technique	Aircraft Position	Primary Reference
Scanning Mobility Particle Sizer (SMPS)	Electrical Mobility	0.010 – 0.60 μm	Particle Size	~ 60 s (dependent on operation mode)	Ammonium Sulphate	Internally Mounted (behind Rosemount Inlet)	Baron and Willeke (2005)
Passive Cavity Aerosol Spectrometer Probe (PCASP)	Light Scattering	0.1 – 3.2 μm		1 Hz / 10 Hz	PSLs / DEHS	Externally mounted on aircraft wing	(Liu et al., 1992)
Volatile Aerosol Concentration and Composition (VACC)		0.15 – 0.5 μm		1 Hz	PSLs / DEHS	Internally Mounted (behind Rosemount Inlet)	(Brooks et al., 2007)
Grimm Sky-OPC		1 – 32 μm		6 s	Comparison with 'master instrument'	Internally Mounted (behind Rosemount Inlet)	(Heim et al., 2008)
Cloud Droplet Probe (CDP)		15 – 930 μm		1 Hz	Spinning pinhole tests and glass bead calibrations	Externally mounted on aircraft wing	(Lance et al., 2010)

Particle Soot Absorption Photometer (PSAP)	Single wavelength absorption photometer	$>10^{-7}$ m^{-1}	Absorption coefficient	1 Hz	N/A	Internally Mounted (behind Rosemount Inlet)	(Bond et al., 1999)
Integrating nephelometer	Three wavelength nephelometer	$>10^{-7}$ m^{-1}	Scattering coefficient	1 Hz	Calibration gas	Internally Mounted (behind Rosemount Inlet)	(Anderson et al., 1999)
Aerodyne compact Time-of-Flight Aerosol Mass Spectrometer (C-ToF-AMS)	Composition and mass concentration	0.050 – $0.80\ \mu m$	Sub-micrometer sulphate, nitrate, ammonium and organic mass concentration	1 Hz	Ammonium nitrate ionisation efficiency (IE) calibration	Internally Mounted (behind Rosemount Inlet)	(Canagaratna et al., 2007)
Single Particle Soot Photometer (SP2)	Light Scattering	0.070 –$0.60\ \mu m$	Black Carbon mass and size distribution	1 Hz	BC mass; DMA-sized fullerene soot and Aquadag Scattering measurements; PSL spheres and DMA-sized ammonium sulphate	Internally Mounted (behind Rosemount Inlet)	(Schwarz et al., 2006b; Stephens et al., 2003)
Light Detection and Ranging (lidar)	Backscatter-depolarisation at 355 nm	$\leq$ 15 km (600 – 1000 m above target boundary)	Backscatter-depolarisation	Vertical resolution 1.5 m		Nadir-viewing geometry, backward tilt of 4.2^{o}	(Klett, 1985; Marenco et al., 2011)

3.1 Instrumentation

3.1.1 Aerosol Microphysical Instrumentation: Optical Particle Counters

Optical particle counters (OPCs) use the technique of single particle sampling to produce a measure of particle size and number concentration. The latter requires the sample volume and flow rate to be known. OPCs do not size particles directly, rather they measure the amount of scattered light from individual particles as they pass through a laser beam in terms of an electrical pulse height representative of a particles scattering cross section. The amount of scattered light depends on particle refractive index and as such OPC response is necessarily calibrated using readily-procured aerosol of specific refractive index.

The scattered light is collected across instruments optics, focused on a photo-detector and converted into electrical pulses. The OPC electronics relate the pulse height and assigns the particle to a specific bin. The pulse height signal from the photodiode is amplified and digitised. The amplification process consists of three amplifiers in parallel called *gain stages* which extend the sizing range of the PCASP. Gain stages work by passing a pulse signal along the amplifiers with a pulse height related to a threshold between 1 – 12288 (table 13); if a pulse saturates the first gain stage (high gain), it passes to the second gain stage (medium gain), and if the second gain stage additional saturates it is passed to the third stage (low gain). If the third gain stage is saturated the particle is out of the sizing range of the PCASP and is registered as oversized (Rosenberg et al., 2012).

Table 13 Classification of PCASP gain stages in terms of pulse height threshold.

	High Gain	Mid Gain	Low Gain
Minimum threshold	1	4097	8193
Maximum threshold	4096	8192	12288

OPCs can operate on the principle of either active cavity or passive cavity lasing; active scattering uses a low power laser combined with a sensing volume which is positioned inside the laser resonator to gain high illumination intensities (Knollenberg and Luehr, 1976). Active Scattering Aerosol Spectrometer Probe (ASASP) uses the intra-cavity

standing wave radiation from a 2 mW He-Ne laser to illuminate particle (Liu et al., 1992). Passive cavity lasing, used by the PCASP does not contain such a sensing medium and has a sensing cavity separate to the laser cavity. Whilst active cavity achieves high intensity through the use of the sensing medium, passive cavity instruments use a 99.9 % reflectivity crystal mirror oscillator, which provides multiple reflections of the original laser.

The use of a mirror oscillator for multiple laser reflections introduces the terms *primary angular range* and *secondary angular range* which are related to the direction of the laser beam on scattering. The primary angular range relates to the instrument collection angle from scattering of the direct laser beam, whilst the secondary angular range relates to the instrument collection angle from scattering of the reflected laser beam. Table 14 presents features of the optical system for three OPCs discussed in detail throughout this thesis.

Instrument scattering detection direction describes the arrangement of the optical cavity in the different instruments i.e. the angles over which the instruments collect scattered light. Instrument optical cells can operate by forward scattering and collect light scattered in a forward direction, for example, the CDP collects between 4 – 12°. In contrast the PCASP and Grimm Sky OPC size particles by collecting side-scattered light, the PCASP between 35 – 145° and the Grimm Sky OPC between 30 – 150°.

Table 14 Features of the optical system for the PCASP, CDP and Grimm Sky OPC.

Instrument	Primary Angular Range	Secondary Angular Range	Wavelength (λ)	Scattering Detection Direction
PCASP	35 – 120°	60 – 145°	632.8 nm	Wide angle collector optic / side scatter
CDP	4-12°	-	658 nm	Forward scatter
Grimm Sky-OPC	30 – 150°	81-99°	655 nm	Wide angle collector optic / side scatter

The PCASP and Grimm Sky OPC have the widest angle optics which increases the total amount of scattered light detected by the photo sensor. The optical chamber has the advantage that it increases the signal to noise ratio, which reduces the minimum particle size which can be detected (Heim et al., 2008).

The relationship between particle scattering, influenced by refractive index, and particle size is determined by calibration. Calibration is carried out pre- and post a field campaign and typically after a change in the instrument such as cleaning the instruments optical cavity and re-alignment of the laser. The calibration procedure shall be discussed in the section 3.3.1.

A laser beams intensity is not uniform; OPCs use the centre portion of the laser beam correlating with highest laser intensity. To gain the greatest accuracy in measurements, sheath airflow narrows the sample airflow towards the centre of the laser beam. OPCs are deemed *misaligned* if the sample flow passes through the laser beam edge; it will be subject to the lower-intensity light from the laser beam than passing through the beam centre. Additionally a large particle passing the beam edge may be mis-sized, that is the pulse-amplitude is decreased and the spectrometer sizes the particle as being smaller than in reality.

OPCs use the technique of single particle scattering, and as such if measurements occur in environments where particle concentrations are high, the instruments are prone to particle *coincidence effects* whereby multiple particles can pass the laser beam at the same time.

3.1.1.1 Passive Cavity Aerosol Spectrometer Probe

The PCASP uses a 632.8 nm wavelength He-Ne laser, with an optical cavity designed to collect over primary scattering angles of 35 – 135°, and secondary scattering angles of 60 – 145°. The light is focused onto a photo-detector, amplified, processed and classified into one of thirty two size channels. The PCASP consists of 30 channels with optical detection in the nominal range of 0.1 µm < D < 3.2 µm.

The PCASPs optic chamber is based on side scattering, that is, light is symmetrically scattered at all azimuth angles around the laser beam. The laser beam is positioned directly at the collecting mirror, passing through its focal point then through a hole in the centre of the mirror where the crystal mirror oscillator and reference photodetector are located. The crystal mirror oscillator has a 99.9 % reflectivity and as such the laser beam is almost entirely reflected back along the same path and the laser beam crosses the focal point twice. The sample comes in from the side and (if well aligned) also passes through the focal point of the mirror. Therefore the sample, direct laser beam

and reflected beam all meet at the mirror focal point. Light is scattered symmetrically by particles and this scattered light is collected by the parabolic mirror. This scattered light is further bent by 90° by a second mirror and focused on the detector by a lens. The mirror itself collects light over the scattering angle 35° – 120° for the direct beam and 60 ° – 145 ° for the reflected beam.

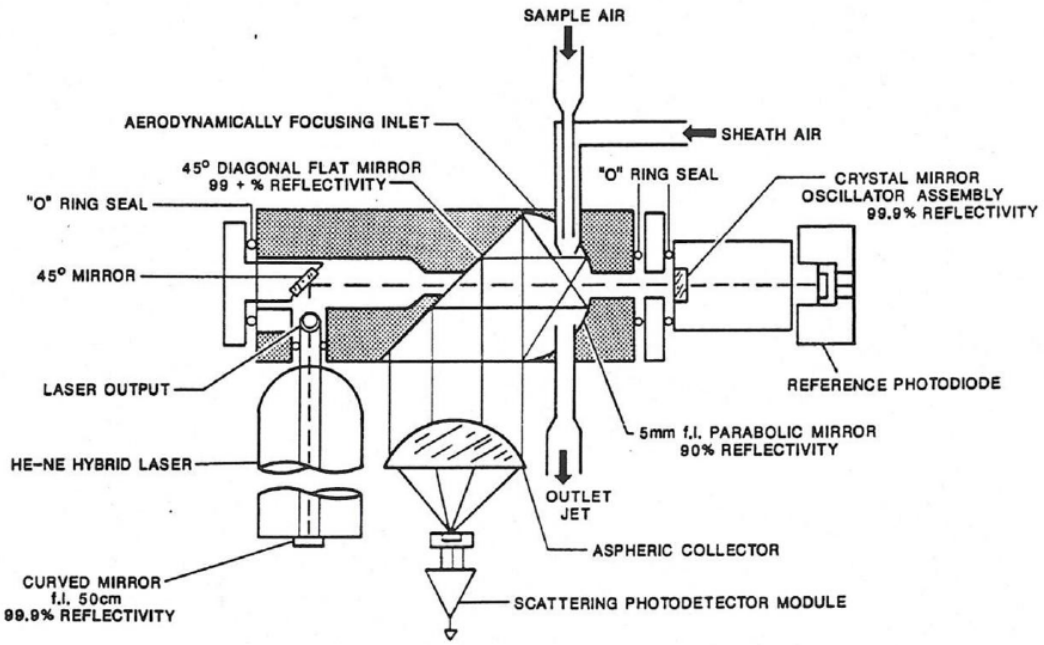

Figure 3.1 Schematic of a bench top Passive Cavity Aerosol Spectrometer Probe.

The FAAM PCASPs are fitted in a PMS (Particle Measurement Systems) pod under the aircraft wings. The FAAM PCASP probe has an external nose cone as a sampling feature; the nose cone is roughly 10 cm in length with a circular inlet of 1 cm diameter which expands to 3 cm, as air is sampled along the length of the nose cone it is slowed to a 10^{th} of the original aircraft speed. Located at the base of the nose cone is a sub-sampler which extracts a proportion of the airflow to sample whilst the remaining airflow passes out through the exhaust. The PCASP data is processed using equations derived by Belyaev and Levin (1974) to correct for the sampling process at a best estimate of the PCASP inlet efficiencies; however sample uncertainties such as deviations from isokinetic flow and turbulent flow exist.

3.1.1.2 Cloud Droplet Probe

The CDP manufactured by Droplet Measurement Technologies (DMT) is designed to measure cloud droplet sizes over the nominal diameter range 2 μm to 50 μm with an open path laser of wavelength 658 nm. The probe is a wing mounted instrument based around a forward-scatter optical system, collecting scattered light across a nominal range of 4° to 12°. These forward scattered photons are focused and directed onto a pair of photodetectors termed the sizer and qualifier, used to determine if the droplet falls within the 'depth of field'. The position the droplet crosses the open laser beam is crucial for assessing if the droplet is in focus, and relates to the qualified sample area, used to calculate sample volume and in turn ambient cloud droplet number concentration. Laser intensity is monitored by a light absorbing photodetector, termed the 'dump spot monitor'.

Forward scattered light is equally split with a beam splitter and the voltage ratio registered by the sizer photodetector (unmasked) and qualifier photodetector (masked) is used to assess if a droplet falls within the depth of field of the qualifier. For cloud droplets which fall within the qualified sample area, the signal at the qualifier should be twice the sizer signal, that is, it is considered within the depth of field and the droplet is counted and sized. Where a cloud droplet falls outside the depth of field, a signal is registered on the sizer (unmasked), but does not register with the qualifier (masked), and the ratio of the signals identified the droplet did not fall within the focal point of the CDP. The cloud droplet is not counted and sized. Figure 3.2 identifies a qualified droplet (black spot), with scattered signal (red light rays) which qualifies within the depth of field, whilst the blue droplet, and corresponding light rays fall outside the instruments field depth of field, and the focused scattered light do not register with the masked qualified photodetector, such that the particle is rejected and uncounted.

The use of the CDP in aerosol applications requires the filtering of data for the presence of water droplets using a threshold applied to data of particle number concentrations of less than 5 cm^{-3}, in conjunction with a threshold of less than 0.04 g m^{-3} of liquid water as measured by the Johnson-Williams water content probe.

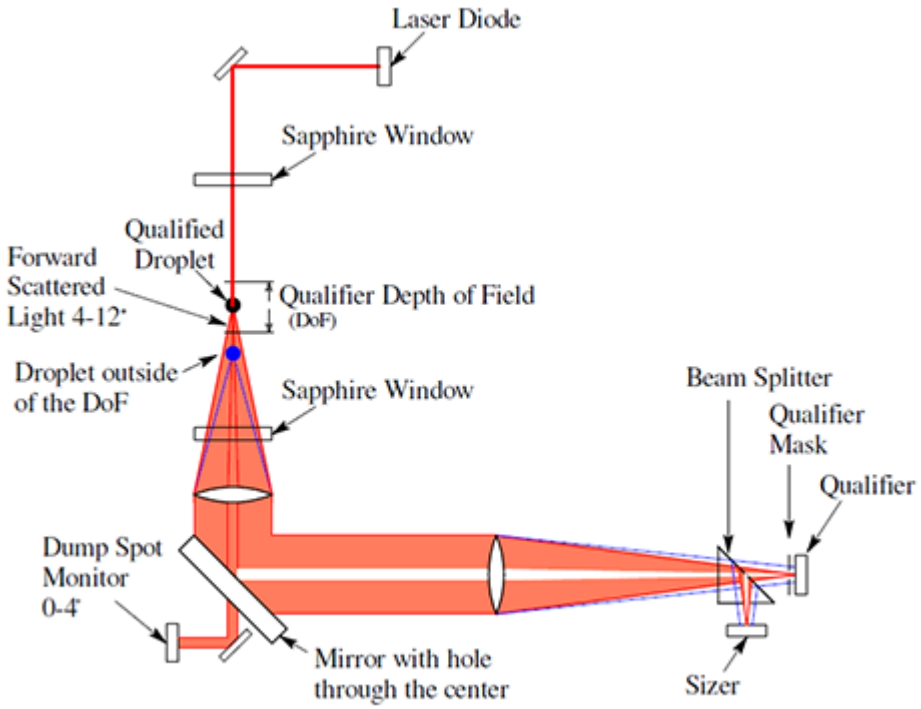

Figure 3.2 Schematic of the optics of a Cloud Droplet Probe. Reproduced from Lance et al. (2010).

3.1.1.3 Grimm Sky OPC

The Grimm Sky-OPC is used to obtain aerosol sizing information across 31 channels from 0.25 μm to 32 μm (manufactures specification) and provides particle concentration output of particles/100 ml. The Sky-OPC provides sizing information continually on a time period of six seconds and has a constant flow rate of 1.2 L min^{-1} achieved due to a built-in critical orifice.

Like the PCASP, the Grimm is a closed cell instrument with light scattering collected through primary scattering angles of 30° to 150° as evident in figure 3.3. The laser diode has a wavelength of 655 nm (Sky-OPC Manual). The parabolic mirror collects light over the primary angular range of 30 ° – 150° for the direct beam (with a mean scattering angle 90◦) with an additional 18° in the secondary angular range of 81 – 99° for the reflected beam. The wide angle optic increases the total amount of scattered light detected by the photo sensor.

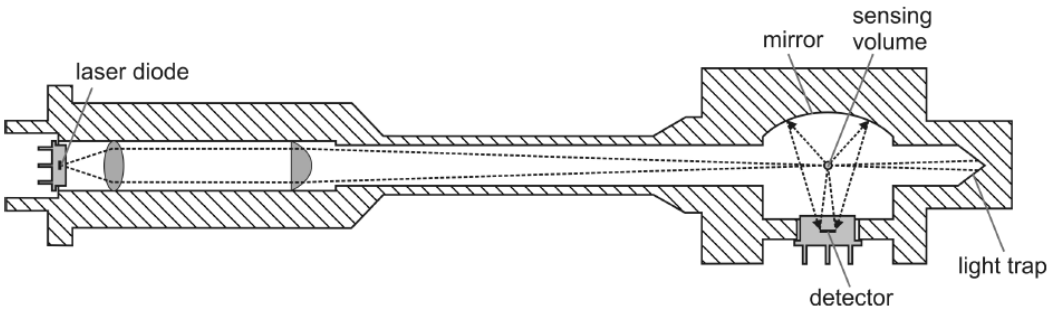

Figure 3.3 Laser Measurement Chamber of the Sky-OPC (Sky-OPC Manual).

The standard operation set-up for the Grimm has a time resolution of 6 seconds of which during the first second the instrument lasers at high intensity for sizing small particles (< 2.5 μm) and the final 5 seconds the instrument lasers at lower intensity for sizing larger particles (2.5 to 32 μm). Due to lack of information about the bin responses, it is not currently possible to fully calibrate the Grimm in the laboratory other than by sending it back to the manufacturer. This puts it at a potential disadvantage compared to the DMT probes.

The Grimm has a constant flow rate achieved due to a built-in critical orifice, and for optimum operation a constant, controlled airflow of 1.2 L min^{-1}. The optical system of the Sky-OPC is protected via a sheath air circulation (prior to every measurement (every 6 s) the Sky-OPC performs a self-test which rinses the measurement chamber with pure air at operating conditions of 0.4 L min^{-1}).

The Grimm Sky-OPC records 4 parameters from four pressure sensors located within the Sky-OPC which can be used in determining its performance. Optimum operation requires pA/p and pR/p values to be less than 120, indicating optimum flow rates are reaching the instrument.

Table 15 Pressure measurements in the Grimm Sky-OPC

Parameter	Parameter Description
pR	Rinsing air pressure after critical orifice
pA	Sample air pressure after critical orifice
p	Pressure before critical orifice – both sheath air and sample air
pM	Pressure inside the measurement cell

3.1.2 Aerosol Microphysical Instrumentation: Scanning Mobility Particle Sizer

The SMPS consists of a TSI Model 3081 long Differential Mobility Analyser (DMA) and a TSI Model 3786 low pressure water Condensation Particle Counter (CPC) (Allen et al., 2011; Wang and Flagan, 1990), and covered a size range of 20 – 290 nm with a resolution of 64 channels. Particles are neutralised using a radioactive source and enter a Differential Mobility Analyser (DMA), where they are sized based on the mobility of charged particles within an electric field.

The flow then enters the CPC where particle number concentration is determined. The CPC operates by supersaturating aerosol flow which causes the aerosols to grow in size to droplet size of several microns in diameter until it is large enough to be detected optically. The droplet flow is focused into a nozzle and passed into a laser beam. Each single particle scatters a light pulse and pulses with amplitude above a threshold value are counted. The particle number concentrations are calculated knowing aerosol flow rate.

3.1.3 Aerosol Optical Instrumentation: Particle Soot Absorption Photometer

The PSAP designed by Radiance Research is an instrument designed to measure light absorption by aerosol. The PSAP operates on the principle of a change of light transmission through a fibrous glass filter as particles are deposited on the filter from the sample flow, as presented in figure 3.4. The optical absorption coefficient ($\sigma_{abs}^{0.567}$), with units of m^{-1}, is determined by relating the change in transmission across the filter using Beer's Law. The optical absorption coefficient can be expressed according to equation (1.24) at a single wavelength of 567 nm.

$$\sigma_{abs}^{0.567} = \frac{A_{PSAP}}{Q_{PSAP}} ln\left(\frac{I_o}{I}\right) \tag{1.24}$$

where A_{PSAP} is the area of the deposited aerosol particles on the filter (spot size), Q_{PSAP} is the sample flow rate through the filter in a given period of time. I_o is the initial transmittance of light through the filter and I is the filter transmittance after a period of time.

The PSAP provides continuous, time resolved measurement of absorption determined over 30 second integration periods. The standard corrections applied to the PSAP are laid out in Appendix A.

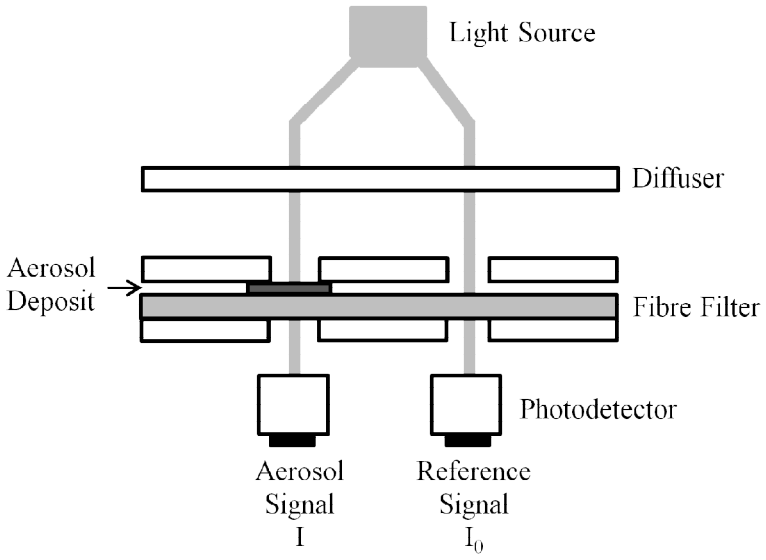

Figure 3.4 Schematic of the operating components of the PSAP.

3.1.4 Aerosol Optical Instrumentation: Nephelometer

The nephelometer is an instrument designed to measure light scattered by aerosol particles over a distance (figure 3.5). Aerosol scattering coefficients (σ_{scat}^{λ}) are measured at three wavelengths (450 nm, 550 nm and 700 nm with a bandwidth of 40 nm) using a TSI 3563 integrating nephelometer. The nephelometer makes measurements of volume scattering coefficients, which is the scattering cross section divided by the unit volume of air. The units of scattering measured by the instrument are $m^2 m^{-3}$ or m^{-1}.

Illumination of the main body of the nephelometer is achieved using an incandescent quartz-halogen lamp which emits across the visible spectrum, whilst the positioning of two dichroic filters within the receiving optics of the instrument filters light into three wavelengths. The first dichroic filter passes light of wavelength 500 – 800 nm and reflects wavelengths of 400 – 500 nm, of which the reflected light further passes through a band pass filter centred at 450 nm into a photomultiplier tube (PMT). A second dichroic filter pass light of wavelength 500 – 600 nm and reflects 600 – 800 nm, of which the reflected light further passes through a band pass filter centred at 700 nm

into a second photomultiplier tube. Light of wavelength 500 – 600 nm pass through both dichroic filters, and finally passes through a band pass filter centred at 500 nm into a third PMT.

Hemispheric backscattering coefficients, ($\sigma^{\lambda}_{b\,scat}$) between 90° and 170° at each of the wavelengths measured which is achieved using a backscatter shutter blade which rotates in front of the light source in the forward direction, that is, 7° – 90° which allows for measurement of the backscatter signal. The standard corrections applied to the nephelometer are laid out in Appendix A.

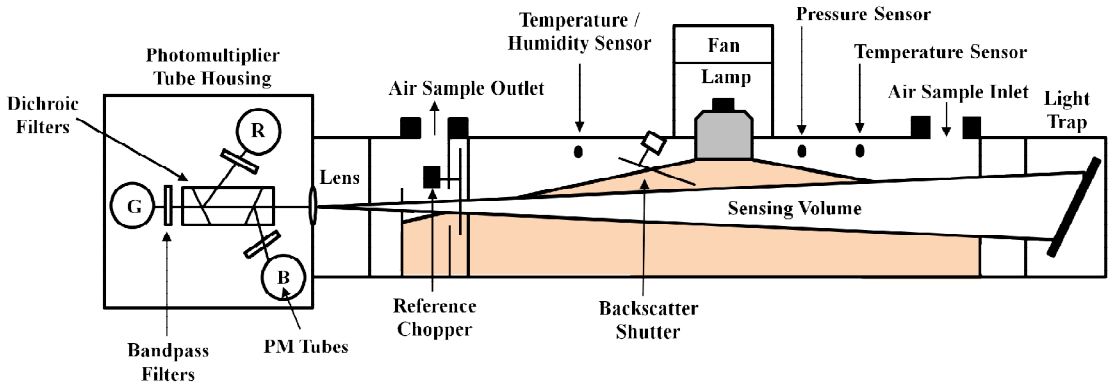

Figure 3.5 Measurement chamber of the 3 wavelength integrating nephelometer.

3.1.5 Aerosol Composition Instrumentation: Aerosol Mass Spectrometer

A compact Aerodyne Time-of-Flight (C-ToF) Aerosol Mass Spectrometer (AMS) is routinely operated on the FAAM research aircraft. The AMS uses thermal volatilisation of aerosol particles (and as such it is not able to volatilise refractory particles and sea salt), and further uses a separate ionisation step using electron impact of the volatilised gaseous material to bring ions into the mass spectrometer detector. The instrument allows for analysis of mass concentrations (μg m^{-3}) of sub-micrometer sulphate, nitrate, ammonium and organic material. Calibrations of the instrument were performed using monodisperse ammonium sulphate and ammonium nitrate (Allan et al., 2014). The author refers to a number of publications for a detailed description of the instrument (Allan et al., 2004; 2003; Canagaratna et al., 2007; Drewnick et al., 2005).

3.1.6 Aerosol Composition Instrumentation: Single Particle Soot Photometer

The DMT SP2 is designed for measuring single particle properties of BC using light absorbing and scattering characteristics. The SP2 uses a Nd:YAG laser at a wavelength of 1064 nm, with a detector positioned to collect light scatter as particles pass through the laser beam. BC containing particles absorb laser energy, and become heated until the particle incandesces, that is it emits visible light. The author refers to a number of publications for a detailed description of instrument operation (Cross et al., 2010; Schwarz et al., 2006b; Stephens et al., 2003).

The intensity of incandescence can be correlated to BC mass through calibration using BC proxies such as DMA-sized fullerene soot and Aquadag. Such standard reference materials are limitations for the SP2 as they are surrogate soot like materials and reliable standards for calibrations do not truly exist; questions of do the refractive index, particle density and morphology of the soot standard reference materials resemble what is measured by the instrument *in-situ* (Baumgardner et al., 2012). Scattering measurements are calibrated with standard Polystyrene Latex Spheres (PSLs) and DMA-sized ammonium sulphate (see section 3.3.1 for a discussion of calibration procedures). The SP2 data is presented for low relative humidity due to the use of active sheath air to dry the sample flow. The SP2 provides measurements of BC number and mass concentration and number and size distributions dN/dlogD and dM/dlogD. For particles which contain a mixture of components, that is they are internally mixed, the additional material surrounding the absorbing particle will vapourise at lower temperatures, delaying the incandesce signal. This time delay can be related to the coating thickness of a particle (Moteki et al., 2007; Schwarz et al., 2008).

3.1.7 Aerosol Composition Instrumentation: Volatile Aerosol Concentration and Composition

The University of Leeds airborne VACC instrument is designed to investigate the volatility properties of aerosol species in order to determine aerosol composition. The system consists of a computer controlled heater unit coupled to a modified PCASP-X (Brooks et al., 2007; Brooks et al., 2002). The modified PCASP-X takes advantage of the scattering characteristics of the PCASP and the sizing characteristics of the ASASP (Peter et al., 2008). The heater unit contains a tube heater of length 20 cm with a 6.4

mm (¼ª) stainless inner diameter (Peter et al., 2008), with an average flow rate through the heater tube of 0.18 L min^{-1}. The minimum temperature of the system reflects the ambient cabin temperature, up to a maximum desired temperature of approximately 850°C.

A Perma Pure PD™-Series Nafion® drier (PD-100T-12SS) was attached to the rear of the Rosemount inlet that served the VACC instrument during the SAMBBA campaign. The Nafion® drier is operated on a counterflow system, where-by moisture is able to be transferred from the sampling line to a counter-flowing purge gas. The Nafion® drier was desired due to the tropical climate and high relative humidity's encountered during the campaign. A Rotronic HygroClip HC2-series digital humidity-temperature sensor was attached to the rear side of the Nafion providing 1 Hz measurements on the aerosol sample line.

The VACC operates on the principle that as aerosol particles are heated they lose mass/size by either mechanical breakdown (shattering) or by undergoing a phase transition. The characteristic temperature at which this occurs is dependent on the chemical species present in the particle / aerosol. The mechanisms for loss of chemical species on an aerosol are discussed by Brooks et al., (2002) whereby i) the physical shattering of a particle results in secondary fragments (the size of which are below the detection limit of the volatility system) ii) decomposition of the species to its component ions and iii) the vaporisation of the chemical species from the aerosol.

The VACC uses a thermo-optical technique measuring changes in the aerosol particle number concentration across a size distribution whilst temperatures are raised beyond the volatilisation temperature of chemical species. This technique separates chemical species to varying degrees; (1) highly volatile organic carbon (low molecular weight organic carbon) and ammonium bisulphate (30 – 150 °C), (2) ammonium nitrate, ammonium sulphate and mid-volatility organic carbons e.g. dicarboxylic acids (T = 170 – 250 °C), (3) low volatile organic carbon such as high molecular weight organic carbon such as anhydrosugars and humic-like substance materials (HULIS) (T = 250 – 500 °C) and (4) refractory aerosols such as elemental carbon, mineral dust and sodium chloride (T > 500 °C). Table 16 and table 17 give an indication of volatility temperatures for a range of atmospheric inorganic chemical species and organic chemical species, respectively.

Table 16 Volatility temperatures for a range of atmospheric inorganic chemical species.

Chemical Species	Chemical Formula	Phase Transition	Volatility Temperature (°C)
Ammonium Bisulphate	$(NH_4)HSO_4$	Melts	147
Ammonium Nitrate	NH_4NO_3	Melts	170
Ammonium Nitrate	NH_4NO_3	Sublimes	210
Ammonium Sulphate	$(NH_4)_2SO_4$	Melts	235

Melts: Phase transition of a substance from solid phase to a liquid phase *Boils:* Phase transition of a substance from the liquid phase to the gaseous phase *Sublimes:* Phase transition of a substance from the solid phase to the gaseous phase without passing through the intermediate liquid phase.

Table 17 Volatility temperatures for a range of atmospheric organic chemical species.

Chemical Species		Chemical Formula	Volatility Temperature (°C)
Isoprene	Alkenes	C_5H_8	34
Glyoxylic Acid	Monocarboxylic Acid ($C_1 - C_3$)	$OCHCO_2H$	111
Malonic Acid	Dicarboxylic Acid (Aliphatic $C_2 - C_9$)	$CH_2(COOH)_2$	135
Oxalic Acid	Dicarboxylic Acid (Aliphatic $C_2 - C_9$)	$C_2H_2O_4$	189
Succinic acid	Dicarboxylic Acid (Aliphatic $C_2 - C_9$)	$C_4H_6O_4$	184
Levoglucosan	Anhydrosugars	$C_6H_{10}O_5$	384

Whilst the SP2 provides mixing state on a single particle basis, the VACC is capable of producing size distributions as a function of volatility temperature which provides a qualitative indication mixing state of the aerosol population. In the simplest case of an externally mixed aerosol population (figure 3.6) consisting of two species A and B, in which the volatilisation temperature of A (red) is higher than B (blue), with a similar size distribution, and therefore have a mono-modal distribution of size D_1 with a number of particles, $N = N_1 + N_2$. As the temperature is raised, aerosol species B volatises at a lower temperature than A; this results in the loss of N_2 particle number leaving N_1 at size D_1. There is an observed change in a reduction of particle number concentration whilst maintaining the size distribution.

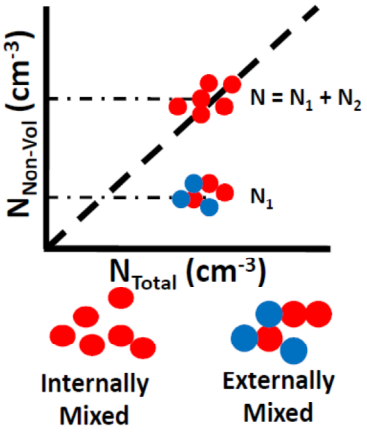

Figure 3.6 The effect of increasing temperature on externally mixed aerosol; change in the aerosol particle number concentrations versus the size range of the distribution. Figure adapted from Weinzierl et al. (2009).

In the case of internally mixed aerosol species (figure 3.7), whereby the core of the aerosol (red) with species B (blue) forming a coating. (Again the volatilisation temperature of A is higher than B). As the temperature is raised, aerosol species B volatises at a lower temperature than A, this results in the loss of size of the aerosol and a shift to a smaller diameter, D_1. There is an observed change in size distribution whilst particle number concentration is conserved.

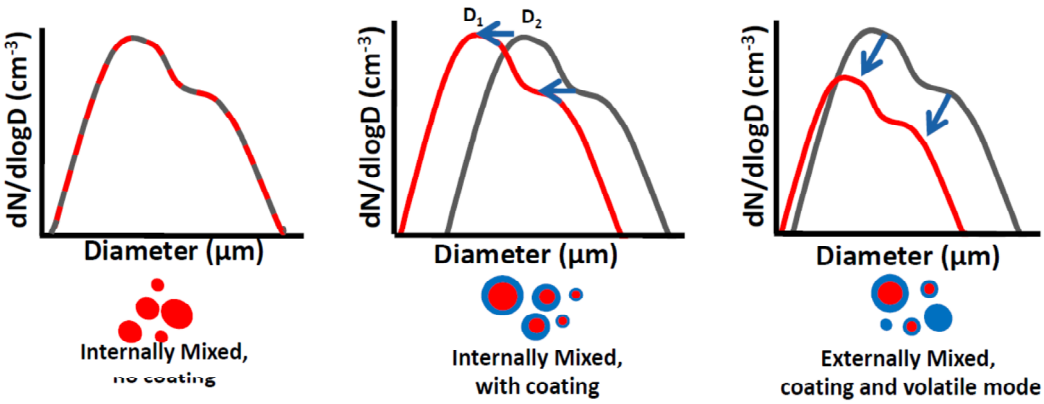

Figure 3.7 The effect of increasing temperature on internally mixed aerosol; change in the aerosol particle number concentrations versus the size range of the distribution. Figure adapted from Weinzierl et al. (2009).

3.1.8 Chemistry Instrumentation: Ozone and Carbon Monoxide

Ozone measurements on the BAe-146 use a commercial gas analyser manufactured by Thermo Scientific; TE49C UV Photometric Ozone Analyser. Ozone measurements use the Beer-Lambert law to relate UV absorption of Ozone at 254 nm directly to the concentration of Ozone in the sample air (Nedelec et al., 2003).

Carbon monoxide measurements on the BAe-146 use a commercial gas analyser manufactured by Aerolaser GmbH; AL 5002 VUV Fast Fluorescence CO Analyser. Ozone measurements use the technique of fluorescence of CO when exposed to UV light at a wavelength of 150 nm, which is proportional to the concentration of CO (Gerbig et al., 1999).

3.2 Technological Developments in Instrumentation

Significant technological advances in instrumentation, relevant to Saharan mineral dust measurements, have occurred since previous campaigns such as SHADE, DODO, DABEX and GERBILS. The use of a newly installed nadir facing Leosphere LIDAR is a vital instrument for remote sensing of the vertical profile of clouds and Saharan mineral dust. Understanding the vertical profiles of mineral dust with respect to cloud height is important for calculating the radiative forcing.

Johnson and Osborne (2011) discuss the potential for under-estimating absorption measurements during GERBILS and DABEX, owing to losses of the coarse mode mineral dust in the sampling inlet and into the absorption instrument. The Fennec campaign saw advances in aerosol sampling characterisation and coarse mode aerosol, which coincided with the installation of the Low Turbulence Inlet (LTI). The LTI is a characterised inlet capable of delivering coarse mode aerosol into the cabin which is achieved by reducing turbulence flow within the tip of the inlet, reducing impaction of particles to the walls of the inlet. Further details on the LTI can be found in chapter 4.

During the SHADE campaign the Fast Forward Scattering Spectrometer Probe (FFSSP) did not functioning correctly for the duration of the campaign and as such size distribution were limited to 3.2 μm. Subsequent campaigns including DABEX and DODO were additionally limited by only using the PCASP to measure mineral dust size distributions. Osborne et al. (2008) was able to compare AERONET retrievals with

aircraft *in-situ* measurements during DABEX that took place in the vicinity of AERONET sites to provide a measure of the coarse mode of the mineral dust encountered. During the GERBILS campaign, the Small Ice Detector (SID-2) probe was deployed to measure coarse mode particles (nominally 2– 60 μm diameter).

Considerable instrument investment in terms of sizing instruments was used during Fennec making measurements in the range of 0.1 – 930 μm, and the strength in the measurements of aerosol size distribution during Fennec is derived from the number of instruments deployed. The Passive Cavity Aerosol Spectrometer Probe (PCASP) measured across the accumulation mode, Grimm Sky-OPC measured the accumulation and lower coarse mode whilst the upper coarse mode was measured using the Cloud Droplet Probe (CDP), Cloud and Aerosol Spectrometer (CAS), Cloud Imaging Probe (*CIP*) and Small Ice Detector (SID-2). These instruments are primarily used as cloud physics instrumentation, but have been used in aerosol measurements.

Significant technological advances in instrumentation, relevant to biomass burning measurements, have occurred since previous campaigns such as SCAR-B, Southern AFricA Regional science Initiative (SAFARI-2000) and DABEX. The use of the Leosphere LIDAR is a vital instrument for remote sensing of the vertical profile of clouds and biomass burning aerosol over large regional areas of Amazonia. Understanding the vertical profiles of absorbing aerosols with respect to cloud height is important for calculating the radiative forcing for both the direct and indirect effects.

The Quadrupole-AMS (Q-AMS) has been upgraded to a ToF-AMS enabling single particle analysis with a detection limit of 0.002 $\mu g\ m^{-3}$ compared with 0.01 $\mu g\ m^{-3}$ and an improved mass range of 1 – 1000 m/z compared with 1 – 300 m/z for the Q-AMS. These upgraded properties mean that detailed organic composition can be measured which is necessary for understanding the optical properties of biomass burning, along with an understanding of how the organic component evolves as the biomass aerosol ages. The availability of the SP2 aboard the BAe-146 enables measurements of BC number and mass concentration and number and size distributions dN/dlogD and dM/dlogD, and detailed single particle analysis of the coatings thickness of biomass burning. These are essential measurements for understanding the aging of biomass burning aerosols.

3.3 Data Processing, Quality Control and Methods

Quality control and processing of the Low Turbulence Inlet and Fennec Grimm data, as laid out in chapter 4, were corrected by the author; corrections for the Grimm sub-sampler were corrected by J. Trembath, FAAM. Corrections for the refractive index of mineral dust were assessed by C. Ryder, University of Reading. Quality control and processing of the VACC data from the SAMBBA campaign was performed solely by the author. Quality control and processing of the SAMBBA Grimm data was performed by J. Trembath, FAAM. The calibrations of the OPCs presented in section 3.3.1 were performed as part of a multi-instrument calibration between FAAM, Met Office, University of Leeds and University of Manchester. The VACC OPC calibration analysis and instrument comparison in section 3.3.1.1 was performed solely by the author. Core meteorological measurements and core cloud measurements were processed by colleagues at FAAM. Measurements from the AMS and SP2 were processed by colleagues at the University of Manchester.

3.3.1 OPC Calibration Procedures

The relationship between particle scattering and particle size is determined through calibration. Calibration is carried out prior to and post a field campaign typically after a change in the instrument such as cleaning of the instrument optical cavity and re-alignment of the laser. The calibration procedures applied are adapted from that of Rosenberg et al. (2012). An overview of the core instrument (PCASP and CDP) calibrations for Fennec and SAMBBA campaigns are given in table 18 and table 19, respectively.

Table 18 Core instrument calibrations for the Fennec campaign.

Instrument	Date of Calibration (2011)	Flight Calibration
PCASP	24 May	Pre-campaign
CDP	17 June	B600, B601, B602
CDP	20 June	B604
CDP	21 June	B605, B606
CDP	24 June	B609
CDP	25 June	B610, B611
CDP	26 June	B612, B613

Table 19 Core instrument calibrations for the SAMBBA campaign.

Instrument	Date of Calibration (2012)	Flight Calibration
PCASP	21 August	Pre-campaign
PCASP	18 October	Post-campaign
CDP	15 September	B732
CDP	3 October	B750

The CDP is calibrated with water droplets (m = 1.33 + 0.000i) of known size and glass beads to account for instrument sample area and droplet size using the procedure developed by Lance et al. (2010) and Rosenberg et al. (2012).

A multi-instrument calibration was carried out at the laboratory facilities at FAAM prior to the SAMBBA field campaign on 21 August 2012 and post SAMBBA on 18 October 2012. The multi-instrument calibration (table 20) involved FAAM wing-mounted PCASP's PCASP1 and PCASP2, the Met Office CVI PCASP and University of Leeds, PCASP-X., FAAM Grimm Sky-OPCs. Instrument optical cavities were cleaned and realigned prior to the calibration procedure and laser reference voltage monitored during the calibration procedure and during the SAMBBA campaign.

Table 20 Instruments involved in SAMBBA multi-instrument calibration.

Instrument	Research Group	Model Number
PCASP1	FAAM	SPP-200
PCASP2	FAAM	SPP-200
PCASP	Met Office, CVI	SPP-200
PCASP-X	University of Leeds, VACC	SPP-100X
Grimm Sky OPC 1.129	FAAM	29G11005
Grimm Sky OPC 1.129	FAAM	29G10011

The Grimm Sky-OPC is run at the manufactures recommendation, with bin boundaries consistent with Grimm calibration. The manufacture does not make information available to the user. Grimm OPC units are calibrated from a 'master' unit from which all other units are calibrated. The initial calibration is based on Polystyrene Latex Spheres (PSLs) with all secondary calibrations based on a dolomite dust, the sub units

are then tuned so threshold tables are comparable with the master unit (J. Trembath, personal communication).

Table 21 Calibration materials corresponding to instrument gain stage and size.

Gain Stage	Sizes	Material	Experimental Set-up
Low	0.269 – 3.0 μm	PSL	Figure 3.8
Medium	0.160 – 0.340 μm	DEHS	Figure 3.9
High	0.110 – 0.160 μm	DEHS	Figure 3.9

PSLs of a know diameter and standard deviation (supplied by Duke Scientific Corporation) were used to calibrate the lower gain stage of the PCASP, with PSLs covering the sizing range of 0.269 μm – 3.002 μm. PSLs have a known refractive index of m = 1.59 - 0.000i. Several drops of PSLs of known sizes are diluted in deionised water, with filtered air of a known flow rate passed into a nebuliser cup PSLs producing a fine mist of nebulised particles. Nebuliser cup used was an Allied Healthcare Aeromist model SA-BF61403 (Rosenberg et al., 2012). Airflow passes through a diffusion dryer and drawn into a mixing volume, from which multiple instruments sample.

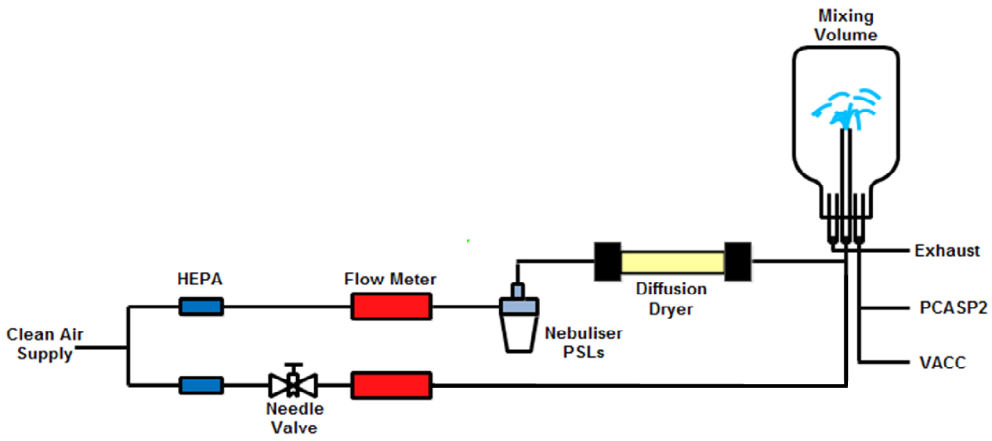

Figure 3.8 Experimental set-up for PSL calibration for multi-instrument calibration. Direction of airflow is from the left to the right of the figure.

The standard procedure for calibrating the mid- and high gain stages of the PCASP (figure 3.9) uses the chemical DEHS (di(2-ethylhexyl)sebacate), an oil with a known refractive index of m = 1.45 - 0.000i, and produces spherical particles when nebulised.

Particles are sized using a TSI model 3080 DMA with a 0.44 m column used to select narrow size distribution which is achieved by varying the sheath flow between 5.8 and 10 L min^{-1}. Sample flow is drawn through the DMA using the combined sample flows of the PCASPs.

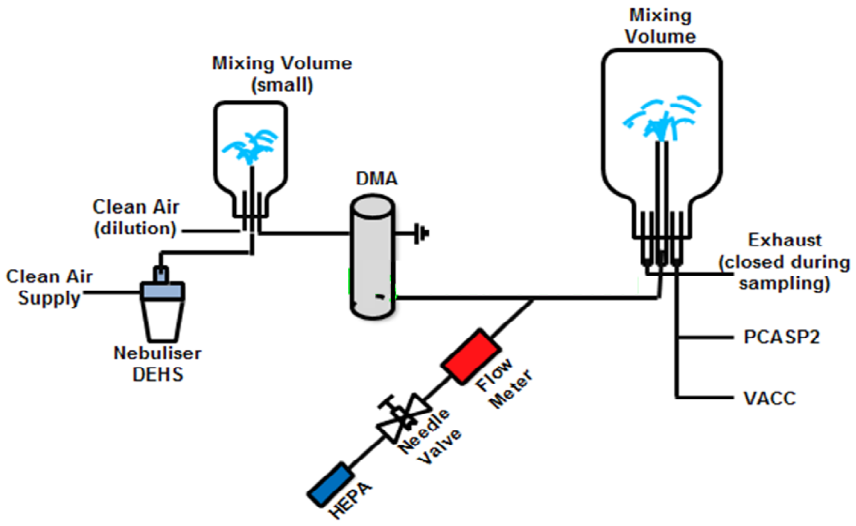

Figure 3.9 Experimental set-up for DEHS calibration for multi-instrument calibration. Direction of airflow is from the left to the right of the figure.

Figure 3.10 i) PSL calibration set-up and ii) DEHS calibration set-up

A PCASP has an approximate beam sample volume of 7 x 10^{-6} cm^3, and as such if the concentration exceed 1 x 10^5 cm^3, the probability of coincidence effects are high with multiple particles passing the beam at the same time (Petzold et al., 2013). The calibration procedure was designed to maintain low concentrations across the size distribution to prevent co-incidence effects being encountered in the calibrations.

The VACC PCASP operates with SPP-100X electronics, and as such it is not possible to record the pulse heights associated with each particle or with the bin boundaries, as the pulse height measurements and binning are performed using analogue electronics. Calibration procedure applied used the scanning method from Rosenberg et al. (2012); as the diameter of particles from the DMA is increased, and the particle distribution moves to higher bins on the PCASP. The diameter where the fraction of the distribution crosses from bin *n* to bin *n* + 1 is used to determine the bin boundary, as presented in figure 3.11. Calibrating with DEHS in high resolution (increasing particle diameter by 0.005 – 0.010 μm) using the DMA, enables to position of the bin boundaries to be determined with good accuracy. Figure 3.12 shows the calibrated diameter comparison using DEHS scanning method for three calibration dates.

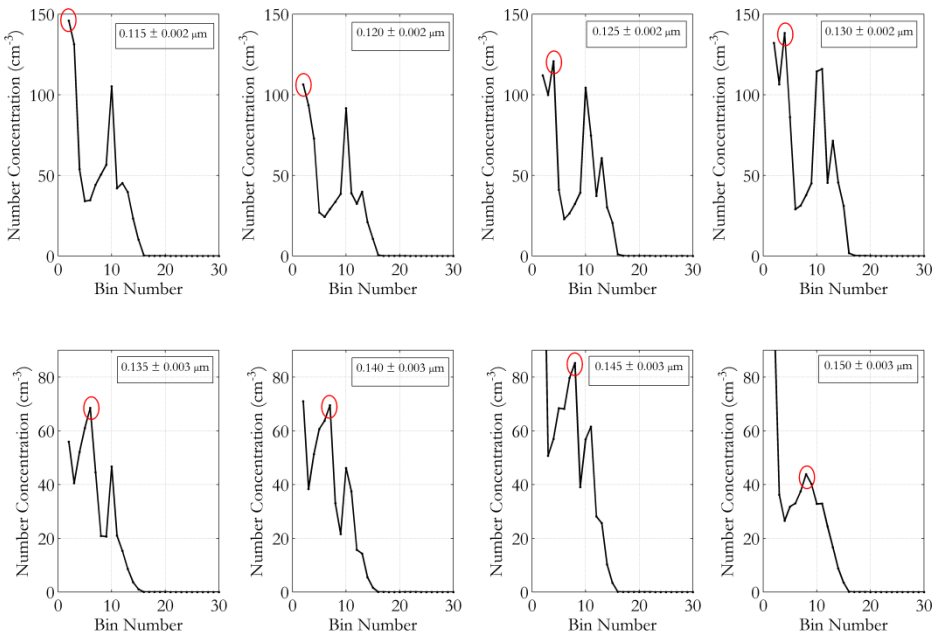

Figure 3.11 Scanning calibration method for the PCASP high gain stage; number concentration vs bin number for increasing particle size of DEHS oil (*red circle*) Singlet peak.

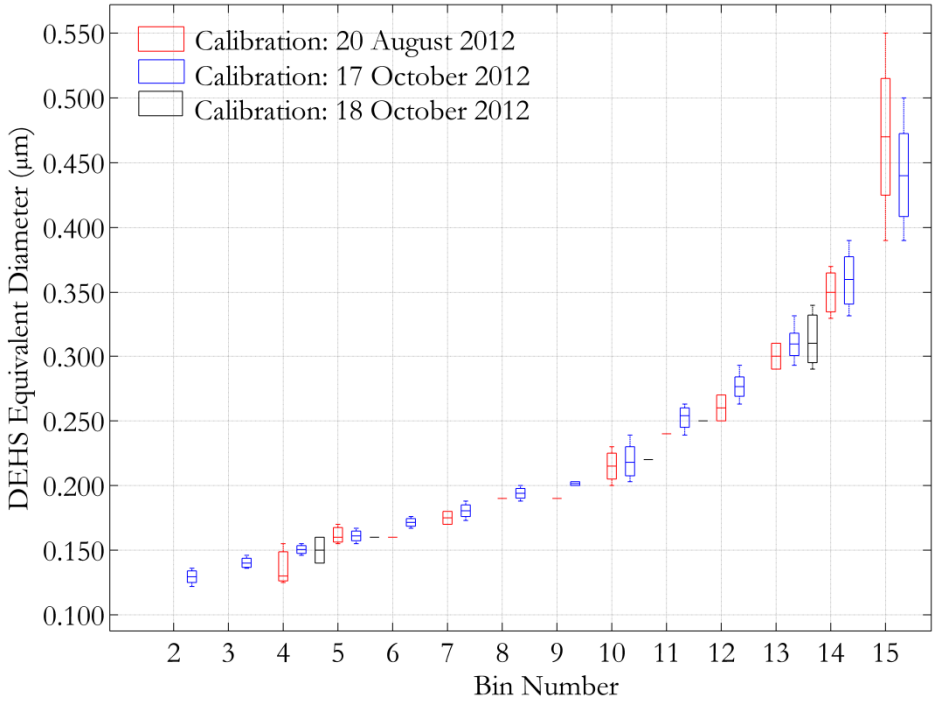

Figure 3.12 Calibrated diameter comparison using DEHS scanning method.

3.3.1.1 OPC Calibration Comparison

The following discussion provides a comparison of the sizing and counting efficiency between the FAAM PCASP2 (from now referred to simply as PCASP) and the University of Leeds VACC PCASP. A comparison in total number concentration between the PCASP and VACC for DEHS between 0.110 μm to 0.170 μm in 0.005 μm size steps is presented in figure 3.13. The PCASP uses the high gain stage threshold table up to 0.155 μm and the mid gain threshold table A for particle sizes greater than 0.160 μm. Figure 3.13 shows that there is a reasonable agreement in total number concentration between the two instruments during the laboratory calibration. Deviations in the observed concentrations, such as those at 0.125 μm, are largely an artefact of the experimental set-up with difficulty maintaining consistent flow rates from the mixing volume to the instruments.

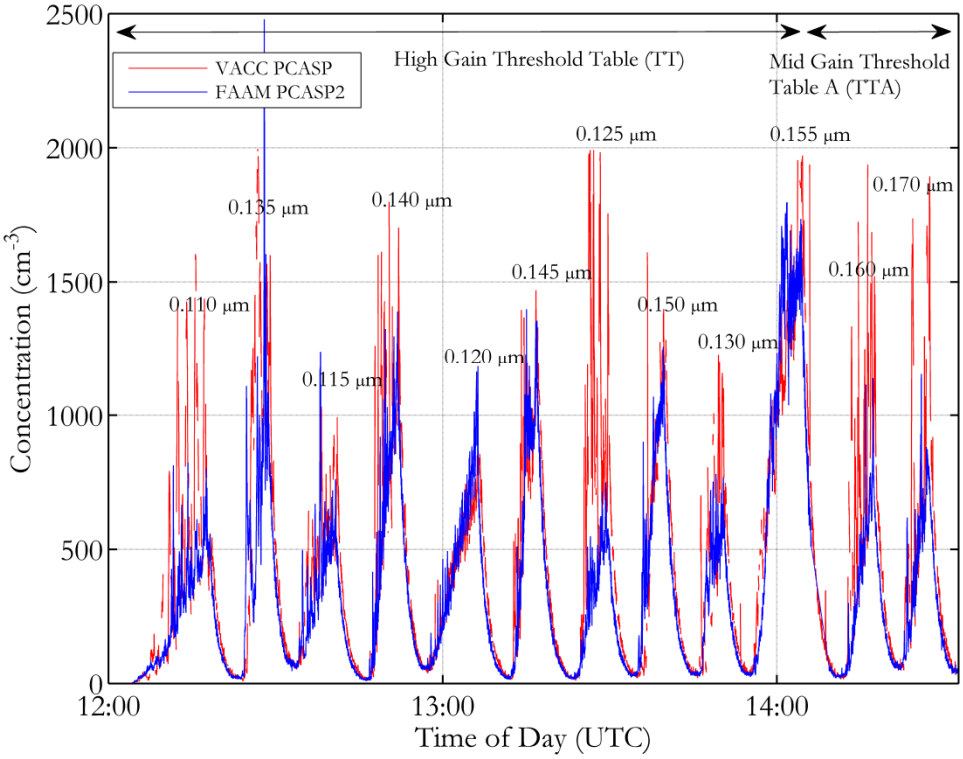

Figure 3.13 Number concentration comparison between (*blue*) FAAM PCASP and (*red*) VACC for DEHS between 0.110 and 0.170 µm, spanning the PCASP high gain stage threshold table and mid gain threshold table A.

Number concentration comparison is presented between PCASP and VACC for PSL beads between 0.350 µm and 0.903 µm in figure 3.14. It is worth noting the PCASP operated using Low Gain Threshold Table A and as such show truncation of the size distribution at 0.27 µm and 0.93 µm. A broad agreement in the mode up to 0.453 µm PSL is evident, whilst beyond this size the VACC PCASP measurements do not show a clear mode. The upper limit of the calibrated bin diameters equates to bin 15 of the VACC PCASP, which is the result of a fault in the amplifier between the medium and low gain stage; as such as an electronic pulse saturates the medium gain stage it does not pass to the low gain stage and is therefore not detected.

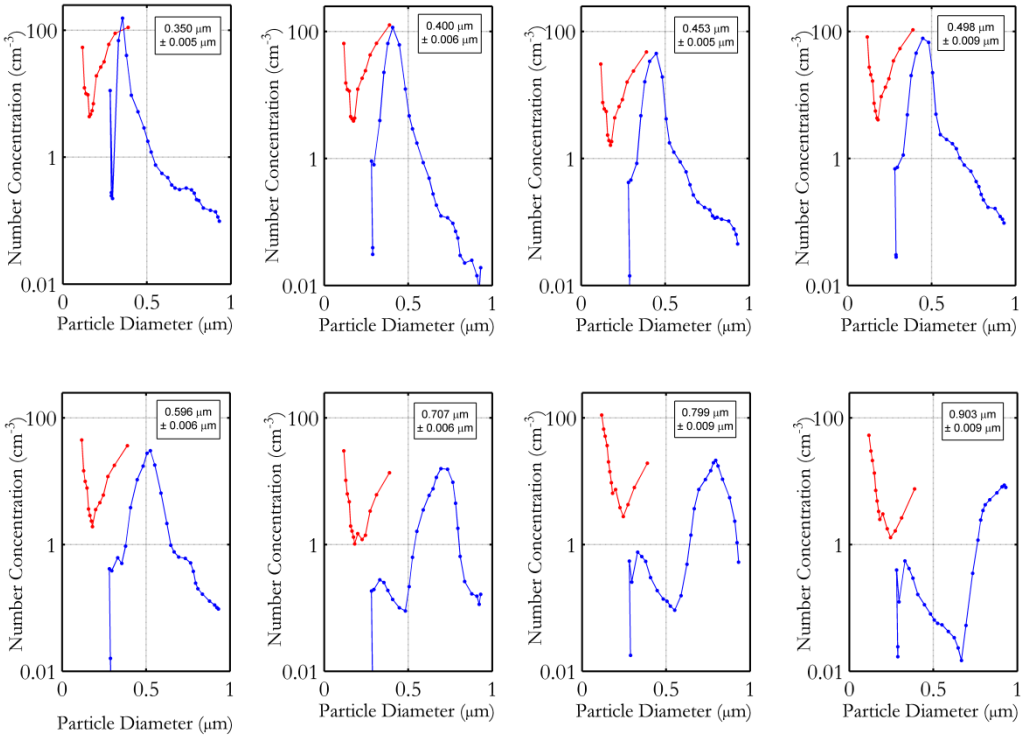

Figure 3.14 Number concentration comparison between (*blue*) PCASP low gain threshold table A, and (*red*) VACC for PSL beads between 0.350 and 0.903 µm. N.B. the prominent peak in the lowest size bins is associated with the surfactant mode associated with PSLs, that is, nebulised PSLs are bimodal.

3.3.1.2 VACC Sheath and Sample Flow Calibration

A rotameter is a device that measures the flow rate of liquid or gas in a closed system. The PCASP-X airflow system prevents particles in the sample flow from contaminating critical optical components. This is accomplished using a filtered sheath flow which aerodynamically focuses the aerosol sample through a jet, directing the sample aerosol directly through the laser beam.

The VACC PCASP sample and sheath internal flow rate sensors were calibrated using a TSI 4140 mass flow meter prior to the SAMBBA campaign. The manufacture recommend a 15:1 sheath flow to sample flow ratio, allowing for an isokinetic match in flows, designed to reduce turbulence within the sample inlet. The standard operation of sample flow was 0.06 - 0.18 L min^{-1} (1 – 3 cm^{-3} s^{-1}) and a sheath flow of 0.90 L min^{-1} (15 cm^{-3} s^{-1}). The calibrated sheath and sample flows are shown in figure 3.15, highlighting of sample flow rates measured by both the internal flow meter and the TSI flow meter

show good consistency across the sample flow rate range. The measured sheath flows show a similar consistency across the lower flow rates, but a divergence in measured flows was observed at flows rates greater than 0.70 L min^{-1}. This offset coincides with the operational sheath flow rate of the PCASP. This offset was noted and a correction applied when setting the desired sheath flow rate.

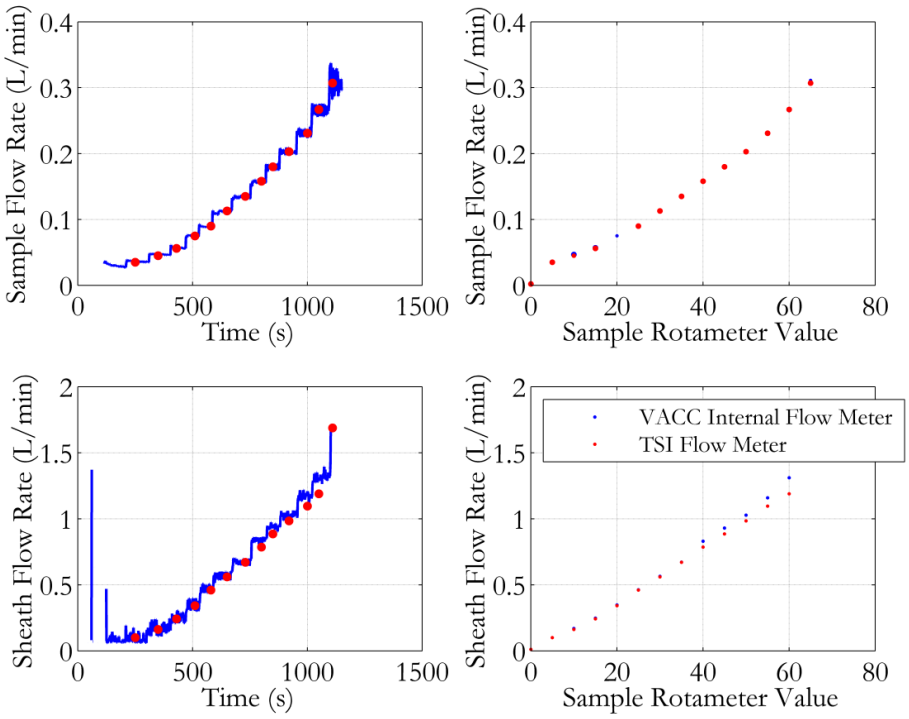

Figure 3.15 (*left*) Time series of sequential increases in (*top*) sample flow rate and (*bottom*) sheath flow rate measured by the VACC PCASP internal flow meter, overlaid red dots a 10 second average from the TSI mass flow meter and (*right*) averaged sample flow rate for VACC PCASP internal flow meter and TSI mass flow meter.

3.3.2 Refractive Index Corrections to Size Distributions

OPCs measure optical diameter based on a reference to a calibration from a purely scattering particle, whilst in reality atmospheric aerosol measured by the OPCs has a complex refractive index which is strongly influenced by composition. A correction procedure applied here for aerosol refractive index are consistent with those outlined in Rosenberg et al. (2012). *MieConScat* generates particle scattering cross sections using Mie-Lorenz theory for a desired refractive index and for a specific OPC provided details of instrument optical angular range and wavelength. *CStoDConverter* uses OPC bin

boundaries defined in terms of scattering cross sections and generates new bin centres and widths in terms of diameter for a required refractive index.

Theoretical Mie scattering curves for PSL spheres with a refractive index of m = 1.59 – 0.000i, for three instruments the PCASP, Grimm and CDP is presented in figure 3.16. The figure highlights the irregularities between a particles scattering cross section and particle diameter, as well as the differences in the theoretical Mie responses as a function of instrument design. The PCASP and Grimm have wide angle collection optics which increases the total amount of scattered light collected by the photo sensor which increases the signal to noise ratio. This also increases the minimum particle size which the instrument can detect. The Grimm and PCASP have a relatively smooth Mie curve except for the region between 2 - 4 μm, where oscillations in the Mie region remain.

The positive effect of the side scattering/wide angle collection optics becomes evident when a comparison with a forward scattering instrument such as the CDP which show large deviations in scattering cross section as a function of particle size. Mean cloud droplet diameter is typically 10 – 15 μm with maximum diameters less than 50 μm, where the CDP response curve shows smaller ambiguities. As such the relative errors associated with the CDP are relatively small for cloud droplets diameter larger than 7 μm. With the increasing use of the CDP in measuring aerosol particle size, these ambiguities must be acknowledged and correspondingly characterise the errors associated in the sizing.

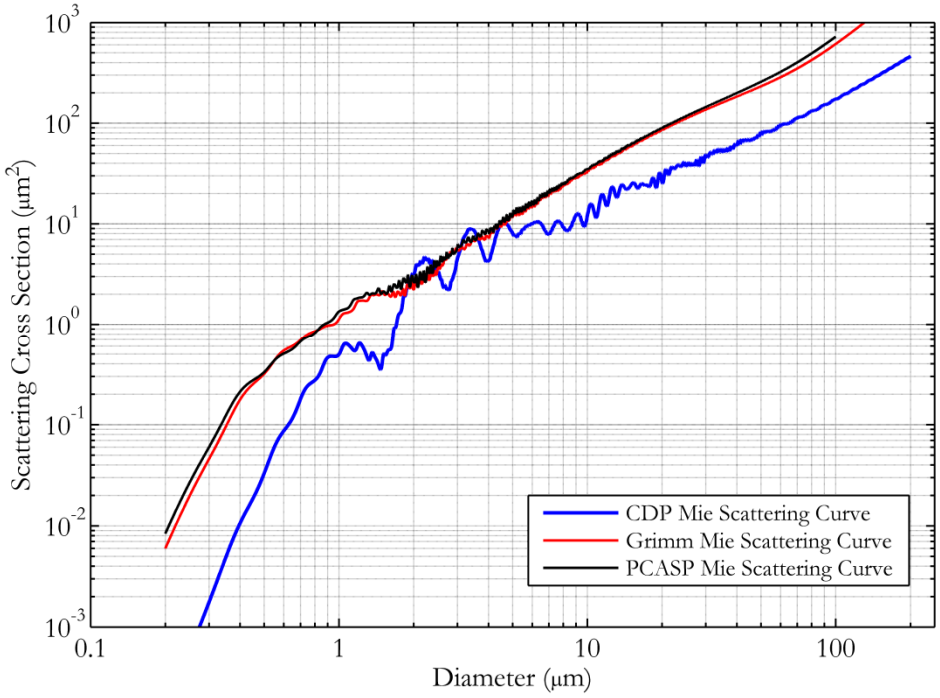

Figure 3.16 Theoretical Mie scattering response curves for the PCASP, Grimm and CDP.

Standard calibrations for the PCASP produce cross section bin boundaries for a PSL reference material (m = 1.59 – 0.000i), and CDP cross section bin boundaries are produced for a water reference material (m = 1.33 – 0.000i). The Grimm instrument is limited to knowledge of fixed diameter bin boundaries as supplied by the manufacture, and the VACC PCASP operates with SPP-100X electronics, and the scanning calibration procedure produces fixed diameter bin boundaries.

For both instruments a roundabout method is applied for determining scattering cross section bin boundaries, used for performing the refractive index corrections. The example below reflects Mie corrections as applied to the Grimm instrument for results presented in chapter 3, the same correction procedure has been applied to the VACC PCASP for results presented in chapter 5.

3.3.2.1 Refractive Index Corrections for Mineral Dust

MieConScat generates scattering response tables using Mie-Lorenz theory specific to the Grimm instrument specifications; i) laser wavelength (0.655 μm) ii) primary angular

range (30 – 150°) and iii) secondary angular range (81 – 99°). In the first instance, the Mie scattering response curve for the calibration material (figure 3.17) is produced. In the figure, each of the red dashed line represents the diameter bin boundaries supplied from the manufacture, by correlating particle diameter and scattering cross section, the corresponding Grimm upper and lower scattering cross sections can be inferred. In the second instance, the Mie scattering response table (figure 3.18) is generated for a mineral dust refractive index of m = 1.53 – 0.001i (Ryder et al. 2013b), with the dashed red lines representing the Grimm equivalent scattering cross sections used for determining new bin diameters for mineral dust.

The *CStoDConverter* program uses the Grimm bin boundaries defined in terms of scattering cross sections and generates scaled-up particle cross sections, calculating new OPC bin centres and bin widths in terms of diameter, corresponding to the new refractive index. The relative change in bin boundaries is evident with changes in refractive index, with largest particles experiencing the largest scale-up factor (figure 3.19).

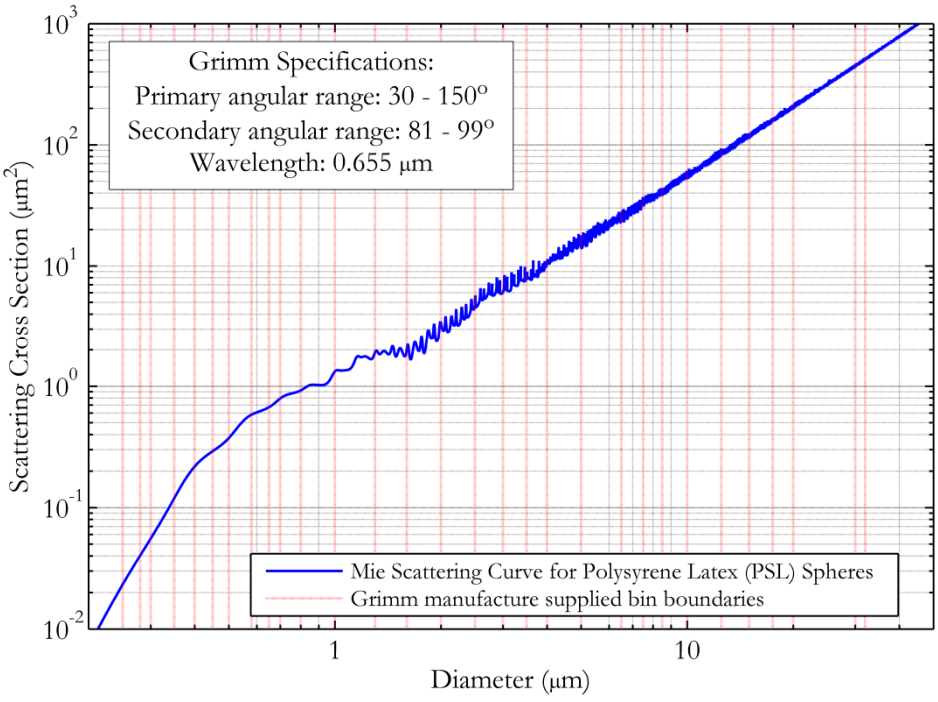

Figure 3.17 PSL spheres (m = 1.59 – 0.000i) theoretical Mie scattering response curve for the Grimm. *Dashed red lines* represent the bin boundaries supplied by the manufacture for determining equivalent scattering cross sections.

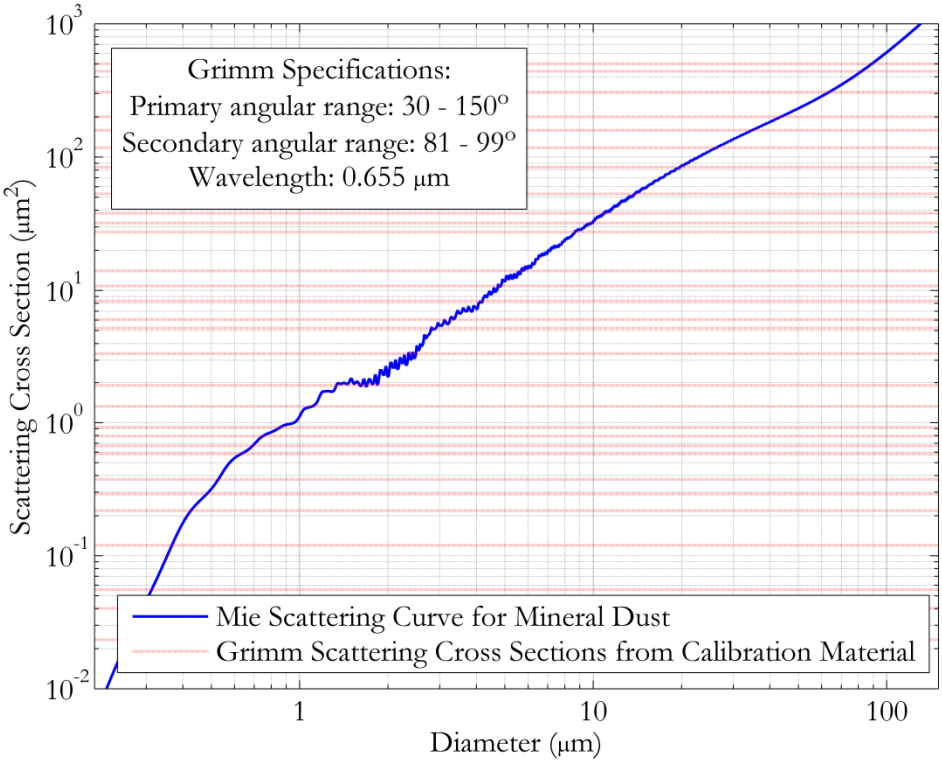

Figure 3.18 Mineral dust (m = 1.53 – 0.001i) theoretical Mie scattering response curve for the Grimm. *Dashed red lines* represent the Grimm equivalent scattering cross sections used for determining new bin diameters for mineral dust.

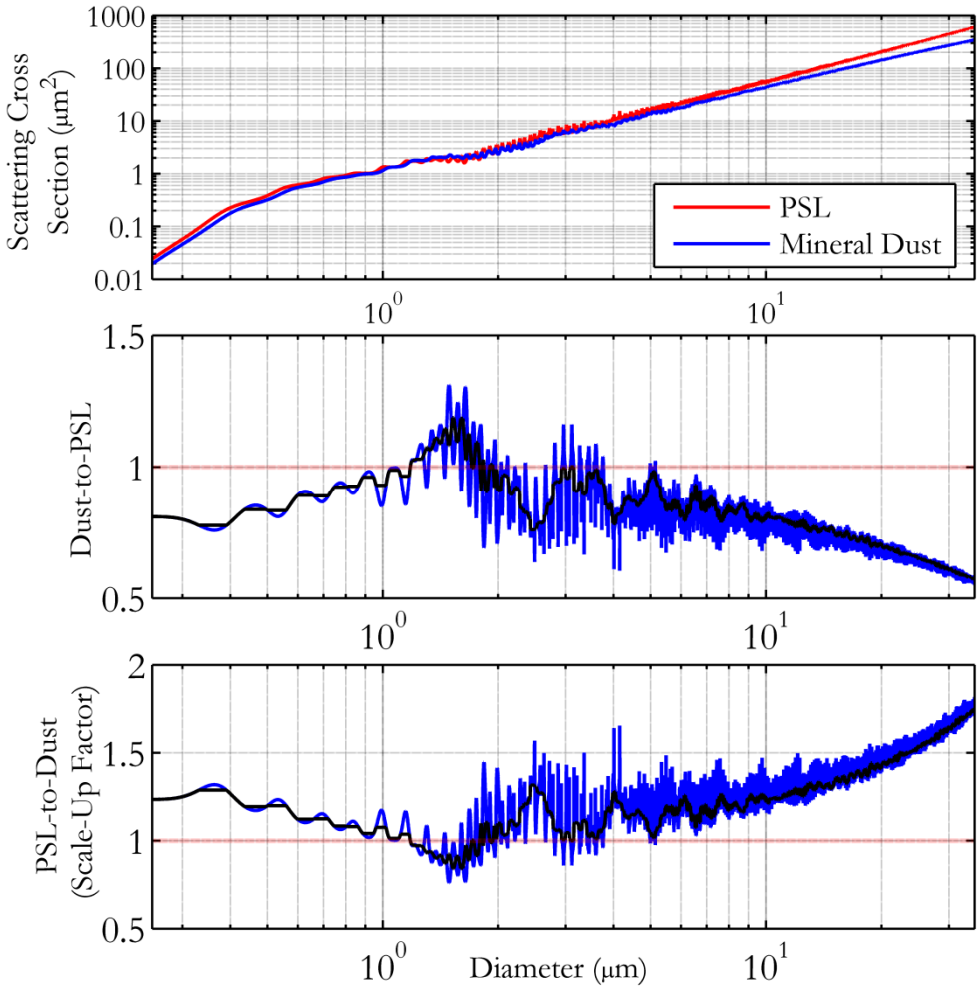

Figure 3.19 (*top*) Theoretical Mie scattering response curves for the Grimm for PSLs (m = 1.59 – 0.000i) and mineral dust (m = 1.53 – 0.001i), (*middle*) mineral dust-to-PSL diameter and (b*ottom*) scale up factor for PSL-to-mineral dust diameter. *Blue line* reflects the true fluctuations between the Mie response curves, *black line* smoothed Mie response.

3.3.3 Size Distribution Fitting Functions

As a method of simplifying an aerosol size distribution four lognormal modes can be fitted across a size distribution which represents the nucleation, Aitken, accumulation and coarse mode of an aerosol. The lognormal distribution are be fitted in which the full size distribution is represented by the combination of the geometric mean diameter, geometric standard deviation and total concentration of the individual lognormal

modes. The initial four lognormal mode fitting parameters are presented in table 22, with the fitting algorithm was adapted from Brito et al. (2014).

Table 22 Four mode aerosol size distribution lognormal fitting parameters. N_{tot} is the total number concentration in the respective mode (cm^3), σ_g is the geometric standard deviation of the mode and *CMD* is the count median diameter of mode (μm).

	Nucleation			Aitken			Accumulation			Coarse		
	N_{tot}	σ_g	CMD	N_{tot}	σ_g	CMD	N_{tot}	σ_g	CMD	N_{tot}	σ_g	CMD
Starting	0	1.1	0.002	0	1.5	0.050	0	1.5	0.100	0	1.5	1.00
Lower-bounds	0	1.1	0.001	0	1.1	0.010	0	1.1	0.100	0	1.1	1.00
Upper-bounds	10^5	1.5	0.010	10^5	2.5	0.100	10^5	2.5	1.000	10^5	2.5	9.00

3.4 Chapter Conclusion

The focus of this chapter was to present a discussion of the instrumentation and techniques applied in making atmospheric observations. An overview of key measurements aboard the research aircraft is presented that are relevant to the results presented in chapters 4 to 6, and the technological advances in instrumentation relevant to both the Fennec and SAMBBA campaigns are detailed. Details and results of a multi-instrument calibration for the SAMBBA field campaign are presented; incorporating a comparison of the sizing and counting efficiency between the FAAM PCASP and the University of Leeds VACC PCASP. A correction procedure is discussed to account for aerosol refractive index with theoretical Mie scattering curves for the OPC instruments presented.

4 Inlet Comparisons

Aerosol measurements require representative sampling in order to obtain an aerosol sample from the ambient free air, however processes that will be discussed within this chapter act on a sampling process so that measured aerosol number/mass concentrations deviate from that in the ambient free stream. Aerosol inlets are designed with the purpose of delivering a representative aerosol sample to the instruments making the measurements. Inlet design can modify aerosol size distribution through either underestimating due to aerosol losses or overestimation due to enhancements.

The literature discussed in section 4.1 of this chapter will show it is not possible to fully design a perfect inlet. The characterisation and quantification of these effects still remain highly uncertain on the BAe-146. As such it is necessary to characterise the performance of complete sampling system, and account for where particle losses occur, to allow corrections to be applied for measurements made on a particular sampling system.

On the FAAM BAe-146 aircraft, the primary aerosol inlets are modified Rosemount 102E housings, introduced in section 4.2 of this chapter, although it has previously been acknowledged of the inherent difficulties in gaining a representative aerosol sample through these inlets. Haywood et al. (2003b) suggested that Rosemount inlet collection efficiency drops from close to unity to zero for particle radii greater than 1 - 2 μm, whilst more recent papers by Johnson et al. (2008) and Johnson and Osborne (2011) omit performing a correction due to the Rosemount inlet, though acknowledged it was potentially a significant source of uncertainty in aerosol measurements.

A critical evaluation of the current aerosol sampling is a limitation aboard the BAe-146 aircraft. Recent advances in sample characterisation have coincided with the installation of the Low Turbulence Inlet (LTI), introduced in section 4.3 of this chapter, which has provided a platform for performing inlet comparison experiments with the aircraft Rosemount inlets. Through understanding Rosemount inlet efficiencies it is possible for

aircraft users to apply corrections to measurements made at an instrument to account for the aerosol sampling system. The LTI was designed to maximise low turbulence and laminar flow during aerosol sampling, and is a fully characterised system (Wilson et al., 2004).

This chapter aims to answer the first question posed at the start of this thesis; how well is the coarse mode of mineral dust presently measured from an aircraft platform on the FAAM BAe-146 and what influence do the current Rosemount inlets have on the sampling of coarse mode aerosol and on aerosol microphysical properties? An assessment of the LTI performance during the Fennec campaign, presented in section 4.4, will draw on the theories and equations presented within the sampling review in section 4.1. Section 4.5 will compare the size distribution measured at the LTI to those measured by the external wing-mounted probes; the PCASP and the CDP. This experiment draws on the ability to measure the ambient distribution with instruments which themselves do not sample from an inlet.

4.1 Inlet Sampling

Instruments require the deceleration of an air sample from the aircraft speed to only several metres per second. This process can lead to the development of a highly turbulent flow inside the tip of the inlet and causes a loss of the largest particles due to impaction with the inlet walls (Baumgardner and Huebert, 1993; Hermann et al., 2001).

Changes to aerosol particle size through the loss of volatile species when sampling are an important consideration, related to the dynamic heating of the sample airstream during the deceleration of air in the inlet (Sheridan and Norton, 1998). Measurements of relative humidity along the sampling line are crucial to understanding these effects. Porter et al. (1992) studied the effects of particle drying on aerosol size distribution and transmission losses; Baumgardner and Huebert (1993) suggest dynamical heating effects in the range 5 – 20 ^{o}C.

Aerosol inlets are a crucial method of achieving a representative aerosol sample and delivering it to the instruments making the measurements. The positioning of aircraft inlets is vital in gaining a representative sample which receives minimal influence due to flow distortion around the aircraft. The design and positioning of aircraft inlets are identified using computational fluid dynamic based flow analysis, particle trajectory

simulations and wind tunnel measurements (Wilson et al., 2004). Baumgardner and Huebert (1993) discussed the need for complimenting these tests with in flight observations, where it is possible to study the effects of the aircraft in terms of changes in aircraft pitch and atmospheric turbulence**.**

The *aspiration efficiency,* E_a, refers to the ratio of particle concentration at the inlet entrance to the concentration in the ambient free stream (Belyaev and Levin, 1972, 1974).

$$E_a = \frac{C}{C_0} = \frac{U_0}{U}\left(\frac{\phi}{d}\right)^2 \tag{4.1}$$

where C is the concentration of particles entering the inlet, C_0 is the concentration of particles in the ambient stream, d is the inner diameter of the inlet, ϕ is the diameter of limiting particle trajectory, U_0 is the ambient gas flow velocity and U is the inlet sample flow velocity.

The *Mach number* is the ratio of the velocity of an object moving through a medium, such as air, to the speed of sound, c, through that medium (Huschke, 1959).

$$Ma = U_0/c \tag{4.2}$$

Streamline geometry through aerosol inlets influence the size distribution, with convergence and divergence of streamlines leading to the loss or enhancement of aerosol concentrations. Aerosol streamlines which do not deviate inside the inlet are *isokinetic*, deviations from the streamline can be described as being *anisokinetic*; being either *sub-isokinetic* or *super-isokinetic*, with examples of these sampling geometries presented below.

Isokinetic ($U = U_0$) streamlines originate when sample flow velocity (U) through the inlet is equal to the ambient gas flow velocity (U_0) generating a laminar flow in the ambient free stream (figure 4.1). For conditions to be truly isokinetic, sampling must also be i*soaxial;* where the ambient gas flow and inlet sample flow are parallel (Fuchs, 1975). Deviations from this result in a non-zero angle between the inlet sampling flow velocity and the ambient gas flow velocity, and are termed *anisoaxial* sampling (figure 4.4).

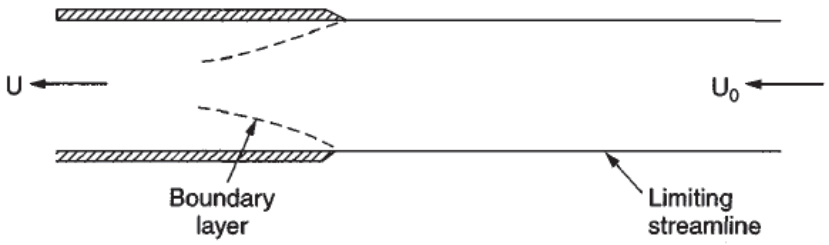

Figure 4.1 Isokinetic streamlines. Reproduced from Baron and Willeke (2001).

Sub-isokinetic ($U < U_0$) streamlines originate when sampling velocity through the inlet is lower than the gas flow velocity (figure 4.2). Streamlines diverge from the ambient free-stream flow into the nozzle.

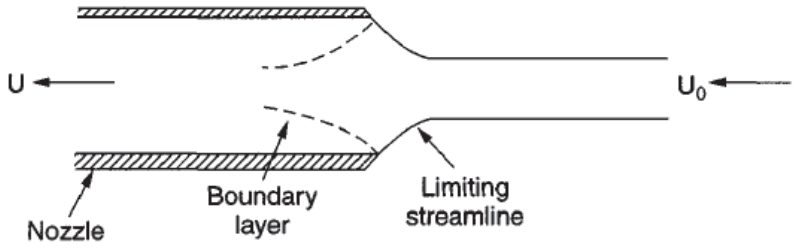

Figure 4.2 Sub-isokinetic streamlines. Reproduced from Baron and Willeke (2001).

Super-isokinetic ($U > U_0$) streamlines originate when sampling velocity through the inlet is higher than in the gas velocity (figure 4.3). Streamlines converge from the ambient free-stream flow into the nozzle. This convergence forms a point known as the vena contracta (where the stream diameter is at a minimum, and air velocity is at a maximum), which sets up secondary flows of a turbulent nature, which leads to particle losses through impaction with the walls of the inlet (Hangal and Willeke, 1990).

The ideal aerosol inlet is often discussed as being isokinetic, however Fahey et al. (1989) demonstrated the practicalities of using inlets which diverge from isokinetic behaviour. Fahey et al. (1989) used a sub-isokinetic inlet taking advantage of the enhancement of large particles in enabling study of the composition of Antarctic polar stratospheric clouds. Concentrations of aerosol particles were calculated to increase by a factor of 9, generating an enhanced sensitivity for NO_y species identified within the aerosol phase.

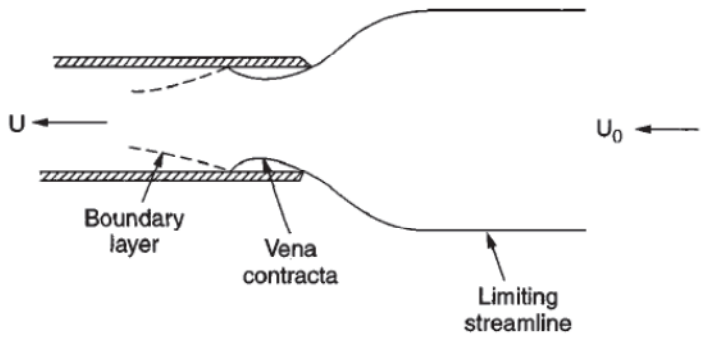

Figure 4.3 Super-isokinetic streamlines. Reproduced from Baron and Willeke (2001).

Anisoaxial sampling refers to a non-zero angle between the ambient gas flow and inlet sample flow. This is characteristic of diverging streamlines with θ representing the angle between the direction of sampling velocity through an inlet and the ambient gas flow (figure 4.4). Isoaxial sampling is generated by aligning the inlet with the aircraft streamlines; however as the aircraft pitch changes throughout the atmosphere such flow angles also change. Durham and Lundgren (1980) studied the aspiration efficiency by performing analysis of material deposited on the inner wall of the inlet; finding as much as 60 % of total particulate matter had impacted and was lost to the inlet walls.

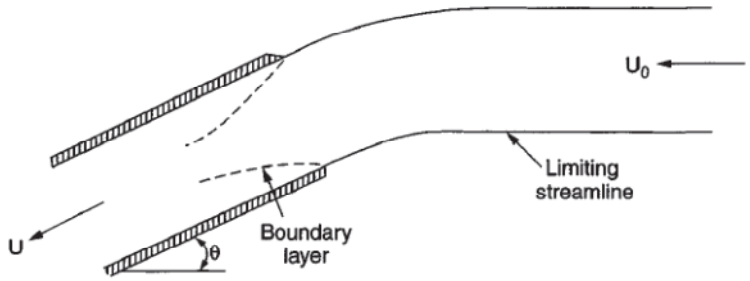

Figure 4.4 Anisoaxial streamlines. Reproduced from Baron and Willeke (2001).

A *boundary layer* feature (demonstrated in the figures above) is known to develop as a fluid flows along the walls of the inlet. Fluid velocity through the inlet is not uniform; relative flow velocity at the wall is zero as gaseous viscous forces exert drag effects on the moving fluid close to the inlet wall. Viscous drag forces spread through the fluid away from the stationary layer at the inlet wall; at the upper limit of the boundary layer (δ) the fluid drag forces are negligible, and the bulk fluid velocity (U) reaches a maximum at the inlet centre (figure 4.5).

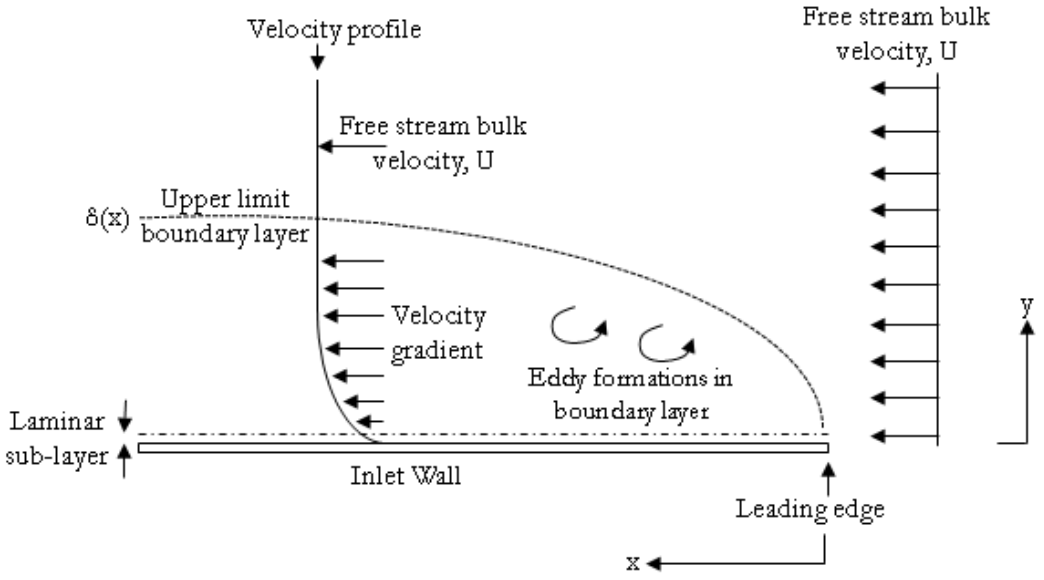

Figure 4.5 Eddy formation in the boundary layer. Adapted from Incropera et al. (2007).

Turbulent flows or eddy movements are known to develop as flow from higher velocity streamlines are forced down into slower velocity streamlines which increases the local velocity relative to the laminar boundary layer flow (Douglas et al., 1985). Okazaki and Willeke (1987) demonstrate that under these conditions particles which penetrate into the boundary layer flow will impact on the inside of the wall of the inlet. Within these eddies, slower velocity flow close to the inlet wall is additionally lifted away from the effects of the wall shear stress. This can slow fluid streamlines away from the inlet wall, effectively increasing the thickness of the boundary layer relative to a laminar boundary layer flow. Laminar flow is formed where gas flow in parallel with no mixing between layers.

The *Reynolds number,* Re of a system gives a measure of turbulence within a system; it is a ratio of the inertial force to the viscous force (Huschke, 1959). To determine the flow Reynolds number within the sampling line, the pipe fluid flow mean velocity, fluid viscosity and internal pipe diameter must be known. Laminar flow occurs when Re < 2300, turbulent flow occurs when Re > 4000 and the transition flow from laminar to turbulent occurs at Reynolds flow between 2300 and 4000 (Huschke, 1959). Low Reynolds numbers implies inertial forces are negligible compared with viscous forces.

$$Re = \frac{\rho U_0 D_D}{\mu} \quad (4.3)$$

ϱ is the density of fluid (kg m^{-3}), U_0 is the mean fluid velocity (m s^{-1}), D_D is the characteristic diameter (m) and μ is the dynamic fluid viscosity (Pa.s $\equiv$ kg m^{-1} s^{-1}).

Particle Reynolds number describes the relative velocity between a particle and the surrounding gas flow. Laminar flow around a particle occurs at Reynolds numbers less than 1 with streamlines resembling that of an ideal fluid, whilst for increasing Reynolds numbers (less than 2) turbulent eddies form in the wake of the particle flow, at high Reynolds numbers flow behind the particle is highly turbulent (Hinds, 1999).

For systems where particles Reynolds number are less than 1, *Stokes law* is the primary parameter that governs movement of particles within streamlines through a sampling system. Stokes law relates to the drag force on a sphere moving relative to the airflow (Huschke, 1959).

$$F_{drag} = 3\pi\mu U_0 d_p \text{ for Re} < 1 \quad (4.4)$$

$$St = \frac{\tau U_0}{d_p} \quad (4.5)$$

where μ is the viscosity of the fluid, U_0 is the free stream velocity of the fluid, τ is the relaxation time of the particle, and d_p is the diameter of the particle.

Stokes number above a value of approximately 1 deviate from the gas flow, whilst below this maintain gas streamlines (Hinds, 1999). Particles with small mass have a corresponding small Stokes numbers; this reflects the low inertia of a particle, which describes the resistance of a particle to a change in its motion (including a change in direction). The sampling and transport of larger particles is more difficult; their higher inertia makes them less susceptible to the influence of the sample flow should streamlines deviate within the sampling line. It is noted by Wu and Colbeck (1996) that a non-spherical particle will experience more drag that the sphere of the same volume. The dynamic shape factor, χ, can be incorporated into Stokes law to account for the effect of shape on particle motion.

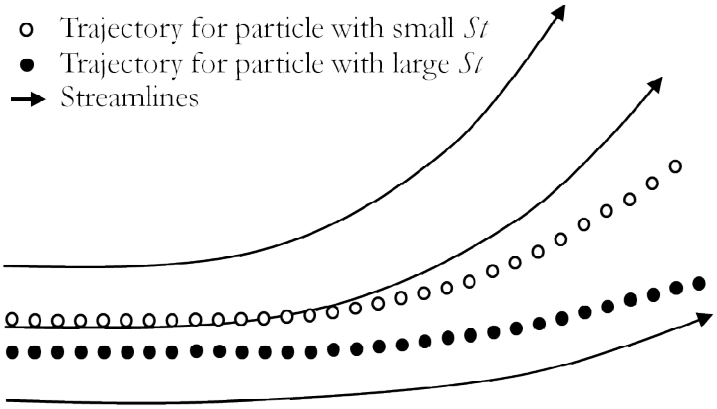

Figure 4.6 Concept of particle inertia with a change in streamline direction. Adapted from Harrison and Van Grieken (1998).

Streamline geometry through aerosol inlets can modify a size distribution, with convergence and divergence of streamlines leading to the loss or enhancement of aerosol concentrations. Super-isokinetic sampling (figure 4.7) leads to the depletion of larger particles in comparison to the ambient. Converging streamlines ($U_0 < U$) occur at the inlet entrance; particles with large Stokes numbers and high inertia deviate from the streamlines and are not sampled through the inlet. Concentrations of larger particles in the sample flow are lost relative to concentrations in the ambient free air.

Sub-isokinetic sampling (figure 4.8) leads to the enrichment of particles of larger sizes due to diverging streamlines ($U_0 > U$) at the inlet entrance; particles with larger Stokes numbers and high inertia cross gas flow streamline and are sampled through the inlet, enhancing concentrations relative to the ambient, whilst particles with smaller Stokes numbers remain within the diverging streamlines and are not sampled through the inlet.

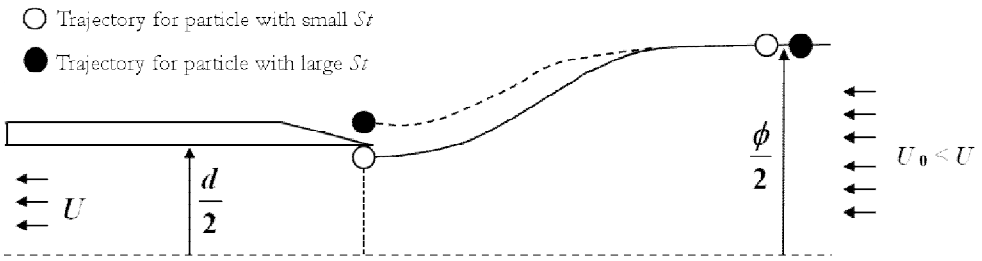

Figure 4.7 Sampling geometry of an isoaxial inlet under highlighting particle trajectories under super-isokinetic sampling conditions.

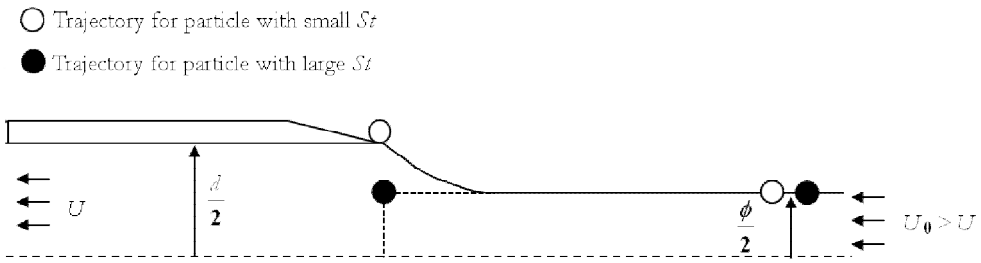

Figure 4.8 Sampling geometry of an isoaxial inlet under highlighting particle trajectories under sub-isokinetic sampling conditions. Adapted from Rader and Marple (1988).

The *transmission efficiency* refers to the system, the plumbing that carries the sample from the inlet to the instrument making the measurements, not the inlet itself. The transmission of a particle is influenced by gravitational settling, the impaction of particles to tubing walls and at bends, and the depositional loss of particles to walls from diffusion processes. In cases of isokinetic flow, the aspiration efficiency of the inlet equals one and as such total particle sampling is limited by the transmission efficiency of the system. Inlets are often curved to bring an aerosol sample from the free stream into the aircraft, and particles can be lost through the transport within the aircraft interior. The equation of particle penetration, η through a bend is;

$$\eta = 1 - St(\theta) \tag{4.6}$$

where η is the transmission efficiency of the bend and θ the angle of the bend. Pui et al. (1987) found for Stokes numbers less than 0.1, particle losses in the bend are negligible. Maintaining low Stokes number throughout a sampling system results in negligible particle losses in the bends.

Diffusional processes are always present (Hermann et al., 2001), though are not dominant loss mechanisms due to the size of aerosol particles under discussion. *Gravitational settling* is not an important process where gas flow velocities are much greater than the gravitational settling, though should be considered as a more dominant process when coarse mode particles are sampled.

4.2 Rosemount Inlet

The primary aerosol inlets on the BAe-146 are modified Rosemount 102E housings (figure 4.9), and each consist of a pair of inlets which provide air samples to rack mounted instruments inside the aircraft cabin. On the starboard side of the aircraft, a single Rosemount pair provides aerosol samples to the VACC instrument and the SP2, whilst on the port side the forward Rosemount pair samples to the PSAP and nephelometer and the second Rosemount pair samples to the AMS and Cloud Condensation Nuclei (CCN) instruments. The Rosemount inlet has been used in aircraft aerosol measurement as it has an official installation certificate required for aircraft use (Foltescu et al., 1995).

Figure 4.9 Modified Rosemount housings on the port side of the aircraft.

The Rosemount inlet was traditionally designed for temperature and humidity measurements (Foltescu et al., 1995). The inlet has been modified with a 0.95 cm (3/8'') stainless steel tube through the length of the inlet. The sampling size of the aerosols is dependent on the geometry of the Rosemount inlet; the greater angle of deflection, the greater the loss of larger aerosols in the airflow. The inlet is a T-piece, with free airflow 90^{o} to the sampled airstream brought into the aircraft. The sampling tube is shaped to streamline the air sample and reduce the speed of the sampled air from the true airspeed of the aircraft to approximately 10 m s^{-1} in the sample tube. No measurements have been made to accurately determine the speed reduction through the inlet.

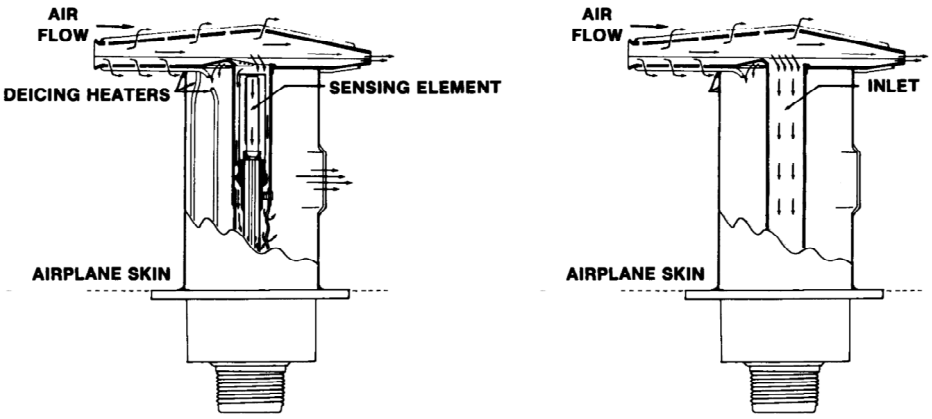

Figure 4.10 (left) Schematic of an unmodified Rosemount 102E housings and (*right*) modified Rosemount 102E housings for aerosol sampling. Image courtesy of J. Trembath, FAAM.

In the first published study of Rosemount inlet sampling efficiencies, Foltescu et al. (1995) made incorrect assumptions regarding the aspiration efficiencies of unity, assuming particle concentration incident to the inlet face and ambient particle concentration are equal. Additionally, Foltescu et al. (1995) assumed that there is no particle bounce from the tip of the inlet; an assumption that the leading edge of the inlet is sufficiently sharp-edged, whilst in reality the inlet is blunt.

Haywood et al. (2003b) initially suggested that the collection efficiency of the Rosemount inlet on the BAe-146 dropped from close to unity to zero for particle radii greater than 1 – 2 μm on board the C-130 during the SHADE campaign in 2000. Recent papers by Johnson et al. (2008) and Johnson and Osborne (2011) omit to performing a correction due to the Rosemount inlet, but acknowledged it was potentially a significant source of uncertainty in aerosol measurements.

4.3 Low Turbulence Inlet

The LTI was designed at the University of Denver to improve aerosol sampling efficiency by reducing turbulence flow within the tip of the inlet and hence reducing particle losses to the inlet walls due to impaction. It has been demonstrated that the inlet can achieve a reduction in sample speed from 150 m s^{-1} to 5 m s^{-1} without generating turbulence (Wilson et al., 2004). The LTI was installed, tested and used on aircraft operated by the National Centre for Atmospheric Research (NCAR) and the National Oceanic and Atmospheric Administration (NOAA). The LTI was initially fitted to the BAe-146 in 2005 and after some extensive work was re-fitted in August 2010 and operated intensively during the Fennec 2011 and 2012 field campaigns. On the BAe-146 the inlet entrance is located 30 cm above the aircraft upper fuselage, and extends from the aircraft fuselage by a length of 93 cm. The inlet tip is designed with a parabolic, aerodynamic shape which encompasses 13 % more area than the throat of the inlet, the straight section upstream of the diffusing section (Wendisch et al., 2004; Wilson et al., 2004). This design aids in reducing the sample flow rate without generating turbulence. On exiting the diffusing section of the inlet, the sample flow passes around a 65º bend, before being brought in the aircraft cabin.

Figure 4.11 Photograph indicating the position of the LTI on the BAe-146 aircraft (*foreground*), including (*right*) the isokinetic inlets which sample to the filter system and (*behind*) the trace gas sample line.

Henri Pitot in 1732 developed the *pitot tube* (figure 4.12) for measuring the velocity pressure of a fluid; it consists of two concentric tubes connected to a pressure measuring device such as a manometer (Hinds, 1999). The inner tube is aligned with the direction of airflow, and measures the total pressure, termed the *stagnation pressure* (P_0).

The outer tube has measurement holes which are perpendicular to the airflow, and measures *static pressure* (P_x). Static pressure does not account for fluid motion but the state of the fluid i.e. is indicative of pressure altitude. The *dynamic pressure* (DP_x) at the point of sampling is the difference between the stagnation and static pressure according to Bernoullis's equation of velocity (Douglas et al., 1985);

$$P_0 = P_x + \frac{1}{2}\rho U^2 \tag{4.7}$$

where ρ is density and U is velocity, and can be re-arranged to solve for velocity.

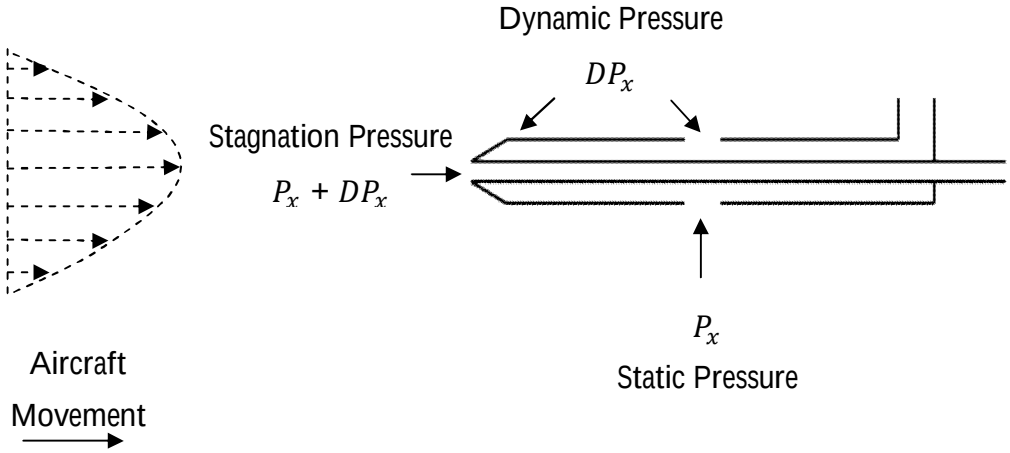

Figure 4.12 Pitot tube pressure measurements. Adapted from Hinds (1999).

A pitot tube is fitted at the head of the LTI so that the airspeed, that is the ambient free stream velocity, is known. Suction mass flow rates are continuously varied to maintain equivalent flows in matching the ambient free stream velocity to the inlet entrance velocity, as aircraft true air speeds, temperature, pressure and altitude vary throughout the flight (Huebert et al., 1990).

The outer structure of the LTI head expands from 11 mm at the inlet entrance to 90 mm, and incorporates a central diffusing section (figure 4.13). It is conical shaped and designed with the purpose of reducing air velocity due to an increasing cross sectional area along the diffusing section (Hermann et al., 2001). The diffusing section consists of a porous diffuser manufactured from 20 μm sintered stainless steel and is made up of three expanding sections, with dimensions provided in Wilson et al. (2004).

The system is designed so that suction flow can be varied throughout the flight removing between 20 - 80 % in order to maintain equivalent flows between the ambient free stream velocity and the inlet entrance velocity (Huebert et al., 2004). Flow rates were monitored using Alicat Scientific and Kurz mass flow. The suction flow suppresses the formation of the boundary layer and the subsequent generation of turbulence (Huebert et al., 2004; Seebaugh et al., 1996). The presence of a suction flow prevents viscous forces exerting a drag on the gas flow close to the inlet wall; the mechanism for boundary layer separation and turbulent flow development. Turbulence decreases with increasing suction flow, with negligible turbulence for a suction fraction of larger than 44 % (Wendisch et al., 2004). The remaining airflow forms the sample flow and is considered to be low turbulence and laminar; it has been shown that theory suggests particle deposition should be negligible if turbulence is negligible (McMurry, 2000).

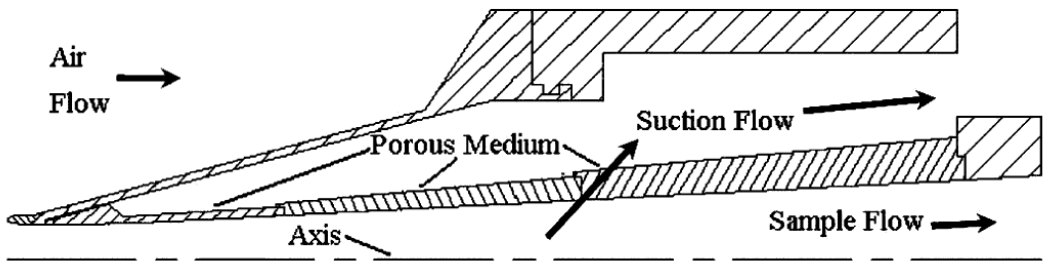

Figure 4.13 Diffusing section of the LTI. Reproduced from Wilson et al. (2004).

Additional pressure measurements are made of the static pressure at the throat entrance (P_1) and the pressure difference across the diffuser (intake static pressure – exit static pressure) (DP_{12}), which allows for the calculation of the total stagnation pressure at the LTI. The porous diffuser material traps ambient aerosol causing pore blockage, and the monitoring of the pressure drop as a function of flow rate is used as a housekeeping tool for instrument maintenance. Turbulence at the rear of the diffuser is measured using a hot film anemometer.

4.3.1 Particle Inertial Enhancement

Inertial enhancement of supermicron particle concentration within the sample flow relative to suction flow occurs due to the removal of suction flow at the porous diffuser. Particles with greater inertia move less fluidly with changing streamlines, and as a result supermicron particles and are enhanced within the sample flow. As a characterised

system with measurements of pressure, temperature and mass flows, it is possible to correct the LTI for these inertial enhancements. In a low turbulence and laminar regime within the inlet tip it can be assumed that gravitational settling and wall losses are negligible.

The following series of equations make up a correction methodology developed by Wilson et al. (2004) to account for the inertial enhancement of supermicron particles. It was developed from monitoring particle trajectories using fluid mechanics software (Fluent 5.4). The corrections account for the complete sampling system of the LTI to the point of particle size distribution measurements using an OPC; including the plumbing that connects this device with the inlet. A complete account of the LTI correction procedure is presented in Appendix B for reference.

4.3.1.1 Stokes Number

The Stokes number is used in assessing the inertial enhancement of the particles the entrance of diffusing section, St_t, and for determining inertial particles losses due to the inlet bend, St_B, as presented in equations (4.8) and (4.9), respectively.

$$St_t = \frac{\rho_p {d_p}^2 U_t Cc}{9\mu_t D_{throat}} \tag{4.8}$$

where ρ_p is the density of the particle, 2650 kg m^{-3} (Haywood et al., 2001), d_p the aerodynamic diameter of the particle in meters, Cc the *Cunningham slip* correction (assumed to be 1 for particles with significant enhancements), U_t is the throat velocity (m s^{-1}), μ_t the throat viscosity (calculated from the throat temperature) and D_{throat} is the throat diameter (1.118 x 10^{-2} m). The Cunningham slip correction accounts for discontinuities which originate as the size of an aerosol particle in a medium approaches the mean free path of gas molecules (Cunningham, 1910; Gussman, 1969).

$$St_B = \frac{\rho_p {d_p}^2 U_D Cc}{9\mu_D D_{tube}} \tag{4.9}$$

where U_D is the diffuser exit velocity (m s^{-1}), μ_D the diffuser exit viscosity (calculated from the stagnation temperature) and D_{tube} is the transport tube diameter (0.0254 m).

Viscosity is a measure of the resistance of a fluid (Douglas et al., 1985) with throat viscosity calculated from measurements of throat temperature, whilst the diffuser exit viscosity is calculated from the stagnation temperature using the equations presented in Appendix B. The *dynamic viscosity* is calculated using *Sutherlands equation* (4.10) from Kulkarni et al. (2011b).

$$\mu = \mu_r \left(\frac{T_t + S_u}{T + S_u}\right)\left(\frac{T}{T_r}\right)^{\frac{3}{2}} \tag{4.10}$$

where μ is dynamic viscosity in (Pa·s) at input temperature T, μ_0 is the reference viscosity in (Pa·s) at reference temperature T_0, T the input temperature in Kelvin, T_0 the reference temperature in Kelvin and Su is the *Sutherland's constant* of 120 K for the gaseous material (air).

4.3.1.2 Penetration of the particles through the LTI bend

Sampled aerosols are subject to losses in transport to the aircraft interior in particular the 65º bend of the LTI. The equation of particle penetration, η through the bend is;

$$\eta = 1 - \varphi\, St_B \tag{4.11}$$

η is the fraction of the particles of size D_p that penetrate the bend, φ the angle of the bend in radians (1.134 for the 65º bend) and St_B the Stokes number of the particles in the bend.

4.3.1.3 Enhancement Factor

The enhancement factor (EF) is the ratio of particles-to-unit mass of air at a given size at the exit of the diffuser (Wilson et al., 2004). The particles-to-unit mass of air ratio in the ambient free air flow is given in equation (4.12).

$$EF = 1.01 + M * St_t \tag{4.12}$$

where M is a fourth order polynomial expressed by equation (4.13) and St_t is the Stokes number of a particle in the throat of the LTI.

$$M = 5.8751x10^{8}.m^{4} - 7.8631x10^{6}.m^{3} + 39357.m^{2} - 101.81.m + 0.25117 \quad (4.13)$$

where the constant m is the mass flow exiting the rear of the diffuser in kg s^{-1} as derived from Fluent fluid dynamic calculations expressed in Wilson et al. (2004).

The overall performance of the inlet is a function of the particle penetration, η through the bend, multiplied by the porous diffusers enhancement factor, as detailed in equation (4.14).

$$Enhancment\ factor\ (EF)\ x\ Particle\ Penetration(\eta) \quad (4.14)$$

4.3.1.4 Sub-sampler Corrections

Particle losses through the sub-sampler plumbing that connect the size distribution measurements at the OPC with the inlet are accounted for and corrections performed by J. Trembath, FAAM. The sub-sampler was designed to match velocities through the sample line to maintain the laminar conditions and reduce turbulence. Corrections for particle losses account for gravitational settling, diffusional deposition and inertial deposition (Trembath et al., 2012).

4.4 Fennec 2011 Case Studies

This section investigates the performance of the LTI during the Fennec 2011 campaign. The inlet has been assessed in terms of the isokinetic behaviour of the inlet, the Reynolds flow through the inlet, and the Stokes number of aerosol particles passing through the inlet. The validation uses flights B611 – B613, which carried out stacked legs at multiple altitudes throughout the boundary layer, and allowed for investigation of the performance in terms of vertical height. B604 and B614 consisted of only low level SLR. Table 23 to table 28 present an overview of each flight in terms of aircraft profiles (P) and straight and level runs (R). Note SLR numbering excludes high-altitude transits.

Table 23 Aircraft profiles (P) and straight and level runs (R) for B604 (20 June 2011).

Run Number	Time (UTC)	Altitude (m)	Pressure (hPa)	Details
P1	12:47 – 13:12	-	-	Profile Ascent FUE
P2	14:44 – 15:22	7620 - 400	-	Profile Descent OpArea
R1	15:22 – 15:40	400	970	SLR
P3	15:40 – 16:15	-	-	Profile Descent FUE

Table 24 Aircraft profiles (P) and straight and level runs (R) for B609 (24 June 2011).

Run Number	Time (UTC)	Altitude (m)	Pressure (hPa)	Details
P1	11.28 – 11.50	-	-	Profile Ascent FUE
P2	12:56 – 13:32	8230 - 430	-	Profile Descent OpArea
R1	13:32 – 13:44	440	960	SLR
R2	13:51– 14:03	1520	840	SLR
R3	14:13 – 14:25	3050	760	SLR
P3	14:29 – 16:44	-	-	Profile Descent FUE

Table 25 Aircraft profiles (P) and straight and level runs (R) for B611 (25 June 2011).

Run Number	Time (UTC)	Altitude (m)	Pressure (hPa)	Details
P1	14:14 – 14.34	-	-	Profile Ascent FUE
P2	15:58 – 16:27	7620 - 400	-	Profile Descent OpArea
R1	16.27 – 16:42	400	960	SLR
R2	16:44 – 16:46	730	925	SLR
R3	16:58 – 17:13	1830	810	SLR
R4	17:16 – 17:19	2750	720	SLR
R5	17:25 – 17:35	3810	630	SLR
P3	18:58 – 19:16	-	-	Profile Descent FUE

Table 26 Aircraft profiles (P) and straight and level runs (R) for B612 (26 June 2011).

Run Number	Time (UTC)	Altitude (m)	Pressure (hPa)	Details
P1	07:28 – 07.50	-	-	Profile Ascent FUE
P2	08:50 – 09:31	7620 - 300	-	Profile Descent OpArea
R1	09:31 – 09:46	300	974	SLR
R2	09:52 – 10:00	1070	890	SLR
R3	10:05 – 10:13	2290	767	SLR
R4	10:23 – 10:31	3810	631	SLR
R5	10:37 – 10:45	5490	505	SLR
P3	12:08 – 12:21	-	-	Profile Descent FUE

Table 27 Aircraft profiles (P) and straight and level runs (R) for B613 (26 June 2011).

Run Number	Time (UTC)	Altitude (m)	Pressure (hPa)	Details
P1	13.55 – 14.17	-	-	Profile Ascent FUE
P2	15.17 – 15.41	7620 - 400	-	Profile Descent OpArea
R1	15.44 – 16.11	400	970	SLR
R2	16.23 – 16.36	2500	760	SLR
R3	16.42 – 16.55	3100	640	SLR
R4	17.00 – 17.13	4170	600	SLR
R5	17.19 – 17.31	4630	560	SLR
R6	17.41 – 17.54	400	970	SLR
P3	18.39 – 18.58	-	-	Profile Descent FUE

Table 28 Aircraft profiles (P) and straight and level runs (R) for B614 (27 June 2011).

Run Number	Time (UTC)	Altitude (m)	Pressure (hPa)	Details
P1	06:34 – 06:51	-	-	Profile Ascent FUE
P2	07:42 – 08:00	7620 - 400	-	Profile Descent OpArea
R1.1	08:00 – 08:52	400	970	SLR (A – B)
R1.2	08:56 – 09:58	400	970	SLR (B – A)
P3	12:08 – 12:21	-	-	Profile Descent FUE

4.4.1 Results: LTI Reynolds Number

The mean Reynolds number of the system was 239, calculated at the exit of the diffusing section and found to be within the laminar regime (Reynolds number less than 2300) throughout the operational limits of the LTI.

4.4.2 Results: LTI Isokinetic Behaviour

The ratio of the LTI diffuser entrance Mach number, M_1 to the ambient Mach number, M_0 in the free stream is used to assess the isokinetic behaviour of the inlet, termed the *isokinetic ratio*. The isokinetic operational limit constrained by Wilson et al. (2004) is an isokinetic ratio in range of 0.75 to 1.25. A ratio of 1.0 characterises the optimum performance where the inlet operates isokinetically. The dependence of the isokinetic behaviour of the inlet with altitude was assessed to determine the maximum operating conditions of the inlet.

Table 29 summarises the isokinetic ranges of the LTI during all flight levels for the Fennec 2011 campaign. A transition region can be identified between 700 hPa and 600 hPa where isokinetic values are typically greater than 0.75 but less than the optimum value of 1.0. The results from flight B613 suggests that the inlet is within the operational constrains to 640 hPa (3100 m). The isokinetic ratios from B611 and B612, presented in table 29, suggest that the isokinetic control breaks down between 810 hPa and 770 hPa (1830 – 2290 m). Wilson et al. (2004) report that with the use of a Venturi pump (that is, where a vacuum pressure is generated as compressed air is forced through a conical nozzle it's velocity increases in the pumping system) the LTI is fully operational up to 7750 m pressure altitude or 370 hPa static pressure.

Figure 4.14 presents the isokinetic ratio as a function of pressure for the selected Fennec 2011 flights; it is evident that as pressure decreases, the ratio of M_1 to M_0 decreases towards the operational limit of 0.75 as identified by Wilson et al. (2004). This indicates there is insufficient airflow through the diffuser head with increasing altitude to maintain the pressure balance in the ambient and within the diffuser; this is a limit to the current operational design of the inlet and suggests the LTI is presently only operational up to approximately 2000 m.

Table 29 Isokinetic ratios and Reynolds numbers calculated for each SLR for during the Fennec campaign; flights B604, B611 – B614.

Flight (2011)	SLR	Pressure (hPa)	Altitude (m)	TAS (m s^{-1})	Isokinetic Ratio	Reynolds Number
B604 (20 June)	R1	970	340	111	1.00	234
B611 (25 June)	R1	960	400	113	1.00	265
	R2	925	730	121	0.96 (> 0.75)	-
	R3	810	1830	120	0.97 (> 0.75)	170
	R4	720	2750	123	0.39	-
	R5	630	3810	132	0.30	-
B612 (26 June)	R1	970	300	115	1.00	271
	R2	890	1070	113	1.00	273
	R3	770	2290	121	0.29 (< 0.75)	38
	R4	630	3810	125	0.31 (< 0.75)	-
	R5	505	5490	141	0.29 (< 0.75)	-
B613 (26 June)	R1	970	400	112	1.00	263
	R2	760	2500	126	0.95 (> 0.75)	305
	R3	640	3100	127	0.91 (> 0.75)	294
	R4	600	4170	137	0.72 (< 0.75)	227
	R5	560	4630	141	0.30 (< 0.75)	-
	R6	970	400	112	1.00	264
B614 (27 June)	R1	970	400	112	1.00	264

The range in the LTI performance across the flights can be observed, with flights B609 – B614 exhibiting a decrease in isokinetic ratio to 0.75 with decreasing pressure, before transitioning into a sub-isokinetic sampling regime, with isokinetic ratios of 0.2. Flight B604 remains in an isokinetic sampling regime up to 550 hPa; beyond this the isokinetic ratio continues to decrease to 0.55 at 370 hPa before transitioning into the sub-isokinetic sampling regime. The cause of this difference cannot be resolved from the current analysis.

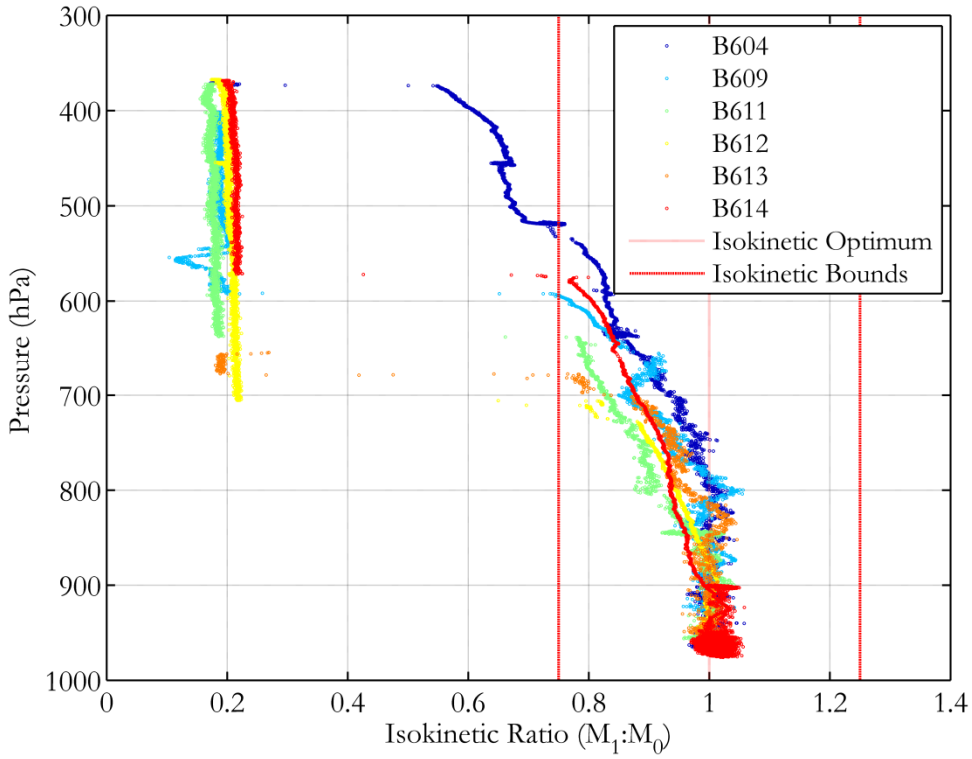

Figure 4.14 LTI isokinetic ratio (ratio of the LTI diffuser entrance Mach number, M_1 to the ambient Mach number, M_0 in the free stream) as a function of pressure height for selected Fennec 2011 flights. Red dotted lines refer to the isokinetic optimum and the red dashed lines refer to the LTI operating boundaries.

Five SLRs at different aircraft heights were performed during B613 (26 June 2011), with figure 4.15 showing a scatter plot of the Mach number at diffuser entrance (M_1) to the ambient Mach number (M_0) with increasing altitude. The SLR average ratio of the Mach number in the diffuser entrance to the ambient Mach number in the free stream at 970 hPa (400 m) is equal to 1.0, showing the LTI operates optimally (table 29). Linear regression of the scatter plots at 970 hPa found a coefficient of determination (R^2) of 0.8180; indicating they were reasonably correlated.

The SLR average ratio of the Mach number in the diffuser entrance to the ambient Mach number in the free stream at 760 hPa (2500 m) is equal to 0.95; this falls within the operational isokinetic limits. Linear regression of the scatter plot found the correlation decreases, with R^2 of 0.4781. Decreasing pressure shows a progressive decrease in the isokinetic ratio; at 560 hPa (2500 m) the ratio drops to 0.3. The inlet transitions to a sub-isokinetic sampling regime where the sampling velocity through the

inlet is lower than the gas flow velocity. Analysis of the scatter plot found a linear regression R^2 falls to 0.2531, that is, with decreasing pressure the R^2 tends towards a zero correlation.

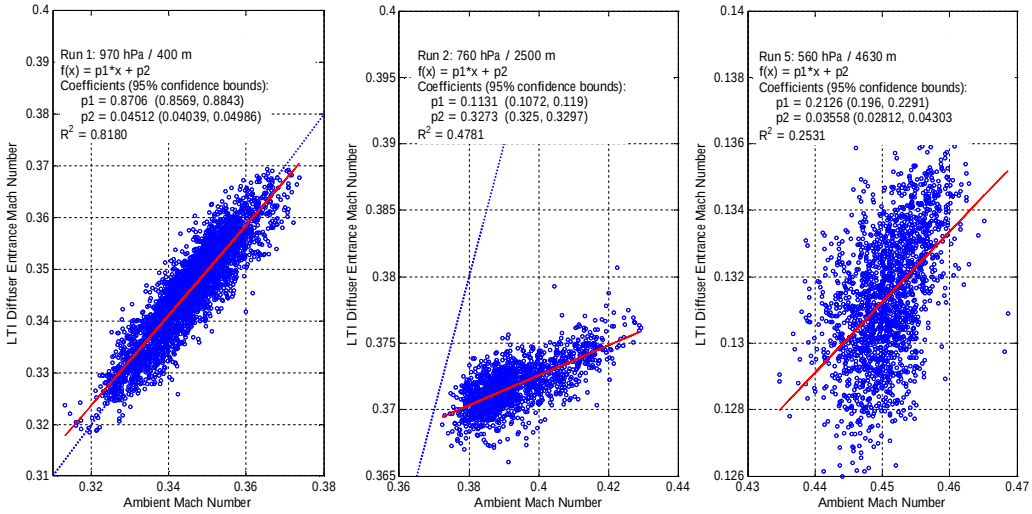

Figure 4.15 Mach number at the LTI diffuser entrance (M_1) to the ambient Mach number (M_0) with increasing altitude for flight B613 (*left*) Run 1: 970 hPa / 400 m, (*middle*) Run 2: 760 hPa / 2500 m, (*bottom*) Run 5: 560 hPa / 4630 m. Note the different scale of plot 3.

4.4.3 Results: LTI Stokes Number

The Stokes numbers of particles are calculated for conditions at the diffuser entrance where air velocity (U_t) is approximately 120 m s^{-1}. Figure 4.16 indentifies that deviation from a Stokes number of 1 occurs for particles greater 4.5 μm; particles above this size are less susceptible to the influence of the sample flow should aerosol streamlines deviate within the sampling line. In the diffuser entrance, the presence of a suction flow removes a portion of main flow entering the LTI; only particles less than 4.5 μm with a Stokes number of 1.0 will flow these streamlines. This results in an enhancement of particles with a diameter greater than 4.5 μm within the sample flow exiting the sample diffuser.

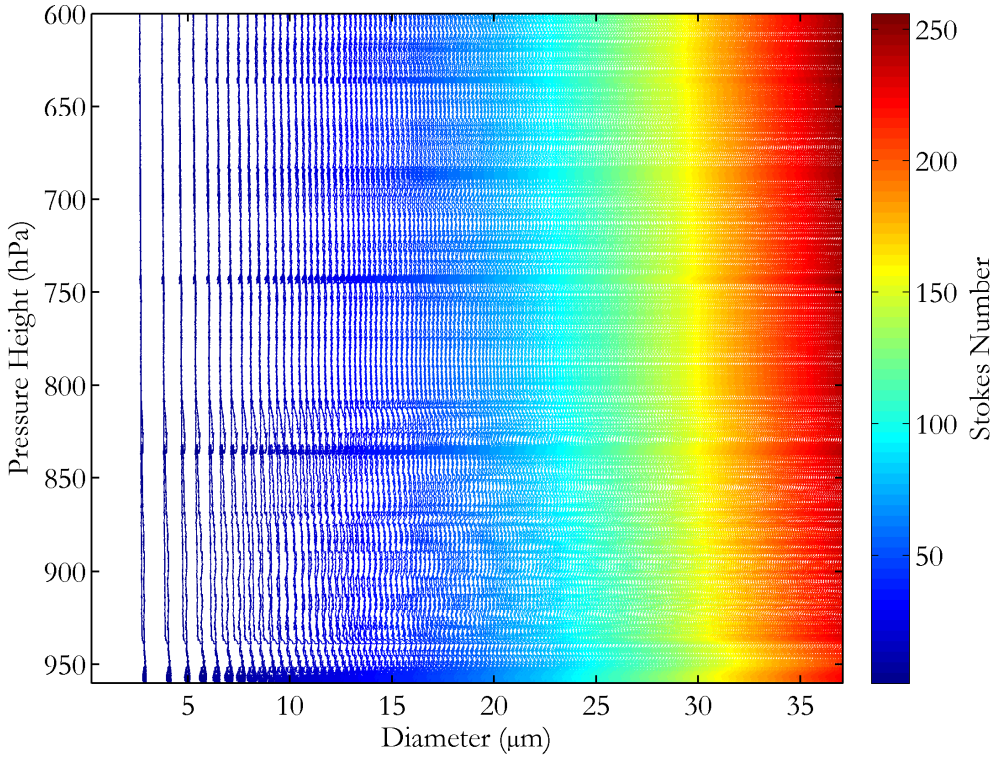

Figure 4.16 Stokes numbers of particles passing the throat (porous diffuser) of the LTI as a function of pressure (hPa).

At the diffuser exit, air velocity (U_D) is slowed to approximately 3 – 5 m s^{-1}, and is equivalent to flow velocity at the inlet bend. The particle Stoke numbers as a function of pressure height at the bend of the LTI is shown in figure 4.16; deviation from particle Stokes number of 1.0 occurs for particles greater than 28 μm. The particle Stokes numbers show a pressure dependence as identified in figure 4.16; the Stokes number for a particular particle diameter increases with decreasing atmospheric pressure. The knowledge of Stokes number for particles across the size distribution, at both the diffuser exit and in the LTI bend, allows for a characterised and methodical approach for accounting for particle enhancement within the LTI sampling system.

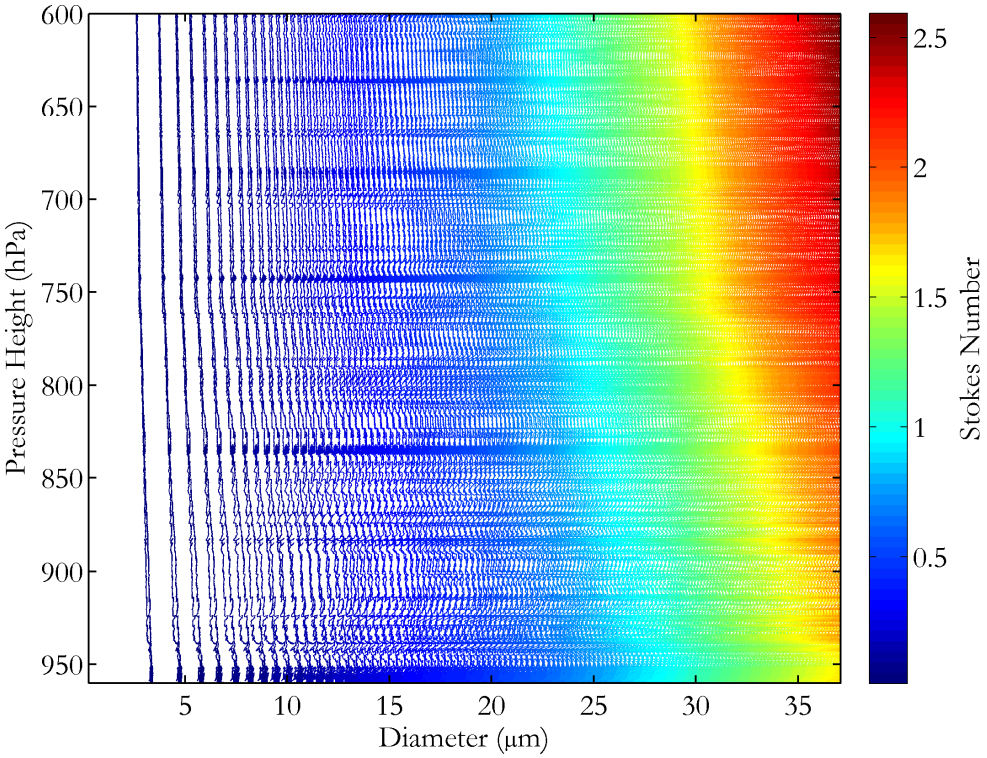

Figure 4.17 Stokes number as a function of particle diameter at the bend of the LTI with changes in pressure (hPa).

4.5 Size Distribution Comparisons

Comparison experiments provide valuable information on the performance of instruments and aid in quantification of uncertainties. Recent advances in characterising the aerosol sampling system have coincided with the installation of the LTI. This has provided a platform for performing inlet comparison experiments with the current aircraft Rosemount inlets. Sampling efficiency of the standard Rosemount inlet is presented in section 4.5.1. Comparisons with reference to the ambient size distribution measured by the external wing-mounted probes are discussed in section 4.5.2.

Aerosol size distribution measurements are made using a Grimm Sky OPC close to the inlet, via a sub-sampler from the main sample line, to make the most of the laminar and turbulence flow. Mineral dust measurements during Fennec provided an ideal study aerosol due to the i) high dust loadings encountered, including supermicron aerosol, and ii) the relatively non-volatile composition associated with mineral dust, and so an

assumption was made of no particle losses due to evaporation of volatile species during sampling.

The methodology for correcting aerosol size distribution measurements was outlined in chapter 3. In practice this methodology requires the generation of theoretical Mie scattering curves, specific to the Grimm instrument. These are generated for a mineral dust refractive index of m = 1.53 – 0.001i (Ryder et al., 2013b), and uses Grimm equivalent scattering cross sections used for determining new bin diameters for mineral dust. These diameters, d_p, are applied to the Stokes equations laid out in the enhancement factor correction methodology of the LTI to account for particle inertia along the LTI sampling system. Size distributions are corrected for the bend leading to the OPC sub-sampler (accounting for transmission efficiency). No measures to account for particle shape irregularities have been made; uncertainties in this assumption are discussed.

4.5.1 Rosemount Comparisons

Continuous size distributions were measured using two Grimm Sky OPCs operating in tandem: one sampling through a Rosemount inlet and the other sampling through the LTI. Time series from B613 (26 June 2011) of number concentrations are presented in figure 4.18 for different sizing groups of the Sky-OPC; channels 2 – 8 (0.26 – 0.63 μm), channels 9 – 14 (0.63 – 1.73 μm), channels 15 – 20 (1.73 – 5.0 μm), channels 21 – 25 (5.0 – 15.0 μm). These four sizing groups represent four size intervals across the sizing region of the Grimm. The number concentrations for both inlets are observed to be relatively constant throughout the flight, with relative ratios between the Rosemount and LTI equally constant. Flight average mineral dust size distributions for B613 measured at the LTI and the Rosemount inlet and the corresponding *Rosemount inlet enhancement* calculated from difference of LTI and Rosemount size distribution is calculated and presented in figure 4.19. The error bars presented in figure 4.19 represent the variance within the data, as according to equation (4.15):

$$Var\left(\sum_{i=1}^{N} X_i\right) = \sum_{i=1}^{N} Var(X_i) \tag{4.15}$$

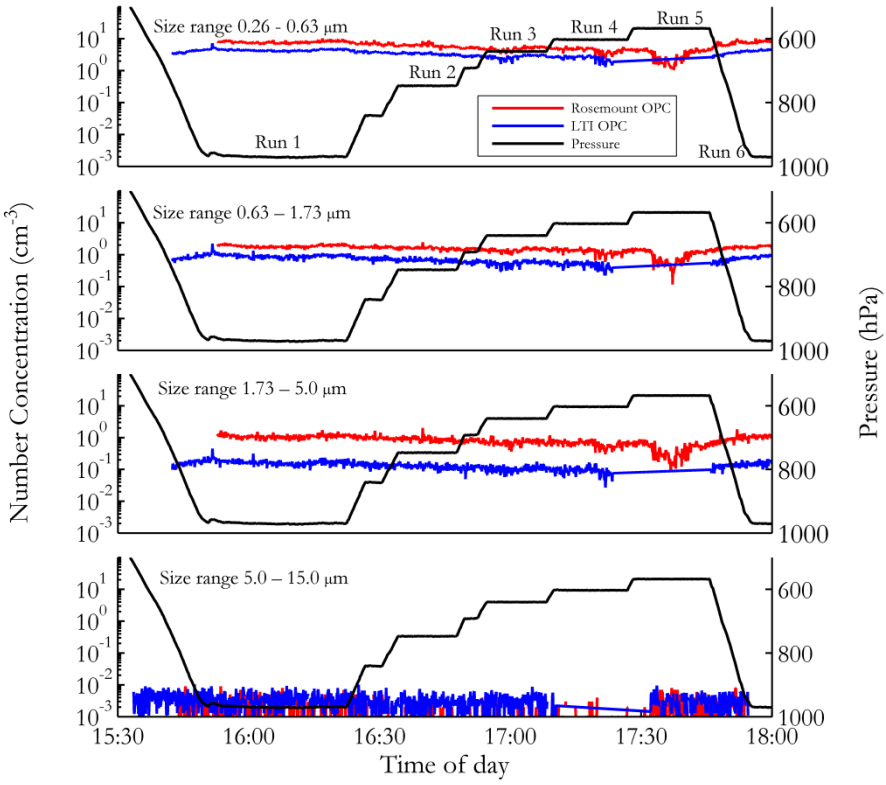

Figure 4.18 Time series from B613 (26 June 2011) of four sizing groups of the Sky-OPC; (*top*) 0.26 – 0.63 μm, (*top mid*) 0.63 – 1.73 μm, (*bottom mid*) 1.73 – 5.0 μm, (*bottom*) 5.0 – 15.0 μm (*blue*) of Rosemount and (*red*) LTI number concentration (*black*) ambient pressure.

The size distributions in figure 4.19 highlight that for particles below 1.0 μm the Rosemount inlet enhancement, that is the concentration at the Rosemount inlet relative to the LTI, is 1.5 - 2 times of that measured at the LTI. For 3.0 μm particles the Rosemount inlet enhancement peaks at approximately 8 times that of the LTI. For particles in the range of 3.0 μm to 7.0 μm the enhancement decreases approaching the unity line where the LTI and Rosemount measure equal concentration. Beyond 7.0 μm, particle concentration is underestimated.

This result indicates a sub-isokinetic sampling regime occurring in the Rosemount inlet, leading to the enrichment of particle concentration observed in figure 4.19. Theory defines a sub-isokinetic inlet as the enhancement of larger particle sizes due to diverging streamlines ($U_0 > U$) at the inlet entrance, whilst particles of lower inertia remain within the diverging streamlines. The results from figure 4.19 show that enhancement efficiency is 1 or more for all particles to 6 μm. It is evident that particles greater than 6

μm, with high inertia deviate from the sampling streamlines and do not pass through the inlet, or are rapidly lost to the inlet walls, and hence are not sampled. The sampling nature of the Rosemount inlet is a particularly important consideration when sampling coarse mode aerosol representatively.

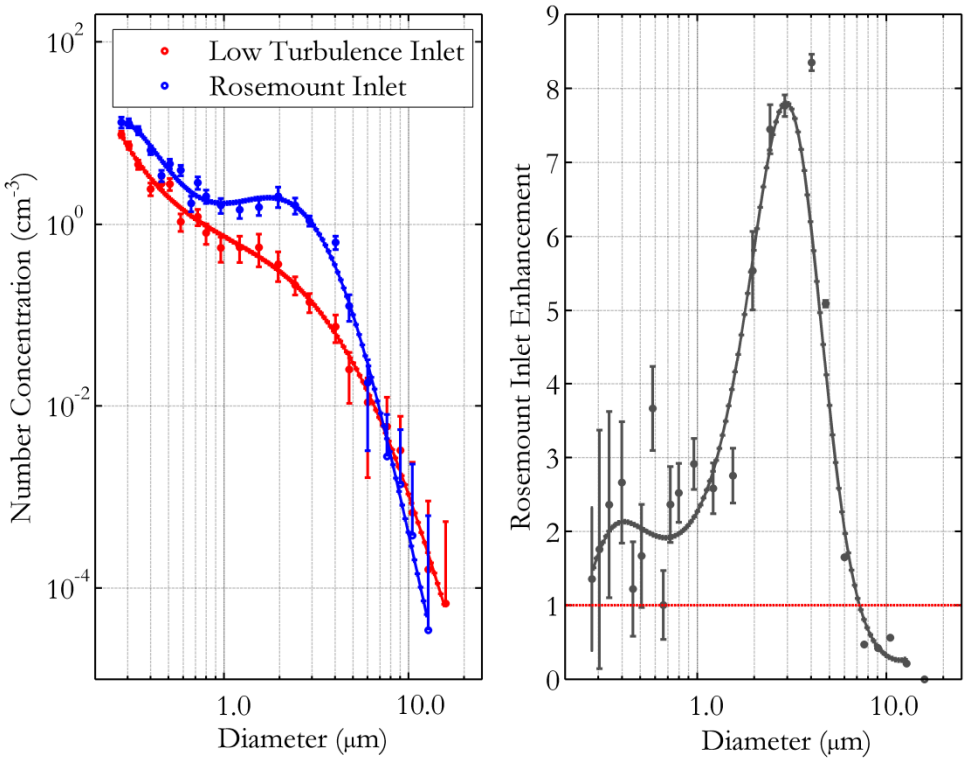

Figure 4.19 *(left)* Average aerosol distributions from B613 (26 June 2011) measured at the LTI *(red)* and the Rosemount inlet *(blue)*. Error bars which extend to negative numbers on the log scale have been omitted for clarity. (*Right*) Rosemount inlet enhancement as a function of size distribution. The red dashed line represents where LTI and Rosemount measure equal particle concentration (unity).

The Rosemount enhancements relative to the LTI across the four sizing groups of the Sky-OPC as a function of pressure are presented in table 30 – table 33 for flights B604, B611 – B614. The Rosemount enhancements from Petzold (2009) are included for comparison for three sizing regimes 0.25 – 0.45 μm, 0.45 – 0.80 μm, and 0.80 – 3.00 μm, presented in (table 34).

These measurements by Petzold (2009) were made during two campaigns; the first the QUANTIFY – SHIPS study in July 2007 using particle emissions from ships and the

second the European Integrated project on Aerosol, Cloud, Climate, and Air Quality Interactions (EUCARRI) campaign. The Petzold (2009) investigation was limited to a maximum particle size of 3.0 μm using the DLR Falcon isokinetic inlet, designed for sampling fine-mode fraction aerosol with particle diameters less than 2.5 μm under isokinetic conditions, free tropospheric conditions, and at a true air speed of the aircraft of 200 m s^{-1} (Fiebig et al., 2002a; Fiebig et al., 2002b; Petzold et al. 2002; Schneider et al., 2006).

Table 30 Measurement conditions and Rosemount enhancement for four of the sizing regimes for B604 (20 June 2011).

Diameter Range (μm)	Pressure (hPa)	Temperature (K)	Altitude (m)	TAS (m s^{-1})	Rosemount enhancement
0.26 – 0.63	970	318	345	111	2.06 ± 4.48
0.63 – 1.73	970	318	345	111	2.41 ± 1.85
1.73 – 5.00	970	318	345	111	6.10 ± 1.77
5.00 – 15.00	970	318	345	111	0.62 ± 0.05

Table 31 Measurement conditions and Rosemount enhancement for four of the sizing regimes for B611 (25 June 2011). Analysis at 925 hPa excluded due to insufficient LTI Grimm OPC data (< 60 sec) during the SLR.

Diameter Range (μm)	Pressure (hPa)	Temperature (K)	Altitude (m)	TAS (m s^{-1})	Rosemount enhancement
0.26 – 0.63	960	315	400	113	2.05 ± 1.71
0.63 – 1.73	960	315	400	113	2.01 ± 0.82
1.73 – 5.00	960	315	400	113	5.70 ± 0.89
5.00 – 15.00	960	315	400	113	0.77 ± 0.02
0.26 – 0.63	925	312	730	121	-
0.63 – 1.73	925	312	730	121	-
1.73 – 5.00	925	312	730	121	-
5.00 – 15.00	925	312	730	121	-

Table 32 Measurement conditions and Rosemount Enhancement for four of the sizing regimes for B612 (26 June 2011).

Diameter Range (μm)	Pressure (hPa)	Temperature (K)	Altitude (m)	TAS (m s^{-1})	Rosemount enhancement
0.26 – 0.63	974	310	300	115	2.10 ± 1.67
0.63 – 1.73	974	310	300	115	2.39 ± 0.56
1.73 – 5.00	974	310	300	115	6.78 ± 0.47
5.00 – 15.00	974	310	300	115	0.85 ± 0.02
0.26 – 0.63	890	307	1070	113	2.11 ± 1.53
0.63 – 1.73	890	307	1070	113	2.47 ± 0.52
1.73 – 5.00	890	307	1070	113	7.06 ± 0.46
5.00 – 15.00	890	307	1070	113	1.66 ± 0.01

Table 33 Measurement conditions and Rosemount Enhancement for four of the sizing regimes for B613 (26 June 2011). Analysis at 560 hPa is excluded as the LTI is not within operational limits.

Diameter Range (μm)	Pressure (hPa)	Temperature (K)	Altitude (m)	TAS (m s^{-1})	Rosemount enhancement
0.26 – 0.63	970	317	371	112	2.10 ± 1.08
0.63 – 1.73	970	317	371	112	2.36 ± 0.41
1.73 – 5.00	970	317	371	112	6.84 ± 0.34
5.00 – 15.00	970	317	371	112	0.55 ± 0.01
0.26 – 0.63	747	293	2500	126	2.16 ± 1.03
0.63 – 1.73	747	293	2500	126	2.73 ± 0.39
1.73 – 5.00	747	293	2500	126	6.40 ± 0.33
5.00 – 15.00	747	293	2500	126	0.88 ± 0.01
0.26 – 0.63	690	288	3100	127	2.15 ± 1.05
0.63 – 1.73	690	288	3100	127	2.96 ± 0.39
1.73 – 5.00	690	288	3100	127	6.39 ± 0.33
5.00 – 15.00	690	288	3100	127	0.16 ± 0.01
0.26 – 0.63	600	277	4170	137	2.12 ± 1.03
0.63 – 1.73	600	277	4170	137	3.10 ± 0.38
1.73 – 5.00	600	277	4170	137	5.63 ± 0.33
5.00 – 15.00	600	277	4170	137	0.30 ± 0.01

Table 34 Measurement conditions for Rosemount testing relative to a standard isokinetic inlet by on the DLR falcon (Petzold, 2009).

Diameter Range (μm)	Pressure (hPa)	Temperature (K)	Altitude (m)	TAS (m s^{-1})	Rosemount enhancement
0.25 – 0.45	873	280	1240	126	1.43 ± 0.28
0.45 – 0.80	873	280	1240	126	1.92 ± 0.60
0.80 – 3.00	873	280	1240	126	6.81 ± 7.00
0.25 – 0.45	725	273	2730	148	1.57 ± 0.20
0.45 – 0.80	725	273	2730	148	2.57 ± 0.89
0.80 – 3.00	725	273	2730	148	7.00 ± 7.80
0.25 – 0.45	290 - 410	233 - 244	7000 - 9400	163 - 200	2.53 ± 1.27
0.45 – 0.80	290 - 410	233 - 244	7000 - 9400	163 - 200	6.32 ± 5.76
0.80 – 3.00	290 - 410	233 - 244	7000 - 9400	163 - 200	7.20 ± 8.95

The analysis of enhancement factors across multiple atmospheric pressures is presented in figure 4.20. The data presented in this figure is primarily from 970 hPa to 560 hPa from flight B613, which performed multiple stacked legs. The enhancement factors from this study show a reasonable agreement to the results presented by Petzold (2009) up to our maximum pressure height of 600 hPa. There is little evidence in figure 4.20 of the increasing enhancement relative to the Rosemount with decreasing pressure height, as was observed by Petzold (2009). The size range 0.67 – 1.75 μm shows an increase in the enhancement factor from 2.29 at 965 hPa to 3.10 at 600 hPa, whilst the smaller size range (0.26 – 0.63 μm) shows no changes with height. Particles in the size region 1.73 – 5.0 μm are inconclusive.

Petzold (2009) was able to extend the study to a maximum pressure height of 290 – 410 hPa, whilst our investigation is limited to a maximum pressure height of 600 hPa, due to the operational set-up of the LTI. Petzold (2009) observed an increase in the enhancement factor across all particle size ranges at 290 – 410 hPa, relative to 873 and 725 hPa. For our study to be extended to assess the enhancement actor at a greater atmospheric pressure range the operational set-up of the LTI would have to be modified to increase that sample flow necessary to maintain isokinetic control to the maximum height.

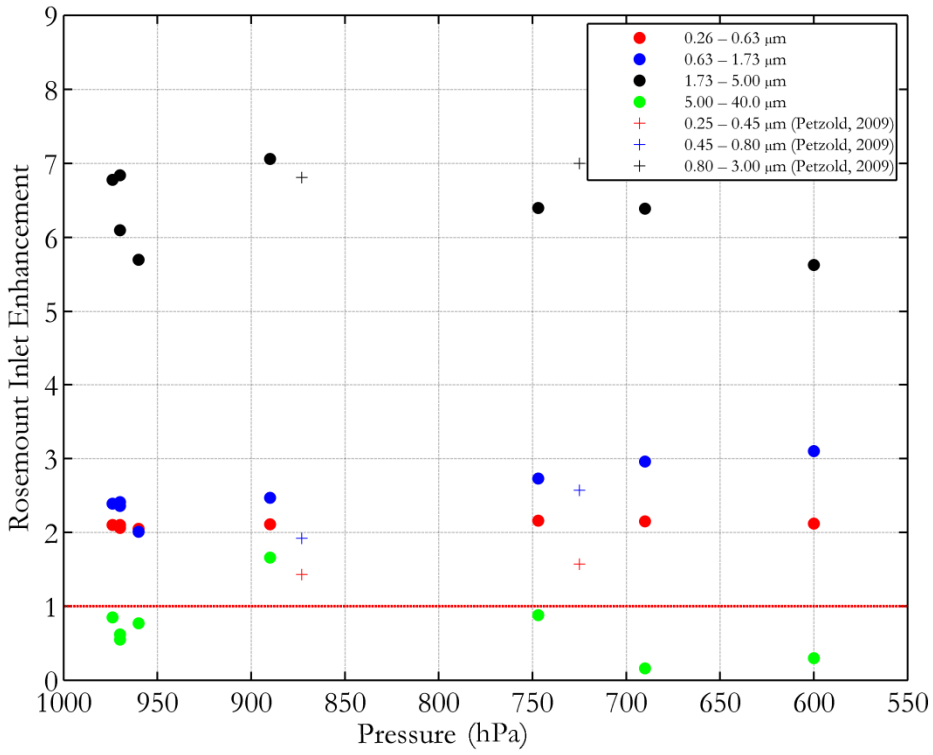

Figure 4.20 Rosemount to LTI number concentration termed Rosemount inlet enhancement, as a function of pressure for four sizing groups of the Sky-OPC. Circles relate to analysis based on flights B604, B612 and B613, and crosses show results from Petzold (2009).

The advantage in the application of the LTI as our reference inlet was the extension of the enhancement factor of the Rosemount inlet to larger particle sizes, whilst the study by Petzold (2009) was limited to 3.0 µm due to the limited isokinetic size range of the inlet on the DLR falcon. The similarity in our results compared with the Petzold study gives confidence that the enhancement factor can be applied to the other Rosemount inlets on the BAe-146. A complete Rosemount characterisation is a priority which should be carried out to remove uncertainty in this assumption.

4.5.2 Wing-Mounted Size Distribution Comparisons

The ambient aerosol size distribution is measured by the wing-mounted probes; the PCASP and CDP. This comparison draws on the ability to measure the ambient distribution with an instrument which itself does not sample from an inlet. The CDP is an open path instrument and sizes particles based on forward scattering; scattered laser

intensity is related to particle size with the application of Mie theory for water droplets over the instrument scattering angles of 4 – 12°. The forward scattering nature of the instrument has the potential to undersize coarse mode mineral dust due to the enhanced side-scattering associated with aspherical particles.

Although the PCASP is an externally mounted probe, a sampling feature of the instrument is an external nose cone, with a sub-sampler located at the base of the nose to extracts a proportion of the airflow to sample. Sampling corrections presented in Belyaev and Levin (1974) are routinely applied to account for the PCASP inlet sampling efficiencies; however sample uncertainties such as deviations from isokinetic flow and turbulent flow exist. Rosenberg et al. (2012) state that Reynolds numbers at the tip of the nose cone could be as high as 60 000 during flight; suggesting to the presence of turbulent eddies along the length of the PCASP nose cone.

In order to investigate the performance of the LTI in terms of coarse mode measurement, the final section of this chapter will compare aerosol characteristics (size distribution and scattering efficiency) measured at the LTI to that of externally mounted probes. Size distributions on a Sky-OPC mounted at the LTI are found to compare reasonably well with that of the externally mounted aircraft probes as presented in figure 4.21. There is a good agreement with the PCASP in the region of overlap (0.26 to 3.0 μm) which gives confidence that the size distribution measured in ambient air agrees with size measured after inlet sampling. There are small scale features in the size distributions presented in figure 4.21 which are instrument artefacts rather than real features in the size distribution. The gain stages of the PCASP are particularly evident (bin 5 and 16), where there is more uncertainty in the terms of the bin widths. The comparison of the PCASP with the LTI suggests the nose cone has a good passing efficiency, with the sampling corrections from Belyaev and Levin (1974) adequately accounting of the transmission efficiencies of the aerosol to the PCASP.

Quantification of the LTI by Wilson et al. (2004) found that at optimum operation that inlet isokinetically samples up to aerodynamic diameters of 15.0 μm, whilst in this study transmission losses are seen to dominate from 10 μm. The deviation in the sampling size of aerosol through the LTI from our results from Fennec data and that from Wilson et al. (2004) which could potentially be explained in two ways.

Stokes calculations for mineral dust were performed using a particle density of mineral dust aerosol of 2650 kg m^{-3} (Haywood et al., 2003a) whilst Wilson et al. (2004) performed the initial LTI characterisation used a lower density of 1750 kg m^{-3} representative of the aerosol composition measured during the testing stages of the LTI. In applying a larger density for the mineral dust aerosol, the corresponding aerodynamic diameter for a 10 μm particle measured by an OPC is greater than 15 μm found by Wilson et al. (2004). This would explain the deviation sooner from the CDP at 10 μm. This suggests that a compositional inlet characterisation is necessary.

Particle Stokes numbers assumed particle sphericity and as Wu and Colbeck (1996) discussed non-spherical particles will experience more drag than that of a sphere of the same volume. The influence of particle sphericity could impact the size distribution measured by the CDP; the shape factor being emphasized for larger particles.

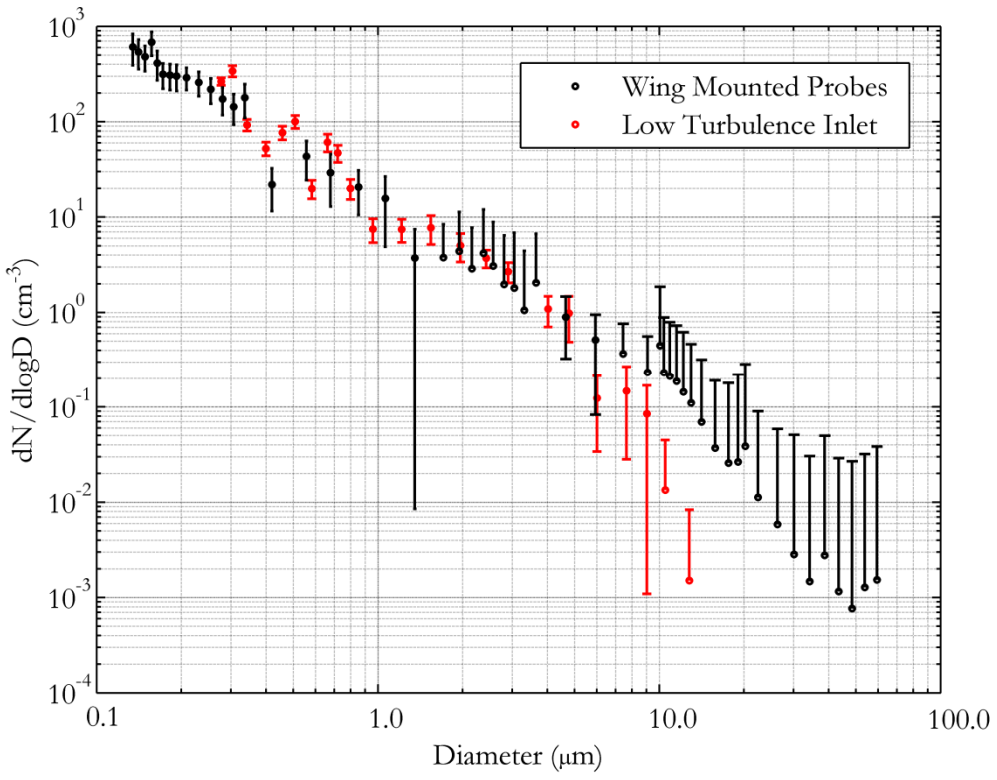

Figure 4.21 Campaign mean number size distribution comparison between the (*red*) LTI and (*black*) wing-mounted probes for runs with optimum isokinetic values of 1.0. Error bars which extend to negative numbers on the log scale have been omitted for clarity.

The size distributions measured at the Rosemount, LTI and wing-mounted probes are converted to a scattering efficiency term using theoretical Mie calculations, and the normalised scattering efficiency is presented in figure 4.22. It can be seen that for the ambient aerosol distribution measured by the wing mounted probes the scattering efficiency peaks at 6 μm. The scattering at the LTI is comparable to the ambient distribution to approximately 2 μm, peaking at 4 μm and the decreased transmission of particles through the LTI beyond 8 μm is emphasised in terms of scattering.

The Rosemount significantly overestimated the scattering efficiency between 2 – 4 μm, with the scattering distribution truncated for larger particle sizes. The LTI shows an improved representation of theoretical scattering distribution, however there is still some underestimation of the scattering efficiency at larger particles relative to the wing-mounted probes.

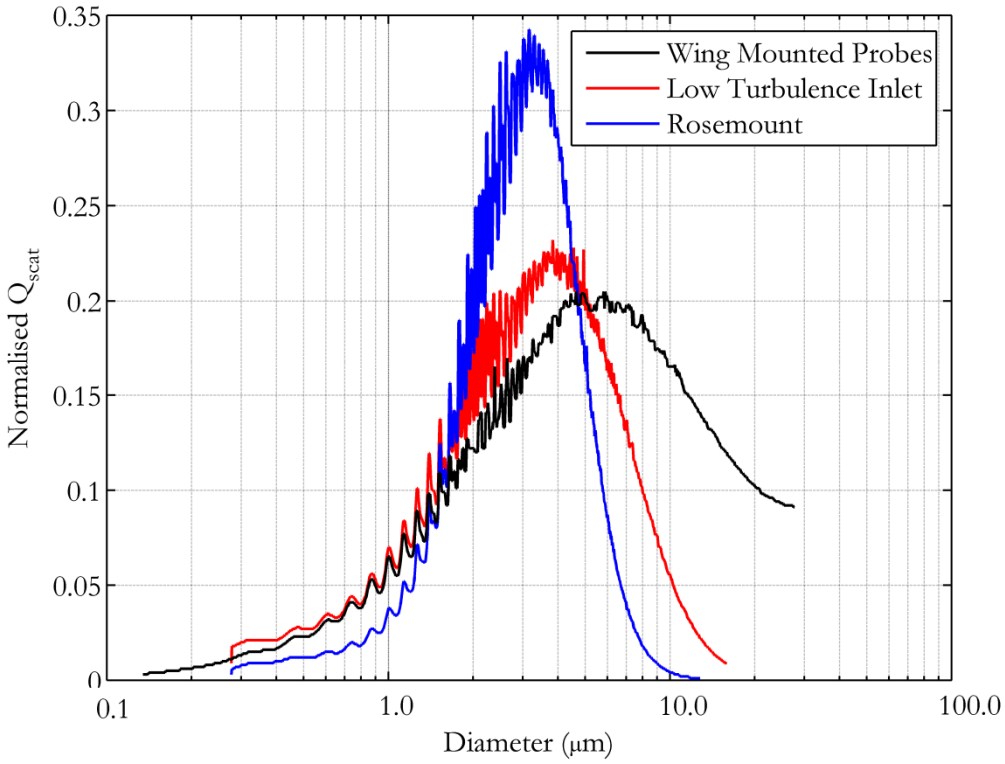

Figure 4.22 Normalised scattering efficiency from theoretical Mie calculations as a function of particle size for run 1 during flight B613 (26 June 2011) *(red)* LTI scattering efficiency, (*blue*) Rosemount scattering efficiency, (*black*) Wing-mounted probes scattering efficiency.

The instrument artefacts discussed in the previous section are accentuated, with large variability between the lowest bins of the Grimm can be seen in the corresponding mean surface area and volume size distributions, presented in figure 4.23. The surface area and volume size distributions also accentuate the deviation in the size distribution between the LTI and the wing-mounted probes for larger particle sizes. The measurements made at the LTI do not accurately represent mineral dust particle surface area or volume distributions beyond 10 μm, where transmission losses of particles are shown to dominate.

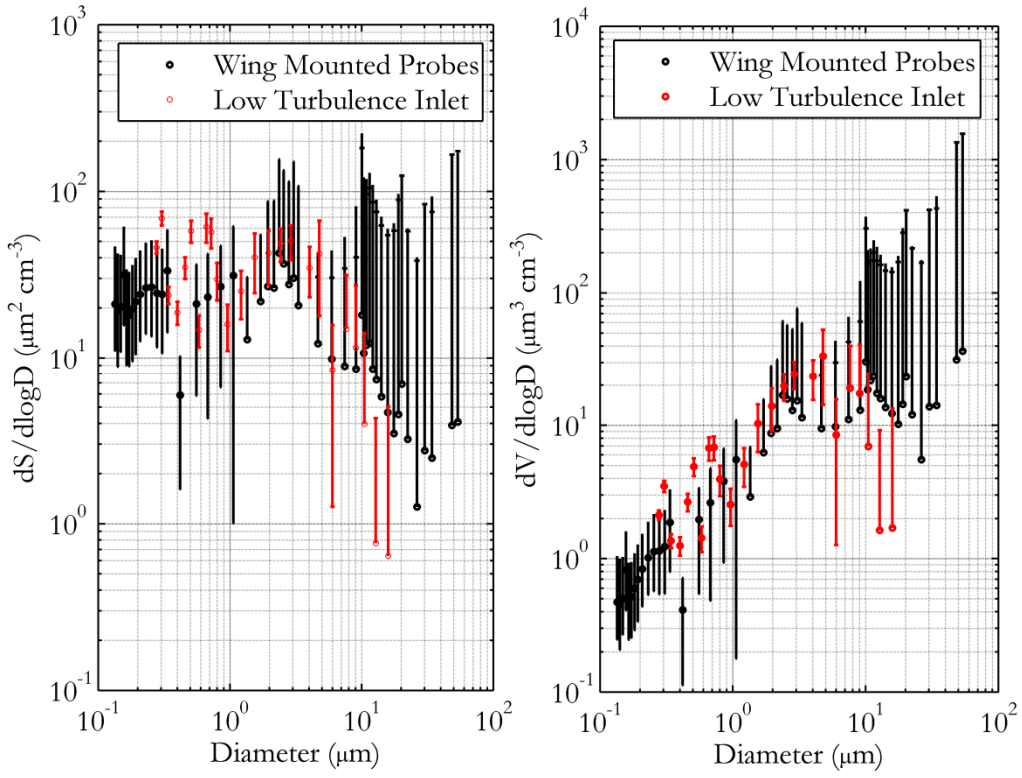

Figure 4.23 Campaign mean (*left*) surface area size distribution (dS/dlogD) and (*right*) volume (dV/dlogD) size distribution for runs with optimum isokinetic values of 1.0. (*red*) LTI Grimm size distributions and (*black*) wing-mounted size distribution. Error bars which extend to negative numbers on the log scale have been omitted for clarity.

4.6 Chapter Conclusion

A critical evaluation of the current aerosol sampling is a current limitation aboard the FAAM BAe-146 aircraft. The characterisation of the inlets is vital, and a necessary step when making aerosol measurements. In reality no inlet will successfully sample the

whole aerosol size distribution without modification, but with well characterised experiments to quantify the inlet efficiencies, it is possible to account for any changes to the measured size distribution. Recent advances in characterising aerosol sampling have coincided with the installation of the LTI, which has provided a platform for performing inlet comparison experiments with the current aircraft Rosemount inlets. Through understanding Rosemount inlet efficiencies it has been possible for aircraft users to apply corrections to measurements made at instrument to account for the aerosol sampling system (Ryder et al. 2013).

The performance of the LTI during the Fennec 2011 campaign was investigated within this chapter. It was found that the LTI is optimally isokinetic up to 800 hPa, with a transition region identified between 700 hPa and 600 hPa, where isokinetic values are greater than 0.75, a lower limit to the inlet performance, but less than the optimum value of 1.0. It has been shown by Wilson et al. (2004) that with the use of a more powerful pumping system controlling the sampling flow, the LTI is fully operational up to 370 hPa. This calls for improvements to the operational set-up of the LTI in this study, which will allow for an extension to the present operational capacity of the inlet. The mean Reynolds numbers of the system was found to be 239 and within the theoretical laminar regime (Reynolds numbers less than 2300) throughout the operational limits of the LTI.

The work presented within this chapter is the first investigative study of inlet characterisation of the primary aerosol inlets (modified Rosemount 102E housings) on the BAe-146 aircraft. It has previously been acknowledged of the inherent difficulties in gaining a representative aerosol sample through these inlets. For particles below 1.0 μm the Rosemount inlet enhancement, that is the concentration at the Rosemount inlet relative to the LTI, is 1.5 - 2 times of that measured at the LTI. For 3.0 μm particles the Rosemount inlet enhancement peaks at approximately 8 times that of the LTI. For particles in the range of 3.0 μm to 7.0 μm the enhancement decreases approaching the unity line where the LTI and Rosemount measure equal concentration. Beyond 7.0 μm, particle concentration is underestimated.

The Rosemount inlet is characterised as sub-isokinetic in nature with particle enhancement greatest in the size range of 1.7 – 5.0 μm. This goes against previous discussions where it was suggested the Rosemount inlet samples within a super-

isokinetic regime. Haywood et al. (2003b) had suggested that the Rosemount inlet collection efficiency drops from close to unity to zero for particle radii greater than 1-2 μm. This has now been shown to be an incorrect representation of how the Rosemount samples aerosol particles.

This study found little evidence of the increasing particle enhancement of the Rosemount inlet as the pressure height of the aircraft varied, that was observed in a study by Petzold (2009). The similarity in our Rosemount enhancement factor in low-level aircraft runs compared with Petzold (2009) gives confidence that the enhancement factor could be applied to the other Rosemount inlets on the BAe-146. However, a complete Rosemount characterisation is a priority to remove uncertainty in this assumption. Although an inlet characterisation is a necessary step forward in aerosol measurements on the BAe-146 aircraft, it should be acknowledged of the unsuitability of the Rosemount inlets as the long-term primary aerosol inlet. This chapter provides motivation for discussions within the research community to investigate the replacement of the Rosemount inlets; details of which will be discussed in the further work and recommendations in section 7.2.1.

Mineral dust size distributions measured at the LTI were compared to size distributions measured by the externally-mounted probes; the PCASP and CDP. This experiment draws on the ability to measure the ambient size distribution with an instrument which itself does not sample from an inlet. Transmission losses of particles through the LTI have been shown to play a role for particle diameters greater than 5 μm. Beyond 10.0 μm transmission losses in the LTI are seen to dominate and there is little agreement in size distribution measurements between the LTI and the CDP. Surface area and volume size distributions presented accentuated these transmission losses.

The installation and use of the LTI represents a significant advance in the ability to representatively sample populations of coarse mode aerosol from the BAe-146 research aircraft. It is emphasised of the importance of measuring aerosol coarse mode and the difficulty in accurately sampling these particles. The impact of accurately measuring the coarse mode of mineral dust on the aerosol optical properties during Fennec is presented in chapter 5.

5 Mineral Dust Aerosol: Fennec Observations

The importance of making reliable size distributions has been emphasised in chapter 4; understanding the contribution of the aerosol coarse mode to parameters used to constrain and assess the radiative properties of mineral dust, in terms of the single scattering albedo and asymmetry parameter, is investigated within this chapter. Mineral dust size distributions measured at the LTI were compared to size distributions measured by the externally-mounted probes; an experiment which draws on the ability to measure the ambient size distribution with an instrument which itself does not sample from an inlet. The quantification will reduce some of the uncertainty in the impact of inlets on the sampling of coarse mode, and help explain the considerable variability which has been observed across previous field campaigns, in terms of the the current microphysical and optical properties of mineral dust. The variability in the optical properties between the pilot, Fennec 2011 and Fennec 2012 campaigns compared with previous campaigns is additionally investigated.

This chapter presents a multi-instrument analysis of mineral dust properties from the Fennec aircraft campaign. *In-situ* optical properties in terms of extinction coefficients, Ångström exponent and single-scattering albedo are presented from the Fennec pilot, the Fennec 2011 and 2012 campaigns in section 5.1. Observations between LTI and the wing-mounted probe measurements are extended to show the impact in terms of the mineral dust optical properties, specifically the single-scattering albedo (section 5.1.2) and the asymmetry parameter (section 5.1.3) from Mie calculations assuming a spherical particle (Wiscombe, 1980).

The coarse mode of mineral dust has been proposed as an important for heterogeneous uptake, with freshly emitted Saharan dust suggested as potentially a significant route of ozone loss. The *in-situ* aerosol and chemistry measurements during the Fennec campaigns will be investigated to identify case studies of increased mineral dust surface

area associated with fresh dust uplift correlated with reduced ozone concentrations. HYSPLIT back trajectories will be used to identify the source of air masses to understand ozone source regions. The regional vertical aerosol structure from the aircraft platform is presented in section 5.2. Previous observations of elevated mineral dust concentrations and ozone depletion events are extended in section 5.3 to include a correlation with increased mineral dust surface area associated with elevated dust concentrations. The observations presented here are low level *in-situ* measurements, that is, close to the source of mineral dust uplift events. Two case studies are presented from the Fennec 2011 and 2012 campaigns, B614 (27 June 2011) and B707 (15 June 2012), respectively. These flights measured localised fresh dust uplift associated with a LLJ. Air-mass back trajectory along the aircraft flight track using the HYSPLIT back-trajectory model is presented in section 5.3.2.

5.1 In-situ Optical Properties

The campaign-average aerosol optical properties in terms of the extinction coefficients, Ångström exponent and single-scattering albedo during the Fennec pilot, Fennec 2011 and Fennec 2012 are presented in table 35. These shall be compared with those from previous field campaigns as were presented in the literature review in chapter 1.

Table 35 Campaign-average *in-situ* dry extinction coefficients at 550 nm (Mm^{-1}), Ångström exponent, single-scattering albedo during Fennec pilot, Fennec 2011 and Fennec 2012. The minimum and maximum ranges of each parameter are presented in brackets. *In-situ* analysis is performed for only the lowest level SLRs for each flight.

	Fennec Pilot	Fennec 2011	Fennec 2012
b_{ext}	120 (50 to 216)	331 (120 to 534)	305 (25 to 1233)
Å	0.06 (0.67 to - 0.18)	-0.21 (-0.05 to -0.36)	-0.22 (0.47 to -0.45)
ω_0	0.96 (0.95 to 0.97)	0.96 (0.94 to 0.97)	0.95 (0.93 to 0.97)

5.1.1 Extinction Coefficients and Ångström Exponents

The average Ångström exponents for the Fennec 2011 and 2012 campaigns were -0.21, which is a significantly smaller campaign-average than from previous observational field campaigns. The average Ångström exponent from the pilot campaign was 0.06 with a range of -0.18 to 0.67, corresponding mineral dust extinction coefficients were in the range of 50 to 216 Mm^{-1}. This result is consistent with measurements from DABEX (Osborne et al., 2008) and GERBILS (Johnson and Osborne, 2011) which ranged from -0.18 to 0.66. Johnson and Osborne (2011) found that the Ångström exponent is anti-correlated with mean particle diameter, which indicates that the large Ångström exponents suggest a dominance of fine mode mineral dust during the pilot campaign.

The Ångström exponent for the Fennec 2011 campaign ranged from -0.36 to -0.05 which indicated a large contribution of the mineral dust coarse mode to the size distribution during all flights of the campaign. The Ångström exponent for the Fennec 2012 campaign saw a larger range from -0.45 to 0.47, attributed to the different meteorological events encountered during the campaign. Considerable variability is shown in terms of the measured *in-situ* extinction coefficients, which ranged from 25 to 1233 Mm^{-1} during the Fennec 2012 campaign.

A strong Atlantic inflow dominated the meteorological situation during the early part of Fennec 2012 field campaign. The inflow in part was driven by a low pressure which deepened in eastern Algeria between 2 June and 6 June. The position of the low pressure brought a north-westerly Atlantic flow, with maritime conditions observed across Western Sahara and Mauritania. The first two flights of Fennec 2012, B699 (6 June 2012) and B700 (8 June 2012), made *in-situ* measurements of the Atlantic inflow. The Atlantic inflow was associated with low aerosol extinction coefficients (25 – 40 Mm^{-1}), and measured a higher Ångström exponent of 0.14 and 0.47, for B699 and B700, respectively. This signified a small coarse mode contribution to the aerosol size distribution.

The variation in the range of mineral dust extinction coefficients presented in table 35, reflects the different dust emission mechanisms sampled during the Fennec campaigns. Strong dust uplifts such as those investigated during B708 (16 June 2012), with a flight average extinction coefficient of 1233 Mm^{-1}, were associated with a strong low level jet

across central-eastern Mauritania into central-western Mali, which was formed by Atlantic inflow converging with Harmattan flow from Algeria.

5.1.2 Single-Scattering Albedo

The *in-situ* single-scattering albedo from PSAP and nephelometer instruments during the Fennec campaign is consistent across the pilot and the two main campaigns, ranging from 0.93 to 0.97. The single-scattering albedo is comparable to that found during the SAMUM (Kandler et al., 2011; Müller et al., 2011) and GERBILS campaigns (Johnson and Osborne, 2011). It was discussed within the literature review of the importance in the single-scattering albedo towards understanding the radiative properties of mineral dust. The consistency in the single-scattering albedo during the three campaigns, and consistency with previous campaigns suggests that the single-scattering albedo is a better understood parameter for Saharan mineral dust.

The cumulative contribution of coarse mode of mineral dust measured by the LTI and wing-mounted probes to the single-scattering albedo for a low dust loading case (B613, 26 June 2011) calculated from Mie theory is presented in figure 5.1**.** A widely used Mie code is MIEV0 Fortran code (Wiscombe, 1980) which treats the aerosol as a homogeneous aerosol distribution; this implies that the particle is characterised by a single refractive index at a given wavelength. Computed outputs include the scattering and extinction efficiencies (Q_{ext}, Q_{scat}) and the asymmetry parameter. The LTI data presented in includes the cumulative effects of bin 15 – bin 30, data below bin 15 has been excluded in the analysis due to large variations in number concentrations in these lowest bins. This made the fitting of the aerosol size distributions unreliable. A refractive index of $m = 1.53 + 0.001i$ has been applied (Ryder et al., 2013b).

The importance of the coarse mode in calculating the single-scattering albedo has been highlighted and thus it is highly important to constrain the radiative properties of mineral dust. Below particle diameters of 10 μm, the single-scattering albedo of mineral dust is captured to a similar extent between the LTI and the wing-mounted probes. It is evident that beyond 10 μm transmission losses in the LTI sampling line dominate, resulting in a truncation of the single-scattering albedo at 0.977. The total cumulative contribution of the CDP size distribution accounts for a single-scattering albedo of 0.966.

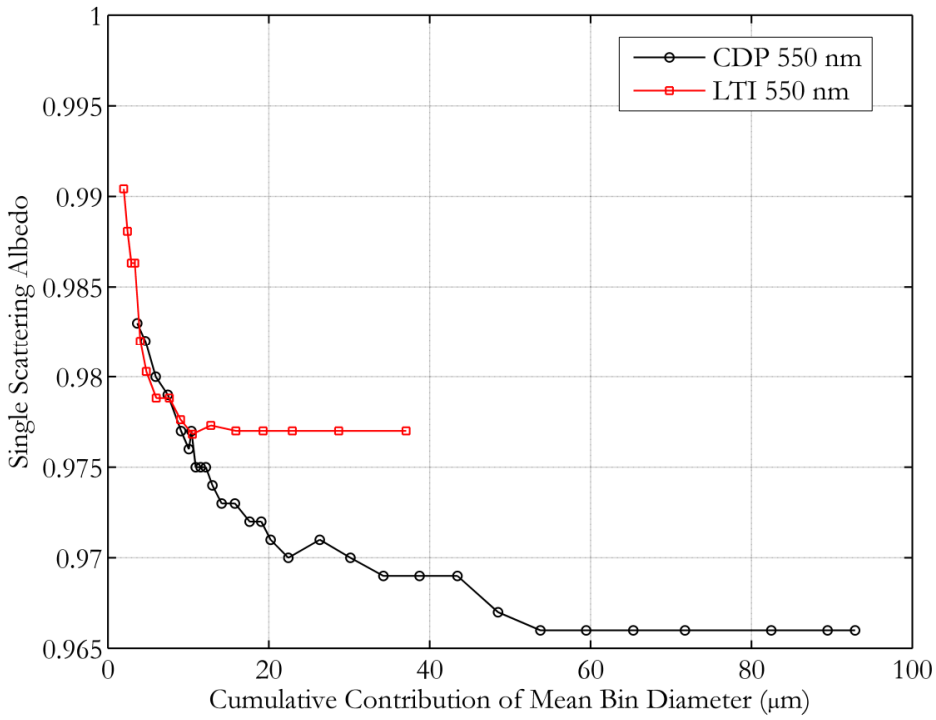

Figure 5.1 Cumulative contribution of coarse mode of mineral dust to the single-scattering albedo measured by (*black*) the CDP compared with the (*red*) LTI for the low dust loading case (B613, 26 June 2011) from theoretical Mie calculations. Values plotted are the flight medians from the PCASP and CDP size distributions assuming $m = 1.53 - 0.001i$ N.B. the first data point at 3.64 μm is equivalent to the contribution of the total PCASP distribution to the single-scattering albedo whilst the first data point of the LTI is equivalent to 2.0 μm.

5.1.3 Asymmetry Parameter

A number of models require a simplification of the phase function and often use a single parameterized value such as the asymmetry parameter for constraining the radiative properties of mineral dust. Establishing the value of the asymmetry parameter for atmospheric mineral dust is highly important. As there is no direct method for measuring the aerosol asymmetry parameter, the parameter is derived from Mie scattering calculations using flight mean number size distribution from the wing-mounted probes.

The asymmetry parameter at 550 nm during Fennec 2011, as presented in figure 5.2, ranged from 0.71 to 0.81 with a mean of 0.77. The largest values of the asymmetry parameter were observed during the first part of the campaign for flights B600 – B602,

consistent with strong dust uplift conditions and a large proportion of coarse mode particles were encountered during these flights. Observations from SAMUM 2006 found large asymmetry parameter of 0.79, which reflects the contribution of coarse mode particles in the dust population, and suggests large forward scattering properties of the mineral dust (Otto et al., 2007). The results of Fennec 2011 are broadly consistent with the results from SAMUM.

The CDP sizes particles based on forward scattering; that is, the scattered laser intensity is related to particle size with the application of Mie theory for water droplets over the instrument scattering angles of 4 – 12°. The forward scattering nature of the instrument has the potential to undersize coarse mode mineral dust due to the enhanced side-scattering associated with aspherical particles. Ryder et al. (2012) have show good agreement between the CDP and the Small Ice Detector 2H (SID2H) and the Cloud Imaging Probe (CIP) for the campaign-average size distributions, which gives confidence in the mineral dust size distribution measured in Fennec. Here no attempts have been made for particle asphericity; accounting for the effects of dust asphericity measured by the CDP would tend to lower the calculated value of the asymmetry parameter, due to the enhanced side-scattering associated with aspherical particles.

Figure 5.3 shows the cumulative contribution of coarse mode of mineral dust measured by the LTI and wing-mounted probes to the asymmetry for two dust cases; high dust loading (B600 17 June 2011) and low dust loading (B613 26 June 2011). Large values of the asymmetry parameter (B600) results in less reflected solar radiation from mineral dust aerosol (i.e. greater forward scatter) than does a small value of the asymmetry parameter such as in the case of the low dust loading (B613).

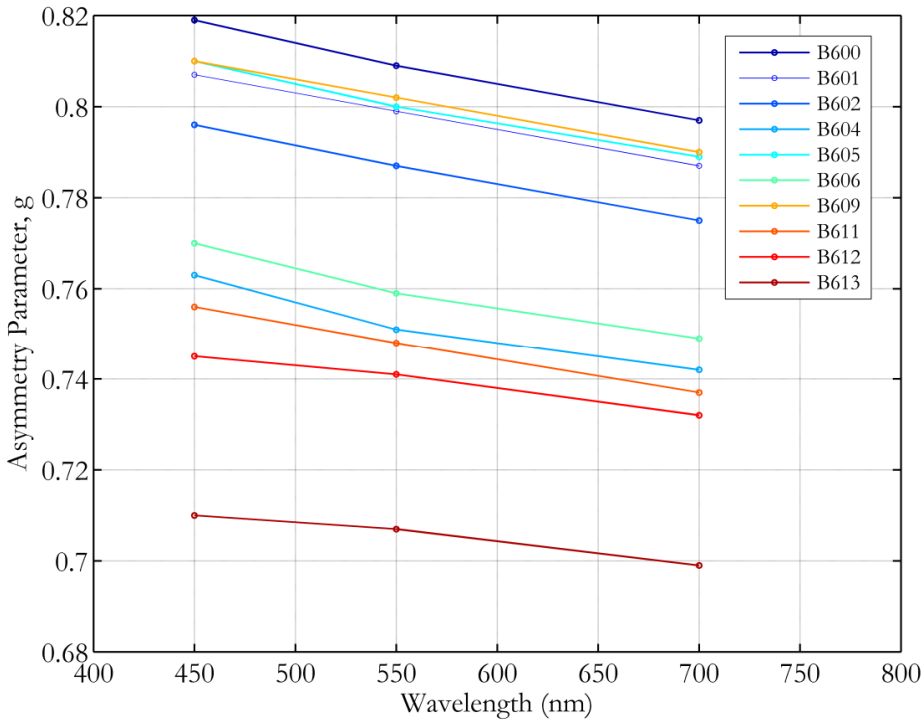

Figure 5.2 Variation in the asymmetry parameter with wavelength during Fennec 2011 from theoretical Mie calculations. Values plotted are the flight medians from the wing-mounted size distributions assuming $m = 1.53 - 0.001i$ (that is, no change was made for spectral dependence of refractive index).

Figure 5.3 shows the cumulative contribution of coarse mode of mineral dust measured by the LTI and wing-mounted probes to the asymmetry for two dust cases; high dust loading (B600 17 June 2011) and low dust loading (B613 26 June 2011). Large values of the asymmetry parameter (B600) results in less reflected solar radiation from mineral dust aerosol (i.e. greater forward scatter) than does a small value of the asymmetry parameter such as in the case of the low dust loading (B613).

The plot emphasises the strong contribution of the coarse mode of mineral dust to the asymmetry parameter as measured by the CDP. The inclusion of the second bin of the CDP increases the asymmetry parameter from 0.70 to 0.76. The largest sensitivity in the asymmetry parameter is the representation of coarse mode mineral dust diameters up to 20 μm. For both dust loadings, it can be seen that the asymmetry parameter is largely unchanged beyond 50 μm, which indicates the low abundance of these ultra large particles. Figure 5.3 emphasises the importance of accurately representing the coarse mode from *in-situ* size distribution measurements.

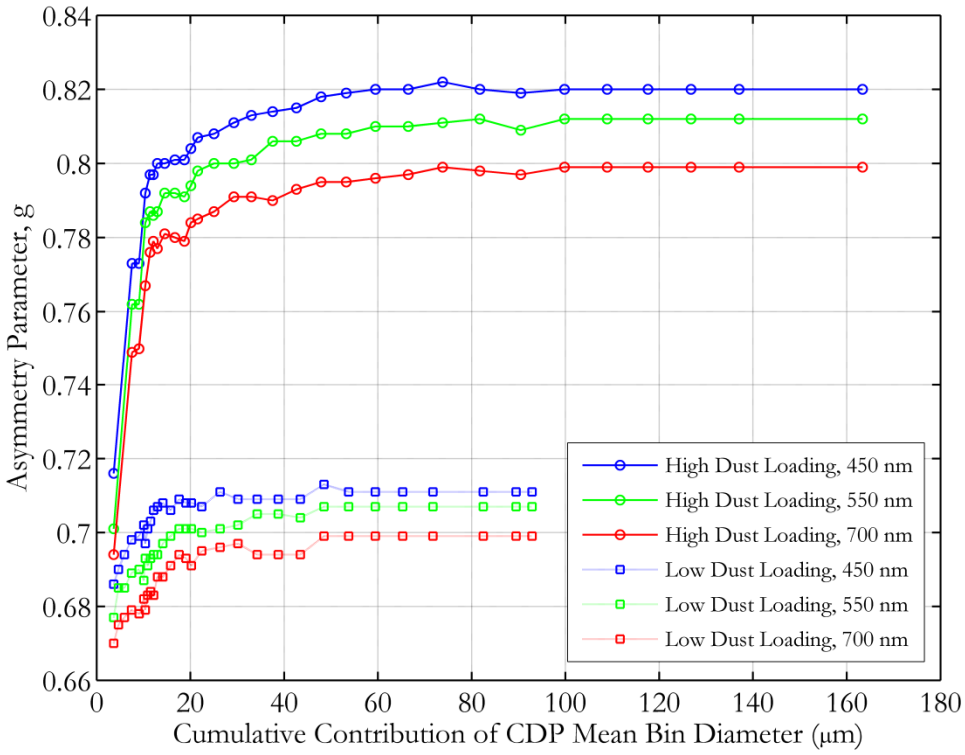

Figure 5.3 Cumulative contribution of coarse mode of mineral dust to the asymmetry parameter measured by the CDP, presented in terms of the CDP mean bin diameter for high dust loading (B600, 17 June 2011) and low dust loading (B613, 26 June 2011) from theoretical Mie calculations. N.B. the first data point at 3.64 μm is equivalent to the contribution of the total PCASP distribution to the asymmetry parameter. Values plotted are the flight medians from the PCASP and CDP size distributions assuming $m = 1.53 - 0.001i$ (that is, no change was made for spectral dependence of refractive index).

Figure 5.4 shows the cumulative contribution of coarse mode mineral dust to the asymmetry parameter measured at the LTI, contrasted with the cumulative contribution of coarse mode mineral dust measured by the CDP. It can be seen that the size distribution measured at the LTI over estimates the asymmetry parameter at smaller particle sizes (< 10 μm) across the three wavelengths (450 – 700 nm). At a wavelength of 450 nm, the total cumulative contribution of coarse mode mineral dust at the LTI converges on that of the total asymmetry parameter. At larger wavelengths, the LTI asymmetry parameter is underestimated relative to that calculated from the CDP measurements from Mie calculations.

Transmission losses of particles through the LTI have been shown to play a role for particle diameters greater than 5 μm. Beyond 10.0 μm transmission losses in the LTI are seen to dominate which is reflected by the differences in the asymmetry between the LTI and the CDP at larger wavelengths. This result places emphasis on the importance of coarse mode contribution to mineral dust optical properties; highlighting the need to make accurate measurements of the initial size distribution. This result stresses the need to carry out further characterisations of the aircraft inlets in order to understand the influence of the sampling system of the inferred mineral dust optical properties.

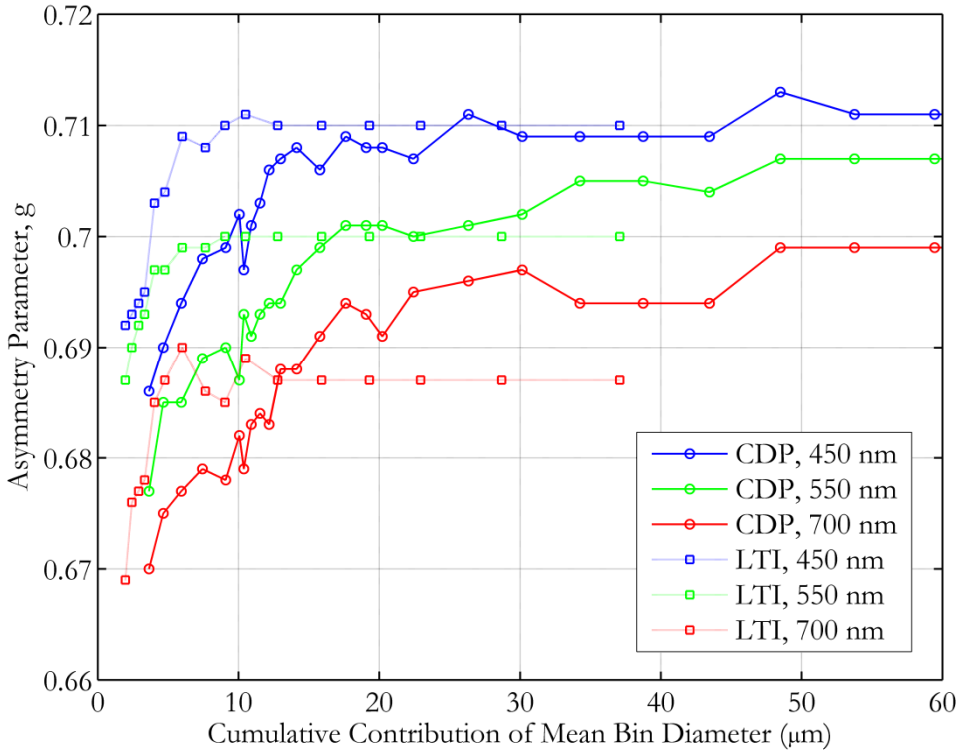

Figure 5.4 Cumulative contribution of coarse mode of mineral dust to the asymmetry parameter measured by the CDP compared with the LTI for the low dust loading case (B613, 26 June 2011) from theoretical Mie calculations. Values plotted are the flight medians from the PCASP and CDP size distributions assuming $m = 1.53 - 0.001i$ (that is, no change was made for spectral dependence of refractive index).

5.2 Mineral dust and ozone

The vertical distribution of mineral dust is important for a number of reasons: the vertical distribution strongly affects aerosol forcing both in the shortwave and longwave (Hansen et al., 1997; Haywood et al., 1999); it also influences aerosol transport between regions (Kim et al., 2009). In representing aerosol vertical profiles, an assumption of that profile is often based on ground-based observations such as aerosol extinction coefficients or mass concentrations. Aerosol concentrations are treated as being constant throughout the boundary layer, with concentrations decreasing exponentially with height above the boundary layer. The representation of the aerosol fine structure is rarely represented, particularly elevated aerosol layers which can be radiatively important. Aerosols attenuate shortwave radiation, reduce surface heating and hence sensible heat transportation from the surface and increase the downward longwave radiance. These processes lead to two opposing effects in terms of warming and cooling; the combined effects depend on the aerosol type, concentration and height and as such it is important to understand the variability in these remote regions (Hansell et al., 2009).

Aircraft profiles of mineral dust extinction coefficients derived from *in-situ* measurements and corresponding tephigrams from B612 (26 June 2011) are presented in figure 5.5. The true air temperature presented in the tephigram is measured by a Rosemount non de-iced temperature sensor, and the dew point temperature from the General Eastern instrument.

Between 920 hPa and 580 hPa the profile of atmospheric temperature is close to the dry adiabatic lapse rate. Air temperature at the close to the surface is 318 K, with the specific humidity is 3.5 g kg^{-1} and shows little variation from the surface up to ~600 hPa. A temperature inversion at 560 hPa is accompanied by a strong hydrolapse (that is temperature increasing with height, in association with a rapid decrease in moisture content of the air). The dry aerosol extinction coefficients show a well mixed dust layer between 950 and 600 hPa, with mineral dust extinction coefficients of 150 Mm^{-1} decreasing to 120 Mm^{-1} with height. A marked temperature inversion (3 K) caps localised mineral dust uplift in stable surface layer below 950 hPa. The mineral dust extinction coefficients in this surface layer reach a maximum of 190 Mm^{-1} reducing to 120 Mm^{-1} above the temperature inversion.

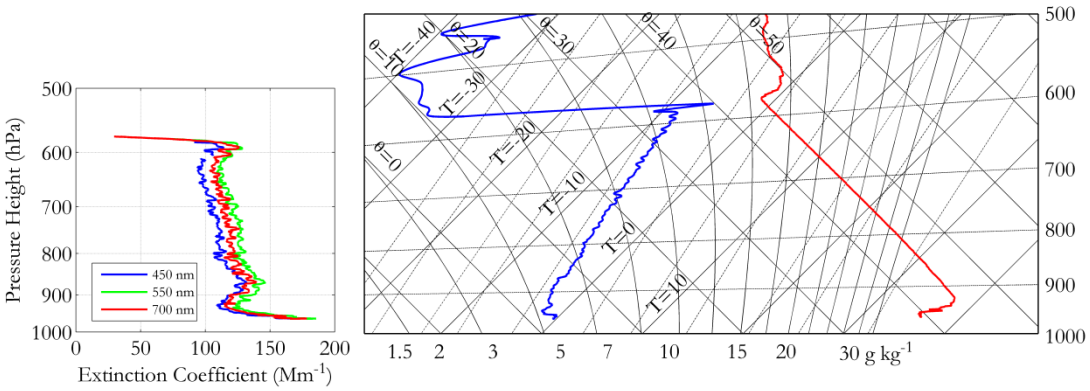

Figure 5.5 (*left.*) Dry aerosol extinction coefficients (*blue*) 450 nm (*green*) 550 nm and (*red*) 700 nm (*right*) tephigram of vertical profiles of temperature and humidity for B612 (26 June 2011).

The corresponding vertical profile of mineral dust extinction coefficient and ozone concentrations is presented in figure 5.6. Above the top of the atmospheric boundary layer at 580 hPa, ozone concentration increase significantly to 70 – 100 ppbv. Within the dust layer the ozone mass mixing ratio decreases sharply from the upper troposphere ozone concentrations to 47 ppbv and remains relatively constant to 920 hPa. This type of vertical profile has been commonly observed (De Reus et al., 2000; McConnell et al., 2008; Osborne et al., 2008). Interestingly, in the surface layer below 920 hPa, a further decrease in ozone concentration to 38 – 39 ppbv is observed, that is a decrease of almost a 20 % in ozone concentration, which correlates with the localised fresh mineral dust uplift in this layer,. The Ångström exponent within the surface layer was -0.35, indicating a coarse mode mineral dust contribution; within the main boundary the Ångström exponent was -0.45.

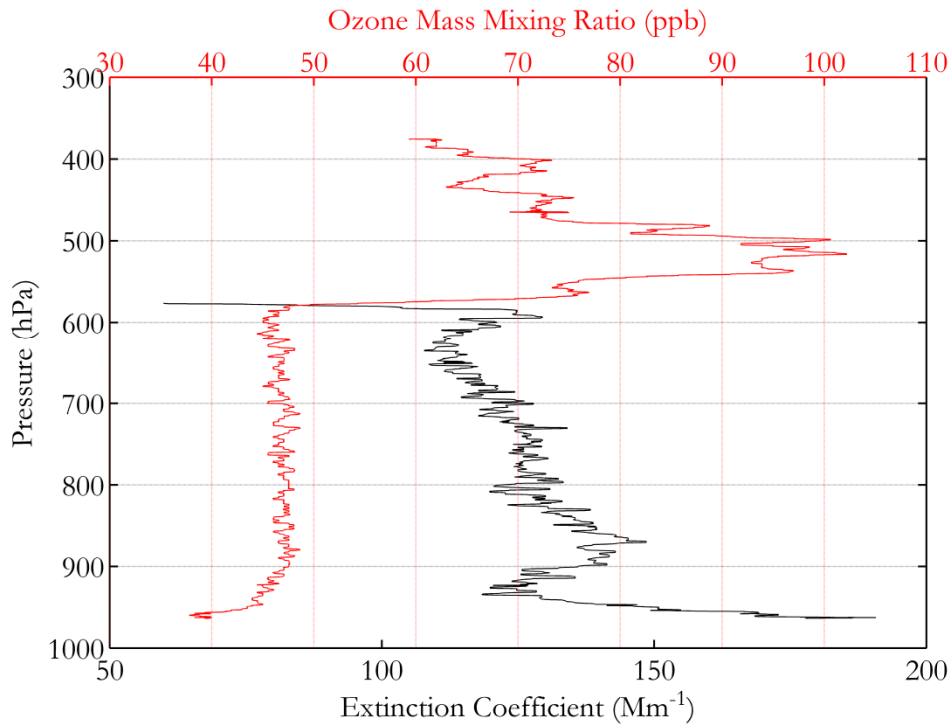

Figure 5.6 Vertical profile of (*black*) dry extinction coefficients at 550 nm and (*red*) ozone mass mixing ratio for B612 (26 June 2011).

5.3 Mineral Dust Mean Surface Area and Ozone

The campaign-average ozone concentrations during the Fennec pilot, Fennec 2011 and Fennec 2012 are presented in table 36. The ozone concentrations show reasonable consistency, with a campaign-average in the range of 36 – 46 ppbv. The Fennec 2012 campaign measured lowest ozone concentrations (22 – 26 ppbv) associated with the Atlantic inflow events observed during the campaign. Placing these observed concentrations in the context of previous measurements is somewhat difficult due to a relatively sparse observations. Güsten et al. (1996) made *in-situ* ozone measurements in the western Libyan desert during March and April, 2003 observing that northerly winds were associated with higher ozone concentrations in the range of 45 – 50 ppbv, with maxima of 60 ppbv. In southerly winds, Güsten et al. (1996) found relatively low ozone concentrations in the range of 25 – 40 ppbv. Bonasoni et al. (2004) made measurements of ozone concentrations at the Mt Cimone sites during Saharan air masses finding

seasonally-detrended ozone concentrations of 50 ± 8 ppbv. These literature values show a broad agreement with those measured during the Fennec campaigns.

Table 36 Campaign-average *in-situ* ozone concentrations (ppbv) during Fennec pilot, Fennec 2011 and Fennec 2012. The minimum and maximum ranges of each parameter are presented in brackets. *In-situ* analysis is performed for only the lowest level SLRs for each flight.

Fennec	O_3 (ppbv)
Pilot	46 (41 to 51)
2011	42 (34 to 50)
2012	36 (22 to 43)

5.3.1 Mineral Dust and Ozone: Case Studies

This section extends previous observations of elevated mineral dust concentrations and ozone depletion events, thereby correlated with increased mineral dust surface area associated with elevated dust concentrations. The observations presented here are low level SLR *in-situ* measurements, that is, associated with fresh mineral dust uplift. The hypothesis presented here suggests that fresh mineral dust uplift have a large coarse mode contribution coupled with freshly exposed mineral dust surface sites which act as a route for the ozone loss observed. Two case studies are presented, B614 on 27 June 2011 (table 37) and B707 on 15 June 2012 (table 38). Mineral dust mean surface area is calculated from the PCASP and CDP datasets in the case of B707. No size distributions measurements are available from the PCASP and CDP during B614, and therefore the Ångström exponent is used as a proxy for particle size.

Table 37 Aircraft profiles (P) and straight and level runs (R) for B614 (27 June 2011).

Run Number	Time (UTC)	Altitude (m)	Pressure (hPa)	Details
P1	06:34 – 06:51	-	-	Profile Ascent FUE
P2	07:42 – 08:00	7620 - 400	-	Profile Descent OpArea
R1.1	08:00 – 08:52	400	970	SLR (A – B)
R1.2	08:56 – 09:58	400	970	SLR (B – A)
P3	12:08 – 12:21	-	-	Profile Descent FUE

Table 38 Aircraft profiles (P) and straight and level runs (R) for B707 (15 June 2012).

Run Number	Time (UTC)	Altitude (m)	Pressure (hPa)	Details
P1	09:13 – 09:29	-	-	Profile Ascent FUE
P2	10:29 – 10:43	8550 - 350	-	Profile Descent OpArea
R1	10:43 – 12:04	350	970	SLR (A – B)
R2	12:32 – 14:03	8800	315	High level SLR (B-A)
P3	14:03 – 14:34	-	-	Profile Descent FUE

5.3.2 HYSPLIT Back Trajectories

The NOAA Air Resources Laboratory (ARL's) HYbrid Single Particle Lagrangian Integrated Trajectory Model (HYSPLIT) was used for the computation of simple air parcel back trajectories from along the BAe-146 flight path of the two case studies (Draxler, 1999; Draxler and Hess, 1997, 1998). HYSPLIT is a well-characterised back trajectory model with 23 vertical pressure levels (1000 – 20 hPa) and computations used the default vertical motion. The model meteorological dataset to drive the simulation uses the NCEP/NCAR Global Data Assimilation System (GDAS1) weekly dataset with data on a 1º (360º by 181º) latitude-longitude grid. A back trajectory was computed every 30 seconds along the flight path, which is constrained by only producing trajectory below 500 m in height along the flight path, that is a back trajectory is only produced for the lowest SLR in the flight. The accuracy of the trajectories are limited by the accuracy and resolution of the 3D wind fields used in GDAS1 dataset (Freitag et al., 2014). Convection in HYSPLIT is not parameterised; the model interpolates the GDAS data onto its terrain-following coordinate system (Draxler and Hess, 1997). For the applications of the back trajectories used here the use of the HYSPLIT model is sufficiently acceptable. This treatment for identifying air mass back trajectories assumes that mineral dust is uplifted along the back trajectory; the use of SEVIRI images are used to identify regions of dust emission.

Atmospheric back trajectories were run along the B614 flight track below 500 m; that is for run 1.1 and 1.2 and excluded the takeoff and landing profiles. Flight B614 consisted of a long low-level run southwards into northern Mauritania with a reciprocal return track travelling north on the same flight path. At the southern end of the flight track the

back trajectory shows low level airflow from 0 – 1500 m, consistent with Harmattan flow whilst the northern part of the flight track the back trajectory shows descending airflow from 3000 – 4500 m.

The LAM output discussed in chapter 2 for the 27 June 2011 forecast a low of 1004 hPa centred on the Algeria and northern Mali border, with an intensification of the Harmattan flow to the north of this low extending out of central Algeria showed a maximum in the horizontal winds at 925 hPa at 0600 UTC of 24 m s^{-1}. The 0900 UTC forecast showed the weakening of the jet with winds decreasing to 12 m s^{-1}.

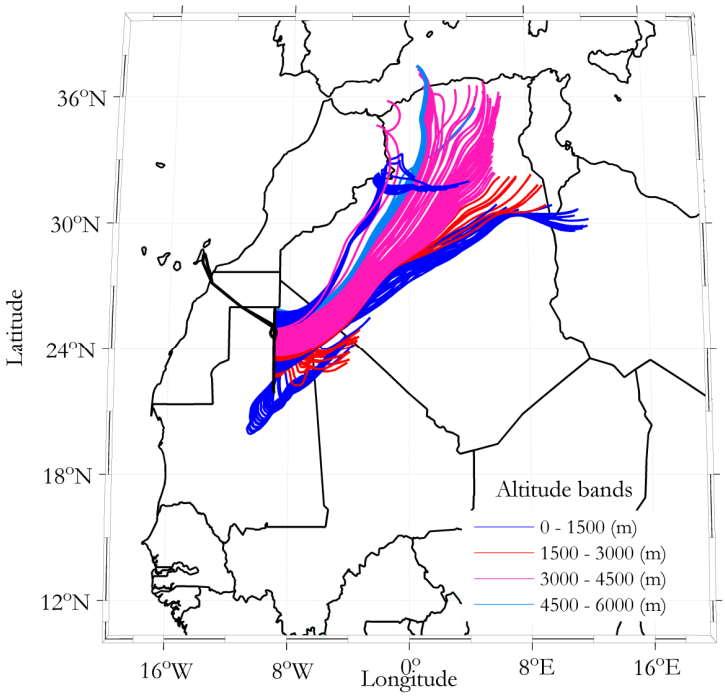

Figure 5.7 HYSPLIT back-trajectories over 90 hours along the flight track of B614 (27 June 2011) for four starting heights (*dark blue*) 0 – 1500 m (*red*) 1500 – 3000 m (*pink*) 3000 – 4500 m (*light blue*) 4500 – 6000 m (*black line)* B614 aircraft flight track.

A north-south transect from 25°N to 22°N of B614 (27 June 2011) is presented in figure 5.8. The bottom panel indicates the aircraft height along the flight track with variability due to the aircraft terrain following. A transition in air mass evident between 23.5°N and 24°N. Water vapour mass mixing ratio at the northern end of the flight track is constant at 4 g kg^{-1} with a transition at 23.75°N. The mass mixing ratio steadily increases towards the southern end of the flight track approaching 10 g kg^{-1}, as derived from the General

Eastern dew point hygrometer. The change in wind direction observed is not correlated with crossing into the low level jet but is positioned further south of the flight transect.

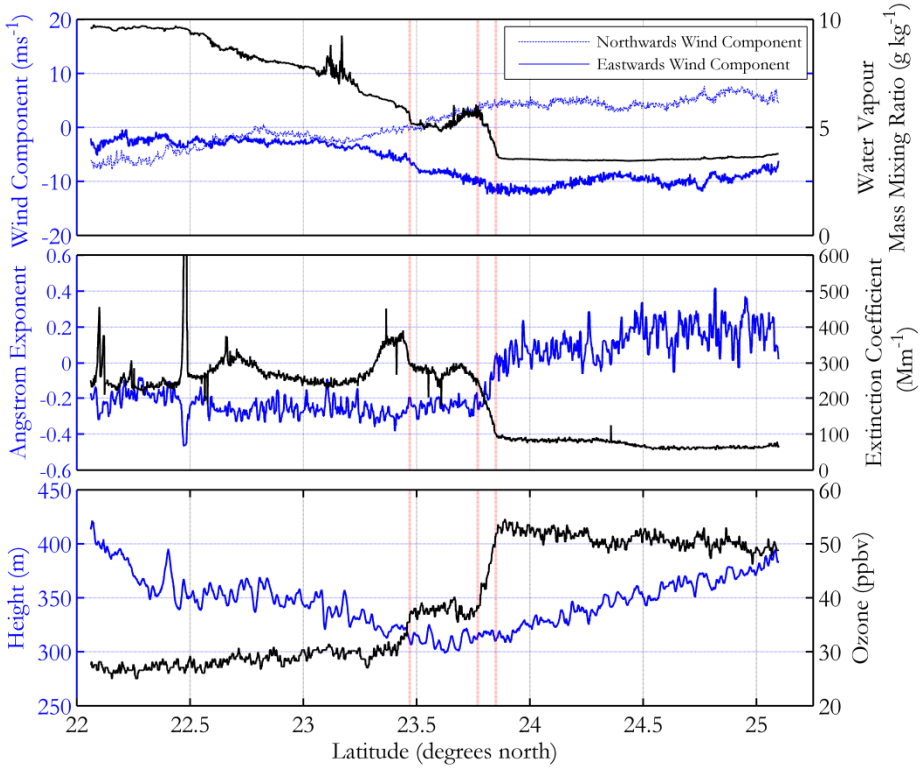

Figure 5.8 North - south transect of B614 (27 June 2011) (*top panel*) wind component (*blue*) water vapour mass mixing ratio (*black*), (*middle panel*) Ångström exponent (*blue*) and dry extinction coefficient at 550 nm (*black*) and (*bottom panel*) aircraft height (*blue*) and ozone mass mixing ratio (ppbv) (*black*). Dashed vertical red lines show the boundaries of different air masses.

Mineral dust mean extinction coefficients of 80 Mm^{-1} in the northern part of the transect increased to 300 Mm^{-1} within the Harmattan airflow. The Ångström exponent, which is strongly anti-correlated with mean particle diameter, shows an average of 0.2 in the northern part of the transect but decreases sharply within the Harmattan airflow with a mean value of -0.2, indicating a greater contribution of coarse mode mineral dust at the southern end of the flight track. These changes in extinction coefficient and Ångström exponent are correlated with a decrease in ozone mass mixing ratio from 50 ppbv to less than 30 ppbv.

Flight B707 on the 15 June 2012 consisted of a low-level leg northwest to southeast from 23.5°N to 21°N, with a reciprocal SLR return at high-level. The low leg transect of B707 and *in-situ* observations are presented in figure 5.9. In contrast with the

observations of B614, higher mineral dust extinction coefficients correlate with lower water vapour mass mixing ratio. Flight mean water vapour mixing ratios were approximately half of that observed in B614.

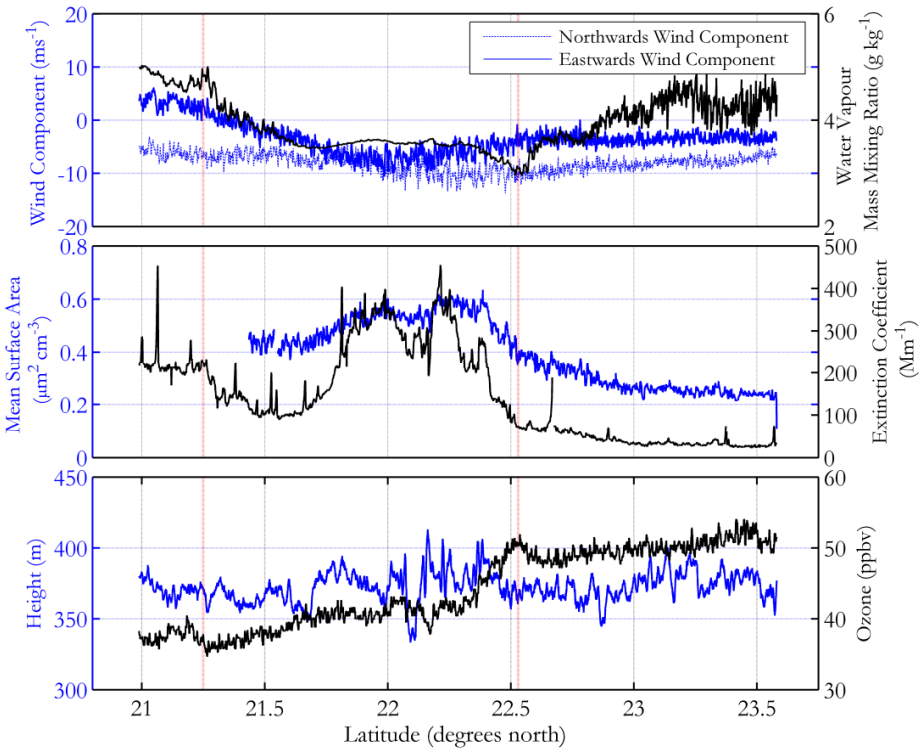

Figure 5.9 Northeast - southwest transect of B707 (15 June 2012) (*top panel*) wind component (*blue*) water vapour mass mixing ratio (*black*), (*middle panel*) mean surface area (*blue*) and dry extinction coefficient at 550 nm (*black*) and (*bottom panel*) aircraft height (*blue*) and ozone mass mixing ratios (ppbv) (*black*). Dashed vertical red lines show the boundaries of different air masses.

A transition between air masses at 22.5°N to 21.25°N was associated with an increase in extinction coefficient of less than 50 Mm^{-1} in the northern section of the transect which increases to 400 Mm^{-1} in the Harmattan airflow. The mean surface area increased to 0.4 – 0.6 μm^2 cm^{-3}, whilst at the northern end of the transect the mean surface area tended towards 0.2 μm^2 cm^{-3}. These increases in mineral dust extinction coefficient and mean surface area are correlated with a decrease in ozone mass mixing ratio from 50 ppbv to 37 – 42 ppbv.

Observations of elevated mineral dust concentrations and ozone depletion events here are correlated with increased mineral dust surface area associated with elevated dust concentrations. Scatter plots of dry extinction coefficient and ozone mass mixing ratio,

coloured for variability in the Ångström exponent during B614 are presented in figure 5.10. Johnson and Osborne (2011) show that the Ångström exponent is anti-correlated with mean particle diameter, which indicates that the large positive Ångström exponents suggest a dominance of fine mode mineral dust, and large negative Ångström exponents suggest a dominance of coarse mode mineral dust. figure 5.11 presents a box-and-whisker plot of mineral dust Ångström exponent correlated with ozone mass mixing ratios. The red central line of the box-and-whisker denotes the median, the edges of the box are the 25th and 75th percentiles and the whiskers extend to the most extreme data points. It is evident that at larger Ångström exponents of -0.05 to 0.45 are correlated with ozone mass mixing ratio of 49 – 52 ppbv. On transitioning into the Harmattan airflow, the Ångström exponent decreases to between -0.35 and -0.45, the ozone mass mixing ratio decreases to 37 – 41 ppbv.

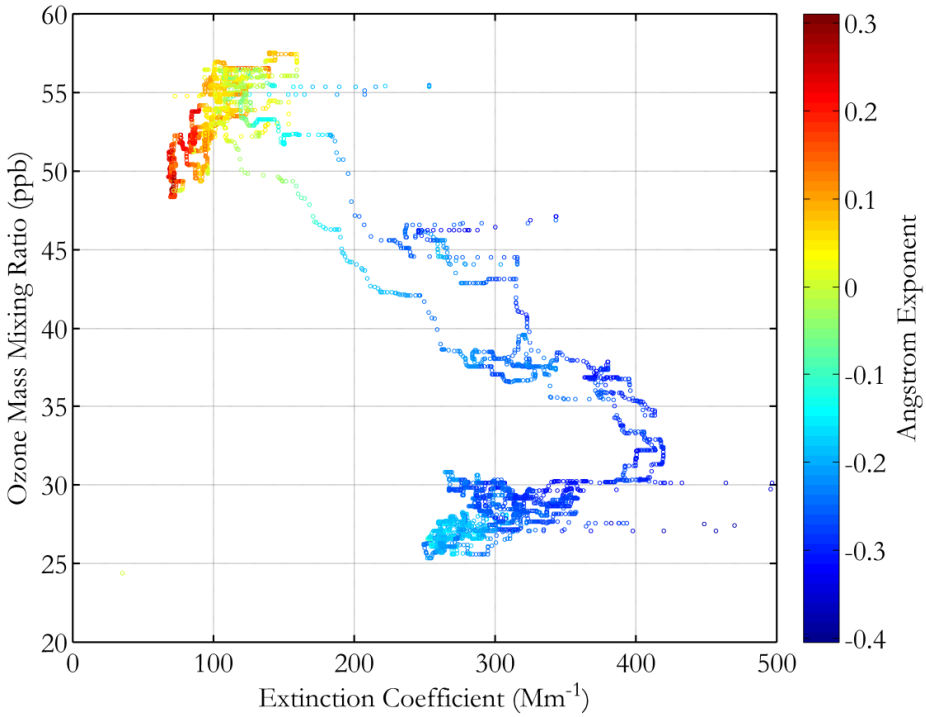

Figure 5.10 Scatter plot of dry extinction coefficient at 550 nm and ozone mass mixing ratio (ppbv), coloured for variability in the Ångström exponent along the B614 (27 June 2011) flight transect. Ångström exponent is anti-correlated with mean particle diameter, which indicates that the large positive Ångström exponents suggest a dominance of fine mode mineral dust, and large negative Ångström exponents suggest a dominance of coarse mode mineral dust.

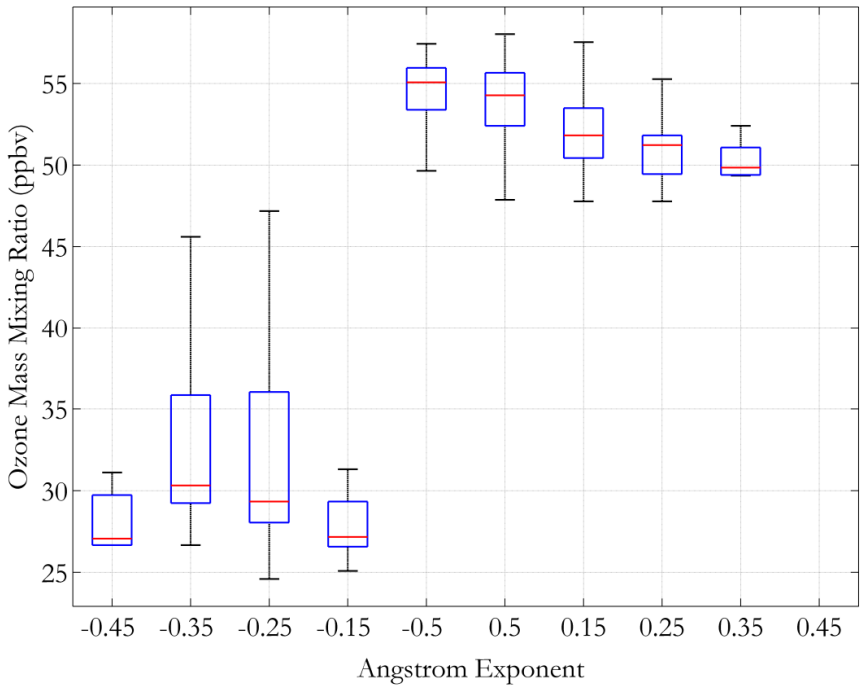

Figure 5.11 Box-and-whisker plots of mineral dust Ångström exponent and ozone mass mixing ratio (ppbv) along the B614 (27 June 2011) flight transect. The red central line denotes the median, the edges of the box are the 25th and 75th percentiles and the whiskers extend to the most extreme data points. Ångström exponent is anti-correlated with mean particle diameter, which indicates that the large positive Ångström exponents suggest a dominance of fine mode mineral dust, and large negative Ångström exponents suggest a dominance of coarse mode mineral dust.

Scatter plots of dry extinction coefficient and ozone mass mixing ratio, coloured for variability in the mineral dust mean surface area during B707 are presented in figure 5.12. Box-and-whisker plots of mineral dust mean surface area correlated with ozone mass mixing ratios are shown in figure 5.13. Low particle mean surface area of 0.15 – 0.35 μm^2 cm^{-3} correspond with larger ozone mass mixing ratio of 49 – 52 ppbv. On transitioning into the Harmattan airflow the mineral dust mean surface area increased to 0.45 – 0.75 μm^2 cm^{-3}, the ozone mass mixing ratio decreases to 41 – 44 ppbv. The spread in ozone concentrations at a mean surface area of $0.45\ \mu m^2$ cm^{-3} can be attributed to a transition between air masses.

The observations here suggest that fresh mineral dust uplift has a large coarse mode contribution coupled with freshly exposed mineral dust surface sites which act as a route for the ozone loss observed. The results presented here support proposals by Bauer et al. (2004) that the coarse mode of mineral dust could be important for heterogeneous

uptake on to mineral dust and Chang et al. (2005) in which freshly emitted Saharan dust is potentially a significant route of ozone loss.

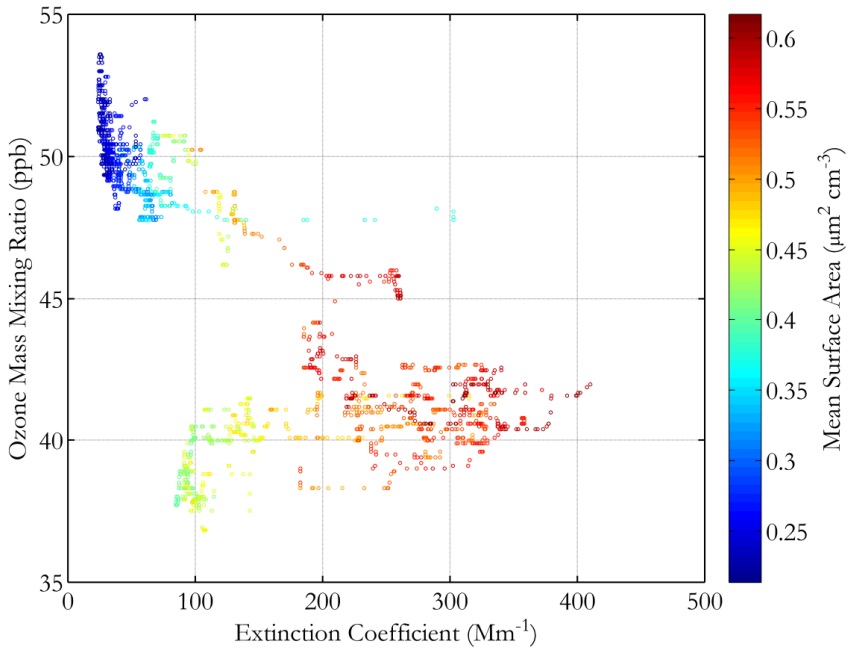

Figure 5.12 Scatter plot of dry extinction coefficient at 550 nm and ozone mass mixing ratio (ppbv), coloured for variability in the mineral dust mean surface area along the B707 (15 June 2012) flight transect.

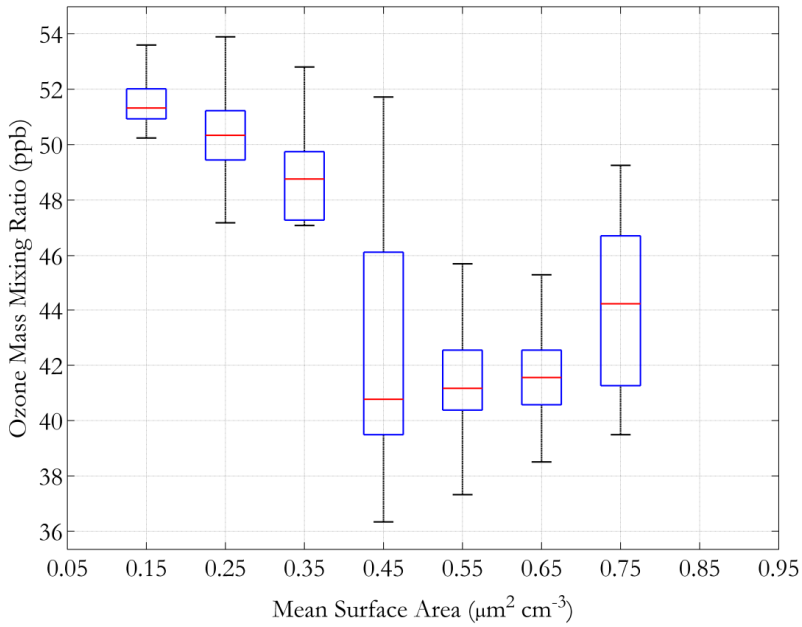

Figure 5.13 Box-and-whisker plot of mineral dust mean surface area and ozone mass mixing ratio (ppbv) along the B707 (15 June 2012) flight transect.

5.4 Chapter Conclusion

The campaign-average aerosol optical properties in terms of the extinction coefficients, Ångström exponents and single-scattering albedo during the Fennec pilot, Fennec 2011 and Fennec 2012 were discussed. The average Ångström exponents were -0.21 for the Fennec 2011 and 2012 campaigns; significantly lower than campaign-averages from previous observational field campaigns. The average Ångström exponent from the pilot campaign was 0.06 with a range of -0.18 to 0.67. This result is consistent with measurements from DABEX (Osborne et al., 2008) and GERBILS (Johnson and Osborne, 2011), which ranged from -0.18 to 0.66.

The Ångström exponent for the Fennec 2011 campaign ranged from -0.36 to -0.05 which indicated a large contribution of the mineral dust coarse mode to the size distribution during all flights of the campaign. The Ångström exponent for the Fennec 2012 campaign saw a larger range from -0.45 to 0.47, which can be attributed to the different meteorological events encountered during the campaign.

The single-scattering albedo from the Fennec campaign was largely consistent across the pilot and the two main campaigns ranging from 0.93 to 0.97. The single-scattering albedo is comparable to that found during the SAMUM (Kandler et al., 2011; Müller et al., 2011) and GERBILS campaigns (Johnson and Osborne, 2011). The importance in the contribution of the coarse mode to the single-scattering albedo has been shown from theoretical Mie calculations. Below 10 μm, the single-scattering albedo of mineral dust is captured to a similar extent between the LTI and the wing-mounted probes. It is evident that beyond 10 μm transmission losses in the LTI sampling line start to dominate, resulting in a truncation of the single-scattering albedo at 0.98. The total cumulative contribution of the wing-mounted size distribution accounted for a single-scattering albedo of 0.97.

The asymmetry parameter during Fennec 2011 ranged from 0.71 to 0.81 with a mean of 0.77. The highest values of the asymmetry parameter were observed during the first part of the campaign during B600 – B602, consistent with the strong dust uplift conditions and the corresponding large contribution of coarse mode particles encountered during these flights. Observations from SAMUM 2006 found large asymmetry parameters of 0.79, which reflects the contribution of coarse mode particles in the dust population, and suggests large forward scattering properties of the mineral dust (Otto et al., 2007).

The results of Fennec 2011 find a higher asymmetry parameter which is broadly consistent with the results from SAMUM.

A strong contribution of the coarse mode of mineral dust to the asymmetry parameter as measured by the wing-mounted probes was emphasised. The inclusion of the second bin of the CDP increased the asymmetry parameter from 0.70 to 0.76. The largest sensitivity to the asymmetry parameter is the representation of coarse mode mineral dust diameters up to 20 μm. For both dust loadings, it can be seen that the asymmetry parameter is largely unchanged beyond 50 μm, which indicates to the low abundance of these ultra large particles. This highlights the large contribution of the coarse mode to the asymmetry parameter and is thus highly important parameter to constrain in assessing the radiative properties of mineral dust. This is additionally important in terms of the phase function, which is necessary for retrievals of aerosol properties from satellites.

It was shown that at a wavelength of 450 nm, the total cumulative contribution of coarse mode mineral dust at the LTI converges on that of the total asymmetry parameter. At larger wavelengths, the LTI asymmetry parameter is underestimated relative to that calculated from the CDP measurements. Transmission losses of particles through the LTI have been shown to play a role for particle diameters greater than 5 μm. Beyond 10 μm transmission losses in the LTI are seen to dominate which is reflected by the differences in the asymmetry between the LTI and the CDP at larger wavelengths. This result places emphasis on the importance of coarse mode contribution to mineral dust optical properties; highlighting the need to make accurate measurements of the initial size distribution. This result stresses the need to carry out further characterisations of the aircraft inlets in order to understand the influence of the sampling system of the inferred mineral dust optical properties.

Vertical profile of enhanced mineral dust extinction coefficients and reduced ozone concentrations are presented. Although this type of vertical profile has been commonly observed (De Reus et al., 2000; McConnell et al., 2008; Osborne et al., 2008), the anti-correlation extends to the surface layer below 920 hPa. Extinction coefficients associated with fresh localised dust reached a maximum of 190 Mm^{-1}, which coincides with a decrease from 47 ppbv above the surface layer to 38 – 39 ppbv. This was found to be equivalent to almost a 20 % decrease in ozone concentration. The Ångström

exponent within the surface layer was - 0.35, indicating a coarse mode mineral dust contribution.

Two case studies of *in-situ* measurements observed increased mineral dust concentrations and larger mineral dust mean surface area anti-correlated with ozone concentrations. The observations presented are associated with localised dust uplift and are not correlated with the long range Saharan dust events that have been be previously reported (De Reus 2000; 2005; Bonasoni et al. 2004). Low particle mean surface area of 0.15 – 0.35 μm^2 cm^{-3} corresponded with larger ozone mass mixing ratio of 49 – 52 ppbv. As mineral dust mean surface area increased to 0.45 – 0.75 μm^2 cm^{-3}, the ozone mass mixing ratio decreased to 41 – 44 ppbv. The *in-situ* observations suggest that increased mineral dust surface area associated with fresh dust uplift and a large coarse mode contribution to the size distribution act as a route for the reduced ozone concentrations. The results presented here support proposals by Bauer et al. (2004) that the coarse mode of mineral dust could be important for heterogeneous uptake on to mineral dust and Chang et al. (2005) in which freshly emitted Saharan dust is potentially a significant route of ozone loss.

The presence of mineral dust seemingly cannot fully explain the differences in ozone concentrations observed in the two case studies. HYSPLIT back trajectories suggest that different air masses were observed with upper tropospheric air intrusions events identified with descending airflow from 3000 – 4500 m. From the analysis presented here it is not possible to say if the air mass initially contained lower ozone concentrations and mineral dust has subsequently been uplifted, or that if mineral dust uplift along the Harmattan flow could have contributed to the reduced ozone concentrations observed.

6 Biomass Burning Aerosol: SAMBBA observations

There has been a significant advance in aerosol instrumentation since the SCAR-B campaign in 1995 including the AMS and SP2. Observations from SAMBBA campaign will be used to improve understanding of the complexity of biomass burning aerosol which has been demonstrated. This thesis will present relationships between biomass burning aerosol properties bringing together size distributions, aerosol mixing state and optical properties from a suite of instruments onboard the FAAM BAe-146. It will be demonstrated that an accurate measurement of size distributions and scattering and absorbing properties of both black carbon and organic carbon are important components in representing the refractive index of biomass burning, and in turn assessing the optical properties of the aerosol.

This chapter presents a multi-instrument analysis of aerosol properties from the SAMBBA aircraft campaign. The variability in the regional vertical aerosol structure from the aircraft platform is discussed in section 6.2 and an air-mass back trajectory along one aircraft flight track using the HYSPLIT back-trajectory model is presented in section 6.3. Aerosol number size distributions based on multi-instrument *in-situ* measurements are presented in section 6.4 for two case studies of i) Rondônian regional haze and ii) remote Amazonian aerosol from the SAMBBA campaign.

A thermal denuder instrument which uses a thermal volatility technique has not previously been used to investigate coating thickness of biomass burning aerosol from an aircraft platform. Results from the thermal technique are compared to measurements from the SP2 instrument which uses laser incandescence and is a well characterised technique for measuring properties of black carbon. Median shell-to-core diameter ratios for each instrument will be derived and compared, which provides a representation of particle coating thickness and mean size distributions of black carbon (section 6.5).

Two approaches in representing the complex refractive index of biomass burning aerosol are discussed; the linear-mixing rule and the Maxwell-Garnett mixing rule. The refractive indices are constrained by aerosol composition measurements from the AMS and SP2 instruments. Light scattering by aerosols is measurable as well as calculable by combining measured size distributions with estimates of the refractive index. This permits closure studies between *in-situ* measurements and theoretical calculations. Aerosol optical parameters comprising of the single-scattering albedo, mass extinction efficiency and the asymmetry factor are calculated using Mie theory (Wiscombe, 1980) assuming spherical particles.

6.1 SAMBBA Flight Case Studies

This chapter presents two case studies from the SAMBBA campaign; the conditions on 18 September 2012 motivated flight B734, a regional haze flight south of the operating base in Porto Vehlo in central Rondônia. The flight consisted of two high level SLRs for remote sensing of the regional haze using lidar, and three SLRs through the boundary layer making *in-situ* measurements (table 39). Kotchenruther and Hobbs (1998) define a regional haze as aerosol within the boundary layer, of uniform concentration and composition, which has dispersed from the biomass burning source across a region. Reid et al. (1998) discuss that regional haze can be made up of fresh emissions (< 2 hours) and aged emission (> 3 days old), as fires are typically ignited late morning and throughout the afternoon. The haze sampled during flight B734 was likely to have been emitted from the previous day, containing aged biomass burning aerosol.

The motivation on 19 September for flight B735 was to fly a series of deep profiles in a cross section between Porto Vehlo and Manaus, intersected with low level horizontal runs to investigate the vertical structure, composition and optical properties over central Amazonia (table 40).

Table 39 Aircraft profiles (P) and straight and level runs (R) for B734 (18 September 2012).

Run Number	Time (UTC)	Pressure (hPa)	Altitude (m)	Details
P1	12:05 – 12:24	-	-	Profile ascent from PVH
R1	12:35 – 13:05	390	7300	High level SLR for remote sensing
P2	13:05 – 13:17	-	7300 – 2100	Profile descent
R2	13:17 – 13:45	780	2100	SLR
R3	13:48 – 14:14	855	1400	SLR
R4	14:24 – 14:48	970	500	SLR
P3	14:49 – 15:28	-	500 – 6100	Profile ascent
R5	15:28 – 15:.36	465	6100	High level SLR for remote sensing
P4	15:28 – 16:01	-	-	Profile descent to PVH

Table 40 Aircraft profiles (P) and straight and level runs (R) for B735 (19 September 2012).

Run Number	Time (UTC)	Pressure (hPa)	Altitude (m)	Details
P1	12:07 – 12:35	-	-	Profile ascent from PVH
R1	12:35 – 12:38	430	7000	High level SLR for remote sensing
P2	12:38 – 13:01	430 – 980	7000 – 500	
R2	13:01 – 13:16	980	500	SLR
P3, P4	13:16 – 13:36	980 – 465	500 – 6000	
	13:36 – 13:54	465 – 980	6000 – 500	
R3	13:54 – 14:11	980	500	SLR
P5, P6	14:11 – 14:30	980 – 465	500 – 6000	
	14:34 – 14:53	465 – 980	6000 – 500	
R4	14:53 – 15:12	980	500	SLR
P7	15:13 – 13:.23	980 – 690	500 – 3000	
P8	15:34 – 15:47	-	-	Profile descent to Manaus

6.2 Atmospheric Profiles

The vertical distribution of biomass burning is important for a number of reasons: the vertical distribution strongly affects the shortwave aerosol forcing (Ban-Weiss et al., 2012; Hansen et al., 1997; Haywood et al., 1999); it also influences aerosol transport between regions (Kim et al., 2009); and studies have observed that mixing state varies with altitude, with coatings of black carbon increasing with height reflecting greater internal mixing (Pratt and Prather, 2010). Variation in particle mixing state with altitude leads to changes in absorption and hygroscopic properties, and must be taken into account in calculating aerosol direct and indirect radiative forcings (Kim et al., 2006; Rissler et al., 2006).

Aircraft profiles of aerosol extinction coefficients derived from *in-situ* measurements and corresponding tephigrams from SAMBBA flights B734 and B735 are presented in figure 6.1 and figure 6.2, respectively. Identification of aircraft profiles are listed in table 39 and table 40. The two profiles highlight the differences in the general features in the vertical structure between Rondônia and Amazonia, with regional differences in the aerosol vertical distribution driven by the meteorological conditions. The small scale structure evident in the aerosol profile relate to small scale changes in the temperature and dew point temperature. There is little to no discussion in the literature bringing together biomass burning aerosol vertical distributions with observed meteorological profiles in the study region. This is a limitation to any possible validation of model vertical distributions. Near-surface air temperatures in the first half of the SAMBBA campaign the Porto Vehlo region were consistently ~ 303 K, and there is little variation in the air temperature through the atmosphere, as was noted by Freud et al. (2008) using sonde profiles during the SMOCC field campaign.

Flight B734, a Rondônian regional haze flight south of the operating base in Porto Vehlo, observed the top of the aerosol layer defined by a small temperature inversion (2 K) and a hydrolapse (rapid decrease in dew point with height). Constant specific humidity of 15 g kg^{-1} is evident from the surface to ~ 880 hPa. A secondary aerosol upper layer is capped by a second temperature inversion (1 K) at 600 hPa. The extinction coefficients remain consistent in magnitude across the three nephelometer wavelengths, indicating little change in the Angstrom exponent with height up to 650 hPa. Atmospheric back-trajectories along the flight track presented in figure 6.5 identify

that the air mass below 850 hPa was advected from a northerly direction, whilst above 850 hPa air was from the east.

Flight B735 consisted of eight aircraft profiles between Porto Vehlo, Rondônia and Manaus, Amazonia, with the aerosol vertical distribution across Amazonia capped by a strong hydrolapse evident in figure 6.2. The aerosol profile in flight B735 reflects a clean boundary layer with near surface aerosol extinction coefficients (at 550 nm) of less than 50 Mm^{-1}, with maximum extinction coefficients at 800 hPa of approximately 80 Mm^{-1}. Figure 6.2 allows for a contrast between two Amazonia atmospheric profiles; in profile 2 (midpoint 6.3°S 64.6°W, approx. 300 km from PVH) the near surface specific humidity decreases from 15 g kg^{-1} to 7 g kg^{-1} at 800 hPa, and the aerosol layer capped by the hydrolapse (specific humidity of 5 g kg^{-1}). A thin elevated aerosol layer lies above the main aerosol layer between 750 – 800 hPa which is capped by a small isothermal layer.

Profile 6 (midpoint 1.95°S 60.5°W, 800 km from PVH, 54 km from Manaus) shows an increase in aerosol extinction, possibly due to the proximity of Manaus and associated urban emissions. Maximum extinction coefficients (550 nm) at 800 hPa were capped at the base of strong hydrolapse at 750 hPa extending up to 630 hPa, with an associated minimum specific humidity of 0.7 g kg^{-1} (750 hPa).

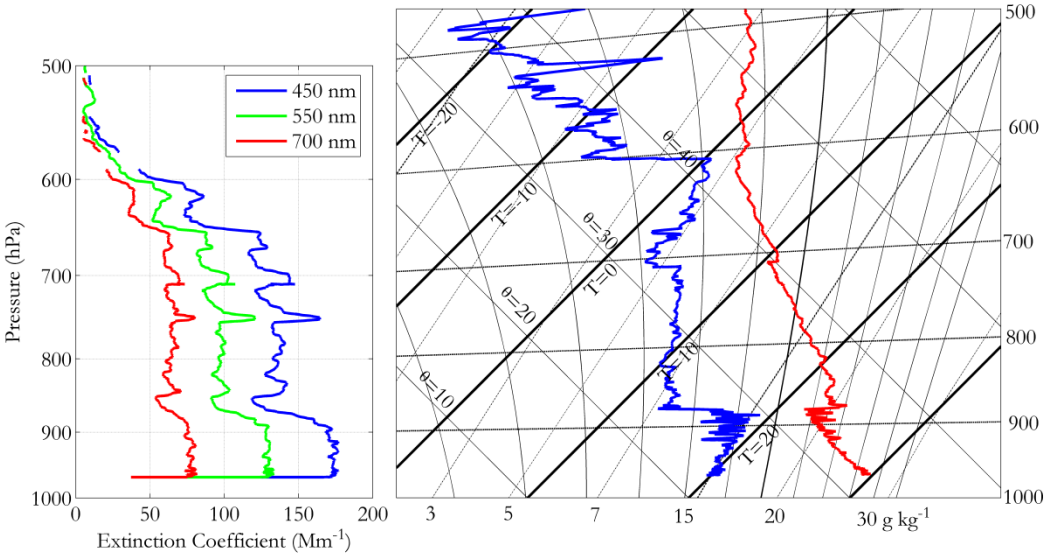

Figure 6.1 (*left*) Dry aerosol extinction coefficients (*blue*) 450 nm *(green)* 550 nm and (*red*) 700 nm for profile 3 (*right*) tephigram of vertical profiles of temperature and humidity (dew point temperature) for B734 (18 September 2012).

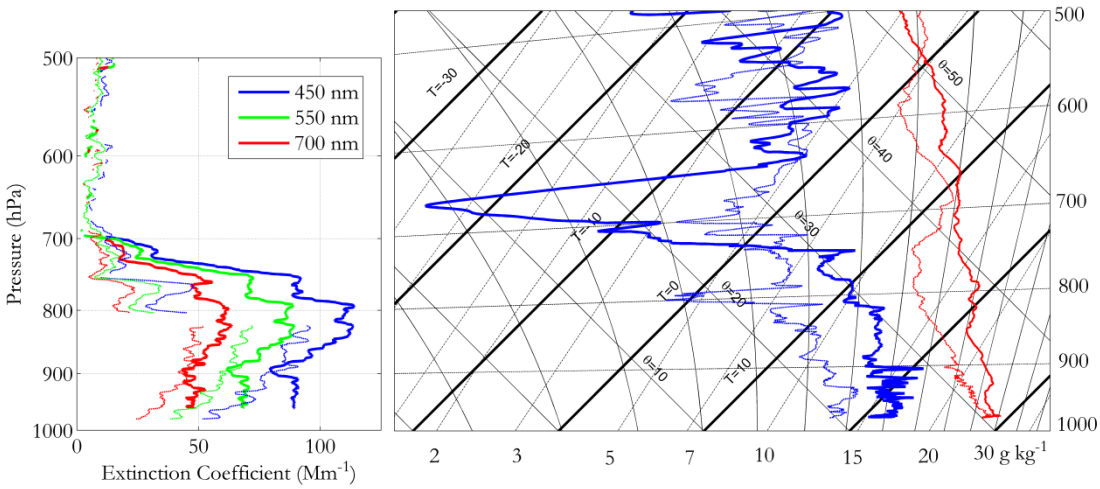

Figure 6.2 (*left*) Dry aerosol extinction coefficients (*blue*) 450 nm *(green)* 550 nm and (*red*) 700 nm (*right*) tephigram of vertical profiles of temperature and humidity (dew point temperature) (*dashed line*) Profile 2 (*solid line*) Profile 6 for B735 (19 September 2012).

In addition to *in-situ* profiles, a nadir-viewing lidar was used to retrieve aerosol extinction coefficients. The retrievals are made by applying a two-component atmosphere approach to the lidar equation (Di Girolamo et al., 1994; Fernald, 1984; Klett, 1985) and a mixed-approach making an assumption of a well-mixed layer near the surface (Marenco, 2013). Full details of the retrieval procedure are presented in Marenco and Hogan (2011). In general the comparison between the lidar retrieval of aerosol extinction coefficients and *in-situ* measurements show a very good agreement, as seen in figure 6.3. There is naturally some offset between the *in-situ* profiles and the lidar profile (as discussed in the methodology); during profiles the aircraft covers a greater distance in the horizontal plane than in the vertical so variability in aerosol concentrations within the boundary layer will influence *in-situ* profiles. Profile retrievals made by the lidar will never be in the same location as the aircraft profile. A lidar time series of retrieved aerosol extinction coefficient for flight B734 is presented in figure 6.4.

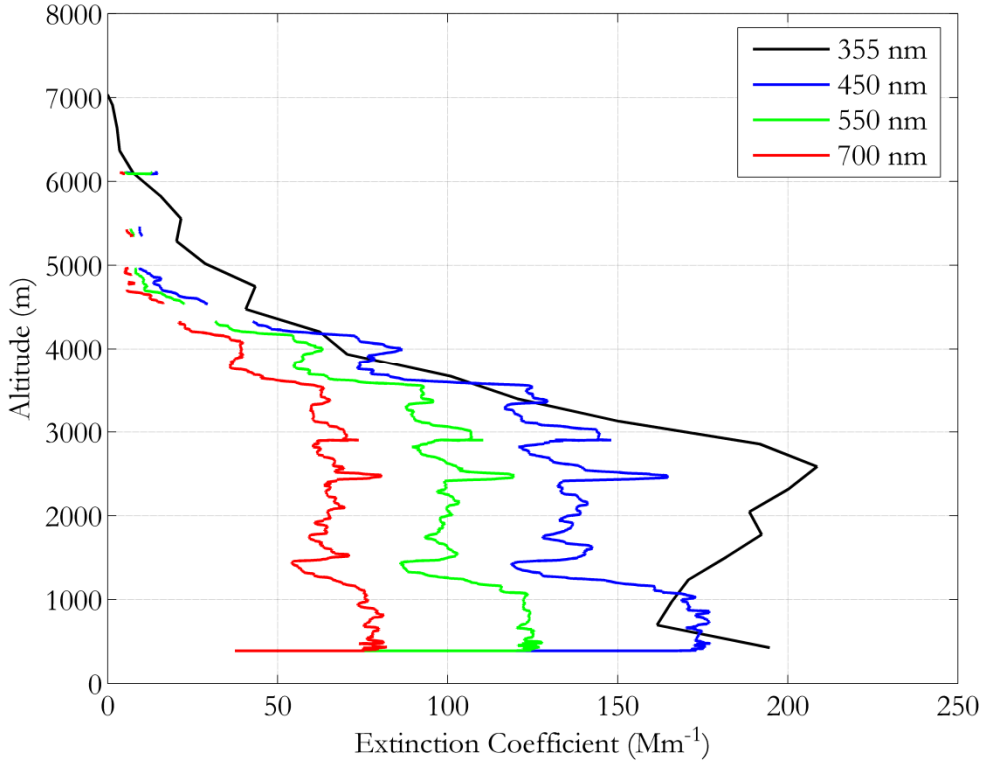

Figure 6.3 Profiles of aerosol extinction coefficient for B734 (18 September 2012) from *in-situ* measurements (*blue*) 450 nm, (*green*) 550 nm, and (*red*) 700 nm from profile 2 and (*black*) retrieved extinction coefficient from Leosphere elastic backscatter 355 nm lidar with depolarization during run 1 at high-level.

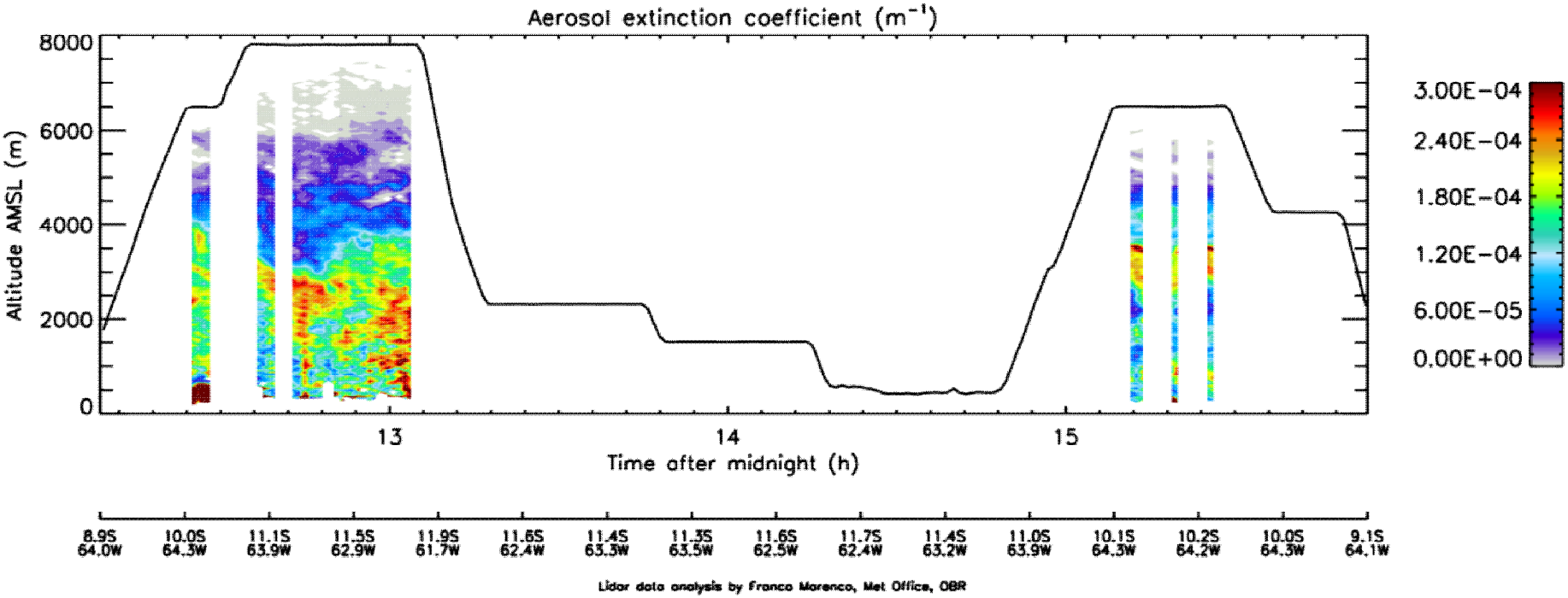

Figure 6.4 Lidar observations of retrieved aerosol extinction coefficient for B734 (18 September 2012). Figure courtesy of F. Marenco (Met Office).

6.3 HYSPLIT Back Trajectories

Atmospheric back trajectories using the HYSPLIT trajectory model were run along the BAe-146 flight path during flight B734 below 1500 m, that is for run 3 (500 m) and 4 (1400 m), excluding the takeoff and landing profiles. The projection in figure 6.5 hides the three dimensional nature of the flight track, but interpretation of the back trajectory finds the lowest run at 500 m encounters air which has been advected from the north (following the trade winds as discussed in chapter 2), whilst the run at 1400 m is consistent with a descending easterly airflow from 2800 – 4200 m. The anticyclonic circulation is typical of the meteorology in South America, with biomass burning emissions from across eastern Brazil transported within the flow.

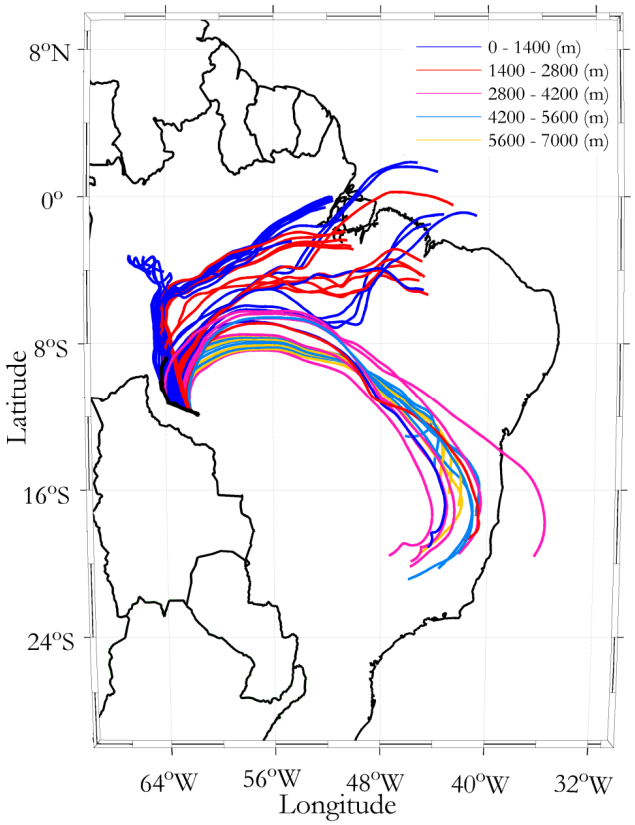

Figure 6.5. HYSPLIT calculated back-trajectories over 120 hours along the flight track of flight B734 (18 September 2012), (*dark blue*) 0 – 1400 m, (*red*) 1400 – 2800 m, (*pink*) 2800 – 4200 m, (*light blue*) 4200 – 5600 m, and (*yellow*) 5600 – 7000 m, (*black line)* B734 aircraft flight track.

6.4 Aerosol Size Distributions

During SAMBBA the aerosol size distribution was measured by 5 sizing instruments across the range of 0.002 μm up to 100 μm particles. The smallest particles were measured by the SMPS which covered the range of 0.002 – 0.300 μm, the wing-mounted PCASP sizes aerosol in the nominal size range of 0.11 – 3.2 μm, the VACC PCASP sizes across a subset of this range: 0.11 – 0.53 μm. The Grimm Sky-OPC provides sizing data for the accumulation and coarse mode aerosol in the nominal range of 0.25 – 32 μm, whilst the CDP provides distributions up to 50 μm diameter. The instrument performance of these instruments for the first half of the SAMBBA campaign is presented in table 41.

A sync error instrument issue was discovered during the analysis of the wing-mounted PCASP data, which was onset from flight B735 and was a consistent problem in the data for the remainder of the campaign. The sync error is an indication of a synchronisation problem in the signal processing modules, which stores particle peak detection signal, area accumulation, and threshold detection, for each of the instrument's three gain stage first-in first-out (FIFO) memories (personal communication G. Nott, FAAM).

Table 41 Instrument performance during SAMBBA from flight B731 – B737.

Flight Number	PCASP	VACC	Grimm	SMPS	CDP
B731	Data	Data	Data	No Data	Data
B732	Data	Data	Data	Data	Data
B734	Data	Data	Data	Data	Data
B735	No Data - sync error	Data	Data	Data	Data
B737	No Data - sync error	Data	Data	No Data	Data

The flight mean aerosol number size distribution from flight B734 during SLRs in the aerosol boundary layer during SAMBBA is presented in figure 6.6. The vertical bars represent the variation in the number concentration during the legs; greatest variability in number concentration is at smallest sizes in the SMPS and at the largest sizes in the CDP. The change in the instrument bin edges as a response of a change in the refractive index was accounted for in the size distribution presented in figure 6.6; a correction of

m = 1.49 – 0.0083i was applied. A discussion of the refractive index is presented in section 6.7.

Comparisons of the instrument performance can be drawn from the size distribution measurements. Overall there is good agreement across the range of probes; highlighting the shoulder of the accumulation mode of the aerosol distribution across the size region of 0.2 – 0.5 μm. The comparison brings together three instruments which use optically based techniques, whilst the fourth the SMPS uses a mobility technique to size particles. The PCASP is an externally mounted instrument, whilst the other three instruments are installed within the aircraft cabin, which gives further confidence in the measurements within this sizing region.

The agreement between the Grimm Sky-OPC and CDP across the measurement range is particularly good between 10 and 100 μm, despite one being an open path measurement external to the aircraft cabin, whilst the Grimm OPC is internally mounted, additionally behind a Rosemount inlet. However it is worth noting the negligible coarse mode contribution to the biomass burning aerosol mass size distribution, and as such size distributions presented from here onwards are only presented up to a diameter of 15 μm.

The greatest discrepancy in the measurements falls between the representation of the accumulation mode by the wing-mounted PCASP and the onboard SMPS, both in terms of number concentration, count mean diameter and the geometric standard deviation. This shall be investigated more fully with lognormal fitting as presented in the following section (6.4.1).

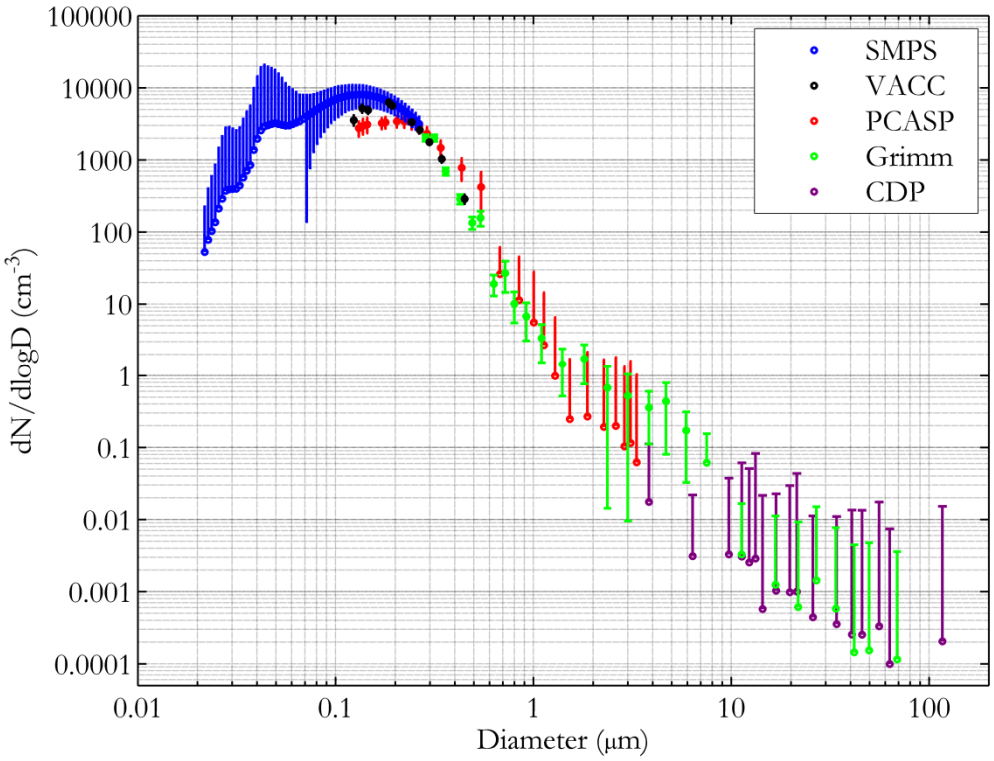

Figure 6.6 Mean number size distribution measured during B734 (18 September 2012) during SLRs. Refractive index corrections have been performed for m = 1.49 - 0.0083i. Colours represent (*blue*) SMPS, (*black*) VACC, (*red*) PCASP, (*green*) Grimm Sky-OPC and (*purple*) CDP. Vertical error bars indicate one standard deviation of the data; where the mean dN/dlogD – standard deviation in dN/dlogD is less than 0.0001, the downward error bar has been removed for clarity.

The flight mean aerosol size distribution from flight B735 during SLRs in the aerosol boundary layer during SAMBBA is presented in figure 6.7. The plot presents a combined size distribution from all the instruments operated during SAMBBA including SMPS, VACC, Grimm and CDP, in terms of number distribution. PCASP data is not presented due to instrumental issues discussed. The response of the OPCs to refractive index was accounted for in the size distribution presented in figure 6.7; a correction of m = 1.48 – 0.0043i was applied. A discussion of the refractive index is presented in section 6.7. The observed number concentrations are lower across Amazonia, in contrast to those of Rondônian regional haze, reflecting the nature of the region.

The size distribution for flight B735 (figure 6.7) shows a discontinuity between the number concentration measured by the SMPS and the Grimm, suggesting the SMPS is

measuring greater number concentration relative to the Grimm. However it is noted that the final 4 bins of the SMPS appear to diverge and count high with respect to the previous bin concentrations. There is considerable difference in the number concentration measured by the VACC and SMPS between the lower bins of the VACC and upper bins of the SMPS, however the two instruments both show the accumulation mode peaking between 0.1 – 0.2 μm. The VACC and Grimm number size distribution are comparable across the overlap region between 0.27 – 0.45 μm.

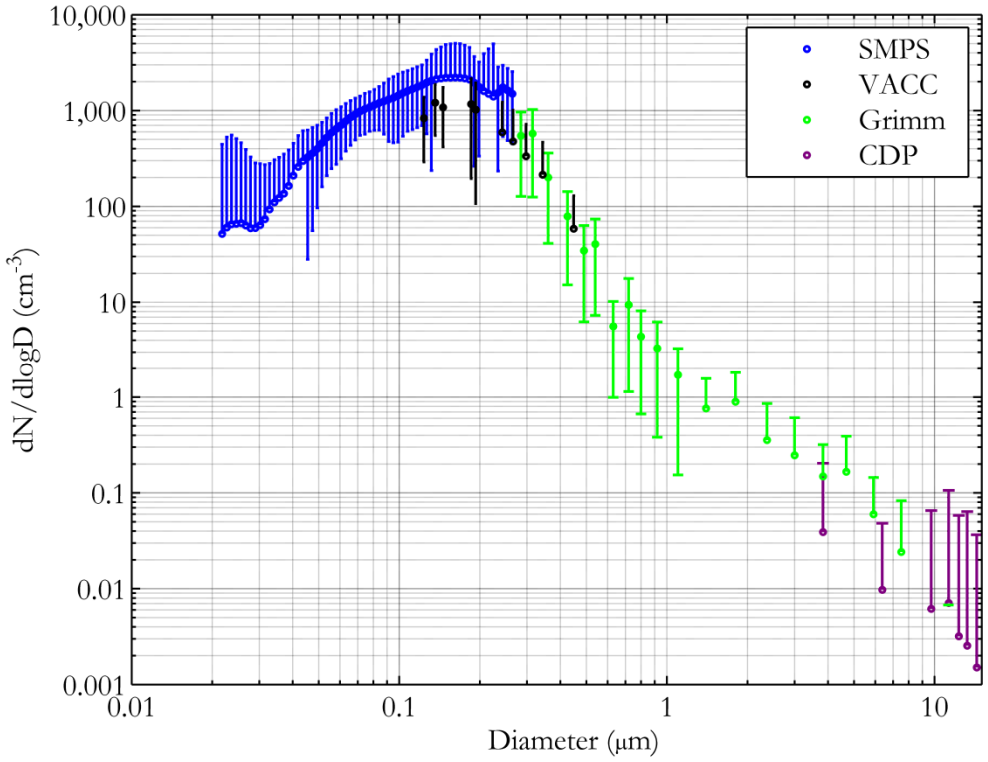

Figure 6.7 Mean size distribution measured during B735 (19 September 2012) during SLRs. Refractive index corrections have been performed for *m* = 1.48 - 0.0043*i*. Colours represent (*blue*) SMPS, (*black*) VACC, (*green*) Grimm and (*purple*) CDP. Vertical error bars indicate one standard deviation of the data. Downward error bars where the instrument mean – instrument standard deviation is less than 0.0001 has been removed for clarity.

6.4.1 Lognormal Fitting to Size Distributions

Lognormals are fitted to flight mean aerosol number size distribution from B734 and B735, in which the full size distribution is represented by the addition of the individual lognormal modes. The lognormal fitting for Rondônian regional haze (B734) from the PCASP is contrasted with the lognormals from the SMPS and Grimm measurements, and presented in table 42. An example of the lognormal fitting to the SMPS and Grimm distribution (run 4) is presented in figure 6.8.

The distribution from SMPS and Grimm measurements highlights that the Aitken and accumulation mode are minimally separated within the overall size distribution. The Aitken modes has a mean diameter of 0.047 μm with a small standard deviation of 1.16, whilst the accumulation mode has the greatest number concentration with a mean diameter of 0.12 μm and standard deviation of 1.73, representing a broad accumulation mode. In contrast, using the distribution from PCASP measurements, the lognormal fit for the accumulation mode has a mean diameter of 0.165 μm and a standard deviation of 1.5, which suggests a narrower accumulation mode. The small coarse mode contribution is evident from the lognormal fits.

Table 42 Mean microphysical properties of the log-normal number distributions from flight B734 using *in-situ* size distribution from PCASP in contrast to size distribution from the SMPS and Grimm. N_{frac} is the fraction (N/N_{Tot}) of number concentration in each mode compared with the total number concentration N_{Tot}. Units of N and N_{Tot} are cm^{-3} and CMD is μm.

	PCASP		SMPS and Grimm		
	Mode 3 Accumulation	Mode 4 Coarse	Mode 2 Aitken	Mode 3 Accumulation	Mode 4 Coarse
N	1894	33	990	6634	0.32
N_{frac}	0.983	0.017	0.13	0.87	-
σ_g	1.50	2.48	1.16	1.73	1.25
CMD	0.165	1.0	0.047	0.12	1.900

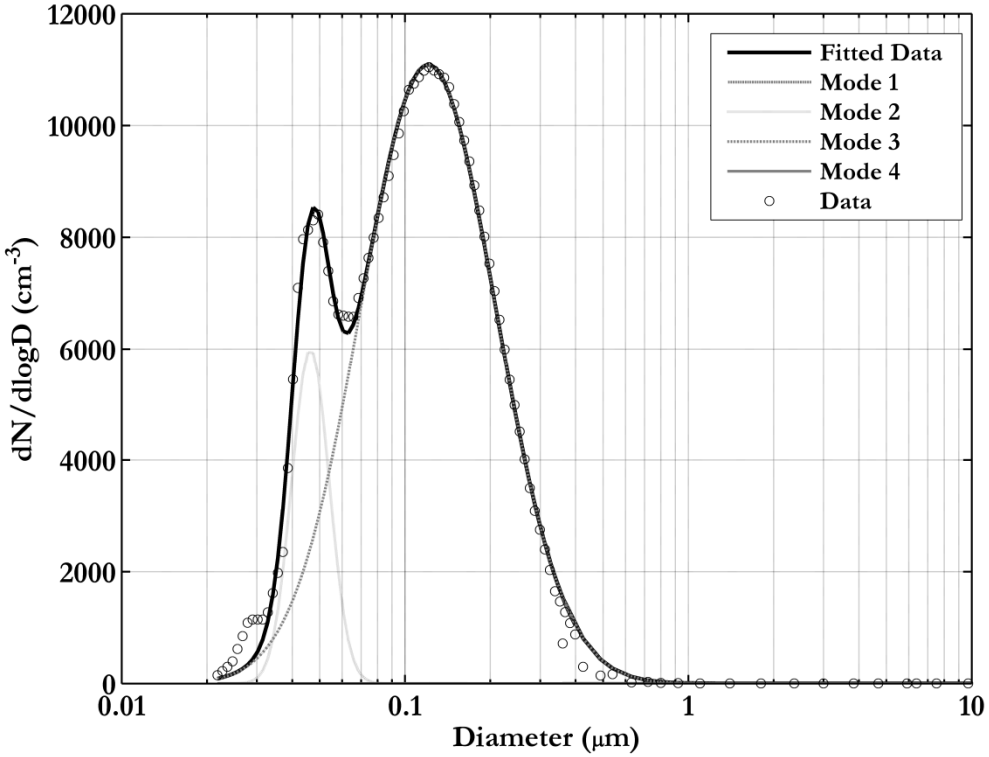

Figure 6.8 (*black circles*) *In-situ* size distribution from SMPS and Grimm (*black solid*) fitted size distribution and (*grey*) four log-normal fits to these measurements from B734, in-boundary layer run 4.

In contrasting the size distributions observed in SAMBBA to observations from previous campaigns as laid out in the literature review, the geometric mean diameter of 0.12 μm for SAMBBA SMPS distribution was found to be consistent with literature values from the SCAR-B campaign from (Reid and Hobbs, 1998). The results from 1 day old aerosol, sized using a Differential Mobility Particle Sizer (DMPS), had a geometric mean diameter of 0.12 μm with a geometric deviation of 1.89. The size distribution from the SMPS and Grimm are consistent with results from the Large-scale Biosphere Atmosphere EUSTACH2 campaign which found mean diameters of 0.110 μm within the boundary layer (Guyon et al., 2003). Reid et al. (1998) found that distributions measured with an OPC generally had a larger mean diameter than those measured with the DMPS, a similar result to that shown here.

The variability in the number size distribution during flight B734 with respect to aircraft height is presented in figure 6.9 and table 43; with accumulation mode aerosol concentrations increasing at the lowest levels. The difference between the size

distribution at 500 m compared to runs at higher level is indicative of the aircraft passing through a fresh biomass burning plume where an associated proportion of emissions are within the Aitken mode (N_{frac} of 0.13). Due to the low temporal resolution of the SMPS the instrument is not sensitive to short timescale features, however as this was an individual plume within a homogenous compositional dataset, it was simple to isolate and analyse the plume from the data. The plume is consistent with identification by other *in-situ* instruments. The mean particle diameter increases with height in the atmosphere from 0.12 μm at 500 m to 0.14 μm at 2100 m. The Aitken mode, at 0.047 μm, was only present in the lowest run at 500 m, and correlates with the aircraft proximity to biomass burning plume identified in figure 6.10. The figure shows the plume consists of white smoke which is indicative of smouldering phase of combustion, whilst it is flaming phase of combustion that leads to darker colouring in the associated plumes.

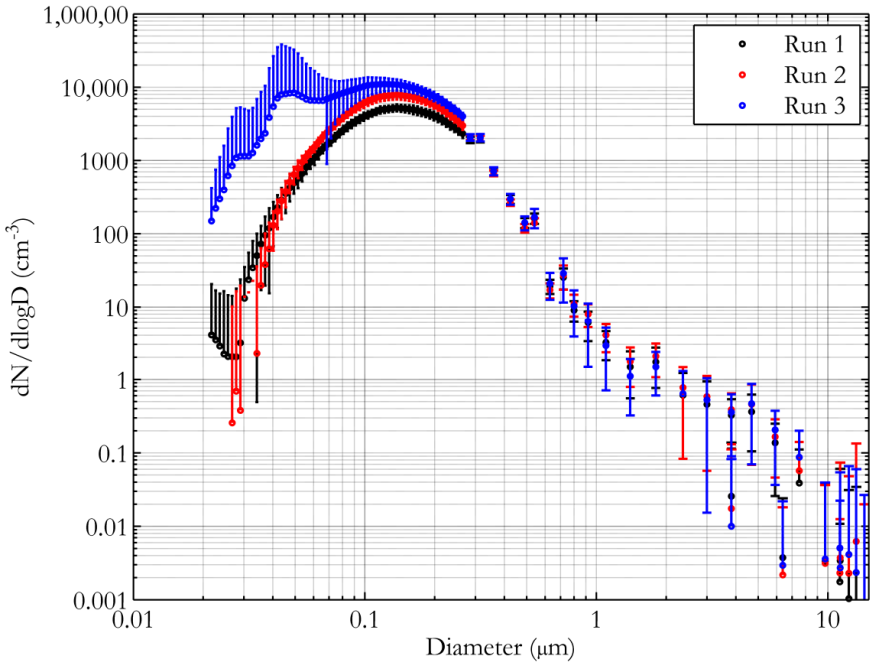

Figure 6.9 Mean number size distribution measured during flight B734 during three SLRs. Colours represent (*black*) Run 1 (2100 m), (*red*) Run 2 (1400 m), and (*blue*) Run 3 (500 m). Vertical error bars indicate one standard deviation of the data; where the mean dN/dlogD – standard deviation in dN/dlogD is less than 0.0001, the downward error bar has been removed for clarity.

Figure 6.10 Biomass burning plume measured along the aircraft flight track at 14:40 UTC during B734 (18 September 2012).

Table 43 Maximum, mean and minimum microphysical properties of the four log-normal number distributions using *in-situ* size distribution from SMPS and Grimm for three runs of flight B734 at 2100 m, 1400 m and 500 m. N_{frac} is the fraction (N / N_{Tot}) of number concentration in each mode compared with the total number concentration N_{Tot}. Units of N and N_{Tot} are cm^{-3} and CMD is μm.

		Mode 2 Aitken	Mode 3 Accumulation	Mode 4 Coarse
Run 2 (2100 m)	N	-	2743	3
	N_{frac}	-	0.999	0.001
	σ_g	-	1.6	1.8
	CMD	-	0.142	3.56
Run 3 (1400 m)	N	-	3942	1.6
	N_{frac}	-	0.999	0.001
	σ_g	-	1.58	1.2
	CMD	-	0.139	1.00
Run 4 (500 m)	N	990	6634	0.32
	N_{frac}	0.13	0.87	-
	σ_g	1.16	1.73	1.25
	CMD	0.046	0.120	1.90

The mean size distribution for Amazonian aerosol (B735) shows an accumulation mode with a CMD of 0.17 μm and a geometric standard deviation of 1.45. There is a reasonable comparison between the mean diameter from the VACC ambient size distribution and the SMPS. The mean diameter of the Amazonian aerosol (0.17 μm) is larger than the mean diameter of Rondônian regional haze (0.12 – 0.16 μm).

Table 44 Minimum, mean and maximum microphysical properties of the log-normal number distributions of Amazonian aerosol (B735, 19 September 2012) from the SMPS and Grimm. N_{frac} is the fraction (N/N_{Tot}) of number concentration in each mode compared with the total number concentration N_{Tot}. Units of N and N_{Tot} are cm^{-3} and CMD is μm.

		Mode 2 Aitken	Mode 3 Accumulation
Minimum	N	152	773
	N_{frac}	0.16	0.84
	σ_g	1.34	1.48
	CMD	0.073	0.159
Mean	N	372	819
	N_{frac}	0.31	0.69
	σ_g	1.51	1.45
	CMD	0.082	0.174
Maximum	N	618	849
	N_{frac}	0.42	0.58
	σ_g	1.66	1.44
	CMD	0.089	0.184

6.5 Aerosol Volatility

This section presents an analysis and discussion of the volatility of Rondônian regional haze and Amazonian aerosol from flights B734 and B735, respectively. A qualitative analysis of aerosol mixing state measurements is presented and shell-to-core diameter ratios derived from thermal techniques using the VACC instrument shall be compared to measurements from laser ablation technique used in the SP2 instrument.

6.5.1 Identification of Ambient and Volatile Operation

The operation of the VACC during SAMBBA involved a period of time at the start of each SLR where the VACC was operated at ambient temperature, that is, without heating applied. This allowed for a comparison of particle number concentrations with the wing-mounted PCASP. The volatile operation temperature of 350 °C was selected as a balance between being a sufficiently high temperature to volatilise the chemical components of the aerosol, but low enough to be able to cool the instrument rapidly enough between the end of one SLR and the start of the next SLR to achieve a robust comparison time of number concentration between the VACC PCASP and the external wing-mounted PCASP. Identification of the VACC ambient and volatile operating conditions, and comparison lengths are presented in table 45, and a time series of VACC volatility scans and atmospheric pressure is presented in figure 6.11.

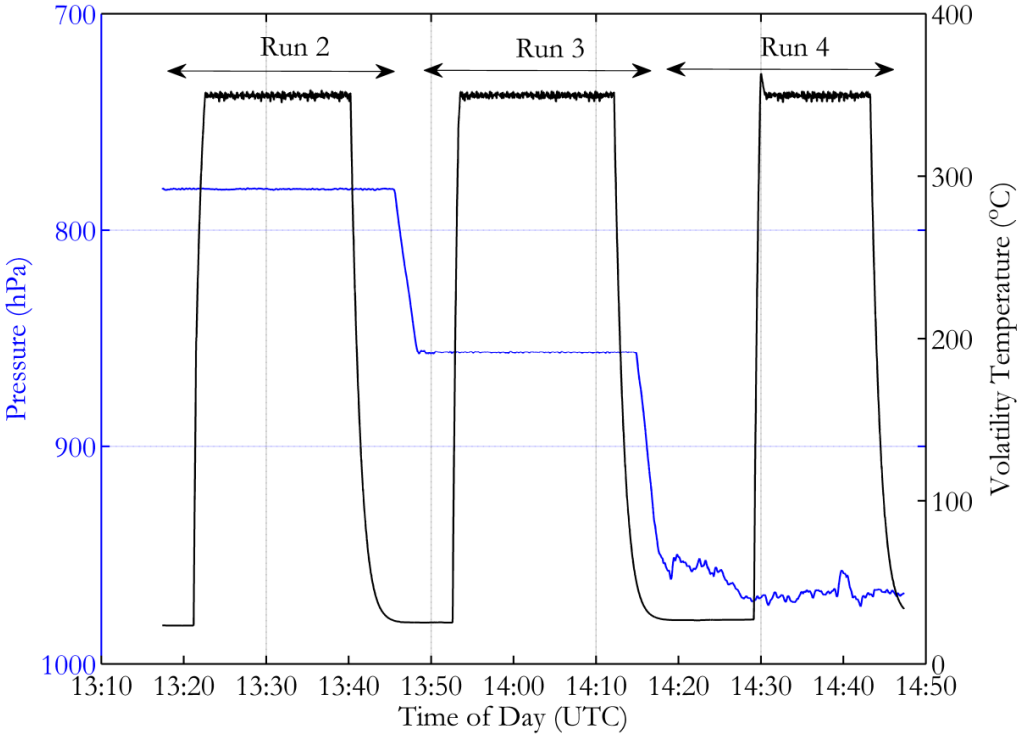

Figure 6.11 Time series from B734 (18 September 2012) of (*blue*) aircraft pressure and (*black*) volatility temperature of the VACC volatility system for runs 2 – 4.

Table 45 Identification of the VACC ambient and volatile operating conditions during B734 (18 September 2012)

	Ambient			Volatile		
	Start Time (UTC)	End Time (UTC)	Comparison Length	Start Time (UTC)	End Time (UTC)	Comparison Length
Run 2	13:17:24	13:21:14	0:03:50	13.22.28	13.40.15	0:17:47
Run 3	13:42:53	13:52:38	0:09:45	13.53.25	14.12.13	0:18:48
Run 4	14:14:54	14:29:11	0:14:17	14.29.57	14.43.17	0:13:20

The first verification step is to assess if the two instruments measure the same number concentration when exposed to the same aerosol. A time series of the total number concentration measured by the external wing-mounted PCASP and the VACC PCASP during ambient operation (< 50 ^{o}C) and volatile operation (350 ^{o}C) is shown in figure 6.12. The time series indicates that there is good agreement in total number concentration between the two instruments.

The theoretical response of total number concentration to aerosol mixing state using thermo-optical techniques was discussed in chapter 3. During ambient operation of the VACC, total particle concentration clusters along the 1:1 line on the scatter plot (figure 6.12, bottom panel), that is the instruments measure particle concentration to a similar degree. The number concentration measured by the VACC at 350 ^{o}C ($N_{Non-Vol}$) falls below the 1:1 line relative to the total number concentration at ambient. This indicates that there is external mixing within the aerosol population, although it is evident that not all of the population is volatile at 350 ^{o}C. Understanding the non-volatile component is further discussed in section 6.5.2. This method allows only for a qualitative interpretation of the aerosol mixing state.

The comparison of total number concentration gives confidence between the two instruments; a further comparison of total number concentration between the two instrument within a subset of sizes (< 0.23 μm and 0.23 – 0.53 μm) is an important comparison to be made, as presented in figure 6.13. The size range < 0.23 μm covers the high and mid instrument gain stages and 0.23 – 0.53 μm covers the low gain of the instruments (or to a maximum of bin 15 for the VACC PCASP).

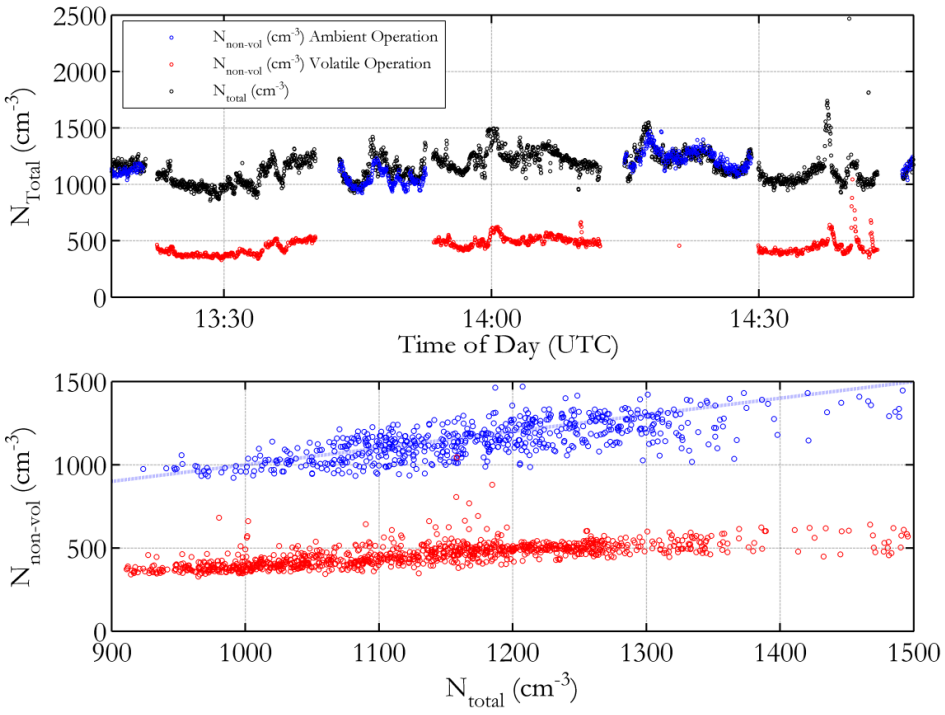

Figure 6.12 (*top*) Time series from B734 (18 September 2012) of (*black*) total number concentration measured by the external PCASP, (*blue*) total number concentration of the VACC during ambient operation, and (*red*) total number concentration of the VACC during volatile operation (350 °C). (*bottom*, *blue*) Scatter plot of total number concentration (N_{Total}) measured by the external PCASP and during ambient operation of the VACC (*red*) scatter plots of total number concentration (N_{Total}) measured by the external PCASP and during volatile operation of the VACC ($N_{Non\text{-}vol}$).

It is evident that whilst total number concentration ($N < 0.53$ μm) agree well, the size segregated plots show that the VACC PCASP overestimates particle number concentration relative to the wing-mounted PCASP in the size range < 0.23 μm. Particle number concentration in the size range of 0.23 – 0.53 μm is underestimated. Whilst an instrument comparison between two instruments does not allow a firm conclusion to be drawn, it points to the potential of laser misalignment in the VACC PCASP. Although this introduces some uncertainty about the performance of the VACC, it has been shown in the size distribution comparison of the excellent agreement between the VACC and Grimm instruments.

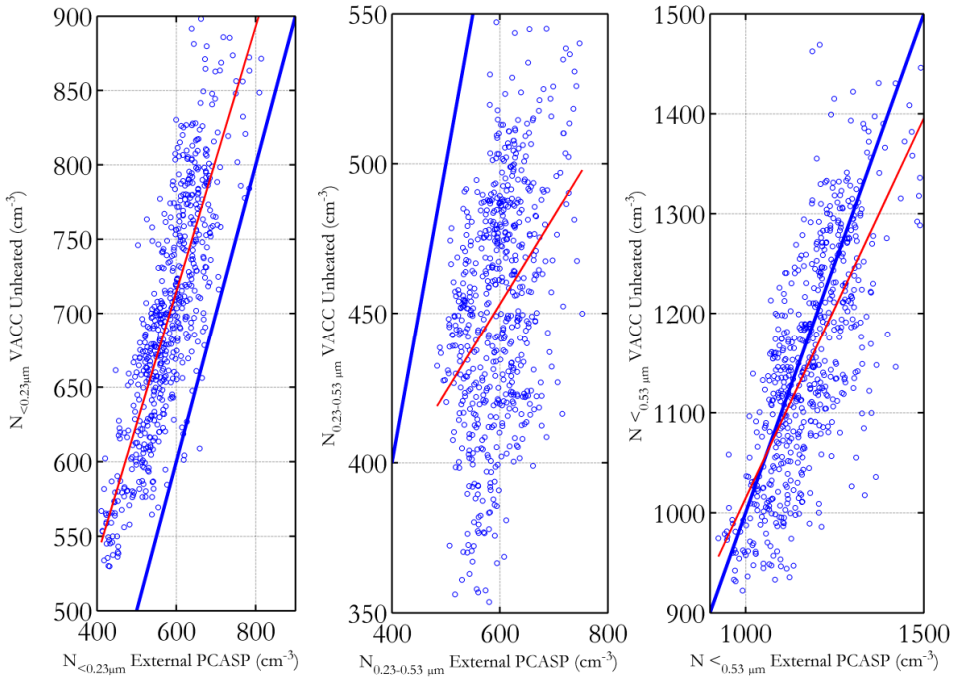

Figure 6.13 Scatter plots of number concentration from flight B734 of (*left*) N < 0.23 μm, (*middle*) N = 0.23 – 0.53 μm, and (*right*) N < 0.53 μm measured by external wing-mounted PCASP and by the VACC PCASP whilst at ambient temperature (*blue dashed line*) 1:1 line of number concentration.

6.5.2 Black Carbon Core and Shell Measurements

The heating of the aerosol in the VACC changes the chemical composition of the aerosol, and as such the refractive index of the aerosol. To account for these changes, the variability in the VACC PCASP bin diameters with respect to refractive index is assessed for 100 refractive indicies over a limited range. The refractive indices of bulk biomass burning and black carbon were chosen based on the range of literature refractive indices from Amazonian field campaigns as presented in Table 7. In representing the bulk biomass burning aerosol, the refractive index real part range of n = 1.45 – 1.65 and imaginary part range of k = 0.000 – 0.030*i* (figure 6.14) have been chosen. In representing the sizing of black carbon measured by the VACC whilst heated a refractive index range of n = 1.85 – 1.95 and imaginary part range of k = 0.200 – 0.800*i* was chosen (figure 6.15). Particularly evident in figure 6.15 is the uncertainty associated with bin 15 with respect to the refractive index, which is partly due to the

difficulty in accurately determining the upper boundary of bin 15 in the calibration of the instrument.

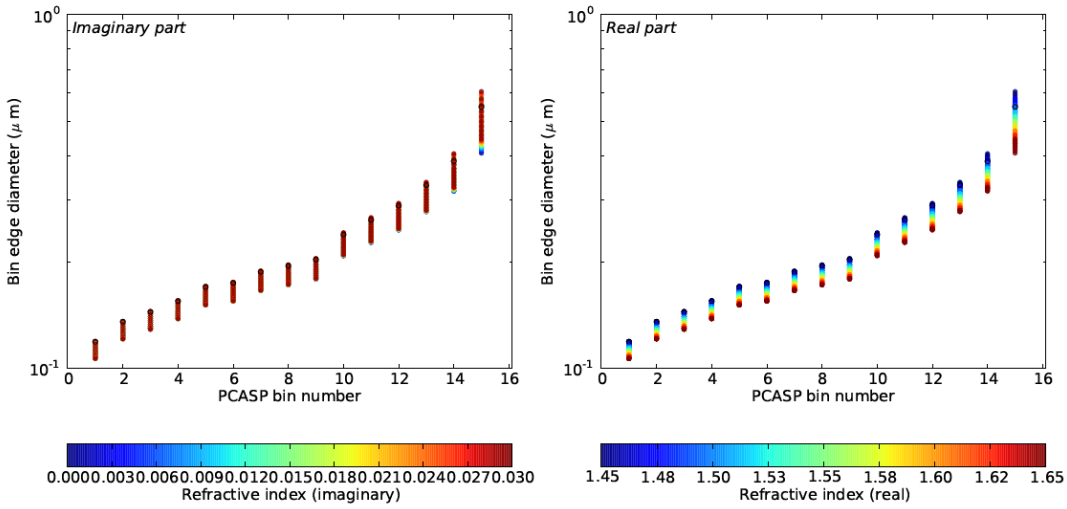

Figure 6.14 Bin edge diameters for the VACC PCASP calculated from calibrated instrument cross sections for bulk biomass burning aerosol. (*left*) Real part refractive index range n = 1.45 – 1.65 and (*right*) imaginary part range of k = 0.000 – 0.030 (*black circle*) calibration equivalent bin edge diameter. Figure courtesy of J. Langridge, Met Office.

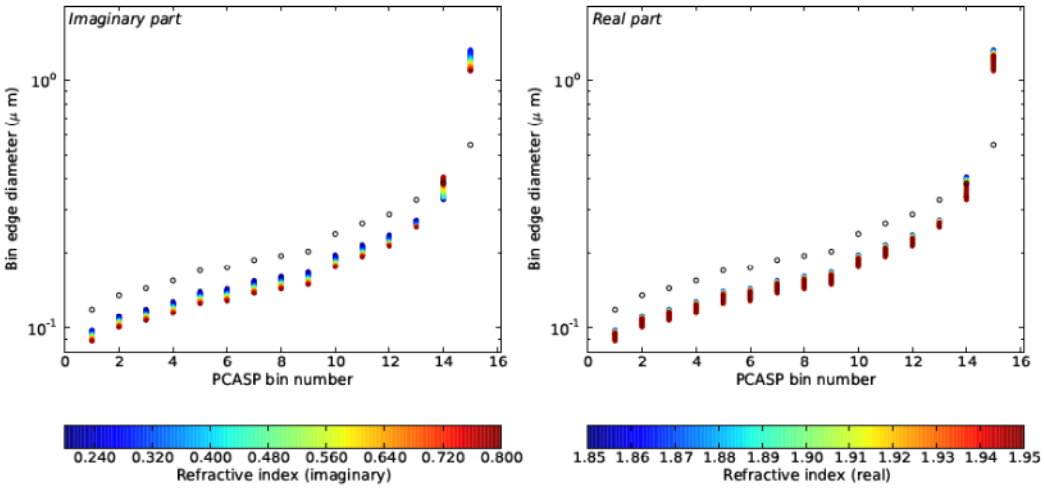

Figure 6.15 Bin edge diameters for the VACC PCASP calculated from calibrated instrument cross sections for black carbon. (*left*) Real part refractive index range of n = 1.85 – 1.95 and (*right*) imaginary part range of k = 0.200 – 0.800 (*black circle*) calibration equivalent bin edge diameter. Figure courtesy of J. Langridge, Met Office.

In the case of measurements with a thermo-optical technique, a median shell-to-core diameter ratio can be derived which provides a representation of particle coating thickness. The median core diameter, termed D_{Core}, is derived from a lognormal fit to the size distribution measured at 350 °C. This assumes that the volatile material is sufficiently volatilised at this temperature, that is, only the non-volatile black carbon core remains. The mean number concentration of the size distribution is termed N_{Core}. The VACC coating thickness presented here is not directly measured using the thermo-optical measurement technique (no direct measurement can be made using this technique); rather the coating distributions discussed are derived by scaling the size distributions measured at 350 °C by the median diameter of the ambient size distribution. The median diameter of this scaled distribution is termed D_{Shell}, and the mean number concentration of this size distribution is termed N_{Shell}.

In an externally mixed aerosol population the median shell-to-core diameter (D_{Shell}/D_{Core}) ratio is equal to 1 and median shell-to-core number concentration (N_{Shell}/N_{Core}) ratio is greater than 1; indicating a change to the number concentration but not to the size of the aerosol population. In an internally mixed aerosol population the median shell-to-core diameter ratio is greater than 1, and N_{Shell}/N_{Core} is equal to 1, indicating a change to the size distribution of the aerosol population, whilst number concentration of the population is maintained.

A comparison between ambient size distribution of the VACC, non-volatile distribution of the VACC when heated at 350 °C, and the size distribution of the black carbon core as measured by the SP2 instrument is presented in figure 6.16 for Rondônian regional haze. The comparison between the VACC and SP2 can enable an assessment the use of thermo-optical techniques in resolving black carbon content of biomass burning within an aerosol population. This is a subject which is not well compared in the literature. In reference to the VACC ambient distributions presented in figure 6.16, the mean diameter refers to the bulk biomass burning refractive index. For the non-volatile size distribution, the mean diameter refers to the mean of the range of black carbon refractive indices. The range in the instrument bin edge diameters are presented as horizontal error bars and indicate the variability in the particle diameter with respect to the aerosol refractive index. Note there is no availability of SP2 data for flight B735 in figure 6.17 for Amazonian aerosol. A two mode lognormal was fitted to cover the accumulation mode size distribution. The accumulation mode lognormal number

distributions for ambient size distribution of the VACC, non-volatile distribution of the VACC when heated at 350 °C are presented in table 46.

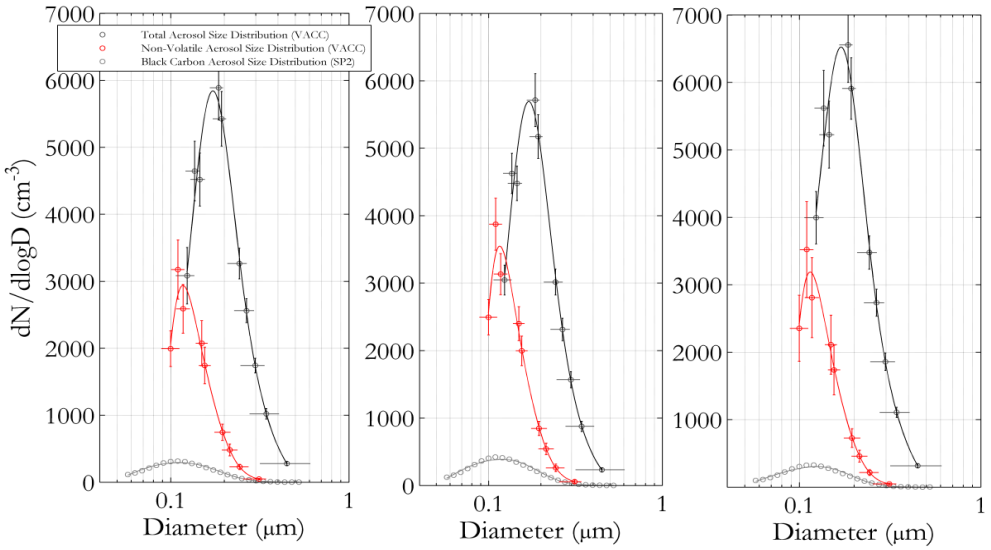

Figure 6.16 (*black*) Ambient aerosol number size distribution, (*red*) non-volatile aerosol number size distribution during 350 °C operation and (*grey*) BC number size distribution measured by the SP2 for flight B734 (*left*) run 2, (*middle*) run 3 and (*right*) run 4.

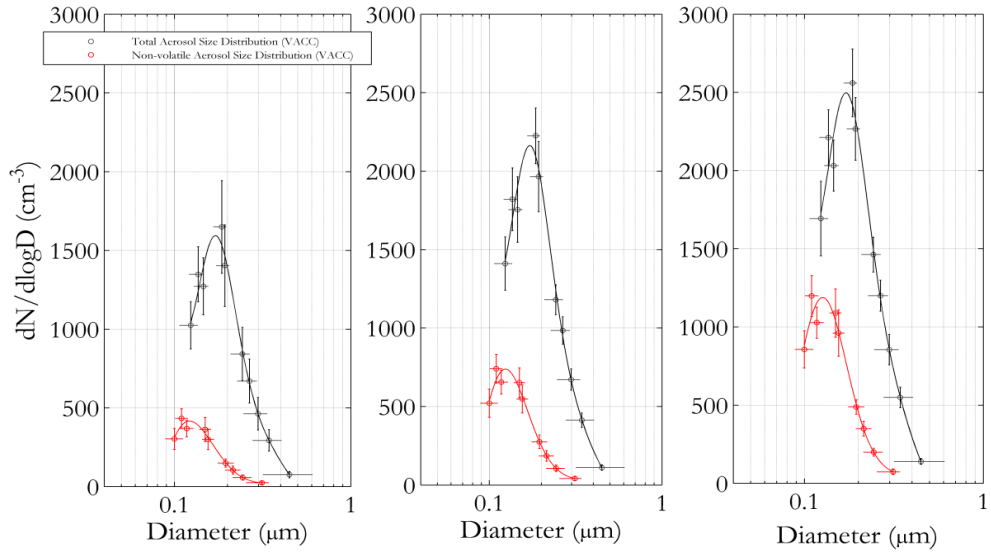

Figure 6.17 (*black*) Ambient aerosol number size distribution and (*red*) non-volatile aerosol number size distribution during 350 °C operation for flight B735 (*left*) run 2, (*middle*) run 3, and (*right*) run 4. Vertical error bars indicate one standard deviation of the data and horizontal error bars indicate the variability in the particle diameter with respect to the aerosol refractive index.

Table 46 Median shell-to-core diameter ratios (D_{Shell}/D_{Core}) and shell-to-core number concentration (N_{Shell}/N_{Core}) for the accumulation mode.

Flight	Aerosol Type	D_{Shell} (μm)	σ_{Shell}	D_{Core} (μm)	σ_{Core}	D_{Shell}/D_{Core}	N_{Shell} (cm^{-3})	N_{Core} (cm^{-3})	N_{Shell}/N_{Core}
B734 Run2	Rondônian regional haze	0.170	1.39	0.118	1.35	1.44	2045	914	2.2
B734 Run3		0.168	1.38	0.116	1.36	1.45	1955	1112	1.8
B734 Run4		0.165	1.40	0.114	1.36	1.45	2378	1018	2.3
B735 Run 2	Amazonian aerosol	0.170	1.40	0.125	1.37	1.36	570	142	4.0
B735 Run 3		0.169	1.42	0.123	1.38	1.36	800	249	3.2
B735 Run 4		0.169	1.45	0.127	1.39	1.33	980	423	2.3

A change in the size of an aerosol size distribution is evident with heating, indicated by a shift to smaller diameters as a result of the loss of volatile material. The Rondônian regional haze size distributions from the VACC reflected a decrease in the count median diameter from 0.170 μm to 0.118 μm with a resultant D_{Shell}/D_{Core} ratio of 1.44. The standard deviations of the two distributions were broadly similar with a small decrease in σ due to the loss volatile material. Analysis of the size distribution for Amazonian aerosol found a D_{Shell}/D_{Core} of 1.36, which was consistent with a larger mean core diameter of 0.125 μm.

The size distribution of black carbon measured by the SP2 can be described with one lognormal mode; the D_{Core} at 0.113 μm and σ_{Core} of 1.53 for Rondônian regional haze. The mean diameter of the core shows a reasonable agreement between the two instruments, although the SP2 measured a broader distribution compared with the VACC. A time series of median shell-to-core diameter ratios measured by the SP2 is presented in figure 6.18 for Rondônian regional haze and indicates a range between 2.3 – 2.5. This range shows very little consistency with the median shell-to-core diameter ratios derived from the VACC, from which it can be concluded that assuming a coating distribution derived by scaling the size distributions measured at 350 °C by the median diameter to the ambient size distribution does not provide a realistic representation of the coating distribution.

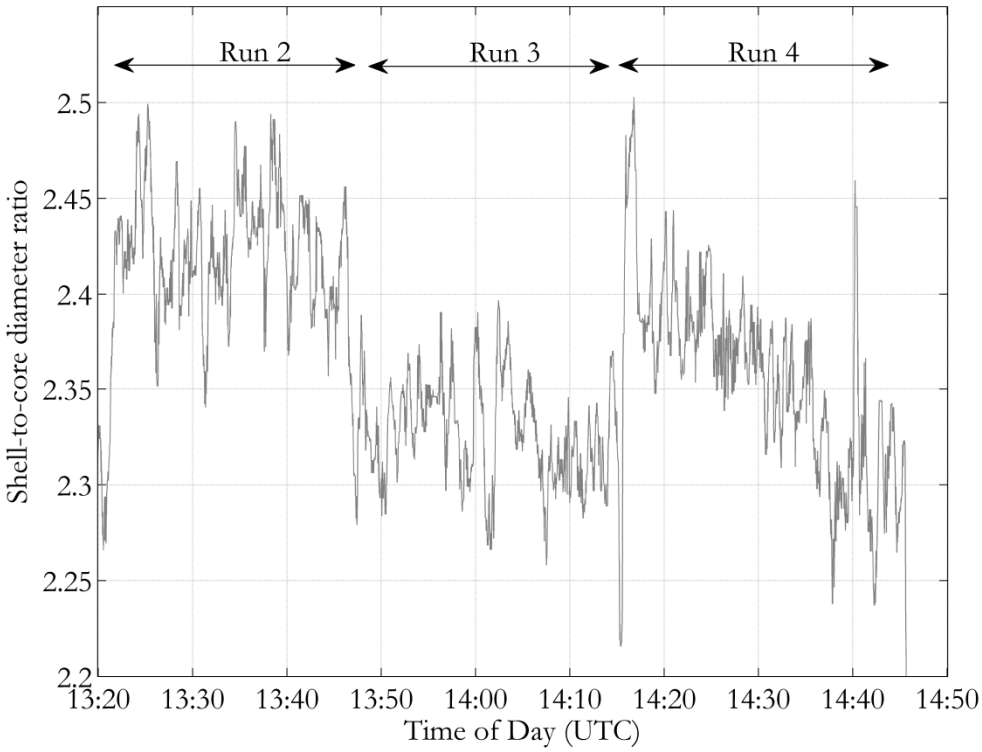

Figure 6.18 Time series of median shell-to-core diameter ratio from the SP2 instrument for Rondônian regional haze (B734, 18 September 2012).

A loss in number concentration on heating of an aerosol size distribution indicates external mixing within the aerosol population. All distributions presented here reflect a change in number, that is, they all exhibit some degree of external mixing. The external mode is assumed to be a mix of sulphate, nitrate and organic compounds. The change in median number concentration, for regional haze consistent with a homogenous aerosol layer, found a flight average N_{Shell}/N_{Core} of 2.1.

The analysis for Amazonian aerosol showed greater variability in the median shell-to-core number concentration throughout the flight with a N_{Shell}/N_{Core} ratio of 4.0 in run 2, decreasing to 2.3 in run 4. The D_{Shell}/D_{Core} has been shown to remain constant indicating there is no change in the coating thickness of particles. The change in the N_{Shell}/N_{Core} ratio indicates twice as much of the aerosol population is volatile at 350 °C in run 2 compared with run 4; it could be suggested that this reflects where the measurement was made, with run 4 close to Manaus and associated urban emissions.

The total number concentration measured at ambient by the SMPS and Grimm is compared with average number concentration measured by the VACC during volatile operation (350 ^{o}C) and average BC number concentration measured by the SP2, as presented in table 47. The results show that of the total number concentration measured by the SMPS and Grimm instruments, 23 % of the total concentration remains at 350 ^{o}C during the volatile operation of the VACC, compared with 4 % of total number concentration remaining measured by the SP2. The result from the SP2 compares well with the composition measurements from AMS and SP2 measurements of black carbon within the aerosol population, presented in section 6.7 of this chapter. The difference between the percentage of material between the SP2 and VACC reflects the mechanism of removal with the VACC using the thermal volatility in comparison to the incandescence technique used in the SP2 to measure black carbon directly.

The difference in the number concentration of the distribution suggests thermal denuder temperature of the VACC does not sufficiently vaporise material in the external mode of the aerosol distribution i.e. there are compounds in the external mode which are non-volatile at 350 ^{o}C. It is known that the volatility temperature of the VACC was sufficiently high to remove inorganic sulphate and nitrate species along with low molecular weight organic compounds. Without a compositional understanding of the different organic carbon compounds it is not possible to discuss with any certainty to the contribution of high molecular weight organic compounds to the overall organic component, as the AMS only provides a bulk composition. Any further investigation into the nature of the organic carbon measured is not within the scope of this investigation.

Table 47 Total number concentration measured at ambient by the SMPS and Grimm, the VACC during volatile operation (350 ^{o}C) and measured by the SP2. The average number concentration is calculated for the size range of the VACC (0.10 – 0.31 μm).

Instrument	Total Number Concentration (cm^{-3})	Percentage of Total Number Concentration
SMPS / Grimm	2880	-
VACC (350 ^{o}C)	667	23
SP2	120	4

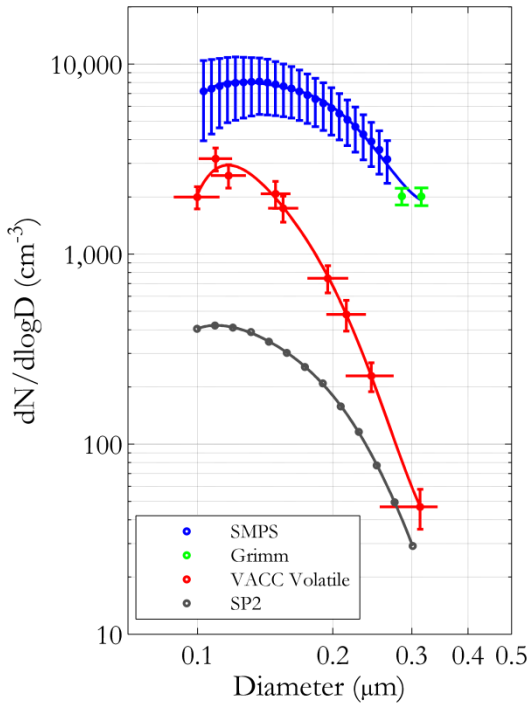

Figure 6.19 (*blue*) SMPS size distribution, (*green*) Grimm size distribution, (*grey*) SP2 black carbon size distribution and (*red*) VACC volatile (350 °C) size distribution across the size range of 0.1 to 0.31 μm.

The use of thermal techniques to resolve black carbon content of biomass burning from *in-situ* airborne measurements is not well characterised in the literature. Laboratory studies such as those by Kondo et al. (2011) investigated the removal of different molecular weight volatile compounds by the means of a heated inlet operated with a residence time of about 0.3 s. Kondo et al. (2011) investigated a number of organic compounds heating between 300 °C and 400 °C involving saccarides, dicarboxylic acid, aromatic acids and Humic-Like Substances (HULIS) sized with an SMPS. Kondo et al. (2011) found that at 400°C, diameters of saccarides, dicarboxylic acids and aromatic acids decreased by factors of 4 – 10. High molecular weight organics such as HULIS showed less significant changes with respect to the volatility technique – when heated at 400 °C, volume changes ranged from 20 – 60 %, and at 300 °C volume changes were 10 % to 30 %, with little change in the sizes measured by the SMPS.

Kondo et al. (2011) additionally assessed the interference of absorption measurements due to the charring of refractory organics; the change in the absorption measurements was estimated to be less than 5 %, at 300 °C and 400 °C, 1.7 % and 4.6 %, respectively.

Although it must be noted that the residence time in this investigation was much shorter compared with the residence time in the VACC heater (33 second residence time).

The most reliable method for determining the black carbon distribution is with the SP2 as there is no interference from the external mode of organic carbon in retrieving the coating thickness of the aerosol. However the SP2 does not provide any information regarding the mixing state of the aerosol, and therefore the VACC has the potential to compliment the SP2 measurements. From the results presented here further investigation in necessary to extend and understand the response of the thermo-optical techniques in resolving the black carbon properties.

6.6 Aerosol Composition and Speciation

In order to understand the refractive index of aerosol (section 6.7) it is necessary to understand the composition, and in turn the speciation of the inorganic component of aerosol. The speciation of atmospheric particulate sulphate is discussed within Seinfeld and Pandis (2006), and is largely determined by the availability of ambient ammonia to neutralise the acidic sulphate species. The main sink for ammonia in the atmosphere is the heterogeneous reaction with sulphuric acid, yielding ammonium sulphate, $(NH_4)_2SO_4$, and ammonium bisulphate, NH_4HSO_4. In order to determine the speciation of the sulphate encountered during B734 and B735, the concentration of sulphate ions to ammonium ions are calculated from AMS mass concentrations.

According to theory given in Seinfeld and Pandis (2006), in cases where the ammonium to sulphate concentration ratio is less than 2, then the regime is defined as ammonia-poor environment, whilst if the ratio is greater than 2, then the system is classified as ammonia-rich environment. In the case of Rondônian regional haze, figure 6.20 shows the ratio of ammonium to sulphate concentration lies above the $2SO_4^{2-}$: NH_4^+ line, indicating all the ammonia is fully neutralized with the sulphate present, and therefore, the predominant aerosol component is $(NH_4)_2SO_4$.

A greater spread in the ratio of ammonium to sulphate concentrations was encountered for Amazonian aerosol as indicated in figure 6.21. The ratio of ammonium to sulphate concentration lies below the $2SO_4^{2-}$: NH_4^+ line for a portion of the flight, indicating measured aerosol is within an ammonia-poor environment; as such the particulate

matter exists as ammonium bisulphate as well as ammonium sulphate. Note, in extreme cases where the NH_4^+/SO_4^{2-} ratio is ≤ 0.5, the aerosol particles exist primarily as H_2SO_4.

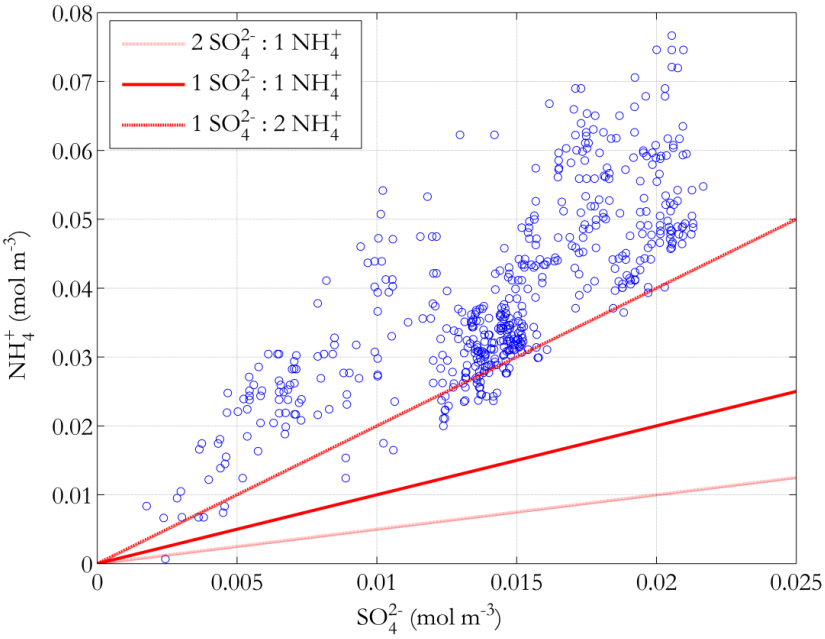

Figure 6.20 Scatter plot of ammonium and sulphate concentrations in submicron particles (*red solid line*) SO_4^{2-} : NH_4^+ (*red dotted line*) $2SO_4^{2-}$: NH_4^+ (*red dashed line*) SO_4^{2-} : $2NH_4^+$ from the AMS for Rondônian regional haze (B734, 18 September 2012).

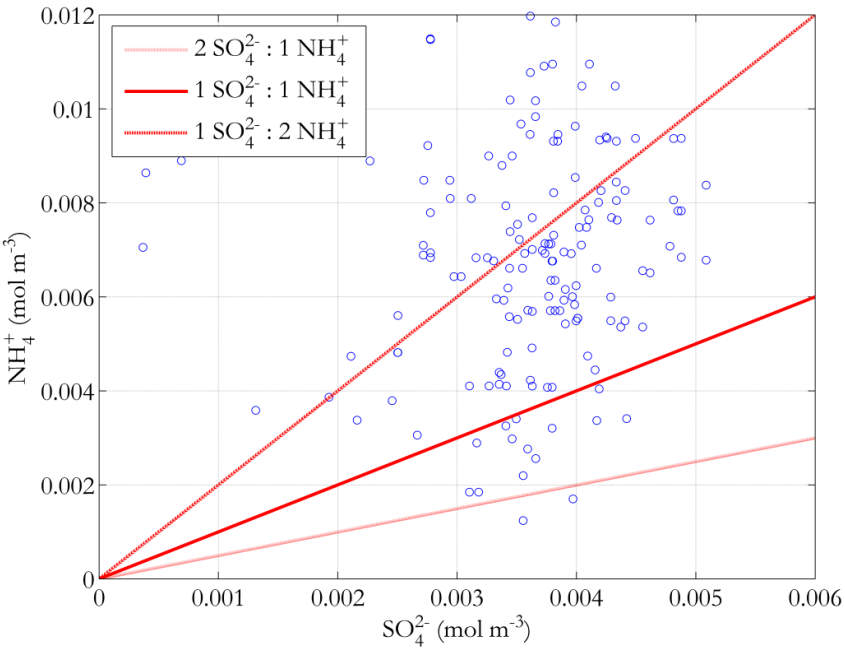

Figure 6.21 Scatter plot of ammonium and sulphate concentrations in submicron particles (*red solid line*) SO_4^{2-} : NH_4^+ (*red dotted line*) $2SO_4^{2-}$: NH_4^+ (*red dashed line*) SO_4^{2-} : $2NH_4^+$ from the AMS for Amazonian aerosol (B735, 19 September 2012).

6.7 Refractive Index Representation

Various approaches can be made in calculating the complex refractive index using mixing rules, and require knowledge of the individual sub-components such as density and refractive index. The simplest approach in assessing an effective refractive index is the linear mixing rule (d'Almeida et al., 1991). The approach treats the aerosol composition as being homogeneously internally mixed with the total real (n_{tot}) and imaginary (k_{tot}) refractive index of an aerosol species is given by a linear average of the indices of the aerosol sub-components weighted by their volume fractions;

$$n_{tot} = f_1 n_1 + f_2 n_2 \qquad (6.1)$$

$$k_{tot} = f_1 k_1 + f_2 k_2$$

where f_i is the volume fraction of the aerosol subcomponents, n_i and k_i are the real and imaginary parts of the refractive index of the aerosol subcomponents.

A number of papers discuss the limitations associated with the linear mixing rule (Jacobson 2000, Bond and Bergstrom, 2006; Bond et al. 2006). Bond and Bergstrom (2006) caution of the use of simply applying volume-mixing procedures due to the unrealistic representation to measured aerosol in the natural atmosphere; on mixing, the sp^2 nature of black carbon particles is redistributed evenly across the particle which would interrupt the medium-range order that governs absorption (Bond et al. 2006). Jacobson (2000) varied the particle mixing representation in a global model and showed the radiative forcing for external mixing of +0.27 W m^{-2}, core-shell representation of +0.54 W m^{-2}, and linear volume mixing of +0.78 W m^{-2}; a forcing factor in the range of 1.6 – 2.9 depending on the representation of the mixing representation.

The Maxwell-Garnett mixing rule makes an assumption of particle internal arrangement which consists of randomly distributed, spherical absorbing inclusions embedded in a homogenous, scattering matrix (Bohren and Huffman, 1983; Garnett, 1904). The Maxwell-Garnett mixing rule represents the multiple component inclusions as encountered in aerosol species, with the complex dielectric constant $\left(\varepsilon_{Maxwell-Garnet}\right)$ given by Lesins et al. (2002).

$$\varepsilon_{\substack{Maxwell-\\Garnet}} = \varepsilon_m \left[\frac{\varepsilon_1 + 2\varepsilon_m + 2f_1(\varepsilon_1 - \varepsilon_m)}{\varepsilon_1 + 2\varepsilon_m - f_1(\varepsilon_1 - \varepsilon_m)} \right] \quad (6.2)$$

where ε_m and ε_1 are the dielectric constants of the host matrix (a linear mix of organic carbon, ammonium sulphate and ammonium nitrate) and embedded inclusions of black carbon, respectively. f_1 is the volume fraction of black carbon.

The bulk dielectric constant is a property of the aerosol material and the representation of the real and imaginary dielectric constants are not independent, rather they are related to the real (6.3) and imaginary (6.4) parts of the refractive index using (equation 9.1 from Bohren and Huffman, 1998, p. 227).

$$\varepsilon_{real} = n^2 - k^2 \quad (6.3)$$

$$\varepsilon_{imag} = 2nk \quad (6.4)$$

Here we consider literature refractive index of principle aerosol components for representation in the linear and the Maxwell-Garnett mixing rules to determine the complex aerosol refractive index of biomass burning aerosol. The assumption of internal mixing is valid due to the aging of biomass burning to form regional haze aerosol. Table 48 summarizes the refractive indices and densities of all the individual aerosol components known to be present in optically significant amounts during the campaign. Well established refractive indicies of ammonium sulphate and ammonium nitrate are used from Toon et al. (1976) and Weast (1985), respectively.

There is considerable the variability in the literature with regards to the refractive indices of black carbon and organic carbon. Bond and Bergstrom (2006) suggest a range in the refractive index of black carbon from a lower absorbing limit of m = 1.75 – 0.63*i* to an upper absorption limit of m = 1.95 – 0.79*i*. The refractive index selected in table 48 from Schmid et al. (2009) suggested m = 1.90 – 0.2*i* and is representative of Amazonian aerosol constrained by measurements from the LBA-SMOCC field campaign. The real part of the selected refractive falls between the range presented by Bond and Bergstrom (2006), whilst the imaginary part of the refractive index is lower than the range presented. It should be noted that when investigating biomass burning aerosol closer to source, that is, where the aerosol composition has a greater contribution of black carbon, a more absorbing refractive index might be more appropriate than that chosen

here. In the two aerosol species considered here the BC mass was less than 5 % of the aerosol composition and therefore is a small cause of uncertainty in the refractive indices derived here.

An assumption has been made about the bulk refractive index of the organic component of biomass burning which is complicated due to the large range of organic compounds emitted during combustion. Levin et al. (2010) found the real part of the refractive index for organic aerosol to be in the range of n = 1.41to 1.61. The refractive index selected in table 48 from Schmid et al. (2009) falls within this range, with the imaginary part set to zero. There is considerable uncertainty due to the imaginary part of the refractive index of organic carbon due to the vast range of organic carbon compounds emitted through biomass burning. Organic carbon additionally dominates the aerosol composition (figure 6.22).

Table 48 Densities and refractive index (at 550 nm) of principle aerosol components

	Density (g cm^{-3})	n	k	Reference
Black Carbon	1.80	1.90	- 0.2i	Schmid et al. (2009)
Organic Carbon	1.39	1.46	0i	Schmid et al. (2009)
Ammonium bisulphate	1.80	1.50	0i	Kreidenweis et al. (2003)
Ammonium sulphate	1.769	1.53	- 1×10^{-7}i	Toon et al. (1976)
Ammonium nitrate	1.725	1.611	- 1×10^{-7}i	Weast (1985)

A flight-mean index of refraction for Rondônia regional haze and Amazonian aerosol is derived here. The aerosol composition used in the calculation of the refractive index is based on AMS and SP2 mass concentrations, with a time series of aerosol mass concentration of Rondônian regional haze presented in figure 6.22. Summary tables of aerosol average mass concentration, percentage composition and density mixing from the AMS and SP2 instruments for Rondônian regional haze and Amazonian aerosol are presented in table 49 and table 50, respectively.

Rondônian regional haze was found to be approximately 5 % black carbon, 80 % organic carbon and 15 % inorganic which was primarily ammonium sulphate. Amazonian aerosol was found to have a lower contribution of black carbon of 2.5 %, 75 % organic carbon and 22.5 % inorganic dominated by ammonium bisulphate.

Concentrations of black carbon across Amazonia were as low as 0.02 μg m^{-3}, up to a maximum of 0.06 μg m^{-3}.

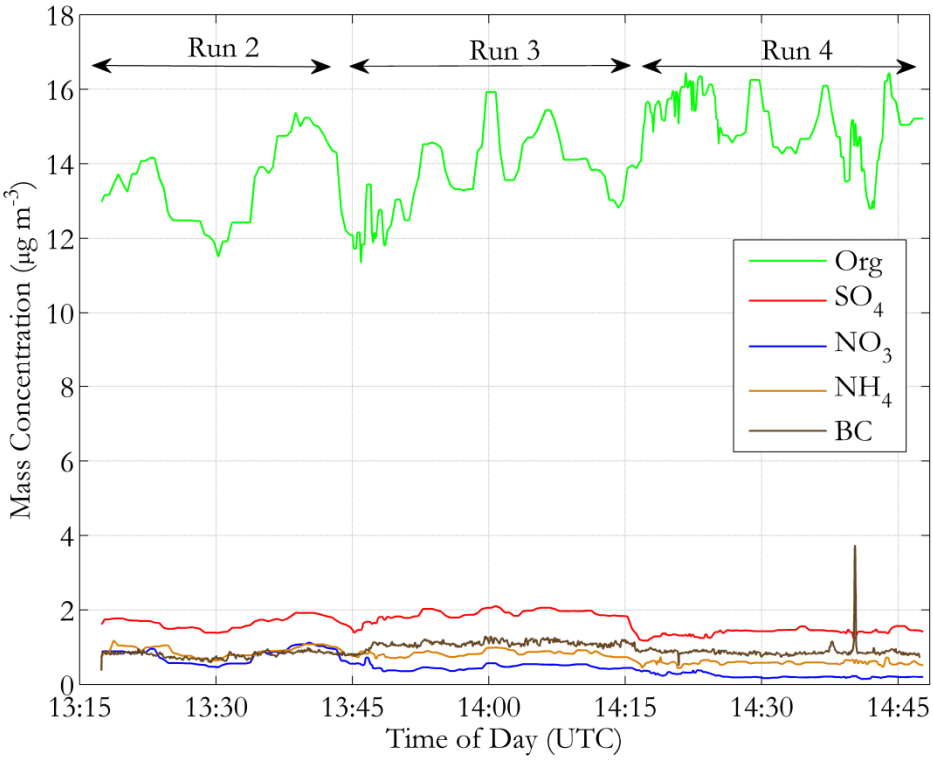

Figure 6.22 Time series of aerosol mass concentration of Rondônian regional haze from the AMS and SP2 instruments for B734 (18 September 2012) (*green*) organic component (*red*) sulphate component (*blue*) nitrate component (*brown*) ammonium component and (*black*) black carbon component.

Table 49 Average mass concentration, percentage composition and density mixing of Rondônian regional haze from the AMS and SP2 (B734, 18 September 2012).

	Mass Concentration (μg m^{-3})	Composition (%)	Density Mixing (g cm^{-3})
Black carbon	0.926 ± 0.178	5.2	0.09
Organics	14.268 ± 1.321	79.8	1.11
Ammonium	0.716 ± 0.159	-	-
Sulphate	1.556 ± 0.242	11.4	0.20
Nitrate	0.421 ± 0.230	3.6	0.06

Table 50 Average mass concentration, percentage composition and density mixing of Amazonian aerosol from the AMS and SP2 instruments (B735, 19 September 2012).

	Mass Concentration ($\mu g\ m^{-3}$)	Composition (%)	Density Mixing ($g\ cm^{-3}$)
Black carbon	0.040	2.6	0.05
Organics	1.146 $\pm$ 0.532	74.6	1.04
Ammonium	0.073 $\pm$ 0.048	-	-
Sulphate	0.231 $\pm$ 0.532	18.3	0.32
Nitrate	0.045 $\pm$ 0.025	4.5	0.08

Linear mixing of the refractive index (table 51) found a general consistency across Rondônia regional haze and Amazonia aerosol for the real part of the refractive index (1.48 – 1.49). The imaginary part of the refractive index for Amazonian aerosol (0.0043*i)* is half that of Rondônia regional haze (0.0083*i)*. This reflects the differing composition between the two flights, partially in terms of black carbon content, 2.6 % compared to 5.2 %. Also contributing to the lower imaginary part of the refractive index is the increased sulphate composition (18 % compared with 11 %). The corresponding density was 1.47 g cm^{-3} and 1.49 g cm^{-3} for Rondônia regional haze and Amazonian aerosol, respectively. Highwood et al. (2012) discussed that the linear mixing rule could hold true due to the low percentage of BC in the aerosol (less than 5 % aerosol mass) which is applicable to the two flights considered here, particularly for Amazonian aerosol (B735) due to the low percentage of black carbon (mass concentrations ranged from 0.02 – 0.06 $\mu g\ m^{-3}$).

Table 51 Refractive index (at 550 nm) from linear-mixing for Rondônian regional haze and Amazonian aerosol.

	Rondônian regional haze		Amazonian aerosol	
	n	k	n	k
Black Carbon	0.079	-0.0083*i*	0.040	-0.0043*i*
Organics	1.217	0.0000*i*	1.154	0.0000*i*
Ammonium Sulphate	0.143	0.0000*i*	-	-
Ammonium Bisulphate	-	-	0.224	0.0000*i*
Ammonium Nitrate	0.050	0.0000*i*	0.062	0.0000*i*
Linear-mixing	1.49	-0.0083*i*	1.48	-0.0043*i*

The imaginary part of the refractive index was approximately 40 % lower using the Maxwell-Garnett mixing rule (table 52) compared with the volume mixing rule. The results found here are somewhat higher but consistent with the study by Schuster et al. (2005) who found that the volume mixing representation resulted in a imaginary refractive index 13 – 30 % greater than the Maxwell-Garnett approximation. The result here is also consistent with the result of Lesins et al. (2002), who found the imaginary part of the refractive index is affected more than the real part. It is important to consider that any difference in the variability in the refractive index due to the mixing approach is small compared to the variability due to the assumed refractive index of the sub-components used in the mixing, primarily due to the large range of literature values, particularly for organic carbon.

Table 52 Refractive index (at 550 nm) from Maxwell-Garnet mixing for Rondônian regional haze and Amazonian aerosol.

	Rondônian regional haze		Amazonian aerosol	
	n	k	n	k
Host Matrix	1.472	$1.30 \times 10^{-8}i$	1.477	$1.94 \times 10^{-8}i$
Inclusions	1.9	$0.2i$	1.9	$0.2i$
Maxwell-Garnet	1.48	$-0.0050i$	1.48	$-0.0025i$

Relating the refractive indicies derived here to those presented in the literature review, it can be seen there is a close agreement to that of Dubovik et al. (2002) for biomass burning aerosol from smouldering phase of combustion from Amazon forest with a refractive index of $m = 1.47 - 0.0093i$ as identified by from the AERONET network. The refractive index of Rondônian regional haze during SCAR-B was identified by Reid et al. (1998a) as $m = 1.50 – 0.02i$, which reflects a larger imaginary part compared with the result derived here. This refractive index shall be contrasted with the B734 derived linear-mixing refractive index in the succeeding section, and used to compare the optical properties of Rondônian regional haze measured during SAMBBA and SCAR-B.

Guyon et al. (2003) present a Rondônian background refractive index of $m = 1.41 - 0.006i$. The derived linear-mixing refractive index for B735 found a smaller real part of the refractive index but is in reasonable agreement with the derived imaginary part of the refractive index from Guyon et al. (2003). In areas away from biomass burning

regions, Rondônian is primary forest and the comparison to Guyon et al. (2003) provides a suitable comparison to Amazonian aerosol.

6.8 Relative Humidity

The humidity effects of aerosol are an important consideration for the optical properties of aerosol, with particles exhibiting growth which changes the scattering characteristics of the aerosol. The influence of humidity on the growth of hygroscopic aerosol must be considered. The PCASP measured dried aerosol and such removes any water and possibly some high-volatility (low molecular weight) organic compounds, and Grimm and SMPS are assumed to dry as they are sampled through the Rosemount inlet and tubing to the instruments. The PSAP and nephelometer are treated as measuring dry aerosol (Highwood et al. 2012), due to the effects of RAM heating both at the Rosemount inlet and contribution of drying along the instrument sample line.

The standard method in assessing the influence of humidity on aerosol growth is using humidograms from a wet nephelometer instrument which measures the dependence of aerosol scattering as a function of relative humidity. A number of problems were encountered during the SAMBBA campaign with regards to the functionality of the wet nephelometer and the resulting data quality. These include elevated cabin and sample temperatures which restricted achievable RH to approximately 70 %, a leak on the outlet to the dry nephelometer, which is in series with the wet nephelometer and a lack of confidence in RH sensor calibration. Due to these factors, the wet nephelometer data was disregarded in assessing the influence of humidity on aerosol growth; the following approach has been implemented as an alternative.

Dew point temperature and relative humidity measurements from B734 for two instruments the General Eastern and the Buck CR2 chilled mirror hygrometers, is presented in figure 6.23. The calculated relative humidity from the dew point temperature from the two hygrometers differ by less than 2 %, with the General Eastern hygrometer biased to a higher humidity than the Buck CR2 hygrometer. The flight average relative humidity was 58 % with variability between 52 and 70 %.

As there is no availability of *in-situ* wet nephelometer data, published humidograph measurements of $\sigma_s(RH)/\sigma$ from Kotchenruther and Hobbs (1998) from the SCAR-B campaign taken at Porto Vehlo, Rondônia, are used as an alternative. These are

presented in table 53. The humidograph measurements of $\sigma_s(RH)/\sigma$ equate to a relative increase in scattering with increasing relative humidity. For humidograph measurements made in Porto Vehlo, Rondônia, the ratio of the light-scattering coefficient at a RH of 60 – 80 % to that at an RH of 30 % ranged from 1.02 – 1.10. These values reflect small growth factors as a function of relative humidity. The extension of the Kotchenruther and Hobbs (1998) humidograph measurements to Amazonian aerosol is not valid; the results of SCAR-B showed significant regional differences in $\sigma_s(RH)/\sigma$ driven by the different vegetation types and corresponding aerosol composition. The effects of relative humidity on optical properties are shown in section 6.9.

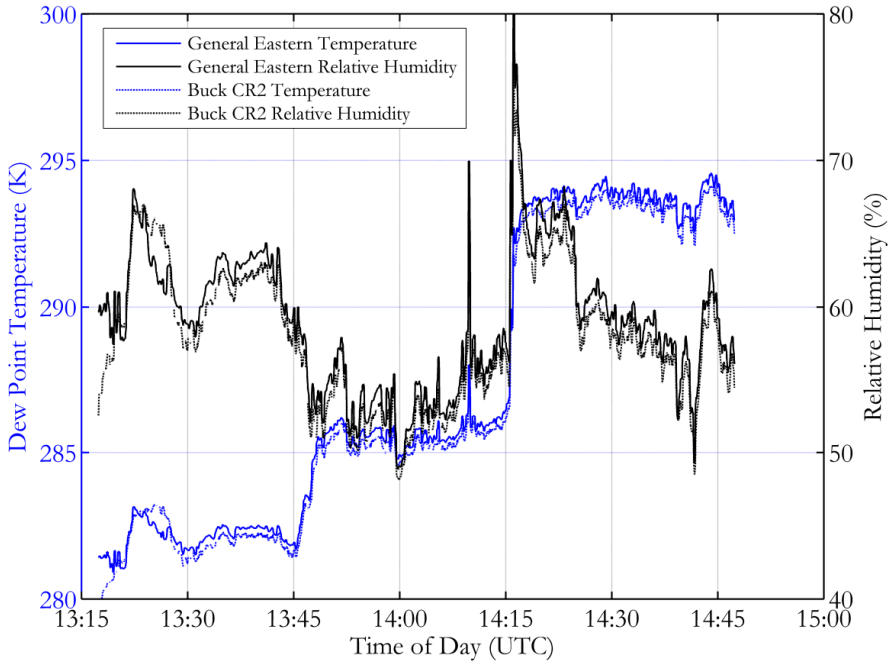

Figure 6.23 Time series from B734 (18 September 2012) of (*blue*) dew point temperature and (*black*) relative humidity (*solid line*) from the General Eastern and (*dashed line*) the Buck CR2 chilled mirror hygrometers.

Table 53 Humidograph measurements (at 550 nm) from Porto Vehlo, Rondônia. Reproduced from Kotchenruther and Hobbs (1998).

Relative Humidity (%)	$\sigma_s(RH)/\sigma$
60	1.020
70	1.056
80	1.100

6.9 Optical Properties

Light scattering by aerosols is measurable as well as calculable from the observed *in-situ* aerosol size and composition measurements. This permits comparisons, called closure studies, of the different measurements for consistency. The use of Mie calculations for the treatment of aerosol optical properties necessarily assumes biomass burning aerosol to be spherical; Martins et al. (1998b) discussed that a spherical approximation is a valid assumption for particles older than one hour. Additionally the effects of nonsphericity are not considered in this study, due partly to the difficulty in correcting properties without knowing any of the fractal dimensions of aerosol freshly emitted from biomass burning.

A widely used Mie code is MIEV0 Fortran code (Wiscombe, 1980) which treats the aerosol as a homogeneous distribution. This implies that the particle is characterised by a single refractive index at a given wavelength. If a particle has a complex composition reflecting multiple refractive indicies, an effective refractive index must be determined. Computed outputs include the scattering and extinction efficiencies (Q_{scat}, Q_{ext}) and the asymmetry parameter. The use of a homogenous approximation is appropriate in the closure studies considered here due to the low fraction of submicron black carbon in both cases (Highwood et al. 2012). *In-situ* optical properties are presented in table 54.

A smaller Angstrom exponent of 1.56 was found for Amazonian aerosol compared with 1.87 for Rondônian regional haze. This is consistent with a bias to larger sizes for Amazonian aerosol observed from *in-situ* size distributions presented at the beginning of this chapter. The low extinction coefficient for Amazonia reflects the low mass loadings of the region, and the corresponding single-scattering albedo of 0.92 is moderately scattering. The average single-scattering albedo of Rondônian regional haze was 0.89 and the difference between the two aerosol species reflects the reduced black carbon in the Amazonian aerosol composition, and the increased inorganic loadings of sulphate and nitrate. The single-scattering albedo is still relatively absorbing which may reflect an absorbing contribution from the organic carbon.

A large uncertainty within in the absorption measurements from the PSAP was realised by Lack et al. (2008); in high organic aerosol loadings (such as those encountered within this chapter) the organic material deposited on the PSAP filters forming an organic film around particulate deposits on filters. This was shown to lead to enhancement of the

measured absorption coefficients and lead to an underestimation in the single-scattering albedo (Lack et al., 2009). Absorption enhancements are beyond the standard PSAP corrections accounted for in Bond et al. (1999) as laid out in the chapter 3 and Appendix A. Lack et al. (2008) suggested the effects of absorption enhancement could lead to a PSAP uncertainty in the range of 20 – 30 %.

Table 54 *In-situ* dry optical properties (at 550 nm) for Rondônian regional haze and Amazonian aerosol in terms of single-scattering albedo, extinction coefficient and Angstrom exponent.

	b_{ext} (Mm^{-1})	ω_0	Å
Rondônian regional haze	111.4 $\pm$ 12.0	0.89 $\pm$ 0.01	1.87 $\pm$ 0.09
Amazonian aerosol	47.2 $\pm$ 16.0	0.92 $\pm$ 0.02	1.56 $\pm$ 0.15

The flight-mean number size distributions from i) PCASP and ii) SMPS and Grimm together with the refractive index (derived from AMS and SP2 measurements) are used in theoretical Mie calculations to determine the optical properties of the accumulation mode aerosol presented in table 55 for Rondônian regional haze. Two refractive index representations are contrasted here; i) the SAMBBA linear-mixing representation where m = 1.49 – 0.0083*i* with a corresponding density of 1.47 g cm^{-3} and ii) SCAR-B campaign literature values of m = 1.50 – 0.02*i* and density is 1.35 g cm^{-3} (Reid et al. 1998). The SMPS size distributions are presented in terms of a mobility diameter and are not subject to sizing changes due to the refractive index. Refractive index corrections apply only to the PCASP and Grimm size distributions.

Changes to the optical properties of regional haze due to the effects of humidity are presented in table 55 using the humidograph measurements at 60 % and 70 % from Kotchenruther and Hobbs (1998). The flight-mean size distributions were grown iteratively until *in-situ* $\sigma_s(RH)/\sigma$ agreed with the ratios of Kotchenruther and Hobbs (1998). It is assumed that absorption properties of the aerosol do not change with relative humidity changes. It should be noted that the refractive index calculations presented here do not take into account the increased water content of the aerosols as relative humidity changes. The inclusion of water (m = 1.33 – 0*i*) in the linear mixing representation would tend to lower the calculated values of the refractive index; if the

mass extinction efficiency is calculated including the mass of water the magnitude of the parameter would decrease.

The chosen refractive index strongly influences the optical properties calculated from the *in-situ* size distribution. Changes to the refractive index applied to the PCASP size distribution reduced the single-scattering albedo from 0.95 (SAMBBA) to 0.88 (SCAR-B). The single-scattering albedo from *in-situ* measurements was found to be 0.89 $\pm$ 0.01 which shows more coherence to theoretical calculations using the SCAR-B refractive index with an imaginary part (0.02*i*) of the refractive index, compared with the SAMBBA linear-mixing representation, with a lower absorbing component of the refractive index.

The optical properties calculated from the combined SMPS and Grimm size distribution are strongly influenced by the assumed refractive index showing the same reduction in the single-scattering albedo from 0.94 to 0.87. The change in refractive index is applied only to the Grimm size distribution and this reflects the small contribution that the SMPS size distribution has to the optical properties of the aerosol. It further enforces the susceptibility and variability of the optical properties to the chosen size and refractive index.

Calculated mass extinction efficiencies of 3.2 m^2 g^{-1} from SMPS measurements were smaller than those from the PCASP of 4.10 m^2 g^{-1}. This reflects the accumulation mode measured by the SMPS being at lower mean diameter (0.12 μm) compared to the PCASP (0.165 μm); giving a smaller scattering cross-section inferred from SMPS measurements. The smaller asymmetry parameter additionally reflects this. The consistency in the mass extinction efficiency for the PCASP measurements with the two refractive indicies representations is explained by the lower aerosol density (1.35 g cm^{-3}) from the SCAR-B campaign compared with SAMBBA (1.47 g cm^{-3}). Reid et al. (2005a) found mass scattering efficiencies in the range of 3.4 – 4.1 m^2 g^{-1} and mass absorption efficiencies varied between 0.6 – 1.0 m^2 g^{-1}; the mass extinction efficiencies from theoretical calculations using PCASP size distributions are in line with the literature.

The asymmetry parameter calculated from the PCASP size distribution of 0.636 for Rondonia regional haze is consistent with the recommendation by Reid et al. (2005a) for aged smoke of 0.63 $\pm$ 0.06 for use in radiative transfer calculations. Martins et al. (1998b) found a lower asymmetry parameter of 0.61, which is more in-line with the

asymmetry parameter calculated using the PCASP and the SCAR-B refractive index. The asymmetry parameters calculated with SMPS and Grimm size distributions of 0.54 are lower than that presented in the literature, suggesting the combination of the instruments does not successfully capture the optical properties of Rondônian regional haze.

The mass extinction efficiency for Amazonian aerosol from Mie calculations using the SMPS and Grimm size distribution (table 56) was 2.89 m^2 g^{-1}; significantly lower than that for the corresponding *in-situ* measurement of 4.74 m^2 g^{-1}. The theoretical scattering coefficients were 29 Mm^{-1}, compared to *in-situ* measurements of 47 Mm^{-1}, which accounts for a 60 % difference between theoretical calculations and *in-situ* measurements. Theoretical calculations of absorption coefficients were as low as 0.90 Mm^{-1} underestimating absorption by a factor of 5 relative to *in-situ* measurements. This is reflected in the disagreement between *in-situ* single-scattering albedo measurements of 0.92 compared with 0.96 from Mie calculations.

The humidification factor from Kotchenruther and Hobbs (1998) is small, and has a negligible effect on the optical properties of the aerosol in terms of the single-scattering albedo and mass extinction efficiency. The angular distribution of scattered light changes as the relative humidity changes; as aerosols take on water with increasing relative humidity, the fraction of light they backscatter is reduced. Changes to the hemispheric scattering result in changes to the direct radiative forcing. The change in the angular distribution of light is very small as shown in changes to the asymmetry parameter, with 0.5 – 0.7 % increase in the asymmetry parameter, i.e. a small increase in radiation scattered in the forward hemisphere.

Aerosol hygroscopicity is compositionally driven with sulphates and nitrates shown to strongly absorb water (Tang, 1996), whilst organic carbon has been shown to vary considerably in its hygroscopic properties (Fors et al., 2010; Kanakidou et al., 2005; Rissler et al., 2006; Wex et al., 2009). In agreement with the measurements of Kotchenruther and Hobbs (1998) and the results found here; Rissler et al. (2006) found that organic carbon originating from biomass burning dominate in the accumulation mode and have low hygroscopic growth factors. Measurements from Reid et al. (1998a) and Ferek et al. (1998) showed that the Rondônian regional haze cases during SCAR-B were dominated by organics (70 – 80 %), emitted from smouldering combustion of

primary forest. This gives confidence in the validity of applying the Kotchenruther and Hobbs (1998) humidification factor to our measurements of regional haze. Black carbon makes up only a small fraction of the aerosol composition in both flights considered here, as such having little influence on the bulk hygroscopic properties.

Table 55 Optical properties (at 550 nm) from theoretical Mie calculations for Rondônian regional haze for dry aerosol, 60 % and 70 % relative humidity.

	RH (%)	ω_0	g	K_{ext} $(m^2 g^{-1})$
PCASP	Dry	0.95	0.636	4.11
m = 1.49 – 0.0083*i*	60	0.95	0.637	4.10
ρ = 1.47 g cm^{-3}	70	0.95	0.639	4.16
PCASP, SCAR-B	Dry	0.88	0.588	4.16
m = 1.50 – 0.02i,	60	0.88	0.590	4.13
ρ = 1.35 g cm^{-3}	70	0.89	0.593	4.17
SMPS / Grimm	Dry	0.94	0.559	3.08
m = 1.49 – 0.0083*i*	60	0.94	0.560	3.09
ρ = 1.47 g cm^{-3}	70	0.94	0.563	3.13
SMPS/Grimm, SCAR-B	Dry	0.87	0.541	3.42
m = 1.50 – 0.02*i*	60	0.87	0.542	3.44
ρ = 1.35 g cm^{-3}	70	0.87	0.545	3.47

Table 56 Dry optical properties (at 550 nm) from theoretical Mie calculations for Amazonian aerosol.

	RH (%)	ω_0	g	K_{ext} $(m^2 g^{-1})$
SMPS and Grimm	Dry	0.96	0.551	2.89
m = 1.48 – 0.0043*i*				
ρ = 1.49 g cm^{-3}				

6.10 Chapter Conclusion

In this chapter measurements of Rondônian regional haze and Amazonia aerosol have been described in terms of their physical and optical properties from a suite of *in-situ* measurements during the SAMBBA 2012 aircraft field campaign. The chapter brings together meteorological profiles of the atmosphere and aerosol extinction profiles for these two regions of Brazil. *In-situ* measurements were found to be in good agreement with those retrieved from remote sensing both in terms of magnitude, aerosol boundary layer depth and boundary layer structure.

Measurements of aerosol size distributions from Rondônian regional haze lognormal and Amazonian aerosol were measured by five sizing instruments across the range of 0.002 to 100 μm particles. Lognormal fits to the PCASP size distribution found a dominant accumulation mode with a mean diameter of 0.165 μm and a standard deviation of 1.5. Only a very small coarse mode contribution is evident. The distribution from SMPS and Grimm measurements isolated a small biomass burning plume and lognormal fits to the distribution highlight that the Aitken and accumulation mode are minimally separated within the overall size distribution. The Aitken mode has a mean diameter of 0.047 μm with a small standard deviation of 1.16; the accumulation mode had a mean diameter of 0.12 μm and standard deviation of 1.73, representing a broader accumulation mode at a smaller diameter than measured by the PCASP. The mean distribution of the Amazonian aerosol (0.17 μm) is larger than the mean distribution of Rondônian regional haze (0.12 – 0.16 μm).

Thermo-optical analysis of biomass burning aerosol was performed using the VACC instrument. Comparisons of total number concentration between the VACC and externally mounted probes were found to compare well; therefore aerosol entering the volatility system can be considered as representative of the external aerosol population being sampled. The use of thermo-optical technique to resolve black carbon content of biomass burning is not well characterised in the literature. Characterisation of airborne thermo-optical techniques for measuring black carbon content is achieved through comparisons with SP2 measurements. Total number concentration was reduced by 77 % compared with 96 % for the SP2, suggesting not all volatile material was removed with the thermo-optical technique. The 4 % of black carbon derived from size distributions compares well with the percentage mass of black carbon from AMS and

SP2 measurements. The design and operation of thermal denuders vary vastly (in terms of flow rate, residence time and volatility temperature), but this study provides an airborne characterisation in the use of thermo-optical techniques for measuring black carbon content using an SP2 instrument as a reference instrument.

The mean diameter of the BC core of 0.11 μm was found to be in reasonable agreement between the SP2 and the VACC. The SP2 median shell-to-core diameter ratio ranged from 2.3 – 2.5 and shows little coherence with the median shell-to-core diameter ratios derived from the VACC of 1.45. As no direct measurement of the VACC shell distribution is made, an assumption in the core-to-shell diameter ratio was achieved by scaling the VACC volatile distribution to the mean ambient distribution. The difference between the SP2 and VACC median shell-to-core diameter ratios identifies this is not a valid assumption and does not provide a realistic representation of the coating distribution.

The bulk composition of Rondônian regional haze from AMS and SP2 measurements was found to be 5 % black carbon, 80 % organic carbon and 15 % inorganic which was primarily ammonium sulphate. Amazonian aerosol was found to have a lower contribution of black carbon of 2.5 %, with 75 % organic carbon and 22.5 % inorganic dominated by ammonium bisulphate. Concentrations of black carbon across Amazonia were as low as 0.02 $\mu g\ cm^{-3}$, up to a maximum of 0.06 $\mu g\ m^{-3}$.

The complex aerosol refractive index of biomass burning aerosol was derived using the linear-mixing and the Maxwell-Garnett mixing rules. The imaginary part of the refractive index was found to be 40 % lower using the Maxwell-Garnett mixing rule compared with the volume mixing rule. The variability in the refractive index due to the mixing approach is small compared to the variability due to the assumed refractive index of the sub-components using in the mixing, primarily due to the large range of literature values for organic carbon.

The single-scattering albedo from *in-situ* measurements was found to be 0.89 $\pm$ 0.01 which shows more coherence to theoretical calculations using the SCAR-B refractive index with an imaginary part (0.02) of the refractive index, compared with the linear-mixing representation derived from SAMBBA compositional measurements. The optical properties of the combined SMPS and Grimm size distribution were strongly influenced by the assumed refractive index applied to the Grimm size distribution

measurements. This reflects the small contribution that the SMPS size distribution has to the optical properties of the aerosol, and enforces the susceptibility and variability of the optical properties to the chosen size and refractive index. The assumed refractive index and density are a significant uncertainty in this study and had a strong impact on the retrieval of the aerosol optical properties; the single-scattering albedo ranged from 0.88 to 0.95 depending on the chosen refractive index.

One of the principle findings in this thesis is the similarity in the optical properties of Rondônian regional haze from the SAMBBA campaign to literature from SCAR-B for the Rondônian region in 1995. This suggests to a consistency both in the vegetation type (primary forest and pasture) and the burning phase (smouldering in preference to flaming combustion) in the two decades between campaigns. The consistencies in optical properties suggest that the Rondônian vegetation cover has not been replaced with cropland where a change in the phase of combustion would be reflected in a change in aerosol optical properties. This suggests that agricultural practices have remained the same over the last two decades; as cleared land becomes less fertile over time, farmers move to new land and continue the process of slash and burn of the Rondônian primary forest. This is reflected in the extent of deforestation throughout Rondônia between 1978 and 2013, as discussed in the literature review.

This chapter has provided an extensive review of the physical, optical and volatility properties for Rondônian and Amazonia. The SAMBBA analysis provided detailed case studies of Rondônian regional haze and Amazonia aerosol, although it is necessary to understand how the optical properties of biomass burning aerosol vary on much larger timescales and spatial areas. The physical and optical properties from biomass burning aerosol are known to be influenced by the underlying vegetation; understanding how agricultural and farming practices have changed vegetation cover in different regions across Brazil, and understand how it may change in the future must be considered.

7 Conclusions

7.1 Key Findings

The microphysical and optical properties of aerosols need to be well quantified to understand the radiative impact, important in climate models and increasingly important in numerical weather predication. The understanding of optical properties is key for validating and improving retrieval algorithms from satellite measurements. The aerosol direct radiative forcings requires the knowledge of a set of aerosol parameters (as a function of wavelength); the aerosol mass extinction efficiency, the single-scattering albedo and the asymmetry parameter in order to fully define the optical properties of an aerosol.

The key theme within this thesis is to improve the understanding of the microphysical and optical properties of two globally-important aerosol species, Saharan mineral dust and Amazonian biomass burning aerosol. This thesis focuses on the technical aspects of aerosol sampling though aircraft inlets and multi-instrumental assessment during two field campaigns using the BAe-146 aircraft; the Fennec campaign in June 2011/12 and the SAMBBA campaign in September 2012. Five key questions were laid out at the start of this thesis in order to assess the strengths and limitations of the current inlets and instrumentation used on the FAAM BAe-146 research aircraft in measuring the microphysical and optical properties of Saharan mineral dust and Amazonian biomass burning aerosol. The results of these research questions are summarised below and recommendations for further work are presented in section 7.2.

1. How well is the coarse mode of mineral dust presently measured from an aircraft platform on the FAAM BAe-146 and what influence do the current Rosemount inlets have on the sampling of coarse mode aerosol?

A critical evaluation of the current aerosol sampling has been a limitation aboard the FAAM BAe-146 aircraft. In reality no inlet will successfully sample aerosol without modification, but with well-characterised experiments to quantify the inlet efficiencies, it is possible to account for any changes to the aerosol size distribution before measurements are made. Recent advances in characterising aerosol sampling, presented in chapter 4, have coincided with the installation of the LTI, which has provided a platform for performing inlet comparison experiments with the current aircraft Rosemount inlets to investigate.

The performance of the LTI during the Fennec 2011 campaign was investigated within this thesis. It was found that the LTI is optimally isokinetic up to 800 hPa, with a transition region identified between 700 hPa and 600 hPa, where isokinetic values are greater than 0.75, a lower limit to the inlet performance, but less than the optimum value of 1.0. It has been shown by Wilson et al. (2004) that with the use of a more powerful pumping system controlling the sampling flow, the LTI is fully operational up to 370 hPa. This calls for improvements to the operational set-up of the LTI in this study, which will allow for an extension to the present operational capacity of the inlet.

The work presented within this thesis is the first investigative study of inlet characterisation of the primary aerosol inlets (modified Rosemount 102E housings) on the BAe-146 aircraft. It has previously been acknowledged of the inherent difficulties in gaining a representative aerosol sample through these inlets. For particles below 1.0 μm the Rosemount inlet enhancement, that is the concentration at the Rosemount inlet relative to the LTI, is 1.5 - 2 times of that measured at the LTI. For 3.0 μm particles the Rosemount inlet enhancement peaks at approximately 8 times that of the LTI. For particles in the range of 3.0 μm to 7.0 μm the enhancement decreases approaching the unity line where the LTI and Rosemount measure equal concentration. Beyond 7.0 μm, particle concentration is underestimated.

The Rosemount inlet is characterised as sub-isokinetic in nature with particle concentration enhancement greatest in the size range of 1.7 – 5.0 μm. This goes against previous discussions where it was suggested the Rosemount inlet operates within the

super-isokinetic sampling regime. Haywood et al. (2003b) had suggested that the Rosemount inlet collection efficiency drops from close to unity to zero for particle radii greater than 1-2 μm. This has now been shown to be an incorrect representation of how the Rosemount samples aerosol particles.

This study found little evidence of the increasing particle enhancement of the Rosemount inlet as the pressure height of the aircraft varied, that was observed in a study by Petzold (2009). The similarity in our Rosemount enhancement factor in low-level aircraft runs compared with Petzold (2009) gives confidence that the enhancement factor could be applied to the other Rosemount inlets on the BAe-146. However, a complete Rosemount characterisation is a priority to remove uncertainty in this assumption. Although an inlet characterisation is a necessary step forward in aerosol measurements on the BAe-146 aircraft, it should be acknowledged of the unsuitability of the Rosemount inlets as the long-term primary aerosol inlet. This thesis has provided a motivation for discussions within the research community to investigate the replacement of the Rosemount inlets.

2. What are the impacts of the current measurement limitations on aerosol microphysical and optical properties?

The installation and use of the LTI represents a significant advance in the ability to representatively sample populations of coarse mode aerosol from the BAe-146 research aircraft. It is emphasised of the importance of measuring aerosol coarse mode and the difficulty in accurately sampling these particles. The importance of the coarse mode of mineral dust in aerosol physical and optical properties was analysed on the back of the LTI findings.

Mineral dust size distributions measured at the LTI were compared to size distributions measured by the externally-mounted probes, the PCASP and CDP. Transmission losses of particles through the LTI have been shown to play a role for particle diameters greater than 5 μm. Beyond 10 μm transmission losses in the LTI are seen to dominate and there is little agreement in size distribution measurements between the LTI and the CDP. Surface area and volume size distributions presented accentuate these transmission losses.

A strong contribution of the coarse mode of mineral dust to the asymmetry parameter as measured by the wing-mounted probes was emphasised. The inclusion of the second bin of the CDP increased the asymmetry parameter from 0.70 to 0.76. The largest sensitivity to the asymmetry parameter is the representation of coarse mode mineral dust diameters up to 20 μm. For both dust loadings, it can be seen that the asymmetry parameter is largely unchanged beyond 50 μm, which indicates to the low abundance of these ultra large particles. The result highlights the large contribution of the coarse mode to the asymmetry parameter and is thus highly important parameter to constrain in assessing the radiative properties of mineral dust.

The campaign-average mineral dust optical properties, in terms of the extinction coefficients, Ångström exponent and single-scattering albedo during the Fennec pilot, Fennec 2011 and Fennec 2012 were presented. The Fennec 2011 and Fennec 2012 campaign-average for Ångström exponents of -0.21 was shown to be significantly smaller than campaign-averages from previous observational field campaigns.

The Ångström exponent for the Fennec 2011 campaign ranged from -0.36 to -0.05 which indicated a large contribution of the mineral dust coarse mode to the size distribution during all flights of the campaign. The Ångström exponent for the Fennec 2012 campaign saw a larger range from -0.45 to 0.47, which can be attributed to the different meteorological events encountered during the campaign. The average Ångström exponent from the pilot campaign from April 2011 was 0.06, ranging from -0.18 to 0.67. This result is consistent with measurements from DABEX (Osborne et al., 2008) and GERBILS (Johnson and Osborne, 2011), which ranged from -0.18 to 0.66.

The *in-situ* single-scattering albedo from PSAP and nephelometer instruments during the Fennec campaign was largely consistent across the pilot and the two main campaigns, ranging from 0.93 to 0.97. The single-scattering albedo is comparable to that found during the SAMUM (Kandler et al., 2011; Müller et al., 2011) and GERBILS campaigns (Johnson and Osborne, 2011). The importance in the contribution of the coarse mode to the single-scattering albedo has been shown. Below 10 μm, the single-scattering albedo of mineral dust is captured to a similar extent between the LTI and the externally-mounted probes. It is evident that beyond 10 μm transmission losses in the LTI sampling line dominate, resulting in a truncation of the single-scattering albedo at 0.98. The total cumulative contribution of the externally-mounted size distribution

accounted for a single-scattering albedo of 0.97. This result supports the proposal of Johnson and Osborne (2011), who suggested that there was the potential for under-estimating absorption measurements during GERBILS and DABEX, owing to losses of the coarse mode mineral dust in the sampling inlet and into the absorption instrument.

The asymmetry parameter during Fennec 2011 ranged from 0.71 to 0.81 with a mean of 0.77. The largest values of the asymmetry parameter were observed during B600 – B602, consistent with strong dust uplift conditions and the corresponding large contribution of coarse mode particles encountered during these flights. It suggests to large forward scattering properties of the mineral dust. The results of Fennec 2011 find a higher asymmetry parameter which is broadly consistent with the results from SAMUM 2006 which found values of 0.79.

3. Increased mineral dust surface area associated with fresh dust uplift has been proposed to be correlated with reduced ozone concentrations – are these correlations observed within the Fennec measurements close to the source of fresh dust emissions?

The vertical profile of enhanced mineral dust extinction coefficients and reduced ozone concentrations were presented. Although this type of vertical profile has been commonly observed (De Reus et al., 2000; McConnell et al., 2008; Osborne et al., 2008), the anti-correlation extends to the surface layer below 920 hPa. Extinction coefficients associated with fresh localised dust reached a maximum of 190 Mm^{-1}, which coincides with a decrease from 47 ppbv above the surface layer to 38 – 39 ppbv. This was found to be equivalent to almost a 20 % decrease in ozone concentration. The Ångström exponent within the surface layer was -0.35, indicating a coarse mode mineral dust contribution.

A case study from the Fennec campaign showed *in-situ* observations of increased mineral dust surface area associated with fresh dust uplift correlated with reduced ozone concentrations. Small mean surface area of 0.15 – 0.35 μm^2 cm^{-3} corresponded with larger ozone mass mixing ratio of 49 – 52 ppbv. As the mineral dust mean surface area increased to 0.45 – 0.75 μm^2 cm^{-3}, the ozone mass mixing ratio decreased to 41 – 44 ppbv. The results presented support proposals by Bauer et al. (2004) that the coarse mode of mineral dust could be important for heterogeneous uptake on to mineral dust

and Chang et al. (2005) in which freshly emitted Saharan dust is potentially a significant route of ozone loss.

The presence of mineral dust seemingly cannot fully explain the differences in ozone concentrations observed in the two case studies. HYSPLIT back trajectories suggest that different air masses were observed with upper tropospheric air intrusions events identified with descending airflow from 3000 – 4500 m. From the analysis presented it was not possible to say if the air mass initially contained lower ozone concentrations and mineral dust has subsequently been uplifted, or that mineral dust uplift along the Harmattan flow could have contributed to the reduced ozone concentrations observed.

4. How do the different instrumental techniques used in the thermal denuder instrument compare with the SP2 in resolving black carbon size and coating thickness of biomass burning aerosol?

The use of thermo-optical technique to resolve black carbon content of biomass burning is not well characterised in the literature. A characterisation of the University of Leeds airborne thermo-optical instrument for measuring black carbon content is achieved through comparisons with SP2 measurements. Total number concentration was shown to be reduced by 77 % compared with 96 % for the SP2, suggesting not all volatile material was removed with the thermo-optical technique. The 4 % of black carbon derived from size distributions compares well with the percentage mass of black carbon from combined AMS and SP2 measurements. The design and operation of thermal denuders vary vastly (in terms of flow rate, residence time and volatility temperature), but this study provides an airborne characterisation in the use of thermo-optical techniques for measuring black carbon content using an SP2 instrument as a reference instrument.

The mean diameter of the black carbon core was found to be 0.11 μm and reasonable agreement was shown in this measurement between the SP2 and the VACC. Median shell diameter to core diameter ratio for Rondônian regional haze ranged from 2.3 – 2.5 from SP2 measurements and little coherence was shown with the ratio derived from the VACC of 1.45. As no direct measurement of the VACC shell distribution is made, an assumption in the treatment of the core-to-shell diameter ratio was achieved by scaling the VACC volatile distribution to the mean ambient distribution. The difference

between the SP2 and VACC median shell-to-core diameter ratios identifies this is not a valid assumption and does not provide a realistic representation of the coating distribution.

5. How does the advancement in aerosol instrumentation used during SAMBBA improve the understanding of regional haze in two regions Rondônia and Amazonia in terms of size distribution, refractive index and optical properties, compared with the previous SCAR-B campaign in the Rondônian region in 1995?

The physical and optical properties and vertical structure of aged Rondônian regional haze from the SAMBBA campaign in Rondônia, Brazil in September 2012 were characterised. *In-situ* measurements were found to be in good agreement with those retrieved from lidar measurements both in terms of magnitude, aerosol boundary layer depth and boundary layer structure.

Measurements of aerosol size distributions from Rondônian regional haze lognormal and Amazonian aerosol were measured by five sizing instruments across the range of 0.002 to 100 μm particles. Lognormal fits to the PCASP size distribution found a dominant accumulation mode with a mean diameter of 0.165 μm and a standard deviation of 1.5. Only a small coarse mode contribution was evident. The distribution from SMPS and Grimm measurements isolated a small biomass burning plume and lognormal fits to the distribution highlight that the Aitken and accumulation mode were minimally separated within the overall size distribution. The Aitken mode has a mean diameter of 0.047 μm with a small standard deviation of 1.16; the accumulation mode had a mean diameter of 0.12 μm and standard deviation of 1.73. This represented a broader accumulation mode than measured by the PCASP. The mean distribution of the Amazonian aerosol (0.17 μm) is larger than the mean distribution of Rondônian regional haze (0.12 – 0.16 μm).

The bulk composition of Rondônian regional haze from AMS and SP2 measurements was found to be 5 % black carbon, 80 % organic carbon and 15 % inorganic which was primarily ammonium sulphate. Amazonian aerosol was found to have a lower contribution of black carbon of 2.5 %, with 75 % organic carbon and 22.5 % inorganic dominated by ammonium bisulphate. Concentrations of black carbon across Amazonia were as low as 0.02 $\mu g\ cm^{-3}$, up to a maximum of 0.06 $\mu g\ m^{-3}$.

The complex aerosol refractive index of biomass burning aerosol was derived using the linear-mixing and the Maxwell-Garnett mixing rules. The imaginary part of the refractive index was found to be 40 % lower using the Maxwell-Garnett mixing rule compared with the volume mixing rule. The variability in the refractive index due to the mixing approach is small compared with the variability due to the assumed refractive index of the sub-components used in the mixing, primarily due to the large range of literature values for organic carbon.

The single-scattering albedo from *in-situ* measurements was found to be 0.89 $\pm$ 0.01 which shows more coherence to theoretical calculations using the SCAR-B refractive index with an imaginary part (0.02) of the refractive index, compared with the linear-mixing representation derived from SAMBBA compositional measurements. The optical properties of the combined SMPS and Grimm size distribution were strongly influenced by the assumed refractive index applied to the Grimm size distribution measurements. This reflects the small contribution that the SMPS size distribution has to the optical properties of the aerosol, and enforces the susceptibility and variability of the optical properties to the chosen size and refractive index. The assumed refractive index and density are a significant uncertainty in this study and had a strong impact on the retrieval of the aerosol optical properties; the single-scattering albedo ranged from 0.88 to 0.95 depending on the chosen refractive index.

One of the principle findings in this thesis is the similarity in the optical properties of Rondônian regional haze from the SAMBBA campaign to literature from SCAR-B for the Rondônian region in 1995. This suggests to a consistency both in the vegetation type (primary forest and pasture) and the burning phase (smouldering in preference to flaming combustion) in the two decades between campaigns. The consistencies in optical properties suggest that the Rondônian vegetation cover has not been replaced with cropland where a change in the phase of combustion would be reflected in a change in aerosol optical properties. This suggests that agricultural practices have remained the same over the last two decades; as cleared land becomes less fertile over time, farmers move to new land and continue the process of slash and burn of the Rondônian primary forest. This is reflected in the extent of deforestation throughout Rondônia between 1978 and 2013, as discussed in the literature review.

7.2 Further work and recommendations

7.2.1 Further Work: Inlet Comparisons

The installation of the LTI represents a significant advance in the ability to representatively sample populations of coarse mode aerosol from the BAe-146 research aircraft. The LTI would benefit from technical developments to extend the altitude range of the inlet to exert a consistent low turbulent performance that is required for long-term aerosol measurements. From this would stem a further intensive characterisation of the inlet.

This thesis provides motivation for discussions within the research community to investigate the replacement of the Rosemount inlets on the BAe-146 aircraft; suitable alternatives which are in consideration include the Himel and Brechtel isokinetic inlet Model 1200. The Brechtel inlet has been characterised through wind tunnel testing and validation, with a transmission efficiency > 90 % for particle aerodynamic diameters < 10 μm. The Brechtel isokinetic inlet contains a two stage diffuser; the first stage is a passive diffuser which reduces the airspeed by a half, and the second stage uses active diffusing which prevents turbulent boundary layer separation in the same manner as the LTI operates. The advantages the Brechtel inlet offers compared with the LTI is greater operating efficiency throughout the altitude range of the aircraft due to the inclusion of the passive diffuser. The Himel is a solid diffuser inlet (SDI) such as that installed on the NCAR C-130 aircraft and uses a passive diffuser to reduce the sample flow rate. The inlet is designed for the accumulation aerosol mode and as such does not sample fine or coarse mode aerosol; due to this reason the Himel is a less desirable inlet for the research aircraft. Any replacement of the Rosemount inlets on the BAe-146 would require a comprehensive characterisation, similar to that undertaken within this thesis, to understand the particle sampling characteristics.

It is a recommendation if this thesis that the future use of the LTI to be predominantly for coarse mode measurements from which this thesis has demonstrated it is well suited. Coarse mode aerosols have an associated large mass fraction and high deposition velocities and such not transported to such high altitudes, and as such the 800 hPa operational limit of the LTI described within this thesis is of less consideration for measuring coarse mode mineral dust.

A limitation of the current Rosemount characterisation is the lower sizing limit of the Grimm Sky-OPC instrument used within this study; an extension to this study could incorporate smaller particle sizes to close the uncertainty in particle enhancement at these smaller sizes, and quantify the particle size at which the Rosemount enhancement tends to unity.

A second method to access inlet sampling characteristics, and associated particle enhancement, could use a combination of measurements including aerosol dry mass deposited on aircraft filter samples and electron microscopy analysis to size particles. The LTI sample line is designed with the capability to collect and size segregate aerosol samples (cascade impactor). An important outcome of this would assess the consistency with the optical-based technique used in this study.

7.2.2 Further Work: Mineral Dust Observations

The size distributions presented in this thesis utilised the CDP in characterising the coarse mode in mineral dust measurements. The forward-scattering nature of the instrument has the potential to undersize coarse mode mineral dust due to the enhanced side-scattering associated with aspherical particles. It is important for the continued use of the CDP in making aerosol coarse mode measurements to characterise and account for instrument artefacts in the measured size distributions of aerosol and the impact of any such artefacts on the derived aerosol optical properties. Characterisation of the CDP for mineral dust measurements would be valuable for future analysis and interpretation of size distributions. Initial steps in characterising the CDP response to aspherical aerosol would involve laboratory testing; such experiments would involve lofting samples of aspherical aerosol such as mineral dust and volcanic ash, detecting the instruments scattering response compared with spherical particles of a known size and refractive index. Using dust and ash samples which has been size segregated will allow for comparisons with spherical particles of known size (PSLs), whilst knowledge of the samples refractive index will reduce uncertainities in the observed instrument response. The SID probe could be flown in conjuction with the CDP to carry out airborne characterisation tests.

The variability in the rates of ozone depletion between modelling, laboratory and field studies is largely due to uncertainty in the uptake coefficients onto mineral dust surfaces (Dentener et al., 1996). Despite a number of laboratory-based investigations, very few dedicated *in-situ* observations of mineral dust and ozone correlations have been carried out. It is likely that these inconsistencies can only be resolved through a multidisciplinary approach incorporating modelling studies, and dedicated *in-situ* measurements both close to mineral dust source regions and at observing sites that Saharan air masses can reach within several days, that is, after long range transport. This was the motivation of the Mineral Dust and Tropospheric Chemistry (MINATROC) campaign however no measurements were made close to the mineral dust source (De Reus et al. 2004).

In terms of trace gases, the Fennec campaign only made measurements of ozone concentrations, whilst Bauer et al. (2004) shows there is still significant uncertainty for other gas phase species, with the uptake coefficient of ozone being one of the better agreed measurements in the literature. This calls for observations with a complete suite of instruments to measure gas phase HNO_3, N_2O_5 and NO_3 and a greater number of observations of the spatial and vertical distribution of these processes would be of benefit.

7.2.3 Further Work: Biomass Burning Aerosol Observations

Theoretical comparisons laid out in this thesis treat biomass burning aerosol as a homogenous aerosol distribution, whilst it is well known that black carbon very quickly after emission becomes coated in inorganic and organic material due to the processes of condensation and coagulation. At this time there is no availability of black carbon coating size distributions which are necessary to represent these black carbon microstructures in theoretical calculations. Mie theory has been extended to concentrically stratified spheres for calculating the scattering and extinction efficiencies for a coated particle (Bohren and Huffman, 1983).

Understanding the representation of shell-to-core diameter of black carbon particles is important when considering the optical properties of atmospheric coated black carbon particles. Consider two coated particles with the same external diameter but different shell to core diameter ratios; the resulting absorption and scattering characteristics of the

two particles will be different. Further investigation into how these microstructures affect aerosol optical properties is an important route to be investigated.

The mass loadings of nitrate, sulphate, and ammonium can be determined using thermo-optical techniques, and would provide a compositional comparison of mass concentrations measured by the AMS; this has been successfully shown in the study by Brooks et al. (2007). The VACC dataset would provide an understanding of the size segregation of the aerosol composition which is not possible from the AMS dataset. Kanakidou et al. (2005) discussed the relatively little attention of organics represented in terms of number concentration as most measurements were made in terms of the total mass of particles. The approach above would represent the size segregation of organic carbon in terms of number concentration.

The use of thermo-optical technique to resolve black carbon content of biomass burning is not well characterised in the literature. The result presented here only holds true for the thermo-optical instrument operated at 350 ^{o}C and further investigation in necessary to extend and understand the response of the thermo-optical techniques in resolving the black carbon properties for a range of volatilisation temperatures. This would further extend the use of the VACC SAMBBA dataset.

The most reliable method for determining the black carbon distribution is with the SP2 as there is no interference from the external mode of organic carbon in retrieving the coating thickness of the aerosol. However the SP2 does not provide any information regarding the mixing state of the aerosol, and therefore the VACC has the potential to compliment the SP2 measurements. From the results presented here further investigation is necessary to extend and understand the response of the thermo-optical techniques in resolving the black carbon properties.

The operation of the VACC during SAMBBA involved a period of time at the start of each SLR where the VACC was operated at ambient temperature, that is, without heating applied. This allowed for a comparison of particle number concentrations with the wing-mounted PCASP. A continual non-heated line coupled to a PCASP would provide a continual comparison both in terms of total number concentration and size distribution to the wing-mounted PCASP. This would mean that a comparison time at the start of each run would no longer be necessary.

The thermo-optical instrument current set-up allows for temperature scanning in order to understand the volatility of the aerosol; changes in particle number and size distribution are associated with changes in temperature. A volatility scan (from cabin temperature to 350°C) has a duration of approximately 10 minutes; during this scan period it is assumed that the microphysical and chemical characteristics of the aerosol population being sampled is unchanged throughout the duration of the scan. The variable nature of biomass burning aerosol associated with plumes makes such volatility analysis difficult to interpret.

During SAMBBA the volatile operation temperature of 350 °C was selected as a balance between being a sufficiently high temperature to volatilise the chemical components of the aerosol, but low enough to be able to cool the instrument rapidly enough between the end of one SLR and the start of the next SLR to achieve a robust comparison time of number concentration between the VACC PCASP and the external wing-mounted PCASP. Future technical developments of the thermo-optical instrument, particularly important when studying aerosols with high temporal and spatial variability, would allow for multiple heated lines at constant temperature (for example, 300°C, 400°C and 500°C) coupled with multiple PCASPs, as well as a continual non-heated line (already discussed). Such a development would extend our understanding of the response of the thermo-optical technique in resolving the black carbon properties at multiple volatility temperatures, and enable changes in the aerosol size distribution at multiple temperatures to be studied.

A number of the uncertainties in terms of the optical properties of aerosol measured during SAMBBA originate in instrumental problems encountered during the campaign or from the difficulty at the time in making these *in-situ* observations;

The PCASP was operational for the first three flights of the campaign, whilst the remainder of the dataset shows significant operational difficulties. Size distribution comparisons were achievable for flight B734 but these showed a discrepancy in the measurements in the representation of the accumulation mode between the wing-mounted PCASP and the onboard SMPS, both in terms of number concentration, count mean diameter and the geometric standard deviation. This offset between similar types of instruments was observed by Reid et al. (1998) who disregarded the mobility sizing instrument in preference for the PCASP due to the increased resolution of the

PCASP data. Further investigation, incorporating laboratory testing of the instruments would be necessary to resolve the instrument discrepancy.

A large uncertainty within in the absorption measurements presented in the thesis were from the PSAP as realised by Lack et al. (2008). It was found that in high organic aerosol loadings, such as those encountered within this chapter, as the organic material deposits on the PSAP filters it forms of organic film around particulate deposits on filters. This was shown to lead to enhancement of the absorption coefficients and lead to an underestimation in the single-scattering albedo (Lack et al., 2009). Lack et al. (2009) suggests this leads to a PSAP uncertainty in the range of 20 – 30 %. For this purpose improved measurements of aerosol absorption should be the focus of future research and instrument development. This would particularly benefit the study of biomass burning aerosol where the aerosol composition is dominated by organic material.

Time-resolved absorption measurements for the PSAP are based over a 30 second time period, and therefore this is a significant limitation for measuring short temporal atmospheric features such as biomass burning plumes. Although this is less of a limitation in the two case studies presented within this chapter, it is a motivating factor for future instrumental development. One such development is a dual airborne cavity-ringdown (extinction measurement) and photoacoustic (absorption measurement) spectrometer which is in developmental stages at the Met Office.

Extinction measurements in this new instrument are made by monitoring the decay of light from an optical cavity and would provide dry extinction coefficients at 405 nm, 532 nm and 662 nm (Langridge et al., 2013). The instrument is designed to benefit from minimal truncation errors which are associated with the current nephelometer. Absorption measurements are derived using a photoacoustic technique which detects an acoustic wave generated at a resonance frequency from the particles when exposed to intensity modulated radiation (Lack and Langridge, 2013). The absorption measurements benefit from being filter-free which removes the uncertainty that has been discussed in relation to current PSAP measurements. The development of this instrument will particularly benefit future *in-situ* measurements of aerosol optical properties where high organic loadings are known to strongly influence absorption measurements.

The greatest uncertainty in terms of calculating optical properties of biomass burning in this chapter is the ambiguity with respect to organic carbon, particularly due to the vast range of organic compounds, and the corresponding uncertainty in the refractive index and density. The organic carbon optical properties have also been shown to be strongly dependent on combustion conditions. Laboratory measurements of refractive index and density, for particles of known composition and generated under controlled conditions, could close the gap in the uncertainty in these parameters from airborne *in-situ* measurements. The atmospheric chemical aging of organic carbon and the resulting changes to optical properties will also require further investigation. One such application for improved measurements of organic carbon light absorption across visible wavelengths could be the use of long-path absorption cells which provide wavelength-resolved measurements in contrast to the several fixed wavelengths by optical instruments; such measurements are shown by Hecobian et al. (2010).

7.3 Final comments

The work presented in this thesis focused on two globally-significant aerosol species from two different aircraft campaigns, mineral dust and biomass burning aerosol. The installation and use of the LTI represents a significant advance in the ability to representatively sample populations of coarse mode aerosol from the BAe-146 research aircraft. The inherent difficulties in making aircraft measurements of coarse mode aerosol were detailed and improvements in the sampling process during Fennec campaigns have been investigated. The importance of the coarse mode of mineral dust in aerosol physical and optical properties was emphasised.

This thesis has provided a review of the physical, optical and volatility properties for Rondônian and Amazonia. The SAMBBA analysis provided detailed case studies of Rondônian regional haze and Amazonia aerosol, although it is necessary to understand how the optical properties of biomass burning vary on much larger timescales and spatial areas. The physical and optical properties of biomass burning are known to be influenced by the underlying vegetation; understanding how agricultural and farming practices have changed vegetation cover in different regions across Brazil and how it may change in the future must be considered.

8 Appendix A: Standard Corrections

The instrumental response of the PSAP is a linear function of both the absorption coefficient, σ_{ap}, and the scattering coefficient, σ_{sp}.

$$\sigma_{meas} = K_1\sigma_{sp} + K_2\sigma_{ap} \quad (8.1)$$

For an ideal measurement of absorption, K_1would be equal to 0, whilst the K_2 term would be equal to 1. Bond et al. (1999) report the values of K_1 and K_2 to be 0.02 $\pm$ 0.02 and 1.22 $\pm$ 0.20, respectively. The constants K_1 and K_2 represent a parameter for the scattering and absorption response of the PSAP. The operation of filter based measurements are subject to a number of possible errors that can arise as highlighted by Bond et al. (1999).

8.1.1.1 PSAP Response to Scattering

An artefact to absorption measured can arise if transmission of light through the filter is reduced by light scattering from aerosol. The design of the PSAP is designed to reduce these effects (i) PSAP rely on optically diffusive properties of the filter medium to reduce the sensitivity to forward scattering (ii) in order to reduce interference from backscattered light the fibre filters allow aerosol particles to become partly or completely embedded in an optically diffusive environment.

The response of scattering in this manner is not accounted for in the constant, K_1. Bond et al. (1999) discuss sensitivity tests to light scattering by particles by measuring the response of the PSAP to non-absorbing salt such as ammonium sulphate or sodium chloride. Haywood and Osborne (2000) use the results of these tests and state that 2% of scattering was interpreted as absorption, and as such would give a single-scattering albedo of 0.98; this correction is applied to the PSAP data.

8.1.1.2 PSAP Response to Absorption

Bond et al. (1999) identify that absorption of particles is enhanced in the PSAP due to the scattering of light by the filter results in the same photon to pass through the layer of absorbing particles more than once, and as such enhancing the potential for absorption. The response of absorption in this manner is not accounted for in the constant, K_2. Haywood and Osborne (2000) found that 22 % of absorption was overestimated; this correction is applied to the PSAP data.

The absorption co-efficient as reported by the PSAP instrument undergoes further corrections as in the equation below;

$$\sigma_{abs\ corrected} = \sigma_{PSAP} C_{Flow} C_{Spot} \tag{8.2}$$

The corrected absorption coefficient, $\sigma_{abs\ corrected}$, is determined from the absorption coefficient from the PSAP, σ_{PSAP}, and correction to the PSAP flow rate C_{Flow} and a correction to the spot size, C_{Spot}.

8.1.1.3 PSAP Flow Rate Correction

Bond et al. (1999) find that the flow rate through the PSAP can be as much as 20 % and use the following equation to apply a flow correction, C_{flow}, based on a measured flow rate directly;

$$C_{flow} = \frac{Q_{PSAP}}{Q_{measured}} \tag{8.3}$$

The correction is based on the flow rate as stated by the manufacture, Q_{PSAP}, compared to the flow rate measured directly, $Q_{measured}$.

Haywood and Osborne (2000) use the above equation and state at the time of writing, flow rate correction of C_{flow} = 0.84$\pm$ 0.02, whilst Turnbull (2010) state a more recent calibration of the PSAP with a C_{flow} = 0.909.

8.1.1.4 PSAP Spot Size Correction

Bond et al. (1999) state that the manufacture's prescribed spot area of 17.83 mm^2 equivalent to a circular spot diameter of 4.765 mm. Bond et al. (1999) acknowledge that the true spot size deviates from this and varies from instrument to instrument, again identifying the need for instrument calibration. Bond et al. (1999) apply the following equation to account for these differences;

$$C_{Spot} = \left(\frac{A_{measured}}{A_{reference}}\right) \tag{8.4}$$

$D_{calibrated}$ is 5.1 mm the spot diameter of the reference PSAP calibrated by the manufacture and $D_{measured}$ is the measured spot diameter for an individual instrument.

Table 57 Spot Size Measurements for Fennec 2012 and SAMBBA 2012 (J. Trembath, personal communication).

Campaign	Spot Diameter	$C_{Spot}{}^{*}$
Fennec 2012	5.24 $\pm$ 0.05 mm	1.210
SAMBBA 2012	5.18 $\pm$ 0.03 mm	1.181

Ogren (2010) published a comment in Aerosol Science and Technology with the aim to clarify the work of Bond et al. (1999) with the conclusion that the spot size correction should compare the actual spot area, $A_{measured}$, for the instrument with the spot area assumed by the PSAP in its internal calculations, A_{PSAP}, rather than comparing it to the reference instrument, $A_{reference}$.

$$C_{Spot}{}^{*} = \left(\frac{A_{measured}}{A_{PSAP}}\right) \tag{8.5}$$

A modified absorption co-efficient undergoes corrections as in the equation below;

$$\sigma_{abs\ corrected}{}^{*} = \sigma_{PSAP} C_{Flow} C_{Spot}{}^{*} \tag{8.6}$$

Ogren (2010) additionally highlights that PSAP users may need to apply an additional factor of 0.873 in determining absorption coefficients. This additional factor arises in the following equation;

$$\sigma_{abs\ corrected} = \left(\frac{A_{PSAP}}{A_{Reference}}\right)\sigma_{abs\ corrected}{}^{*} \quad (8.7)$$

$$= \left(\frac{17.83}{20.43}\right)\sigma_{abs\ corrected}{}^{*}$$

$$= 0.873\sigma_{abs\ corrected}{}^{*}$$

where the factor 0.873, which is the ratio of the filter spot area used internally by the PSAP (A_{PSAP} = 17.83 mm^2) and the measured spot area of the manufacturers reference instrument ($A_{Reference}$ = 20.43 mm^2).

Turnbull (2010) state a $C_{Spot}{}^{*}$ = 1.186 using the technique from Ogren (2010), in contrast to the value of C_{Spot} = 1.035 using the equation from Bond et al. (1999). The value of 1.186 is determined using a diameter spot of 5.19 mm or equivalent to an area of $A_{measured}$ = 21.16 mm^2 from Haywood and Osborne (2000).

In summary, the aerosol absorption coefficient as recommended by Ogren (2010);

$$\sigma_{abs} = 0.873\left(\frac{Q_{PSAP}}{Q_{measured}}\right)\left(\frac{A_{measured}}{A_{PSAP}}\right)\frac{\sigma_{PSAP}}{K_2} - \frac{K_1}{K_2}\sigma_{sct} \quad (8.8)$$

As modified from the equation from Bond et al. (1999)

$$\sigma_{abs} = \left(\frac{Q_{PSAP}}{Q_{measured}}\right)\left(\frac{A_{measured}}{A_{Reference}}\right)\frac{\sigma_{PSAP}}{K_2} - \frac{K_1}{K_2}\sigma_{sct} \quad (8.9)$$

Bond et al. (1999) report the values of K_1 and K_2 to be 0.02 $\pm$ 0.02 and 1.22 $\pm$ 0.20, respectively.

8.1.1.5 Nephelometer Correction for Missing Forward Scattering

Nephelometer truncates the scattered radiation, cutting off at angles less than 7^o and greater than 170^o, and therefore there is a need to perform a correction to account for the missing scattering angles. The scattering coefficient corrected for total scattering,

$\sigma^{\lambda}_{total\ scat}$, relating the measured scattering coefficient at the three wavelengths, $\sigma^{\lambda}_{measured\ \ scat}$, by a correction factor, $C^{\lambda}_{total\ scat}$;

$$C^{\lambda}_{total\ scat} = \frac{\sigma^{\lambda}_{total\ scat}}{\sigma^{\lambda}_{measured\ \ scat}} \tag{8.10}$$

$$C^{\lambda}_{total\ scat} = b.\text{Å}(\lambda_1/\lambda_2) + a \tag{8.11}$$

Table 58 Correction factors for total scatter as function of Ångström exponent. Reproduced from Müller et al. (2011).

Wavelength (μm)	0.45		0.55		0.70	
Ångström exponent	$\text{Å}^{0.45}_{ts}$(0.45/0.55)		$\text{Å}^{0.55}_{ts}$(0.45/0.70)		$\text{Å}^{0.70}_{ts}$(0.55/0.70)	
Parameters	a	b	a	b	a	b
No cut	1.345	-0.146	1.319	-0.129	1.279	-0.105
Sub-micron cut	1.148	-0.041	1.137	-0.040	1.109	-0.033

The Ångström exponent and the relationship between the correction factor, $C^{\lambda}_{total\ scat}$, was published by Anderson and Ogren (1998). The Ångström exponent is determined from equation (8.12). The Ångström exponent describes the dependency of aerosol optical depth with wavelength

$$\text{Å}(\lambda_1/\lambda_2) = -\frac{\log\left(\sigma^{\lambda_1}_{measured\ \ scat}/\sigma^{\lambda_2}_{measured\ \ scat}\right)}{\log\left(\lambda_1/\lambda_2\right)} \tag{8.12}$$

The error associated with the correction factor, $C^{\lambda}_{total\ scat}$, is estimated using equation (8.13) from Haywood and Osborne (2000).

$$\in_{C^{\lambda}_{total\ scat}} = 0.33C^{\lambda}_{total\ scat} \tag{8.13}$$

9 Appendix B: LTI Parameters and Equations

The equations laid out in table 59 account for the complete correction methodology applied to the LTI dataset during processing.

Table 59 Parameters measured and calculated for the LTI correction methodology.

Parameter	Parameters and Equation
Ambient stagnation pressure, P_o	$P_0 = P_x + \left(\frac{1}{2}\rho v^2\right)$
Ambient Mach number, M	$M = \sqrt{5 * \left[\left(\frac{P_0}{P_x}\right)^{\frac{2}{7}} - 1\right]}$
Diffuser exit pressure, A	$A = P_1 + DP12$
Diffuser entrance Mach number, M_1	$M_1 = \sqrt{5 * \left[\left(\frac{P_0}{P_1}\right)^{\frac{2}{7}} - 1\right]}$
Stagnation temperature, T_0	$\frac{T}{T_o} = \left[1 + \frac{M^2}{5}\right]^{-1}$
Stagnation air density, ρ_o	$P_o = \rho_o R T_0$, R = 287 $m^{-2} s^{-2} K^{-1}$
Throat air density, ρ_1	$\frac{\rho_1}{\rho_o} = \left(1 + \left[\frac{{M_1}^2}{5}\right]\right)^{-\frac{5}{2}} \left(\frac{P_1}{P_0}\right)^{\frac{1}{1.4}}$

Throat speed of sound, a_1	$\frac{a_1}{a_o} = \left(1 + \left[\frac{{M_1}^2}{5}\right]\right)^{-\frac{1}{2}} \left(\frac{P_1}{P_0}\right)^{\frac{1}{7}}$ a_0 is the stagnation speed of sound
Throat temperature, T_1	$\frac{T_1}{T_o} = \left[1 + \frac{{M_1}^2}{5}\right]^{-1}$
Throat mass flow, m_1	$m_1 = \rho_1 * M_1 * a_1 * 3.14159 * d^2/4$ d = 1.118 x 10^{-2} m (throat diameter)
Diffuser exit flow, m	$m = Alicat\ Sample\ Flow + Alicate\ Bypass\ Flow$
Throat gas viscosity, μ	$\mu = \mu_0 \left(\frac{T_0 + S_u}{T + S_u}\right) \left(\frac{T}{T_0}\right)^{\frac{3}{2}}$ μ = Dynamic viscosity (Pa.s) at T μ_0 = Reference viscosity (Pa.s) at T_0 S_u = Sutherlands constant (120 K)
Stagnation gas viscosity, μ_1	$\mu_1 = \mu_{r0} \left(\frac{T_0 + S_u}{T + S_u}\right) \left(\frac{T}{T_0}\right)^{\frac{3}{2}}$ μ = Dynamic viscosity (Pa.s) at T μ_0 = Reference viscosity (Pa.s) at T_0 S_u = Sutherlands constant (120 K)
Air density at diffuser exit, ρ_a	$\rho_a = \frac{Pressure\ at\ diffuser\ exit}{287 \times T}$
Reynolds number, Re	$Re = \frac{\rho v L}{\mu} = \frac{Volume\ Flow}{(\pi \times 0.0254).\left(\frac{\mu}{\rho}\right)}$
Throat velocity, U_t	$U_t = \frac{m_1}{\rho.D} = \frac{Mass\ Flow}{\rho.Throat\ Size}$
Diffuser exit velocity, U_d	$U_d = \frac{m}{\rho.D} = \frac{Diffuser\ Exit\ Flow}{\rho.Diffuser\ Exit\ Size}$

True air speed, TAS	$$TAS = a_o M \sqrt{\frac{T}{T_0}}$$ T_0 is temperature at standard sea level (288.15 K)
Stokes number of the particle in the throat of the inlet, St_t	$$St_t = \frac{\rho_p {d_p}^2 U_t Cc}{9\mu d_{throat}}$$ ρ_p = density of the particle d_p = diameter of the particle in meters Cc = Cunningham slip correction U_t = throat velocity (m s^{-1}) μ = throat viscosity d_{throat} = throat diameter (1.118 x 10^{-2} m)
Stokes number of the particles in the bend, St_B	$$St_B = \frac{\rho_p {d_p}^2 U_D Cc}{9\mu D_{tube}}$$ ρ_p = particle density (kg m^{-3}) d_p = particle diameter (m) Cc = Cunningham slip correction U_D = diffuser exit velocity (m s^{-1}) μ = diffuser exit viscosity D_{tube} = transport tube diameter (0.0254 m)
Penetration of the particles through the bend, η	$$\eta = 1 - \varphi St_D$$ η = fraction of the particles of size d_p that penetrate the bend φ = angle of the bend in radians (φ is 1.134 for the 65 degree bend) St_D = Stokes number of the particles in the bend

10 Appendix C: International System of Units

The aim of this section is to present a coherent system of units of measurements used throughout the thesis; the International System of Units (SI) are in the most part used, however where appropriate the centimetre-gram-second system made be used.

Atmospheric pressure is expressed in terms of Newton's per meter squared (Nm^{-2}), also known as Pascal (Pa). Standard atmospheric pressure is 1.01325 x 10^5 Pa and atmospheric profiles presented throughout this thesis are in the common unit of hectopascal (hPa). Atmospheric temperature is presented in terms of Kelvin (K). Terms such as Standard Temperature and Pressure (STP) are referred to which correspond to values of 10^5 Pa and 273.15 K, respectively.

Aerosol particle size throughout this thesis refers to a particle's diameter. Aerosol particle size ranges from 10^{-9} to 10^{-4} m, with size distributions presented in terms in terms of micrometer (1 μm = 10^{-6} m). The smallest aerosol size range are presented in terms of nanometre (1 nm = 0.001 μm = 10^{-9} m). It is also important to explain the term *particle* which refers to a single unit of matter (Kulkarni et al., 2011a). Where size distributions are presented as a number concentration the units are expressed in cm^{-3}, surface area distributions are expressed as μm^2 cm^{-3}, volume distributions have units of μm^3 cm^{-3} and, mass concentration distributions use $\mu g\ cm^{-3}$.

The SI unit for the amount of a substance is expressed in terms of the mole (mol) however for the remainder of this thesis gas phase species will be presented in terms of a mixing ratio with the units parts per million ($1 ppm = \mu mol\ mol^{-1}$), parts per billion (1 ppb = nmol mol^{-1}), and parts per trillion (1 ppb = pmol mol^{-1}). Mixing ratios can be expressed in terms of mass or volume for example, ppbv.

11 References

Alberecht, B.A., 1989. Aerosols, Cloud Microphysics, and Fractional Cloudiness. Science 245, 1227-1230.

Allan, J.D., Delia, A.E., Coe, H., Bower, K.N., Alfarra, M.R., Jimenez, J.L., Middlebrook, A.M., Drewnick, F., Onasch, T.B., Canagaratna, M.R., Jayne, J.T., Worsnop, D.R., 2004. A generalised method for the extraction of chemically resolved mass spectra from Aerodyne aerosol mass spectrometer data. Journal of Aerosol Science 35, 909-922.

Allan, J.D., Jimenez, J.L., Williams, P.I., Alfarra, M.R., Bower, K.N., Jayne, J.T., Coe, H., Worsnop, D.R., 2003. Quantitative sampling using an Aerodyne aerosol mass spectrometer 1. Techniques of data interpretation and error analysis. Journal of Geophysical Research: Atmospheres 108, 4090.

Allan, J.D., Morgan, W.T., Darbyshire, E., Flynn, M.J., Williams, P.I., Oram, D.E., Artaxo, P., Brito, J., Lee, J.D., Coe, H., 2014. Airborne observations of IEPOX-derived isoprene SOA in the Amazon during SAMBBA. Atmos. Chem. Phys. Discuss. 14, 12635-12671.

Allen, G., Coe, H., Clarke, A., Bretherton, C., Wood, R., Abel, S.J., Barrett, P., Brown, P., George, R., Freitag, S., McNaughton, C., Howell, S., Shank, L., Kapustin, V., Brekhovskikh, V., Kleinman, L., Lee, Y.-N., Springston, S., Toniazzo, T., Krejci, R., Fochesatto, J., Shaw, G., Krecl, P., Brooks, B., McMeeking, G., Bower, K.N., Williams, P.I., Crosier, J., Crawford, I., Connolly, P., Allan, J.D., Covert, D., Bandy, A.R., Russell, L.M., Trembath, J., Bart, M., McQuaid, J.B., Wang, J., Chand, D., 2011. South East Pacific atmospheric composition and variability sampled along 20° S during VOCALS-REx. Atmos. Chem. Phys. 11.

Anderson, T.L., Covert, D.S., Wheeler, J.D., Harris, J.M., Perry, K.D., Trost, B.E., Jaffe, D.J., Ogren, J.A., 1999. Aerosol backscatter fraction and single scattering albedo: Measured values and uncertainties at a coastal station in the Pacific Northwest. Journal of Geophysical Research: Atmospheres 104, 26793-26807.

Anderson, T.L., Ogren, J.A., 1998. Determining Aerosol Radiative Properties Using the TSI 3563 Integrating Nephelometer. Aerosol Science and Technology 29, 57-69.

Andreae, M.O., Gelencsér, A., 2006. Black carbon or brown carbon? The nature of light-absorbing carbonaceous aerosols. Atmos. Chem. Phys. 6, 3131-3148.

Andreae, M.O., Rosenfeld, D., 2008. Aerosol-cloud-precipitation interactions. Part 1. The nature and sources of cloud-active aerosols. Earth-Science Reviews 89, 13-41.

Andreae, M.O., Rosenfeld, D., Artaxo, P., Costa, A.A., Frank, G.P., Longo, K.M., Silva-Dias, M.A.F., 2004. Smoking Rain Clouds over the Amazon. Science 303, 1337.

Ångström, A., 1929. On the Atmospheric Transmission of Sun Radiation and on Dust in the Air. Geografiska Annaler 11, 156-166.

Artaxo, P., Martins, J.V., Yamasoe, M.A., Procópio, A.S., Pauliquevis, T.M., Andreae, M.O., Guyon, P., Gatti, L.V., Leal, A.M.C., 2002. Physical and chemical properties of aerosols in the wet and dry seasons in Rondônia, Amazonia. Journal of Geophysical Research: Atmospheres 107, 8081.

Ban-Weiss, G., Cao, L., Bala, G., Caldeira, K., 2012. Dependence of climate forcing and response on the altitude of black carbon aerosols. Clim Dyn 38, 897-911.

Banks, J.R., Brindley, H.E., Flamant, C., Garay, M.J., Hsu, N.C., Kalashnikova, O.V., Klüser, L., Sayer, A.M., 2013. Intercomparison of satellite dust retrieval products over the west African Sahara during the Fennec campaign in June 2011. Remote Sensing of Environment 136, 99-116.

Baron, P.A., Willeke, K., 2001. Aerosol Measurement: Principles, Techniques, and Applications. John Wiley & Sons.

Bauer, S.E., Balkanski, Y., Schulz, M., Hauglustaine, D.A., Dentener, F., 2004. Global modeling of heterogeneous chemistry on mineral aerosol surfaces: Influence on tropospheric ozone chemistry and comparison to observations. Journal of Geophysical Research: Atmospheres 109, D02304.

Baumgardner, D., Huebert, B., 1993. The airborne aerosol inlet workshop: Meeting report. Journal of Aerosol Science 24, 835-846.

Baumgardner, D., Popovicheva, O., Allan, J., Bernardoni, V., Cao, J., Cavalli, F., Cozic, J., Diapouli, E., Eleftheriadis, K., Genberg, P.J., Gonzalez, C., Gysel, M., John, A., Kirchstetter, T.W., Kuhlbusch, T.A.J., Laborde, M., Lack, D., Müller, T., Niessner, R., Petzold, A., Piazzalunga, A., Putaud, J.P., Schwarz, J., Sheridan, P., Subramanian, R., Swietlicki, E., Valli, G., Vecchi, R., Viana, M., 2012. Soot reference materials for instrument calibration and intercomparisons: a workshop summary with recommendations. Atmos. Meas. Tech. 5, 1869-1887.

Belyaev, S.P., Levin, L.M., 1972. Investigation of aerosol aspiration by photographing particle tracks under flash illumination. Journal of Aerosol Science 3, 127-140.

Belyaev, S.P., Levin, L.M., 1974. Techniques for collection of representative aerosol samples. Journal of Aerosol Science 5, 325-338.

Ben-Ami, Y., Koren, I., Altaratz, O., Kostinski, A., Lehahn, Y., 2011. Discernible rhythm in the spatio/temporal distributions of transatlantic dust. Atmos. Chem. Phys. 12, 2253 - 2262.

Bergstrom, R.W., Pilewskie, P., Russell, P.B., Redemann, J., Bond, T.C., Quinn, P.K., Sierau, B., 2007. Spectral absorption properties of atmospheric aerosols. Atmos. Chem. Phys. 7, 5937.

Bergstrom, R.W., Russell, P.B., Hignett, P., 2002. Wavelength Dependence of the Absorption of Black Carbon Particles: Predictions and Results from the TARFOX Experiment and Implications for the Aerosol Single Scattering Albedo. Journal of the Atmospheric Sciences 59, 567-577.

Bevan, S.L., North, P.R.J.G., William M. F. Los, Sietse O. Plummer, Stephen E., 2009. Impact of atmospheric aerosol from biomass burning on Amazon dry-season drought. J. Geophys. Res. 114, D09204.

Bian, H., Zender, C.S., 2003. Mineral dust and global tropospheric chemistry: Relative roles of photolysis and heterogeneous uptake. Journal of Geophysical Research: Atmospheres 108, 4672.

Bohren, Huffman, 1983. Absorption and Scattering of Light by Small Particles.

Bonasoni, P., Cristofanelli, P., Calzolari, F., Bonafè, U., Evangelisti, F., Stohl, A., Zauli Sajani, van Dingenen, S., Colombo, T., Balkanski, Y., 2004. Aerosol-ozone correlations during dust transport episodes. Atmos. Chem. Phys. 4, 1201-1215.

Bond, T.C., 2001. Spectral dependence of visible light absorption by carbonaceous particles emitted from coal combustion. Geophysical Research Letters 28, 4075-4078.

Bond, T.C., Anderson, T.L., Campbell, D., 1999. Calibration and Intercomparison of Filter-Based Measurements of Visible Light Absorption by Aerosols. Aerosol Science and Technology 30, 582-600.

Bond, T.C., Bergstrom, R.W., 2006. Light Absorption by Carbonaceous Particles: An Investigative Review. Aerosol Science and Technology 40, 27-67.

Bond, T.C., Doherty, S.J., Fahey, D.W., Forster, P.M., Berntsen, T., DeAngelo, B.J., Flanner, M.G., Ghan, S., Kärcher, B., Koch, D., Kinne, S., Kondo, Y., Quinn, P.K., Sarofim, M.C., Schultz, M.G., Schulz, M., Venkataraman, C., Zhang, H., Zhang, S., Bellouin, N., Guttikunda, S.K., Hopke, P.K., Jacobson, M.Z., Kaiser, J.W., Klimont, Z., Lohmann, U., Schwarz, J.P., Shindell, D., Storelvmo, T., Warren, S.G., Zender, C.S., 2013. Bounding the role of black carbon in the climate system: A scientific assessment. Journal of Geophysical Research: Atmospheres 118, 5380-5552.

Bond, T.C., Sun, H., 2005. Can Reducing Black Carbon Emissions Counteract Global Warming? Environmental Science & Technology 39, 5921-5926.

Bond, T.C., Zarzycki, C., Flanner, M.G., Koch, D.M., 2011. Quantifying immediate radiative forcing by black carbon and organic matter with the Specific Forcing Pulse. Atmos. Chem. Phys. 11, 1505 - 1525.

Brindley, H., Knippertz, P., Ryder, C., Ashpole, I., 2012. A critical evaluation of the ability of the Spinning Enhanced Visible and Infrared Imager (SEVIRI) thermal infrared red-green-blue rendering to identify dust events: Theoretical analysis. Journal of Geophysical Research: Atmospheres 117, D07201.

Brito, J., Rizzo, L.V., Morgan, W.T., Coe, H., Johnson, B., Haywood, J., Longo, K., Freitas, S., Andreae, M.O., Artaxo, P., 2014. Ground based aerosol characterization during the South American Biomass Burning Analysis (SAMBBA) field experiment. Atmos. Chem. Phys. Discuss. 14, 12279-12322.

Brooks, B.J., McQuaid, J.B., Smith, M.H., Crosier, J., Williams, P.I., Coe, H., Osborne, S., 2007. Intercomparison of VACC- and AMS-derived nitrate, sulphate and ammonium aerosol loadings during ADRIEX. Quarterly Journal of the Royal Meteorological Society 133, 77-84.

Brooks, B.J., Smith, M.H., Hill, M.K., O'Dowd, C.D., 2002. Size-differentiated volatility analysis of internally mixed laboratory-generated aerosol. Journal of Aerosol Science 33, 555-579.

Canagaratna, M.R., Jayne, J.T., Jimenez, J.L., Allan, J.D., Alfarra, M.R., Zhang, Q., Onasch, T.B., Drewnick, F., Coe, H., Middlebrook, A., Delia, A., Williams, L.R., Trimborn, A.M., Northway, M.J., DeCarlo, P.F., Kolb, C.E., Davidovits, P., Worsnop, D.R., 2007. Chemical and microphysical characterization of ambient aerosols with the aerodyne aerosol mass spectrometer. Mass Spectrometry Reviews 26, 185-222.

Capes, G., Johnson, B., McFiggans, G., Williams, P.I., Haywood, J., Coe, H., 2008. Aging of biomass burning aerosols over West Africa: Aircraft measurements of chemical composition, microphysical properties, and emission ratios. J. Geophys. Res. 113.

Carpenter, L.J., Fleming, Z.L., Read, K.A., Lee, J.D., Moller, S.J., Hopkins, J.R., Purvis, R.M., Lewis, A.C., Müller, K., Heinold, B., Herrmann, H., Fomba, K.W., Pinxteren, D., Müller, C., Tegen, I., Wiedensohler, A., Müller, T., Niedermeier, N., Achterberg, E.P., Patey, M.D., Kozlova, E.A., Heimann, M., Heard, D.E., Plane, J.M.C., Mahajan, A., Oetjen, H., Ingham, T., Stone, D., Whalley, L.K., Evans, M.J., Pilling, M.J., Leigh, R.J., Monks, P.S., Karunaharan, A., Vaughan, S., Arnold, S.R., Tschritter, J., Pöhler, D., Frieß, U., Holla, R., Mendes, L.M., Lopez, H., Faria, B., Manning, A.J., Wallace, D.W.R., 2010. Seasonal characteristics of tropical marine boundary layer air measured at the Cape Verde Atmospheric Observatory. J Atmos Chem 67, 87-140.

Chand, D., Guyon, P., Artaxo, P., Schmid, O., Frank, G.P., Rizzo, L.V., Mayol-Bracero, O.L., Gatti, L.V., Andreae, M.O., 2006. Optical and physical properties of aerosols in the boundary layer and free troposphere over the Amazon Basin during the biomass burning season. Atmos. Chem. Phys. 6, 2911-2925.

Chang, R.Y.W., Sullivan, R.C., Abbatt, J.P.D., 2005. Initial uptake of ozone on Saharan dust at atmospheric relative humidities. Geophysical Research Letters 32, L14815.

Cochrane, M.A., Ane Alencar, Mark D. Schulze, M., C., Souza, J., Nepstad, D., Paul Lefebvre, Davidson, E.A., 1999. Positive Feedbacks in the Fire Dynamic of Closed Canopy Tropical Forests. Science 284.

Costa, M.J., Levizzani, V., Silva, A.M., 2004. Aerosol Characterization and Direct Radiative Forcing Assessment over the Ocean. Part II: Application to Test Cases and Validation. Journal of Applied Meteorology 43, 1818-1833.

Cross, E.S., Onasch, T.B., Ahern, A., Wrobel, W., Slowik, J.G., Olfert, J., Lack, D.A., Massoli, P., Cappa, C.D., Schwarz, J.P., Spackman, J.R., Fahey, D.W., Sedlacek, A., Trimborn, A., Jayne, J.T., Freedman, A., Williams, L.R., Ng, N.L., Mazzoleni, C., Dubey, M., Brem, B., Kok, G., Subramanian, R., Freitag, S., Clarke, A., Thornhill, D., Marr, L.C., Kolb, C.E., Worsnop, D.R., Davidovits, P., 2010. Soot Particle Studies—Instrument Inter-Comparison—Project Overview. Aerosol Science and Technology 44, 592-611.

Cunningham, E., 1910. On the Velocity of Steady Fall of Spherical Particles through Fluid Medium. Proceedings of the Royal Society of London. Series A 83, 357-365.

d'Almeida, G.A., 1986. A Model for Saharan Dust Transport. Journal of Climate and Applied Meteorology 25, 903-916.

d'Almeida, G.A., P. Koepke, Shettle, E.P., 1991. Atmospheric aerosols: Global climatology and radiative characteristics. A Deepak Publishing, Hampton, Virginia.

De Reus, M., Dentener, F., Thomas, A., Borrmann, S., Strom, S., Lelieveld, J., 2000. Airborne observations of dust aerosol over the North Atlantic Ocean during ACE 2: Indications for heterogeneous ozone destruction. J. Geophys. Res. 105, 15263-15275.

De Reus, M., Fischer, H., Sander, R., Gros, V., Kormann, R., Salisbury, G., Van Dingenen, R., Williams, J., Zöllner, M., Lelieveld, J., 2005. Observations and model calculations of trace gas scavenging in a dense Saharan dust plume during MINATROC. Atmos. Chem. Phys. 5, 1787-1803.

Decesari, S., Fuzzi, S., Facchini, M.C., Mircea, M., Emblico, L., Cavalli, F., Maenhaut, W., Chi, X., Schkolnik, G., Falkovich, A., Rudich, Y., Claeys, M., Pashynska, V., Vas, G., Kourtchev, I., Vermeylen, R., Hoffer, A., Andreae, M.O., Tagliavini, E., Moretti,

F., Artaxo, P., 2006. Characterization of the organic composition of aerosols from RondÃ´nia, Brazil, during the LBA-SMOCC 2002 experiment and its representation through model compounds. Atmos. Chem. Phys. 6.

Dentener, F.J., Carmichael, G.R., Zhang, Y., Lelieveld, J., Crutzen, P.J., 1996. Role of mineral aerosol as a reactive surface in the global troposphere. Journal of Geophysical Research: Atmospheres 101, 22869-22889.

Derimian, Y., Karnieli, A., Kaufman, Y.J., Andreae, M.O., Andreae, T.W., Dubovik, O., Maenhaut, W., Koren, I., 2008a. The role of iron and black carbon in aerosol light absorption. Atmos. Chem. Phys. 8, 3623 - 3637.

Derimian, Y., Léon, J.F., Dubovik, O., Chiapello, I., Tanré, D., Sinyuk, A., Auriol, F., Podvin, T., Brogniez, G., Holben, B.N., 2008b. Radiative properties of aerosol mixture observed during the dry season 2006 over M'Bour, Senegal (African Monsoon Multidisciplinary Analysis campaign). Journal of Geophysical Research: Atmospheres 113, D00C09.

Deroubaix, A., Martiny, N., Chiapello, I., Marticorena, B., 2013. Suitability of OMI aerosol index to reflect mineral dust surface conditions: Preliminary application for studying the link with meningitis epidemics in the Sahel. Remote Sensing of Environment 133, 116-127.

Di Girolamo, P., Cacciani, M., di Sarra, A., Fiocco, G., Fuà, D., 1994. Lidar observations of the Pinatubo aerosol layer at Thule, Greenland. Geophysical Research Letters 21, 1295-1298.

Ding, Z., Yu, Z., Rutter, N.W., Liu, T., 1994. Towards an orbital time scale for chinese loess deposits. Quaternary Science Reviews 13, 39-70.

Douglas, J.F., Gasiorek, J.M., Swaffield, J.A., 1985. Fluid Mechanics. Longman Scientific & Technical 2nd Edition, 271-294.

Draine, B.T., Flatau, P.J., 1994. Discrete-dipole approximation for scattering calculations. J. Opt. Soc. Am. A 11, 1491-1499.

Draxler, R.R., 1999. HYSPLIT4 user's guide. NOAA Tech. Memo ERL ARL-230, NOAA Air Resources Laboratory, Silver Spring, MD.

Draxler, R.R., Hess, G.D. 1997. Description of the HYSPLIT_4 modeling system (Silver Springs, Maryland).

Draxler, R.R., Hess, G.D., 1998. An Overview of the HYSPLIT_4 modeling system for trajectories, dispersion and deposition. Aust. Met. Mag. 47, 295-308.

Drewnick, F., Hings, S.S., DeCarlo, P., Jayne, J.T., Gonin, M., Fuhrer, K., Weimer, S., Jimenez, J.L., Demerjian, K.L., Borrmann, S., Worsnop, D.R., 2005. A New Time-of-Flight Aerosol Mass Spectrometer (TOF-AMS)—Instrument Description and First Field Deployment. Aerosol Science and Technology 39, 637-658.

Dubovik, O., Holben, B., Eck, T.F., Smirnov, A., Kaufman, Y.J., King, M.D., Tanré, D., Slutsker, I., 2002. Variability of Absorption and Optical Properties of Key Aerosol Types Observed in Worldwide Locations. Journal of the Atmospheric Sciences 59, 590-608.

Dubovik, O., King, M.D., 2000. A flexible inversion algorithm for retrieval of aerosol optical properties from Sun and sky radiance measurements. Journal of Geophysical Research: Atmospheres 105, 20673-20696.

Durham, M.D., Lundgren, D.A., 1980. Evaluation of aerosol aspiration efficiency as a function of stokes number, velocity ratio and nozzle angle. Journal of Aerosol Science 11, 179-188.

Eck, T.F., Holben, B.N., Reid, J.S., Dubovik, O., Smirnov, A., O'Neill, N.T., Slutsker, I., Kinne, S., 1999. Wavelength dependence of the optical depth of biomass burning, urban, and desert dust aerosols. Journal of Geophysical Research: Atmospheres 104, 31333-31349.

Eck, T.F., Holben, B.N., Reid, J.S., O'Neill, N.T., Schafer, J.S., Dubovik, O., Smirnov, A., Yamasoe, M.A., Artaxo, P., 2003. High aerosol optical depth biomass burning events: A comparison of optical properties for different source regions. Geophysical Research Letters 30, 2035.

Engelstaedter, S., Tegen, I., Washington, R., 2006. North African dust emissions and transport. Earth-Science Reviews 79, 73-100.

Engelstaedter, S., Washington, R., 2007. Atmospheric controls on the annual cycle of North African dust. Journal of Geophysical Research: Atmospheres 112, D03103.

Eva, H.D., Miranda, E.E.d., Bella, C.M.D., O.Huber, V.G., M.Sgrenzaroli, S.Jones, A.Coutinho, A.Dorado, M.Guimarães, C.Elvidge, F.Achard, A.S.Belward, E.Bartholomé, A.Baraldi, Grandi, G.D., P.Vogt, S.Fritz, A.Hartley, 1999. Vegetation Map of South America, Scale 1/5M. REES Publications Series D,European Commission, Luxembourg, EUR 18658 2.

Fahey, D.W., Kelly, K.K., Ferry, G.V., Poole, L.R., Wilson, J.C., Murphy, D.M., Loewenstein, M., Chan, K.R., 1989. In situ measurements of total reactive nitrogen, total water, and aerosol in a polar stratospheric cloud in the Antarctic. Journal of Geophysical Research: Atmospheres 94, 11299-11315.

Falkovich, A.H., Graber, E.R., Schkolnik, G., Rudich, Y., Maenhaut, W., Artaxo, P., 2005. Low molecular weight organic acids in aerosol particles from Rondônia, Brazil, during the biomass-burning, transition and wet periods. Atmos. Chem. Phys. 5, 781.

Fearnside, P.M., 2005. Deforestation in brazilian amazonia history rates and consequences. Conserv. Biol. 19, 680 - 688.

Ferek, R.J., Reid, J.S., Hobbs, P.V., Blake, D.R., Liousse, C., 1998. Emission factors of hydrocarbons, halocarbons, trace gases and particles from biomass burning in Brazil. Journal of Geophysical Research: Atmospheres 103, 32107-32118.

Fernald, F.G., 1984. Analysis of atmospheric lidar observations: some comments. Applied Optics 23, 652-653.

Fiedler, S., Schepanski, K., Heinold, B., Knippertz, P., Tegen, I., 2013. Climatology of nocturnal low-level jets over North Africa and implications for modeling mineral dust emission. Journal of Geophysical Research: Atmospheres 118, 1-22.

Flannigan, M.D., Krawchuk, M.A., de Groot, W.J., Wotton, B.M., Gowman, L.M., 2009. Implications of changing climate for global wildland fire. International Journal of Wildland Fire 18, 483-507.

Foltescu, V.L., Selin, E., Below, M., 1995. Corrections for particle losses and sizing errors during aircraft aerosol sampling using a rosemount inlet and the PMS LAS-X. Atmospheric Environment 29, 449-453.

Formenti, P., Elbert, W., Maenhaut, W., Haywood, J., Andreae, M.O., 2003. Chemical composition of mineral dust aerosol during the Saharan Dust Experiment (SHADE)

airborne campaign in the Cape Verde region, September 2000. J. Geophys. Res. 108, 8576.

Formenti, P., Rajot, J.L., Desboeufs, K., Caquineau, S., Chevaillier, S., Nava, S., Gaudichet, A., Journet, E., Triquet, S., Alfaro, S., Chiari, M., Haywood, J., Coe, H., Highwood, E., 2008. Regional variability of the composition of mineral dust from western Africa: Results from the AMMA SOP0/DABEX and DODO field campaigns. Journal of Geophysical Research: Atmospheres 113, D00C13.

Fors, E.O., Rissler, J., Massling, A., Svenningsson, B., Andreae, M.O., Dusek, U., Frank, G.P., Hoffer, A., Bilde, M., Kiss, G., Janitsek, S., Henning, S., Facchini, M.C., Decesari, S., Swietlicki, E., 2010. Hygroscopic properties of Amazonian biomass burning and European background HULIS and investigation of their effects on surface tension with two models linking H-TDMA to CCNC data. Atmos. Chem. Phys. 10, 5625-5639.

Forster, P., V. Ramaswamy, P. Artaxo, T. Berntsen, R. Betts, D.W. Fahey, J. Haywood, J. Lean, D.C. Lowe, G. Myhre, J. Nganga, R. Prinn, G. Raga, Schulz, M., Dorland, R.V., 2007. 2007: Changes in Atmospheric Constituents and in Radiative Forcing. In: Climate Change 2007: The Physical Science Basis. Contribution of Working Group I to the Fourth Assessment Report of the Intergovernmental Panel on Climate Change. Cambridge University Press.

Forster, P.M.d.F., Shine, K.P., 1997. Radiative forcing and temperature trends from stratospheric ozone changes. Journal of Geophysical Research: Atmospheres 102, 10841-10855.

Freitag, S., Clarke, A.D., Howell, S.G., Kapustin, V.N., Campos, T., Brekhovskikh, V.L., Zhou, J., 2014. Combining airborne gas and aerosol measurements with HYSPLIT: a visualization tool for simultaneous evaluation of air mass history and back trajectory consistency. Atmos. Meas. Tech. 7, 107-128.

Freud, E., Rosenfeld, D., Andreae, M.O., Costa, A.A., Artaxo, P., 2008. Robust relations between CCN and the vertical evolution of cloud drop size distribution in deep convective clouds. Atmos. Chem. Phys. 8, 1661-1675.

Fuchs, N.A., 1975. Sampling of aerosols. Atmospheric Environment (1967) 9, 697-707.

Fuller, K.A., Malm, W.C., Kreidenweis, S.M., 1999. Effects of mixing on extinction by carbonaceous particles. Journal of Geophysical Research: Atmospheres 104, 15941-15954.

Fuzzi, S., S. Decesari, M. C. Facchini, F. Cavalli, L. Emblico, M. Mircea, M. O. Andreae, I. Trebs, A. Hoffer, P. Guyon, P. Artaxo, L. V. Rizzo, L. L. Lara, T. Pauliquevis, W. Maenhaut, N. Raes, X. G. Chi, O. L. Mayol-Bracero, L. L. Soto-Garcia, M. Claeys, I. Kourtchev, J. Rissler, E. Swietlicki, E. Tagliavini, G. Schkolnik, A. H. Falkovich, Y. Rudich, G. Fisch, a., Gatti, L.V., 2007. Overview of the inorganic and organic composition of size-segregated aerosol in Rondônia, Brazil, from the biomass-burning period to the onset of the wet season. J. Geophys. Res. 112.

Garnett, J.C.M., 1904. Colours in Metal Glasses and in Metallic Films. Philosophical Transactions of the Royal Society of London. Series A, Containing Papers of a Mathematical or Physical Character 203, 385-420.

Garratt, J.R., 1994. The Atmospheric Boundary Layer. Cambridge Atmospheric and Space Science Series.

Gerbig, C., Schmitgen, S., Kley, D., Volz-Thomas, A., Dewey, K., Haaks, D., 1999. An improved fast-response vacuum-UV resonance fluorescence CO instrument. Journal of Geophysical Research: Atmospheres 104, 1699-1704.

Giles, J., 2005. Climate science: The dustiest place on Earth. Nature 434, 816.

Golodets, G.I., 1983. Heterogeneous catalytic reactions involving molecular oxygen in: Studies in surface science and catalysis. Elsevier, Amsterdam.

Gong, S.L., Barrie, L.A., Blanchet, J.P., von Salzen, K., Lohmann, U., Lesins, G., Spacek, L., Zhang, L.M., Girard, E., Lin, H., Leaitch, R., Leighton, H., Chylek, P., Huang, P., 2003. Canadian Aerosol Module: A size-segregated simulation of atmospheric aerosol processes for climate and air quality models 1. Module development. Journal of Geophysical Research: Atmospheres 108, 4007.

Graedel, T.E., 1979. Terpenoids in the atmosphere. Reviews of Geophysics 17, 937-947.

Graham, B., Mayol-Bracero, O.L., Guyon, P., Roberts, G.C., Decesari, S., Facchini, M.C., Artaxo, P., Maenhaut, W., Köll, P., Andreae, M.O., 2002. Water-soluble organic compounds in biomass burning aerosols over Amazonia 1. Characterization

by NMR and GC-MS. Journal of Geophysical Research: Atmospheres 107, LBA 14-11-LBA 14-16.

Grassian, V.H., 2002. Chemical Reactions of Nitrogen Oxides on the Surface of Oxide, Carbonate, Soot, and Mineral Dust Particles: Implications for the Chemical Balance of the Troposphere. The Journal of Physical Chemistry A 106, 860-877.

Griffin, D.W., 2007. Atmospheric movement of microorganisms in clouds of desert dust and implications for human health. Clinical Microbiology Reviews 20, 459-477

Guo, S., Hu, M., Wang, Z.B., Slanina, J., Zhao, Y.L., 2010. Size-resolved aerosol water-soluble ionic compositions in the summer of Beijing: implication of regional secondary formation. Atmos. Chem. Phys. Discuss. 10, 947 - 959.

Gussman, R.A., 1969. On the Aerosol Particle Slip Correction Factor. Journal of Applied Meteorology 8, 999-1001.

Güsten, H., Heinrich, G., Mönnich, E., Sprung, D., Weppner, J., Ramadan, A.B., Ezz El-Din, M.R.M., Ahmed, D.M., Hassan, G.K.Y., 1996. On-line measurements of ozone surface fluxes: Part II. Surface-level ozone fluxes onto the Sahara desert. Atmospheric Environment 30, 911-918.

Guyon, P., Graham, B., Beck, J., Boucher, O., Gerasopoulos, E., Mayol-Bracero, O.L., Roberts, G.C., Artaxo, P., Andreae, M.O., 2003. Physical properties and concentration of aerosol particles over the Amazon tropical forest during background and biomass burning conditions. Atmos. Chem. Phys. 3, 951 - 967.

Hangal, S., Willeke, K., 1990. Overall efficiency of tubular inlets sampling at 0–90 degrees from horizontal aerosol flows. Atmospheric Environment. Part A. General Topics 24, 2379-2386.

Hanisch, F., Crowley, J.N., 2003. Ozone decomposition on Saharan dust: an experimental investigation. Atmos. Chem. Phys. 3, 119-130.

Hansell, R.A., Tsay, S.C., Ji, Q., Hsu, N.C., Jeong, M.J., Wang, S.H., Reid, J.S., Liou, K.N., Ou, S.C., 2009. An Assessment of the Surface Longwave Direct Radiative Effect of Airborne Saharan Dust during the NAMMA Field Campaign. Journal of the Atmospheric Sciences 67, 1048-1065.

Hansen, J., Russell, G., Rind, D., Stone, P., Lacis, A., Lebedeff, S., Ruedy, R., Travis, L., 1983. Efficient Three-Dimensional Global Models for Climate Studies: Models I and II. Monthly Weather Review 111, 609-662.

Hansen, J., Sato, M., Ruedy, R., 1997. Radiative forcing and climate response. Journal of Geophysical Research: Atmospheres 102, 6831-6864.

Hansen, J.E., Travis, L.D., 1974. Light scattering in planetary atmospheres. Space Sci. Rev. 16, 527-610.

Harrison, R.M., Van Grieken, R., 1998. Atmospheric Particles. John Wiley & Sons IUPAC Series on Analytical and Physical Chemistry of Environmental Systems Volume 5, 30 - 42.

Harrison, R.M., Yin, J., 2000. Particulate matter in the atmosphere: which particle properties are important for its effects on health? Science of The Total Environment 249, 85-101.

Harrison, S.P., Kohfeld, K.E., Roelandt, C., Claquin, T., 2001. The role of dust in climate changes today, at the last glacial maximum and in the future. Earth-Science Reviews 54, 43-80.

Haywood, J., Francis, P., Osborne, S., Glew, M., Loeb, N., Highwood, E., Tanré, D., Myhre, G., Formenti, P., Hirst, E., 2003a. Radiative properties and direct radiative effect of Saharan dust measured by the C-130 aircraft during SHADE: 1. Solar spectrum. J. Geophys. Res. 108, 8577.

Haywood, J., Francis, P., Osborne, S., Glew, M., Loeb, N., Highwood, E., Tanré, D., Myhre, G., Formenti, P., Hirst, E., 2003b. Radiative properties and direct radiative effect of Saharan dust measured by the C-130 aircraft during SHADE: 1. Solar spectrum. Journal of Geophysical Research: Atmospheres 108, 8577.

Haywood, J.M., Allan, R.P., Culverwell, I., Slingo, T., Milton, S., Edwards, J., Clerbaux, N., 2005. Can desert dust explain the outgoing longwave radiation anomaly over the Sahara during July 2003? Journal of Geophysical Research: Atmospheres 110, D05105.

Haywood, J.M., Francis, P.N., Glew, M.D., Taylor, J.P., 2001. Optical properties and direct radiative effect of Saharan dust: A case study of two Saharan dust outbreaks using aircraft data. J. Geophys. Res. 106, 18417-18430.

Haywood, J.M., Johnson, B.T., Osborne, S.R., Baran, A.J., Brooks, M., Milton, S.F., Mulcahy, J., Walters, D., Allan, R.P., Klaver, A., Formenti, P., Brindley, H.E., Christopher, S., Gupta, P., 2011. Motivation, rationale and key results from the GERBILS Saharan dust measurement campaign. Quarterly Journal of the Royal Meteorological Society 137, 1106-1116.

Haywood, J.M., Osborne, S., 2000. Corrections to be applied to the PSAP and nephelometer for accurate determination of the absorption coefficient, scattering coefficient and single scattering albedo. MRF Technical Note No. 31, Met Office, Exeter, UK.

Haywood, J.M., Pelon, J., Formenti, P., Bharmal, N., Brooks, M., Capes, G., Chazette, P., Chou, C., Christopher, S., Coe, H., Cuesta, J., Derimian, Y., Desboeufs, K., Greed, G., Harrison, M., Heese, B., Highwood, E.J., Johnson, B., Mallet, M., Marticorena, B., Marsham, J., Milton, S., Myhre, G., Osborne, S.R., Parker, D.J., Rajot, J.L., Schulz, M., Slingo, A., Tanré, D., Tulet, P., 2008. Overview of the Dust and Biomass-burning Experiment and African Monsoon Multidisciplinary Analysis Special Observing Period-0. Journal of Geophysical Research: Atmospheres 113, D00C17.

Haywood, J.M., Ramaswamy, V., Soden, B.J., 1999. Tropospheric Aerosol Climate Forcing in Clear-Sky Satellite Observations over the Oceans. Science 283, 1299-1303.

Hecobian, A., Zhang, X., Zheng, M., Frank, N., Edgerton, E.S., Weber, R.J., 2010. Water-Soluble Organic Aerosol material and the light-absorption characteristics of aqueous extracts measured over the Southeastern United States. Atmos. Chem. Phys. 10, 5965-5977.

Heim, M., Mullins, B.J., Umhauer, H., Kasper, G., 2008. Performance evaluation of three optical particle counters with an efficient “multimodal” calibration method. Journal of Aerosol Science 39, 1019-1031.

Heintzenberg, J., 2009. The SAMUM-1 experiment over Southern Morocco: overview and introduction. Tellus B 61, 2-11.

Hermann, M., Stratmann, F., Wilck, M., Wiedensohler, A., 2001. Sampling Characteristics of an Aircraft-Borne Aerosol Inlet System. Journal of Atmospheric and Oceanic Technology 18, 7-19.

Highwood, E.J., Northway, M.J., McMeeking, G.R., Morgan, W.T., Liu, D., Osborne, S., Bower, K., Coe, H., Ryder, C., Williams, P., 2012. Aerosol scattering and absorption during the EUCAARI-LONGREX flights of the Facility for Airborne Atmospheric Measurements (FAAM) BAe-146: can measurements and models agree? Atmos. Chem. Phys. 12, 7251-7267.

Hinds, W.C., 1999. Aerosol Technology (2nd Edition). Wiley - Interscience.

Hobby, M., Gascoyne, M., Marsham, J.H., Bart, M., Allen, C., Engelstaedter, S., Fadel, D.M., Gandega, A., Lane, R., McQuaid, J.B., Ouchene, B., Ouladichir, A., Parker, D.J., Rosenberg, P., Ferroudj, M.S., Saci, A., Seddik, F., Todd, M., Walker, D., Washington, R., 2012. The Fennec Automatic Weather Station (AWS) Network: Monitoring the Saharan Climate System. Journal of Atmospheric and Oceanic Technology 30, 709-724.

Holben, B.N., Eck, T.F., Slutsker, I., Tanré, D., Buis, J.P., Setzer, A., Vermote, E., Reagan, J.A., Kaufman, Y.J., Nakajima, T., Lavenu, F., Jankowiak, I., Smirnov, A., 1998. AERONET—A Federated Instrument Network and Data Archive for Aerosol Characterization. Remote Sensing of Environment 66, 1-16.

Hopkins, R.J., Lewis, K., Desyaterik, Y., Wang, Z., Tivanski, A.V., Arnott, W.P., Laskin, A., Gilles, M.K., 2007a. Correlations between optical, chemical and physical properties of biomass burn aerosols. Geophys. Res. Lett. 34, L18806.

Hopkins, R.J., Tivanski, A.V., Marten, B.D., Gilles, M.K., 2007b. Chemical bonding and structure of black carbon reference materials and individual carbonaceous atmospheric aerosols. Journal of Aerosol Science 38, 573-591.

Houghton, J.T., Meira Filho, L.G., Callander, B.A., Harris, N., Kattenberg, A., Maskell, K., 1996. Climate Change 1995: The Science of Climate Change, Contribution of Working Group I to the second assessment report of the Intergovernmental Panel on Climate Change,. Cambridge University Press, Cambridge.

Hovan, S.A., Rea, D.K., Pisias, N.G., 1991. Late Pleistocene Continental Climate and Oceanic Variability Recorded in Northwest Pacific Sediments. Paleoceanography 6, 349-370.

Huebert, B., S. G. Howell, D. S. Covert, T. Bertram, A. D. Clarke, J. R. Anderson, B. Lafleur, W. Seebaugh, J. C. Wilson, D. Gesler, B. W. Blomquist, Fox, J., 2004.

PELTI: Measuring the passing efficiency of an airborne low turbulence aerosol inlet. Aerosol Science and Technology, Vol. 38, No. 8. (2004), pp. 803-824. Key: citeulike:6344644 38.

Huebert, B.J., Lee, G., Warren, W.L., 1990. Airborne Aerosol Inlet Passing Efficiency Measurement. J. Geophys. Res. 95, 16369-16381.

Huschke, R.E., 1959. Glossary of Meteorology. American Meteorological Society, Boston, Mass.

Incropera, F.P., Dewitt, D.P., Bergman, T.L., Lavine, A.S., 2007. Introduction to Heat Transfer. John Wiley & Sons 5th Edition, 348 - 366.

Jacob, D.J., 2000. Heterogeneous chemistry and tropospheric ozone. Atmospheric Environment 34, 2131-2159.

Jaenicke, R., Davies, C.N., 1976. The mathematical expression of the size distribution of atmospheric aerosols. Journal of Aerosol Science 7, 255-259.

Janhall, S., Andreae, M.O., Poschl, U., 2010. Biomass burning aerosol emissions from vegetation fires: particle number and mass emission factors and size distributions. Atmos. Chem. Phys. 10, 1427.

Johnson, B.T., Heese, B., McFarlane, S.A., Chazette, P., Jones, A., Bellouin, N., 2008. Vertical distribution and radiative effects of mineral dust and biomass burning aerosol over West Africa during DABEX. Journal of Geophysical Research: Atmospheres 113, D00C12.

Johnson, B.T., Osborne, S.R., 2011. Physical and optical properties of mineral dust aerosol measured by aircraft during the GERBILS campaign. Quarterly Journal of the Royal Meteorological Society 137, 1117-1130.

Kanakidou, M., Seinfeld, J.H., Pandis, S.N., Barnes, I., Dentener, F.J., Facchini, M.C., Van Dingenen, R., Ervens, B., Nenes, A., Nielsen, C.J., Swietlicki, E., Putaud, J.P., Balkanski, Y., Fuzzi, S., Horth, J., Moortgat, G.K., Winterhalter, R., Myhre, C.E.L., Tsigaridis, K., Vignati, E., Stephanou, E.G., Wilson, J., 2005. Organic aerosol and global climate modelling: a review. Atmos. Chem. Phys., 1053-1123.

Kandler, K., Benker, N., Bundke, U., Cuevas, E., Ebert, M., Knippertz, P., Rodríguez, S., Schütz, L., Weinbruch, S., 2007. Chemical composition and complex refractive

index of Saharan Mineral Dust at Izaña, Tenerife (Spain) derived by electron microscopy. Atmospheric Environment 41, 8058-8074.

Kandler, K., Lieke, K., Benker, N., Emmel, C., KÜPper, M., MÜLler-Ebert, D., Ebert, M., Scheuvens, D., Schladitz, A., SchÜTz, L., Weinbruch, S., 2011. Electron microscopy of particles collected at Praia, Cape Verde, during the Saharan Mineral Dust Experiment: particle chemistry, shape, mixing state and complex refractive index. Tellus B 63, 475-496.

Kandler, K., Schultz, L., Deutscher, C., Ebert, M., Hofmann, H., JÄCkel, S., Jaenicke, R., Knippertz, P., Lieke, K., Massling, A., Petzold, A., Schladitz, A., Weinzierl, B., Wiedensohler, A., Zorn, S., Weinbruch, S., 2009. Size distribution, mass concentration, chemical and mineralogical composition and derived optical parameters of the boundary layer aerosol at Tinfou, Morocco, during SAMUM 2006. Tellus B 61, 32-50.

Kaufman, Y.J., Fraser, R.S., 1983. Light Extinction by Aerosols during Summer Air Pollution. Journal of Climate and Applied Meteorology 22, 1694-1706.

Kaufman, Y.J., Hobbs, P.V., Kirchhoff, V.W.J.H., Artaxo, P., Remer, L.A., Holben, B.N., King, M.D., Ward, D.E., Prins, E.M., Longo, K.M., Mattos, L.F., Nobre, C.A., Spinhirne, J.D., Ji, Q., Thompson, A.M., Gleason, J.F., Christopher, S.A., Tsay, S.C., 1998. Smoke, Clouds, and Radiation-Brazil (SCAR-B) experiment. Journal of Geophysical Research: Atmospheres 103, 31783-31808.

Khain, A., Rosenfeld, D. and Pokrovsky, A., 2005. Aerosol impact on the dynamics and microphysics of convective clouds. Quarterly Journal of the Royal Meteorological Society 131, 2639 - 2663.

Kim, J., Yoon, S.-C., Jefferson, A., Kim, S.-W., 2006. Aerosol hygroscopic properties during Asian dust, pollution, and biomass burning episodes at Gosan, Korea in April 2001. Atmospheric Environment 40, 1550-1560.

Kim, S.W., Chazette, P., Dulac, F., Sanak, J., Johnson, B., Yoon, S.C., 2009. Vertical structure of aerosols and water vapor over West Africa during the African monsoon dry season. Atmos. Chem. Phys. 9, 8017-8038.

Klett, J.D., 1985. Lidar inversion with variable backscatter/extinction ratios. Appl. Opt. 24, 1638-1643.

Knippertz, P., Todd, M.C., 2012. Mineral dust aerosols over the Sahara: Meteorological controls on emission and transport and implications for modeling. Rev. Geophys. 50, RG1007.

Knollenberg, R.G., Luehr, R., 1976. Open cavity laser 'active' scattering particle spectrometry from 0.05 to 5 microns. Fine Particles: Aerosol Generation, Measurement, Sampling and Analysis Academic, San Diego, Calif., 669–697.

Kohfeld, K.E., Harrison, S.P., 2001. DIRTMAP: the geological record of dust. Earth-Science Reviews 54, 81-114.

Kok, J.F., Parteli, E.J.R., Michaels, T.I., Karam, D.B., 2012. The physics of wind-blown sand and dust. Rep. Prog. Phys 75, 106901.

Kondo, Y., Sahu, L., Moteki, N., Khan, F., Takegawa, N., Liu, X., Koike, M., Miyakawa, T., 2011. Consistency and Traceability of Black Carbon Measurements Made by Laser-Induced Incandescence, Thermal-Optical Transmittance, and Filter-Based Photo-Absorption Techniques. Aerosol Science and Technology 45, 295-312.

Koren, I., Yoram J. Kaufman, Lorraine A. Remer, Martins, J.V., 2004. Measurement of the Effect of Amazon Smoke on Inhibition of Cloud Formation. Science 303, 5662.

Kotchenruther, R.A., Hobbs, P.V., 1998. Humidification factors of aerosols from biomass burning in Brazil. J. Geophys. Res. 103, 32081-32089.

Kreidenweis, S.M., Walcek, C.J., Feingold, G., Gong, W., Jacobson, M.Z., Kim, C.-H., Liu, X., Penner, J.E., Nenes, A., Seinfeld, J.H., 2003. Modification of aerosol mass and size distribution due to aqueous-phase SO2 oxidation in clouds: Comparisons of several models. Journal of Geophysical Research: Atmospheres 108, 4213.

Kulkarni, P., Baron, P., Willeke, K., 2011a. Aerosol Measurement - Principles, Techniques, and Applications.

Kulkarni, P., Baron, P.A., Willeke, K. 2011b. Introduction to Aerosol Characterization, In: Aerosol Measurement. John Wiley & Sons, Inc., 1-13.

Kulmala, M., Kontkanen, J., Junninen, H., Lehtipalo, K., Manninen, H.E., Nieminen, T., Petäjä, T., Sipilä, M., Schobesberger, S., Rantala, P., Franchin, A., Jokinen, T., Järvinen, E., Äijälä, M., Kangasluoma, J., Hakala, J., Aalto, P.P., Paasonen, P., Mikkilä, J., Vanhanen, J., Aalto, J., Hakola, H., Makkonen, U., Ruuskanen, T.,

Mauldin, R.L., Duplissy, J., Vehkamäki, H., Bäck, J., Kortelainen, A., Riipinen, I., Kurtén, T., Johnston, M.V., Smith, J.N., Ehn, M., Mentel, T.F., Lehtinen, K.E.J., Laaksonen, A., Kerminen, V.-M., Worsnop, D.R., 2013. Direct Observations of Atmospheric Aerosol Nucleation. Science 339, 943-946.

Kulmala, M., Laakso, L., Lehtinen, K.E.J., Riipinen, I., Dal Maso, M., Anttila, T., Kerminen, V.M., Hõrrak, U., Vana, M., Tammet, H., 2004a. Initial steps of aerosol growth. Atmos. Chem. Phys. 4, 2553-2560.

Kulmala, M., Vehkamäki, H., Petäjä, T., Dal Maso, M., Lauri, A., Kerminen, V.M., Birmili, W., McMurry, P.H., 2004b. Formation and growth rates of ultrafine atmospheric particles: a review of observations. Journal of Aerosol Science 35, 143-176.

Lack, D.A., Cappa, C.D., Covert, D.S., Baynard, T., Massoli, P., Sierau, B., Bates, T.S., Quinn, P.K., Lovejoy, E.R., Ravishankara, A.R., 2008. Bias in Filter-Based Aerosol Light Absorption Measurements Due to Organic Aerosol Loading: Evidence from Ambient Measurements. Aerosol Science and Technology 42, 1033-1041.

Lack, D.A., Cappa, C.D., Cross, E.S., Massoli, P., Ahern, A.T., Davidovits, P., Onasch, T.B., 2009. Absorption Enhancement of Coated Absorbing Aerosols: Validation of the Photo-Acoustic Technique for Measuring the Enhancement. Aerosol Science and Technology 43, 1006-1012.

Lack, D.A., Langridge, J.M., 2013. On the attribution of black and brown carbon light absorption using the Ångström exponent. Atmos. Chem. Phys. Discuss. 13, 15493-15515.

Lambert, F., Delmonte, B., Petit, J.R., Bigler, M., Kaufmann, P.R., Hutterli, M.A., Stocker, T.F., Ruth, U., Steffensen, J.P., Maggi, V., 2008. Dust-climate couplings over the past 800,000[thinsp]years from the EPICA Dome C ice core. Nature 452, 616-619.

Lance, S., Brock, C.A., Rogers, D., Gordon, J.A., 2010. Water droplet calibration of the Cloud Droplet Probe (CDP) and in-flight performance in liquid, ice and mixed-phase clouds during ARCPAC. Atmos. Meas. Tech. 3, 1683 - 1706.

Langmann, B., Duncan, B., Textor, C., Trentmann, J., van der Werf, G.R., 2009. Vegetation fire emissions and their impact on air pollution and climate. Atmospheric Environment 43, 107-116.

Langridge, J.M., Richardson, M.S., Lack, D.A., Brock, C.A., Murphy, D.M., 2013. Limitations of the Photoacoustic Technique for Aerosol Absorption Measurement at High Relative Humidity. Aerosol Science and Technology 47, 1163-1173.

Laurance, W.F., S. Bergen, M.A. Cochrane, P.M. Fearnside, P. Delamonica, S. D'Angelo, Barber, C., Fernandes., T., 2005. The future of the Amazon. Tropical Rainforests: Past, Present, and Future, 583-609.

Lavaysse, C., Flamant, C., Janicot, S., Parker, D.J., Lafore, J.P., Sultan, B., Pelon, J., 2009. Seasonal evolution of the West African heat low: a climatological perspective. Clim Dyn 33, 313-330.

Lensky, I.M., Rosenfeld, D., 2008. Clouds-Aerosols-Precipitation Satellite Analysis Tool (CAPSAT). Atmos. Chem. Phys. 8, 6739 - 6753.

Lesins, G., Chylek, P., Lohmann, U., 2002. A study of internal and external mixing scenarios and its effect on aerosol optical properties and direct radiative forcing. Journal of Geophysical Research: Atmospheres 107, AAC 5-1-AAC 5-12.

Levin, E.J.T., McMeeking, G.R., Carrico, C.M., Mack, L.E., Kreidenweis, S.M., Wold, C.E., Moosmüller, H., Arnott, W.P., Hao, W.M., Collett, J.L., Jr., Malm, W.C., 2010. Biomass burning smoke aerosol properties measured during Fire Laboratory at Missoula Experiments (FLAME). J. Geophys. Res. 115, D18210.

Li, J., Pósfai, M., Hobbs, P.V., Buseck, P.R., 2003. Individual aerosol particles from biomass burning in southern Africa: 2, Compositions and aging of inorganic particles. Journal of Geophysical Research: Atmospheres 108, 8484.

Liao, H., Seinfeld, J.H., 1998a. Radiative forcing by mineral dust aerosols: sensitivity to key variables. J. Geophys. Res. 103, 31637-31645.

Liao, H., Seinfeld, J.H., 1998b. Radiative forcing by mineral dust aerosols: Sensitivity to key variables. Journal of Geophysical Research: Atmospheres 103, 31637-31645.

Liousse, C., Cachier, H., Jennings, S.G., 1993. Optical and thermal measurements of black carbon aerosol content in different environments: Variation of the specific

attenuation cross-section, sigma (σ). Atmospheric Environment. Part A. General Topics 27, 1203-1211.

Liousse, C., Penner, J.E., Chuang, C., Walton, J.J., Eddleman, H., Cachier, H., 1996. A global three-dimensional model study of carbonaceous aerosols. Journal of Geophysical Research: Atmospheres 101, 19411-19432.

Liu, P.S.K., Leaitch, W.R., Strapp, J.W., Wasey, M.A., 1992. Response of Particle Measuring Systems Airborne ASASP and PCASP to NaCl and Latex Particles. Aerosol Science and Technology 16, 83-95.

Lorenz, L.V., 1890. Lysbevaegelsen i og uder en plane lysbolger belyst kulge. Vidensk. Selk. Skr 6, 1 - 62.

Maher, B.A., Prospero, J.M., Mackie, D., Gaiero, D., Hesse, P.P., Balkanski, Y., 2010. Global connections between aeolian dust, climate and ocean biogeochemistry at the present day and at the last glacial maximum. Earth-Science Reviews 99, 61-97.

Mahowald, N.M., Baker, A.R., Bergametti, G., Brooks, N., Duce, R.A., Jickells, T.D., Kubilay, N., Prospero, J.M., Tegen, I., 2005. Atmospheric global dust cycle and iron inputs to the ocean. Global Biogeochemical Cycles 19, GB4025.

Marenco, F., 2013. Nadir airborne lidar observations of deep aerosol layers. Atmos. Meas. Tech. 6, 2055-2064.

Marenco, F., Hogan, R.J., 2011. Determining the contribution of volcanic ash and boundary layer aerosol in backscatter lidar returns: A three-component atmosphere approach. Journal of Geophysical Research: Atmospheres 116, D00U06.

Marenco, F., Johnson, B., Turnbull, K., Newman, S., Haywood, J., Webster, H., Ricketts, H., 2011. Airborne lidar observations of the 2010 Eyjafjallajökull volcanic ash plume. Journal of Geophysical Research: Atmospheres 116, D00U05.

Marsham, J.H., Dixon, N.S., Garcia-Carreras, L., Lister, G.M.S., Parker, D.J., Knippertz, P., Birch, C.E., 2013a. The role of moist convection in the West African monsoon system: Insights from continental-scale convection-permitting simulations. Geophysical Research Letters 40, 1843-1849.

Marsham, J.H., Hobby, M., Allen, C.J.T., Banks, J.R., Bart, M., Brooks, B.J., Cavazos-Guerra, C., Engelstaedter, S., Gascoyne, M., Lima, A.R., Martins, J.V., McQuaid, J.B.,

O'Leary, A., Ouchene, B., Ouladichir, A., Parker, D.J., Saci, A., Salah-Ferroudj, M., Todd, M.C., Washington, R., 2013b. Meteorology and dust in the central Sahara: Observations from Fennec supersite-1 during the June 2011 Intensive Observation Period. Journal of Geophysical Research: Atmospheres 118, 4069-4089.

Marsham, J.H., Knippertz, P., Dixon, N.S., Parker, D.J., Lister, G.M.S., 2011. The importance of the representation of deep convection for modeled dust-generating winds over West Africa during summer. Geophysical Research Letters 38, L16803.

Marsham, J.H., Parker, D.J., Grams, C.M., Johnson, B.T., Grey, W.M.F., Ross, A.N., 2008a. Observations of mesoscale and boundary-layer scale circulations affecting dust transport and uplift over the Sahara. Atmos. Chem. Phys. 8, 6979 - 6993.

Marsham, J.H., Parker, D.J., Grams, C.M., Taylor, C.M., Haywood, J.M., 2008b. Uplift of Saharan dust south of the intertropical discontinuity. Journal of Geophysical Research: Atmospheres 113, D21102.

Martin, S.T., Andreae, M.O., Artaxo, P., Baumgardner, D., Chen, Q., Goldstein, A.H., Guenther, A., Heald, C.L., Mayol-Bracero, Olga L. McMurry, Peter H., Pauliquevis, T., Pöschl, U., Prather, K.A., Roberts, G.C., Saleska, S.R., Silva Dias, M.A., Spracklen, D.V., Swietlicki, E., Trebs, I., 2010. Sources and properties of Amazonian aerosol particles. Rev. Geophys. 48, RG2002.

Martin, S.T., Meinrat O. Andreae, Paulo Artaxo, Darrel Baumgardner, Qi Chen, Allen H.Goldstein, Alex Guenther, Colette L. Heald, Olga L. Mayol-Bracero, Peter H. McMurry, Theotonio Pauliquevis, Ulrich Pöschl, Kimberly A. Prather, Gregory C. Roberts, Scott R. Saleska, M.A. Silva Dias, Dominick V. Spracklen, Erik Swietlicki, a., Trebs, I., 2009. Sources and Properties of Amazonian Aerosol Particles. Reviews of Geophysics.

Martins, J.V., Artaxo, P., Liousse, C., Reid, J.S., Hobbs, P.V., Kaufman, Y.J., 1998a. Effects of black carbon content, particle size, and mixing on light absorption by aerosols from biomass burning in Brazil. J. Geophys. Res. 103, 32041-32050.

Martins, J.V., Artaxo, P., Liousse, C., Reid, J.S., Hobbs, P.V., Kaufman, Y.J., 1998b. Effects of black carbon content, particle size, and mixing on light absorption by aerosols from biomass burning in Brazil. Journal of Geophysical Research: Atmospheres 103, 32041-32050.

Martiny, N., Chiapello, I., 2013. Assessments for the impact of mineral dust on the meningitis incidence in West Africa. Atmospheric Environment 70, 245-253.

Matsui, H., Kondo, Y., Moteki, N., Takegawa, N., Sahu, L.K., Koike, M., Zhao, Y., Fuelberg, H.E., Sessions, W.R., Diskin, G., Anderson, B.E., Blake, D.R., Wisthaler, A., Cubison, M.J., Jimenez, J.L., 2011. Accumulation-mode aerosol number concentrations in the Arctic during the ARCTAS aircraft campaign: Long-range transport of polluted and clean air from the Asian continent. Journal of Geophysical Research: Atmospheres 116, D20217.

McConnell, C.L., Highwood, E.J., Coe, H., Formenti, P., Anderson, B., Osborne, S., Nava, S., Desboeufs, K., Chen, G., Harrison, M.A.J., 2008. Seasonal variations of the physical and optical characteristics of Saharan dust: Results from the Dust Outflow and Deposition to the Ocean (DODO) experiment. J. Geophys. Res. 113, D14S05.

McMeeking, G.R., Kreidenweis, S.M., Baker, S., Carrico, C.M., Chow, J.C., Collett, J.L., Jr., Hao, W.M., Holden, A.S., Kirchstetter, T.W., Malm, W.C., Moosmüller, H., Sullivan, A.P., Wold, C.E., 2009. Emissions of trace gases and aerosols during the open combustion of biomass in the laboratory. J. Geophys. Res. 114, D19210.

McMurry, P.H., 2000. A review of atmospheric aerosol measurements. Atmospheric Environment 34, 1959-1999.

Mie, G., 1908. Beiträge zur Optik trüber Medien, speziell kolloidaler Metallösungen. Annalen der Physik 330, 377-445.

Miller, R.L., Tegen, I., 1998. Climate Response to Soil Dust Aerosols. Journal of Climate 11, 3247-3267.

Min, Q.-L., Li, R., Lin, B., Joseph, E., Wang, S., Hu, Y., Morris, V., Chang, F., 2009. Evidence of mineral dust altering cloud microphysics and precipitation. Atmos. Chem. Phys. 9.

Ming, Y., Ramaswamy, V., Donner, L.J., Phillips, V.T.J., Klein, S.A., Ginoux, P.A., Horowitz, L.W., 2007. Modeling the Interactions between Aerosols and Liquid Water Clouds with a Self-Consistent Cloud Scheme in a General Circulation Model. Journal of the Atmospheric Sciences 64, 1189-1209.

Moffet, R.C., Prather, K.A., 2009. In-situ measurements of the mixing state and optical properties of soot with implications for radiative forcing estimates. Proceedings of the National Academy of Sciences 106, 11872-11877.

Moosmüller, H., Engelbrecht, J.P., Skiba, M., Frey, G., Chakrabarty, R.K., Arnott, W.P., 2012. Single scattering albedo of fine mineral dust aerosols controlled by iron concentration. Journal of Geophysical Research: Atmospheres 117, D11210.

Moteki, N., Kondo, Y., Miyazaki, Y., Takegawa, N., Komazaki, Y., Kurata, G., Shirai, T., Blake, D.R., Miyakawa, T., Koike, M., 2007. Evolution of mixing state of black carbon particles: Aircraft measurements over the western Pacific in March 2004. Geophys. Res. Lett. 34.

Müller, D., Heinold, B., Tesche, M., Tegen, I., Althausen, D., Arboledas, L.A., Amiridis, V., Amodeo, A., Ansmann, A., Balis, D., Comeron, A., D'Amico, G., Gerasopoulos, E., Guerrero-Rascado, J.L., Freudenthaler, V., Giannakaki, E., Heese, B., Iarlori, M., Knippertz, P., Mamouri, R.E., Mona, L., Papayannis, A., Pappalardo, G., Perrone, R.M., Pisani, G., Rizi, V., Sicard, M., Spinelli, N., Tafuro, A., Wiegner, M., 2009. EARLINET observations of the 14–22-May long-range dust transport event during SAMUM 2006: validation of results from dust transport modelling. Tellus B 61, 325-339.

Müller, T., Laborde, M., Kassell, G., Wiedensohler, A., 2011. Design and performance of a three-wavelength LED-based total scatter and backscatter integrating nephelometer. Atmos. Meas. Tech. 4, 1291-1303.

Nedelec, P., Cammas, J.-P., Thouret, V., Athier, G., Cousin, J.-M., Legrand, C., Abonnel, C., Lecoeur, F., Cayez, G., Marizy, C., 2003. An improved infrared carbon monoxide analyser for routine measurements aboard commercial Airbus aircraft: technical validation and first scientific results of the MOZAIC III programme. Atmos. Chem. Phys. 3, 1551 - 1564.

Nepstad, D.C., Adalberto VerõÂssimo, Ane Alencar, Carlos Nobre, Eirivelthon Lima, Paul Lefebvre, Peter Schlesinger, Christopher Potterk, Paulo Moutinho, Elsa Mendoza, Mark Cochrane, Vanessa Brooksk, 1999. Large-scale impoverishment of Amazonian forests by logging and fire. Nature 398, 505 - 508.

Oberdorster, G., Oberdorster, E., Oberdorster, J., 2005. Nanotoxicology: An Emerging Disciplne Evolving from Studies of Ultrafine Particles. Environmental Health Perspectives. Environmental Health Perspectives 113, 823-839.

Ogren, J., 2010. Comment on Calibration and Intercomparison of Filter-Based Measurements of Visible Light Absorption by Aerosols. Aerosol Science and Technology 44, 589-591.

Okazaki, K., Willeke, K., 1987. Transmission and Deposition Behavior of Aerosols in Sampling Inlets. Aerosol Science and Technology 7, 275-283.

Osborne, S.R., Baran, A.J., Johnson, B.T., Haywood, J.M., Hesse, E., Newman, S., 2011. Short-wave and long-wave radiative properties of Saharan dust aerosol. Quarterly Journal of the Royal Meteorological Society 137, 1149-1167.

Osborne, S.R., Haywood, J.M., 2005. Aircraft observations of the microphysical and optical properties of major aerosol species. Atmospheric Research 73, 173-201.

Osborne, S.R., Haywood, J.M., Bellouin, N., 2007. In situ and remote-sensing measurements of the mean microphysical and optical properties of industrial pollution aerosol during ADRIEX. Quarterly Journal of the Royal Meteorological Society 133, 17-32.

Osborne, S.R., Johnson, B.T., Haywood, J.M., Baran, A.J., Harrison, M.A.J., McConnell, C.L., 2008. Physical and optical properties of mineral dust aerosol during the Dust and Biomass-burning Experiment. J. Geophys. Res. 113, D00C03.

Otto, S., Bierwirth, E., Weinzierl, B., Kandler, K., Esselborn, M., Tesche, M., Schladitz, A., Wendisch, M., Trautmann, T., 2009. Solar radiative effects of a Saharan dust plume observed during SAMUM assuming spheroidal model particles. Tellus B 61, 270-296.

Pedlowski, M.A., Dale, V.H., Matricardi, Eraldo A. T., d.S.F., Pereira, E., 1997. Patterns and impacts of deforestation in Rondônia, Brazil. Landscape and Urban Planning 38, 149-157.

Peter, J.R., Blyth, A.M., Brooks, B., McQuaid, J.B., Lingard, J.J.N., Smith, M.H., 2008. On the composition of Caribbean maritime aerosol particles measured during RICO. Quarterly Journal of the Royal Meteorological Society 134, 1059-1063.

Petit, J.R., Mourner, L., Jouzel, J., Korotkevich, Y.S., Kotlyakov, V.I., Lorius, C., 1990. Palaeoclimatological and chronological implications of the Vostok core dust record. Nature 343, 56-58.

Petzold, A. 2009. Interim Report to Subtask 4.1: Characterisation of a Rosemount inlet for airborne aerosol measurement. In IAGOS Integration of routine Aircraft measurements into a Global Observing System.

Petzold, A., Formenti, P., Baumgardner, D., Bundke, U., Coe, H., Curtius, J., DeMott, P.J., Flagan, R.C., Fiebig, M., Hudson, J.G., McQuaid, J., Minikin, A., Roberts, G.C., Wang, J. 2013. In Situ Measurements of Aerosol Particles, In: Airborne Measurements for Environmental Research. Wiley-VCH Verlag GmbH & Co. KGaA, 157-223.

Petzold, A., Rasp, K., Weinzierl, B., Esselborn, M., Hamburger, T., DÖRnbrack, A., Kandler, K., SchÜTz, L., Knippertz, P., Fiebig, M., Virkkula, A.K.I., 2009. Saharan dust absorption and refractive index from aircraft-based observations during SAMUM 2006. Tellus B 61, 118-130.

Porter, J.N., Clarke, A.D., Ferry, G., Pueschel, R.F., 1992. Aircraft studies of size-dependent aerosol sampling through inlets. Journal of Geophysical Research: Atmospheres 97, 3815-3824.

Pósfai, M., Gelencsér, A., Simonics, R., Arató, K., Li, J., Hobbs, P.V., Buseck, P.R., 2004. Atmospheric tar balls: Particles from biomass and biofuel burning. J. Geophys. Res. 109, D06213.

Pratt, K.A., Prather, K.A., 2010. Aircraft measurements of vertical profiles of aerosol mixing states. J. Geophys. Res. 115, D11305.

Prospero, J., Carlson, T., 1980. Saharan air outbreaks over the tropical North Atlantic. PAGEOPH 119, 677-691.

Prospero, J.M., Carlson, T.N., 1972. Vertical and areal distribution of Saharan dust over the western equatorial north Atlantic Ocean. Journal of Geophysical Research 77, 5255-5265.

Prospero, J.M., Lamb, P.J., 2003. African Droughts and Dust Transport to the Caribbean: Climate Change Implications. Science 302, 1024-1027.

Pui, D., Romay-Novas, F., Liu, B.Y.H., 1987. Experimental Study of Particle Deposition in Bends of Circular Cross Section. Aerosol Science and Technology 7, 301-315.

Rabier, F., 2005. Overview of global data assimilation developments in numerical weather-prediction centres. Quarterly Journal of the Royal Meteorological Society 131, 3215-3233.

Rader, D.J., Marple, V.A., 1988. A Study of the Effects of Anisokinetic Sampling. Aerosol Science and Technology 8, 283-299.

Ramaswamy, V., Boucher, O., Haigh, J., Hauglustaine, D., Haywood, J., Myhre, G., Nakajima, T., Shi, G.Y., Solomon, S., 2001. Radiative forcing of climate change. In: Houghton JT et al. (eds) Climate change 2001, contribution of working group I to the third assessment report of the intergovernmental panel on climate change. Cambridge University Press, Cambridge, 349 - 416.

Redelsperger, J.-L., Thorncroft, C.D., Diedhiou, A., Lebel, T., Parker, D.J., Polcher, J., 2006. African Monsoon Multidisciplinary Analysis: An International Research Project and Field Campaign. Bulletin of the American Meteorological Society 87, 1739-1746.

Regalado, A., 2010. Brazil Says Rate of Deforestation in Amazon Continues to Plunge. Science 329, 1270-1271.

Reid, J.S., Eck, T.F., Christopher, S.A., Koppmann, R., Dubovik, O., Eleuterio, D.P., Holben, B.N., Reid, E.A., Zhang, J., 2005a. A review of biomass burning emissions part III: intensive optical properties of biomass burning particles. Atmos. Chem. Phys. 5, 827 - 849.

Reid, J.S., Hobbs, P.V., 1998. Physical and optical properties of young smoke from individual biomass fires in Brazil. Journal of Geophysical Research: Atmospheres 103, 32013-32030.

Reid, J.S., Hobbs, P.V., Ferek, R.J., Blake, D.R., Martins, J.V., Dunlap, M.R., Liousse, C., 1998a. Physical, chemical, and optical properties of regional hazes dominated by smoke in Brazil. Journal of Geophysical Research: Atmospheres 103, 32059-32080.

Reid, J.S., Hobbs, P.V., Liousse, C., Martins, J.V., Weiss, R.E., Eck, T.F., 1998b. Comparisons of techniques for measuring shortwave absorption and black carbon content of aerosols from biomass burning in Brazil. Journal of Geophysical Research: Atmospheres 103, 32031-32040.

Reid, J.S., Koppmann, R., Eck, T.F., and , Eleuterio, D.P., 2005b. A review of biomass burning emissions part II: intensive physical properties of biomass burning particles. Atmos. Chem. Phys. 5.

Remer, L.A., Kaufman, Y.J., Holben, B.N., Thompson, A.M., McNamara, D., 1998. Biomass burning aerosol size distribution and modeled optical properties. Journal of Geophysical Research: Atmospheres 103, 31879-31891.

Riemer, N., Vogel, H., Vogel, B., 2004. Soot aging time scales in polluted regions during day and night. Atmos. Chem. Phys. 4, 1885 - 1893.

Rissler, J., Vestin, A., Swietlicki, E., Fisch, G., Zhou, J., Artaxo, P., Andreae, M.O., 2006. Size distribution and hygroscopic properties of aerosol particles from dry-season biomass burning in Amazonia. Atmos. Chem. Phys. 6, 471 - 491.

Rosenberg, P.D., Dean, A.R., Williams, P.I., Dorsey, J.R., Minikin, A., Pickering, M.A., Petzold, A., 2012. Particle sizing calibration with refractive index correction for light scattering optical particle counters and impacts upon PCASP and CDP data collected during the Fennec campaign. Atmos. Meas. Tech. 5, 1147 - 1163.

Rosenfeld, D., Rudich, Y., Lahav, R., 2001. Desert dust suppressing precipitation: A possible desertification feedback loop. Proceedings of the National Academy of Sciences 98, 5975-5980.

Ryder, C.L., Highwood, E.J., Lai, T.M., Sodemann, H., Marsham, J.H., 2013a. Impact of atmospheric transport on the evolution of microphysical and optical properties of Saharan dust. Geophysical Research Letters 40, 2433-2438.

Ryder, C.L., Highwood, E.J., Rosenberg, P.D., Trembath, J., Brooke, J.K., Bart, M., Dean, A., Crosier, J., Dorsey, J., Brindley, H., Banks, J., Marsham, J.H., McQuaid, J.B., Sodemann, H., Washington, R., 2013b. Optical properties of Saharan dust aerosol and contribution from the coarse mode as measured during the Fennec 2011 aircraft campaign. Atmos. Chem. Phys. 13.

Sanford, T.J., Murphy, D.M., Thomson*, D.S., Fox, R.W., 2008. Albedo Measurements and Optical Sizing of Single Aerosol Particles. Aerosol Science and Technology 42, 958-969.

Sarthou, G., Baker, A.R., Blain, S., Achterberg, E.P., Boye, M., Bowie, , Andrew R., C., Peter, L., Patrick, d.B., Hein J. W., Jickells, T.D., Worsfold, P.J., 2003. Atmospheric

iron deposition and sea-surface dissolved iron concentrations in the eastern Atlantic Ocean. Deep Sea Research Part I: Oceanographic Research Papers 50, 1339-1352.

Schafer, J.S., Eck, T.F., Holben, B.N., Artaxo, P., Duarte, A.F., 2008. Characterization of the optical properties of atmospheric aerosols in Amazônia from long-term AERONET monitoring (1993–1995 and 1999–2006). Journal of Geophysical Research: Atmospheres 113, D04204.

Schepanski, K., Tegen, I., Macke, A., 2009. Saharan dust transport and deposition towards the tropical northern Atlantic. Atmos. Chem. Phys. 9, 1173 - 1189.

Schkolnik, G., Chand, D., Hoffer, A., Andreae, M.O., Erlick, C., Swietlicki, E., Rudich, Y., 2007. Constraining the density and complex refractive index of elemental and organic carbon in biomass burning aerosol using optical and chemical measurements. Atmospheric Environment 41, 1107-1118.

Schladitz, A., Muller, T., Kaaden, N., Massling, A., Kandler, K., Ebert, M., Weinbruch, S., Deutscher, C., Wiedensohler, A., 2009. In situ measurements of optical properties at Tinfou (Morocco) during the Saharan Mineral Dust Experiment SAMUM 2006. Tellus B 61, 64-78.

Schladitz, A., Muller, T., Nowak, A., Kandler, K., Lieke, K., Massling, A., Wiedensohler, A., 2011. In situ aerosol characterization at Cape Verde. Tellus B 63, 531-548.

Schmetz, J., Pili, P., Tjemkes, S., Just, D., Kerkmann, J., Rota, S., Ratier, A., 2002. An Introduction to Meteosat Second Generation (MSG). Bulletin of the American Meteorological Society 83, 977-992.

Schmid, O., Chand, D., Karg, E., Guyon, P., Frank, G.r.P., Swietlicki, E., Andreae, M.O., 2009. Derivation of the Density and Refractive Index of Organic Matter and Elemental Carbon from Closure between Physical and Chemical Aerosol Properties. Environmental Science & Technology 43, 1166-1172.

Schroeder, W., Prins, E., Giglio, L., Csiszar, I., Schmidt, C., Morisette, J., Morton, D., 2008. Validation of GOES and MODIS active fire detection products using ASTER and ETM+ data. Remote Sensing of Environment 112, 2711-2726.

Schuster, G.L., Dubovik, O., Holben, B.N., Clothiaux, E.E., 2005. Inferring black carbon content and specific absorption from Aerosol Robotic Network

(AERONET) aerosol retrievals. Journal of Geophysical Research: Atmospheres 110, D10S17.

Schwarz, J.P., Gao, R.S., Fahey, D.W., Thomson, D.S., Watts, L.A., Wilson, J.C., Reeves, J.M., Darbeheshti, M., Baumgardner, D.G., Kok, G.L., Chung, S.H., Schulz, M., Hendricks, J., Lauer, A., KÃ¤rcher, B., Slowik, J.G., Rosenlof, K.H., Thompson, T.L., Langford, A.O., Loewenstein, M., Aikin, K.C., 2006a. Single-particle measurements of midlatitude black carbon and light-scattering aerosols from the boundary layer to the lower stratosphere. J. Geophys. Res. 111.

Schwarz, J.P., Gao, R.S., Fahey, D.W., Thomson, D.S., Watts, L.A., Wilson, J.C., Reeves, J.M., Darbeheshti, M., Baumgardner, D.G., Kok, G.L., Chung, S.H., Schulz, M., Hendricks, J., Lauer, A., Kärcher, B., Slowik, J.G., Rosenlof, K.H., Thompson, T.L., Langford, A.O., Loewenstein, M., Aikin, K.C., 2006b. Single-particle measurements of midlatitude black carbon and light-scattering aerosols from the boundary layer to the lower stratosphere. Journal of Geophysical Research: Atmospheres 111, D16207.

Schwarz, J.P., Gao, R.S., Spackman, J.R., Watts, L.A., Thomson, D.S., Fahey, D.W., Ryerson, T.B., Peischl, J., Holloway, J.S., Trainer, M., Frost, G.J., Baynard, T., Lack, D.A., de Gouw, J.A., Warneke, C., Del Negro, L.A., 2008. Measurement of the mixing state, mass, and optical size of individual black carbon particles in urban and biomass burning emissions. Geophys. Res. Lett. 35, L13810.

Seebaugh, W.R., Lafleur, B.G., Wilson, J.C. 1996. Low Turbulence Inlet for Aerosol Sampling from Aircraft. In AAR Fifteenth Annual Conference, (Orlando, FL).

Seinfeld, J.H., Pandis, S.N., 2006. Atmospheric Chemistry and Physics from Air Pollution to Climate Change.

Shao, Y., Fink, A.H., Klose, M., 2010. Numerical simulation of a continental-scale Saharan dust event. J. Geophys. Res. 115, D13205.

Sheridan, P.J., Norton, R.B., 1998. Determination of the passing efficiency for aerosol chemical species through a typical aircraft-mounted, diffuser-type aerosol inlet system. Journal of Geophysical Research: Atmospheres 103, 8215-8225.

Slinn, W.G.N., Hasse, L., Hicks, B.B., Hogan, A.W., Lal, D., Liss, P.S., Munnich, K.O., Sehmel, G.A., Vittori, O., 1978. Some aspects of the transfer of atmospheric trace

constituents past the air-sea interface. Atmospheric Environment (1967) 12, 2055-2087.

Sokolik, I.N., Toon, O.B., 1996. Direct radiative forcing by anthropogenic airborne mineral aerosols. Nature 381, 681 - 683.

Song, C.H., Carmichael, G.R., 1999. The aging process of naturally emitted aerosol (sea-salt and mineral aerosol) during long range transport. Atmospheric Environment 33, 2203-2218.

Song, C.H., Carmichael, G.R., 2001. A three-dimensional modeling investigation of the evolution processes of dust and sea-salt particles in east Asia. Journal of Geophysical Research: Atmospheres 106, 18131-18154.

Stephens, M., Turner, N., Sandberg, J., 2003. Particle Identification by Laser-Induced Incandescence in a Solid-State Laser Cavity. Appl. Opt. 42, 3726-3736.

Stevenson, D.S., Dentener, F.J., Schultz, M.G., Ellingsen, K., van Noije, T.P.C., Wild, O., Zeng, G., Amann, M., Atherton, C.S., Bell, N., Bergmann, D.J., Bey, I., Butler, T., Cofala, J., Collins, W.J., Derwent, R.G., Doherty, R.M., Drevet, J., Eskes, H.J., Fiore, A.M., Gauss, M., Hauglustaine, D.A., Horowitz, L.W., Isaksen, I.S.A., Krol, M.C., Lamarque, J.F., Lawrence, M.G., Montanaro, V., Müller, J.F., Pitari, G., Prather, M.J., Pyle, J.A., Rast, S., Rodriguez, J.M., Sanderson, M.G., Savage, N.H., Shindell, D.T., Strahan, S.E., Sudo, K., Szopa, S., 2006. Multimodel ensemble simulations of present-day and near-future tropospheric ozone. Journal of Geophysical Research: Atmospheres 111, D08301.

Stocker, T.F., Qin, D., Plattner, G.-K., Tignor, M., Allen, S.K., Boschung, J., Nauels, A., Xia, Y., and, V.B., Midgley, P.M., (eds.) 2013. IPCC, 2013: Climate Change 2013: The Physical Science Basis. Contribution of Working Group I to the Fifth Assessment Report of the Intergovernmental Panel on Climate Change (Cambridge University Press, Cambridge, United Kingdom and New York, NY, USA,), 1535

Streets, D.G., Bond, T.C., Lee, T., Jang, C., 2004. On the future of carbonaceous aerosol emissions. J. Geophys. Res. 109, D24212.

Swap, R., Garstang, M., Greco, S., Talbot, R., Kallberg, P., 2011. Saharan dust in the Amazon Basin. Tellus B 44.

Tang, I.N., 1996. Chemical and size effects of hygroscopic aerosols on light scattering coefficients. Journal of Geophysical Research: Atmospheres 101, 19245-19250.

Tegen, I., Lacis, A., Fung, I., 1996. The influence on climate forcing of mineral aerosols from disturbed soils. Nature 380, 419 - 422.

Textor, C., Schulz, M., Guibert, S., Kinne, S., Balkanski, Y., Bauer, S., Berntsen, T., Berglen, T., Boucher, O., Chin, M., Dentener, F., Diehl, T., Easter, R., Feichter, H., Fillmore, D., Ghan, S., Ginoux, P., Gong, S., Grini, A., Hendricks, J., Horowitz, L., Huang, P., Isaksen, I., Iversen, I., Kloster, S., Koch, D., KirkevÃ¥g, A., Kristjansson, J.E., Krol, M., Lauer, A., Lamarque, J.F., Liu, X., Montanaro, V., Myhre, G., Penner, J., Pitari, G., Reddy, S., Seland, Ã., Stier, P., Takemura, T., Tie, X., 2006. Analysis and quantification of the diversities of aerosol life cycles within AeroCom. Atmos. Chem. Phys. 6.

Todd, M.C., Allen, C.J.T., Bart, M., Bechir, M., Bentefouet, J., Brooks, B.J., Cavazos-Guerra, C., Clovis, T., Deyane, S., Dieh, M., Engelstaedter, S., Flamant, C., Garcia-Carreras, L., Gandega, A., Gascoyne, M., Hobby, M., Kocha, C., Lavaysse, C., Marsham, J.H., Martins, J.V., McQuaid, J.B., Ngamini, J.B., Parker, D.J., Podvin, T., Rocha-Lima, A., Traore, S., Wang, Y., Washington, R., 2013. Meteorological and dust aerosol conditions over the Western Saharan region observed at Fennec supersite-2 during the Intensive Observation Period in June 2011. Journal of Geophysical Research: Atmospheres 118, 8426 - 8446.

Todd, M.C., Washington, R., Martins, J.V., Dubovik, O., Lizcano, G., M'Bainayel, S., Engelstaedter, S., 2007. Mineral dust emission from the Bodélé Depression, northern Chad, during BoDEx 2005. J. Geophys. Res. 112, D06207.

Toon, O.B., Pollack, J.B., Khare, B.N., 1976. The optical constants of several atmospheric aerosol species: Ammonium sulfate, aluminum oxide, and sodium chloride. Journal of Geophysical Research 81, 5733-5748.

Trembath, J., Bart, M., Brooke, J.K. 2012. Efficiencies of Modified Rosemount Housings for Sampling Aerosol on a Fast Atmospheric Research Aircraft (FAAM Technical Note 01).

Turnbull, K., 2010. PSAP Corrections. OBR Technical Note No. 80, Met Office, Exeter, UK.

Twomey, S., 1977. The Influence of Pollution on the Shortwave Albedo of Clouds. Journal of the Atmospheric Sciences 34, 1149-1152.

Van de Hulst, H.C., 1957. Light scattering by small particles. New York (John Wiley and Sons).

Wang, J., Cubison, M.J., Aiken, A.C., Jimenez, J.L., Collins, D.R., 2010. The importance of aerosol mixing state and size-resolved composition on CCN concentration and the variation of the importance with atmospheric aging of aerosols. Atmos. Chem. Phys. 10.

Wang, S.C., Flagan, R.C., 1990. Scanning Electrical Mobility Spectrometer. Aerosol Science and Technology 13, 230-240.

Washington, R., Flamant, C., Parker, D.J., Marsham, J., McQuaid, J.B., Brindley, H., Todd, M., Highwood, E.J., R., C.L., , Chaboreau, J.-P., Kocha, C., Bechir, M., Saci, A., 2012. Fennec - The Saharan Climate System. CLIVAR Exchanges 60, 31-32.

Washington, R., Todd, M., Middleton, N.J., Goudie, A.S., 2003. Dust-Storm Source Areas Determined by the Total Ozone Monitoring Spectrometer and Surface Observations. Annals of The Association of American Geographers 93, 297-313.

Washington, R., Todd, M.C., Lizcano, G., Tegen, I., Flamant, C., Koren, I., Ginoux, P., Engelstaedter, S., Bristow, C.S., Zender, C.S., Goudie, A.S., Warren, A., Prospero, J.M., 2006. Links between topography, wind, deflation, lakes and dust: The case of the Bodélé Depression, Chad. Geophysical Research Letters 33, L09401.

Weast, R.C., 1985. CRC Handbook of Chemistry and Physics, 67th edition Edition. CRC press, Boca Raton, Florida.

Weinzierl, B., Petzold, A., Esselborn, M., Wirth, M., Rasp, K., Kandler, K., SchÜTz, L., Koepke, P., Fiebig, M., 2009. Airborne measurements of dust layer properties, particle size distribution and mixing state of Saharan dust during SAMUM 2006. Tellus B 61, 96-117.

Wendisch, M., Coe, H., Baumgardner, D., Brenguier, J.L., Dreiling, V., Fiebig, M., Formenti, P., Hermann, M., Krämer, M., Levin, Z., Maser, R., Mathieu, E., Nacass, P., Noone, K., Osborne, S., Schneider, J., Schütz, L., Schwarzenböck, A., Stratmann, F., Wilson, J.C., 2004. Aircraft Particle Inlets: State-of-the-Art and Future Needs. Bulletin of the American Meteorological Society 85, 89-91.

Wex, H., Petters, M.D., Carrico, C.M., Hallbauer, E., Massling, A., McMeeking, G.R., Poulain, L., Wu, Z., Kreidenweis, S.M., Stratmann, F., 2009. Towards closing the gap between hygroscopic growth and activation for secondary organic aerosol: Part 1 – Evidence from measurements. Atmos. Chem. Phys. Discuss. 9, 955-989.

Whitby, K.T., 1978. The physical characteristics of sulfur aerosols. Atmospheric Environment (1967) 12, 135-159.

Willeke, K., Brockmann, J.E., 1977. Extinction coefficients for multimodal atmospheric particle size distributions. Atmospheric Environment (1967) 11, 995-999.

Williams, E., Rosenfeld, D.M., N. Gerlach, J. Gears, N. Atkinson, L. Dunnemann, N. Frostrom, G. Antonio, M. Biazon, B. Camargo, R. Franca, H. Gomes, A. Lima, M.M., R. Manhaes, S. Nachtigall, L. Piva, H.Q., W. Machado, L. Artaxo, P. Roberts, G. Renno, N. Blakeslee, R. Bailey, J, B., D. Betts, A. Wolff, D. Roy, B. Halverson, J. Rickenbach, T. Fuentes, J. Avelino, E., 2002. Contrasting convective regimes over the Amazon: Implications for cloud electrification. J. Geophys. Res. 107, 8082.

Wilson, J.C., Lafleu, B.G., Hilbert, H., Seebaugh, W.R., Fox, J., Gesler, D.W., Brock, C.A., Huebert, B.J., Mullen, J., 2004. Function and Performance of a Low Turbulence Inlet for Sampling Supermicron Particles from Aircraft Platforms. Aerosol Science and Technology 38, 790-802.

Wiscombe, W.J., 1980. Improved Mie scattering algorithms. Appl. Opt. 19, 1505-1509.

Wu, Z., Colbeck, I., 1996. Studies of the dynamic shape factor of aerosol agglomerates. Europhys. Lett. 33, 719.